



**HAL**  
open science

# Quantum dots and upconverting nanoparticles : Bioconjugation and time-resolved multiplexed FRET spectroscopy for cancer diagnostics

Shashi Bhuckory

► **To cite this version:**

Shashi Bhuckory. Quantum dots and upconverting nanoparticles : Bioconjugation and time-resolved multiplexed FRET spectroscopy for cancer diagnostics. Biotechnology. Université Paris Saclay (COMUE), 2016. English. NNT : 2016SACLS447 . tel-01548910

**HAL Id: tel-01548910**

**<https://theses.hal.science/tel-01548910>**

Submitted on 28 Jun 2017

**HAL** is a multi-disciplinary open access archive for the deposit and dissemination of scientific research documents, whether they are published or not. The documents may come from teaching and research institutions in France or abroad, or from public or private research centers.

L'archive ouverte pluridisciplinaire **HAL**, est destinée au dépôt et à la diffusion de documents scientifiques de niveau recherche, publiés ou non, émanant des établissements d'enseignement et de recherche français ou étrangers, des laboratoires publics ou privés.

NNT : 2016SACLS447

THESE DE DOCTORAT  
DE  
L'UNIVERSITE PARIS-SACLAY  
PREPAREE A  
UNIVERSITE PARIS-SUD

ECOLE DOCTORALE N° 575  
Physique et ingénierie : électrons, photons, sciences du vivant  
(Electrical, optical, bio-physics and engineering)

Spécialité de doctorat : Physique

**M. Shashi Bhuckory**

Quantum dots and upconverting nanoparticles: Bioconjugation and time-resolved  
multiplexed FRET spectroscopy for cancer diagnostics

**Thèse présentée et soutenue à Orsay, le 13.12.2016 :**

**Composition du Jury :**

M. Treussart, François	Professeur, Université Paris-Sud	Président
M. Soukka, Tero	Professeur, Université de Turku	Rapporteur
M. Schäferling, Michael	Maître de conférences, BAM	Rapporteur
M. Charbonnière, Loïc	Directeur de Recherche, CNRS, LIMAA, IPHC	Examinateur
Mme. Fragola, Alexandra	Maître de conférences, ESPCI	Examinatrice
M. Reiss, Peter	Directeur de Recherche, CEA, INAC	Examinateur
M. Hildebrandt, Niko	Professeur, Université Paris-Sud	Directeur de thèse



**Titre :** Boîtes quantiques et nanoparticules à conversion ascendante: Bioconjugaison et spectroscopie multiplexé de FRET résolue en temps pour le diagnostic du cancer

**Mots clés :** Boîtes quantiques, complexe de lanthanides, FRET, bioconjugaison, nanoparticules à conversion ascendante, spectroscopie résolue en temps

**Résumé :** La haute sensibilité et l'analyse simultanée de plusieurs biomarqueurs (multiplexage) sont des enjeux essentiels pour permettre des avancées significatives pour le diagnostic médical. De telles avancées permettraient d'augmenter la précocité des diagnostics pour de nombreuses maladies comme le cancer ou des maladies cardiaques. Les immunodosages de FRET (transfert d'énergie par résonance de type Förster) sont basées sur la reconnaissance de biomarqueurs par des anticorps marqués avec des fluorophores et le FRET qui résulte du processus de reconnaissance immunologique. Aujourd'hui des telles immunodosages sont établis en utilisant des lanthanides comme donneurs de FRET et des fluorophores organiques comme accepteurs de FRET.

Néanmoins, ils ne permettent pas de réaliser un multiplexage efficace car l'utilisation de plusieurs différents fluorophores organiques résulte dans un recouvrement spectral. Ce projet a pour but de mettre en application les propriétés optiques exceptionnelles des complexes de terbium (Tb) et des boîtes quantiques (QDs) pour parvenir à des analyses biologiques de FRET multiplexées et ultrasensibles. Nous avons également étudié les propriétés optiques et morphologiques de nouvelles nanoparticules à conversion ascendante de type coeur et coeur/coquille dopées à l'ytterbium (Yb) et des ions d'erbium (Er) comme donneurs de FRET.

**Title :** Quantum dots and upconverting nanoparticles: Bioconjugation and time-resolved multiplexed FRET spectroscopy for cancer diagnostics

**Keywords :** Quantum dots, lanthanide complex, FRET, bioconjugation, upconverting nanoparticles, time-resolved spectroscopy

**Abstract :** Combining high sensitivity with simultaneous analysis of numerous biomarkers (multiplexing) is an essential requirement for significantly improving the field of biomedical diagnostics. Such progresses would allow earlier diagnosis, which is required for numerous diseases such as cancer or cardiac diseases. FRET-immunoassays are based on biomolecular recognition events that occur between biomarkers and two specific antibodies conjugated with different fluorophores. The spatial proximity of the two fluorophores can lead to Förster resonance energy transfer (FRET), which can be detected for biomarker quantification. To date, such assays are established using lanthanide complexes as FRET donors and fluorescence dyes as FRET acceptors.

However, these assays do not provide sufficient multiplexing capability due to spectral overlap, when several acceptor dyes are used. This project aims at exploiting the exceptional photophysical properties of terbium complexes (Tb) and semiconductor quantum dots (QDs) to provide ultrasensitive multiplexed FRET-immunoassays. We also studied the optical and morphological properties of novel core and core/shell upconverting nanoparticles doped with ytterbium (Yb) and erbium (Er) ions as possible FRET-donors for biosensing.





# Acknowledgement

First and foremost I wish to thank my supervisor Prof. Dr. Niko Hildebrandt for his fundamental role and support in my doctoral work. I am grateful for his great trust in my abilities, and his offer of a PhD position in his NanoBioPhotonics group. His guidance, wealth of ideas, knowledge and experience taught me how good experiments are done and made my PhD experience productive, motivating and stimulating. I still remember the first day I started my PhD studies when he said: “always ask how and why! and have fun in your PhD”.

I thank Prof. Dr. Tero Soukka and P.D Dr. Michael Schäferling for being the reviewers of my PhD thesis.

I also want to thank our collaborators Lucia Mattera, Peter Reiss, Loïc Charbonnière, Eva Hemmer and Fiorenzo Vetrone for their kindness, availability and scientific advice they have given me in this work.

Many thanks to all former members who I encountered and current members of the NanoBioPhotonics group, Dr. Jean-François Bryche, Dr. Gregory Barbillon and Dr. Bernard Bartenlian from the C2N, for their encouragement, moral support and for creating a fantastic working atmosphere. My special thanks to Dr. David Wegner and Dr. Xue Qiu for their continuous guidance, patience and valuable time devoted in sharing their technical and scientific knowledge with me. I also thank Koro Sokhona from the C2N for his great humor and annual BBQs during summer in the university.

Many thanks to Molinari fresh grounded coffee for giving me the correct amount of energy to get through the long hours of this thesis writing. Without you I would feel like a zombie every morning and afternoon. Thank you for being the right combination of bitter and sweet.

Last but not least, I am very much indebted to my family and Anna Miodek, who supported me in every possible way to see the completion of this work.

# Publications and Communications

## Publications:

1. S. Bhuckory, O. Lefebvre, X. Qiu, K. D. Wegner, and N. Hildebrandt. Evaluating quantum dot performance in homogeneous FRET immunoassays for prostate specific antigen. *Sensors* **2016**, 16(2), 197 (11 pages).
2. L. Mattera, S. Bhuckory, K. D. Wegner, X. Qiu, F. Agnese, C. Lincheneau, T. Senden, D. Djurado, L. J. Charbonnière, N. Hildebrandt, and P. Reiss. Compact quantum dot-antibody conjugates for FRET immunoassays with subnanomolar detection limits. *Nanoscale* **2016**, 8, 11275-11283.
3. S. Bhuckory, L. Mattera, K. D. Wegner, X. Qiu, Y-T. Wu, L. J. Charbonnière, P. Reiss, and N. Hildebrandt. Direct conjugation of antibodies to the ZnS shell of quantum dots for FRET immunoassays with low picomolar detection limits. *Chemical Communications* **2016**, 52, 14423-14425.

## Patent:

N. Hildebrandt, L.J. Charbonnière, P. Reiss, S. Bhuckory, L. Mattera, K.D. Wegner. Nouveaux conjugués comprenant des nanocristaux semi-conducteurs et leur méthode de préparation. FR 1660647. **11/2016**

## Oral communications :

1. 12<sup>th</sup> International Conference on Nanosciences & Nanotechnologies [5-8 July 2015]  
Thessaloniki, Greece  
Quantum dots for multiplexed clinical diagnostics: rapid FRET immunoassays for simultaneous and sensitive detection of three cancer biomarkers.
2. 1st Conference and Spring School on Properties, Design and Applications of Upconverting Nanomaterials [23-27 May 2016]  
Wrocław, Poland  
Morphological and optical characterization of PEG-modified Er<sup>3+</sup>, Yb<sup>3+</sup>-doped NaGdF<sub>4</sub> upconverting nanoparticles for FRET.
3. Fluorescent Biomolecules and their Building Blocks: Design and Applications [7-11 July 2016]  
Tianjin, China  
Homogeneous time-resolved FRET immunoassays for cancer diagnostics.

### **Poster communications:**

1. International Workshop Nanomaterials for Energy and Environment [18-20 March 2015]  
Université Paris-Sud  
Quantum dot biosensors for clinical diagnostics of prostate specific antigen using homogeneous time-resolved FRET immunoassays.
2. 12<sup>th</sup> International Conference on Nanosciences & Nanotechnologies [5-8 July 2015]  
Thessaloniki, Greece  
Quantum dots for multiplexed clinical diagnostics: rapid FRET immunoassays for simultaneous and sensitive detection of three cancer biomarkers.
3. 14<sup>th</sup> Conference on Methods and Applications in Fluorescence [13-16 September 2015]  
Würzburg, Germany  
Three-dimensional structural analysis of quantum dots using lanthanide-based Förster Resonance Energy Transfer (FRET).
4. 2<sup>nd</sup> meeting on Förster Resonance Energy Transfer in life sciences [3-6 April 2016]  
Göttingen, Germany  
Multiplexed detection of three different tumor biomarkers in a rapid time-gated terbium-to-quantum dot homogeneous FRET immunoassay.

## Contents

1. General introduction .....	1
1.1 Introduction .....	1
1.2 Summary .....	4
2. Background .....	10
2.1 Biomarkers.....	10
2.2 Antibodies .....	13
2.3 Lanthanides .....	17
2.3.1 Introduction.....	17
2.3.2 Lanthanide chelates .....	18
2.3.3 Upconversion nanoparticles.....	23
2.3.4 Applications of lanthanides.....	27
2.4 Quantum dots .....	29
2.4.1 Introduction.....	29
2.4.2 Optical properties of QDs.....	30
2.4.3 Biofunctionalization.....	31
2.5 Immunoassays .....	36
2.6 Förster Resonance Energy Transfer.....	39
2.6.1 Introduction.....	39
2.6.2 FRET theory.....	40
2.6.3 FRET applications.....	44
2.6.4 Measurement techniques.....	50
2.6.5 Time-resolved FRET.....	57

3.	Terbium to commercial QDs FRET immunoassays for PSA detection .....	60
3.1	Introduction.....	60
3.2	Materials and Methods .....	61
3.2.1	Materials.....	61
3.2.2	Methods .....	62
3.3	Results and discussion.....	64
3.3.1	Tb and QD AB conjugates and Tb-QD FRET-pairs .....	65
3.3.2	Homogeneous Time-Resolved FRET immunoassay.....	67
3.3.3	Duplexed Tb-to-QD FRET immunoassay.....	70
3.4	Conclusions.....	71
4.	Terbium to compact QDs FRET immunoassay for PSA detection.....	73
4.1	Introduction.....	73
4.2	Materials and Methods .....	75
4.2.1	Materials.....	75
4.2.2	Methods .....	76
4.3	Results and discussion.....	80
4.3.1	Surface functionalization of the QDs .....	80
4.3.2	Tb-AB and QD-AB conjugates .....	82
4.3.3	FRET immunoassays.....	90
4.4	Conclusions .....	98
5.	Multiplexed detection of tumor markers .....	100
5.1	Introduction.....	100
5.2	Materials and Methods .....	101
5.2.1	Materials.....	101
5.2.2	Methods .....	102
5.3	Results and discussion.....	104
5.3.1	Tb-AB and QD-AB conjugate characterization .....	104

5.3.2	Single quantitative detection of tumor markers.....	107
5.3.3	Multiplexed quantitative detection of tumor markers.....	110
5.4	Conclusions.....	117
6.	Upconverting nanoparticles for bio-sensing .....	119
6.1	Introduction.....	119
6.2	Materials and Methods .....	120
6.2.1	Materials.....	120
6.2.2	Methods .....	120
6.3	Results and discussion .....	125
6.3.1	Morphological characterization.....	125
6.3.2	Optical characterization.....	127
6.3.3	FRET hybridization assay.....	133
6.4	Conclusions.....	136
7.	Summary and Outlook .....	137
7.1	Summary .....	137
7.2	Outlook .....	140
8.	Appendix.....	141
8.1	Abbreviations .....	141
8.2	Antibody fragmentation SDS-PAGE .....	143
8.3	Decay curve fitting.....	145
8.4	Calibration curves for LOD calculation.....	149
9.	Bibliography.....	153
10.	Synthèse en français .....	166

# 1. General introduction

## 1.1 Introduction

“There is plenty of room at the bottom”. Richard P. Feynman, December 1959

The physicist Richard Phillips Feynman, in December 1959, during a talk to the American Physical Society in Pasadena, expressed a hypothesis that there is plenty of room at the bottom. He was undoubtedly referring to the nanoworld, where he imagined the possibilities of man manipulating and controlling individual atoms and molecules but had not the appropriate instruments to validate his hypothesis at that time. Decades later, the advent of the scanning tunneling microscope and of atomic force microscopy became the fundamental events in the history of nanoscience and nanotechnology [1]. To quote Michael Berger: “The development of nanotechnologies is not based on a few big and bold discoveries or inventions. Rather it is a painstakingly slow journey of gradual development; at result of which will be some truly revolutionary products and applications”. These novel materials and their applications have already appeared and by exploiting the new phenomena that take place only at the nanometer scale, scientists and engineers are bringing considerable improvement and revolution in different fields from information technology to medicine. In the medical field, nanoscience and nanotechnology have interesting assets as they represent the ideal scale that biological molecules and structures inside living cells operate. One way of probing inside the infinitely small biological world is by using nano-biosensors. A biosensor is a sensor that contains a biological element capable of recognizing and signaling the presence of an activity of a specific biological molecule in solution. A transducer, which in our case are fluorescent nanoparticles, is used to convert the biochemical signal into a quantifiable signal [2]. Designing nano-biosensors would therefore provide tools for better disease prevention, diagnosis and finding the appropriate treatment faster. This would furthermore enable to realize earlier and more refined diagnosis providing tailor-made effective treatments and therefore reduce the recourse to biopsies and surgeries. These nano-biosensors would therefore be of tremendous utility for the quantification of very low concentrations of cancer biomarkers (also referred to as tumor markers) in bodily fluids and tissues. Detection of these markers would not only allow early prognosis of different cancers and diseases, hence improving the survival rate, but also provide treatment with little or no side-effects on the human body as compared to harsh treatment as chemotherapy when cancer is already at an advanced stage. Blood is the “Alibaba cave” of biomarkers that can reveal the current physiological state of all tissues and the simultaneous

detection in blood/plasma/serum-based samples of ultra-low concentrations of different cancer biomarkers, which are secreted by tumors at the very early stages of growth where treatments are more efficient, are very challenging as they contain loads of different proteins in relatively high content [3–5]. In order to discriminate between the low-abundance of the desired tumor markers we want to identify from a complex mixture of proteins and for the direct application of the sensor in clinical applications, the nano-biosensor should be specific, simple to use, rapid, able to perform multiplexing (*i.e* detection of several targets from a single sample), high-throughput and be highly sensitive.

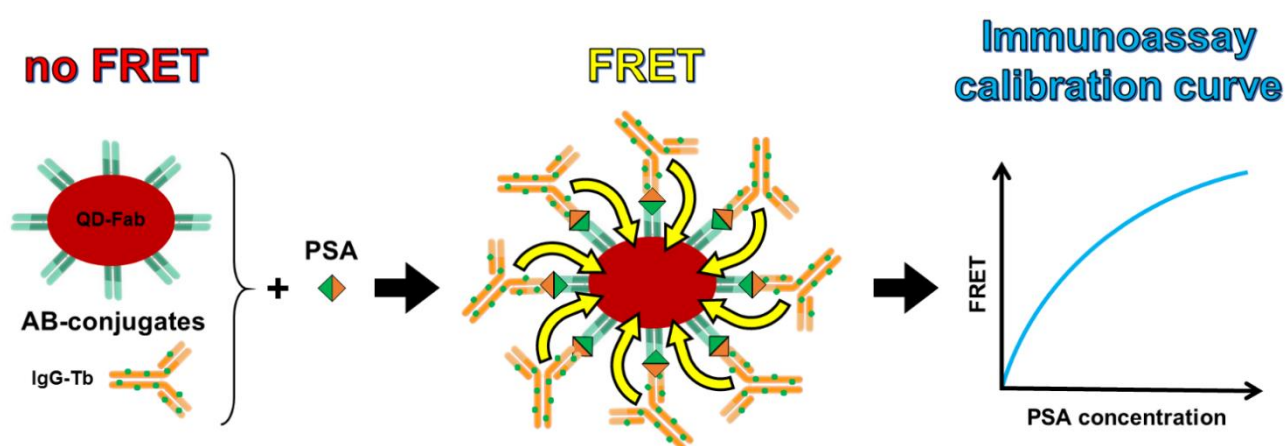
Förster Resonance Energy Transfer (FRET)-based biosensors are among the sensitive techniques, which are currently used for a number of sensing applications in the medical field as they meet with the aforementioned demands. FRET is a non-radiative energy transfer between two molecules and is strongly distance-dependent. Non-radiative energy transfer occurs from an excited donor (FRET-donor) molecule to an acceptor molecule (FRET-acceptor) in its ground state through long-range dipole-dipole interactions. The FRET-donor must be a fluorophore and the FRET acceptor should be able to absorb light at the emission wavelength(s) of the donor but does not necessarily have to emit photons. In order for FRET to occur, the emission spectrum of the donor must overlap with the absorption spectrum of the acceptor, so great care should be taken while choosing the appropriate FRET-pairs (FRET-donor and FRET-acceptor) for the planned experiments. This spectral overlap can be described in terms of Förster distance ( $R_0$ ), which defines the distance between the donor and acceptor at which FRET efficiency is 50%. There exists a multitude of FRET-pairs for bioanalysis, among which we can find organic dyes, fluorescent proteins, metal chelates (*e.g*, lanthanide complexes), upconverting nanoparticles and, semiconductor nanocrystals (quantum dots). The typical  $R_0$  between dyes and/or fluorescent proteins are generally between 2 - 5 nm and can extend to 11 nm by using lanthanides and quantum dots. Ruled by the physics of molecular proximity, the strong distance dependency to  $r^{-6}$ , where  $r$  corresponds to the distance between the FRET-pairs, allows obtaining information on small structural changes in biological processes, kinetic data of reactions and binding events among others. FRET generally takes place at a distance range of *c.a* 1-10, nm which is comparable to the dimensions of most biological interactions. In the case of antibody-antigen association, when a FRET-pair labelled on specific antibodies for specific target recognition are brought close together, changes in the photophysical properties of the FRET-pairs appears due to the extent of energy transfer, which depends on the distance between the FRET-pairs [6–9].

FRET-based immunosensing can be heterogeneous or homogeneous immunoassays. In this thesis we will focus exclusively on homogeneous time-resolved (TR) sandwich based FRET immunoassays since they are sensitive, require no separation or purification steps, allow for short incubation times due to fast solution-phase kinetics and are less time consuming, while the time-resolved mode allows for efficient suppression of short-lived autofluorescence. Briefly, in one-step homogeneous immunoassays the FRET-pairs are “simply” conjugated to specific antibodies and incubated in a solution containing the targeted antigens and upon biological recognition, specific FRET signals can be recorded with no washing steps required[10]. Organic dyes and/or fluorescent proteins are generally the most commonly used FRET-pairs in assays but they are usually pH sensitive, prone to photobleaching and chemical degradation, low quantum yields (QY), and their broad emission spectra leading to spectral crosstalk [11] thus limiting multiplexing capabilities, significantly complicate FRET formats. Furthermore, their short luminescence lifetimes in the nanosecond (ns) range limit their application to steady-state spectroscopy rather than time-resolved spectroscopy, which can be more sensitive [9,12]. Luminescent lanthanide complexes (LLC) as FRET-donor represent an excellent choice in combination to different FRET-acceptors, such as organic dyes, fluorescent proteins and quantum dots (QDs), because the lanthanide ions (for *e.g.*, samarium, europium, terbium) offers unique photophysical properties. Upon chelation with ligands, a large Stokes shift arises and due to the forbidden f-f transitions in the lanthanide ions, LLC emit with very characteristic and narrow emission lines in the visible and near-infrared regions, with luminescence lifetimes up to the millisecond (ms) range [13,14]. Upconverting nanoparticles are lanthanide-doped crystals which have the ability of upconversion emission [15]. Upconversion is a process where low energy light (near-infrared (NIR) or infrared (IR)) is converted to higher energies (UV to NIR) by means of stepwise absorption and energy transfer processes. Similar to lanthanide complexes, lanthanide-doped upconversion nanoparticles (UCNPs) possess very narrow emission bands in the broad wavelength region spanning the UV, visible and NIR allowing them to function as energy donors with an assortment of acceptors in FRET-based biosensing [16–19]. Quantum dots are semiconductor nanocrystals that possess exceptional optical properties and offer several advantages over traditional organic fluorescent dyes such as higher absorption cross-sections, fluorescence quantum yields and photostability. As the size of the QDs is reduced, the phenomena of quantum confinement arises which results in size-tunable absorption and emission bands. The narrow symmetrical Gaussian emission and broad excitation spectra, nanosecond lifetimes together with the aforementioned properties of the QDs (FRET-acceptor), and in combination with luminescent terbium complexes (Tb, FRET-donor) and TR-FRET spectroscopy (the long decay time in the millisecond range of Tb can be

time-gated after pulse excitation to allow for suppression of short-lived sample fluorescence and fluorescence from directly excited QDs), make these FRET-pairs ideal for sensitive and multiplexed detection with large  $R_0$  (7 – 11 nm). Moreover, the ratiometric format, by analyzing the photoluminescence (PL) intensities of the FRET-pairs in presence of FRET, can be very advantageous for analytical applications as they offer an instantaneous suppression of sample and excitation source fluctuations [13,20–22].

## 1.2 Summary

The aim of this thesis is to utilize the exceptional photophysical properties of Tb complexes and QDs systems for ultrasensitive multiplexed TR-FRET immunoassays of cancer protein biomarkers detection, and the study of the optical and morphological properties of novel core and core/shell upconverting nanoparticles doped with ytterbium (Yb) and erbium (Er) ions as possible FRET-donors for biosensing. For TR-FRET sandwich immunoassays, monoclonal antibodies (ABs) against differently sized antigens - carcinoembryonic antigen (CEA), neuron-specific enolase (NSE) and total prostate specific antigen (TPSA) - have been labelled to Tb and different emitting QDs. The immunoassay gives rise to the formation of [donor-AB]-antigen-[acceptor-AB] complexes and a close proximity of Tb and QD results in FRET as depicted in **Scheme 1.1**. It should be noted in our FRET system that the FRET efficiency for multiple Tb-donor per QD-acceptor does not change as compared to a single-donor/acceptor system.



**Scheme 1.1.** Principle of a sandwich Tb-to-QD FRET immunoassay which contains (left) monoclonal Tb- and QD-antibody conjugates against an antigen. (Middle) Formation of [Tb-AB]-antigen-[QD-AB] complexes upon addition of antigen resulting in FRET due to a close proximity of Tb and QD. (Right) The assay leads to a typical immunoassay calibration curve, for which the FRET signal increases with increasing antigen concentration until a saturation point when antigen concentration equals to Tb-ABs or QD-ABs concentration.

However, there is an increased probability of QD FRET-sensitization with an increasing number of Tb-donors due to the long luminescence lifetimes of Tb [23,24]. The use of bulky QDs and large biomolecules such as full sized IgGs and relatively large antigens, in a sandwich based format might affect the FRET efficiency, hence the sensitivity of detection due to the strong distance dependency between the FRET-pairs [7].

The first study (**Chapter 3**) demonstrates the possibility to overcome the large distances in homogeneous FRET immunoassays and providing at the same time high sensitivity and multiplexing capability in the use of luminescent terbium complexes as FRET-donors for thick polymer PEG coated QD-acceptors. Tb-AB conjugates were obtained by a fully random labeling of Tb-NHS via various amino groups available on the antibody surface. In a less random coupling, three commercially available QDs with emission maxima at 605, 655 and 705 nm (denoted as QD605, QD655 and QD705 respectively) from Life Technologies possessing a thick polymer poly(ethylene) glycol (PEG) coating and surface amino functionalized were conjugated to fragmented antibodies (F(ab)) through sulfhydryl chemistry [25]. The amine-reactive QDs were converted to maleimide-reactive QDs by using the heterobifunctional crosslinker sulfo-EMCS having NHS ester and maleimide reactive groups [26]. The maleimide activated QDs were then conjugated to the F(ab) via free sulfhydryl groups which showed to be advantageous for FRET immunoassays due to their smaller size and the higher amount of ABs per QD [25]. The performance of our immunoassays were evaluated with QD605, QD655 and QD705 as acceptors in FRET assays with Tb donors because the variations in shapes, sizes, spectral overlap and PL wavelength range leads to differences in FRET and detection efficiencies. The photophysical properties (steady-state and time-resolved) of the assay constituents (Tb and QD AB-conjugates) and their performance in Tb-QD FRET immunoassays for the detection of PSA in low volume serum samples were carried-out. Such characterization and assay evaluation within comparable immunoassays for the same antigen are indispensable for designing and optimizing such homogeneous FRET immunoassays, in particular for multiplexed detection with different QD colors. Calculation of the overlap integrals resulted in large  $R_0$  for all the Tb-QD systems and provided measurable QD-FRET sensitization within the [Tb-AB]-PSA-[QD-AB] binding system even with the thick QD polymer coatings. All three Tb-to-QD FRET systems showed increasing time-gated FRET signals with increasing PSA concentrations and immunoassay calibration curves could be successfully recorded. Limits of detection (LODs) calculated using the calibration curves showed the highest sensitivity (low LOD) for the Tb-QD705 system followed by Tb-QD655 and Tb-QD605 systems. We also show that factors as labeling ratios,  $R_0$ , and Tb PL background were found to influence the detection

sensitivity. Multiplexed capability using different Tb-QD FRET-pairs were demonstrated by preparing a duplexed immunoassay against PSA that contained the two QD-conjugates (QD655 and QD705) with the lowest LODs and their calibration curves were observed to follow a similar trend as the single Tb-QD FRET-pairs. The LODs for PSA in 50  $\mu$ L serum samples measured on a commercially available clinical fluorescence plate reader were in the sub-nanomolar concentration range and below the clinical cut-off value of 4 ng/mL for the QD655 and QD705 based FRET-pairs. As most biomarkers have different clinical cut-off values, we also concluded that QD705 should be used for the biomarker with the lowest cut-off and QD605 for the one with the highest cut-off. Duplexing capability was demonstrated in PSA assays containing both QD655 and QD705 AB conjugates. Our results provide important information concerning the development of QD-based FRET immunoassays for multiplexed clinical diagnostics because the AB-conjugation method we developed is applicable to any commercially available amino-functionalized QDs, which exist in many other colors than the three used in this study.

The second study focuses on a novel QD functionalization and bioconjugation approach, which yielded stable compact QDs and highly luminescent QD-AB conjugates for improved Tb-QD TR-FRET immunoassay against PSA. These QDs were synthesized by the INAC-SyMMES laboratory, CEA Grenoble. Based on the results of the first study involving QDs with thick polymer coating that showed the possibility of detecting sub-nanomolar range of PSA, the design of compact QDs would allow overcoming the major limitations for developing QD-FRET immunoassays with LODs competitive to commercial kits which are: (i) insufficient colloidal stability of compact QDs in biological media, (ii) thick QD surface coatings (e.g., PEG, polymer, or lipid coatings that protect the inorganic QD from the biological environment and render them hydrosoluble), and (iii) insufficient AB-conjugation strategies for QDs with thinner organic capping. For this purpose aqueous phase transfer of InPZnS/ZnSe/ZnS QDs emitting at 530 nm (QD530) and of commercial hydrophobic (Life Technologies) CdSe-based QDs emitting at 605 and 705 nm (QD605 and QD705 respectively) was achieved by ligand exchange with zwitterionic penicillamine (Pen) and post-functionalization was carried-out to produce maleimide-activated QDs using a Mal1 bifunctional ligand containing a lipoic acid anchoring function and a maleimide functional group space by three PEG moieties for conjugation with free sulfhydryl containing groups of F(ab). We also show for the first time another post-functionalization strategy which involved direct coupling ABs (IgGs, F(ab)<sub>2</sub> and F(ab)) on the surface of the colloidal compact QD705 (highest sensitivity) without any crosslinkers to further reduce the distance of energy transfer between Tb-donor and QD-acceptor. TEM analysis was

performed on the QDs to confirm their size and dispersibility while Fourier transform infrared (FTIR) spectra and gel-agarose proved the successful functionalization and conjugation with Mal1 and F(ab) respectively. For these Tb-QD FRET-pairs, large  $R_0$  were calculated revealing the highest  $R_0$  for QD705 and small changes in the photophysical properties of the QDs at different stages of phase transfer, post-functionalization with Mal1 and upon conjugation to F(ab) were observed. In this study only full photophysical characterization of the direct conjugation of IgGs to QD705 was performed due to low collected volume samples from the direct conjugation of F(ab)<sub>2</sub> and F(ab). FRET-assays against PSA in serum-based samples, using QDs conjugated to F(ab) through Mal1, corresponding to the Tb-QD605/705 systems allowed quantification of the LOD, while the Tb-QD530 assay yielded a very low FRET signal most probably related to the lower  $R_0$  (6.1 nm), which could not be used to calculate a LOD. Tb-QD705 assay using the direct conjugation of ABs to the QD's surface provided even better sensitivities than when using Mal1. Our LODs of the two Tb-QD FRET immunoassays (using 605 nm and 705 nm emitting QDs) are not only well below the clinical cut-off value of PSA (4 ng/mL), but the utilization of the compact QD-AB conjugates also provided a 6.2 and 25 fold sensitivity improvement compared to the same commercially available QDs that were purchased with a standard PEG/polymer-based coating used in the first study. These highly sensitive and homogeneous Tb-to-QD FRET immunoassays are suitable for any other biomarker against which two specific ABs exist. Our results show that the compact QD-AB conjugates have a large potential for improving diagnostic applications, and given the multiplexing capability of Tb-QD FRET, we are confident that these small nanoparticle-AB fluorescent probes will become important players in clinical *in vitro* diagnostics.

In the third study we attempt to detect CEA, NSE and TPSA from a single serum-based sample. The importance of detecting several biomarkers lies within the fact that a single biomarker does not contain sufficient information in order to make a clear diagnosis about a disease and the combination of different biomarkers increases the content of information about the state or type of cancer. CEA and NSE are among the tumor markers where their levels are monitored in combination with other tumor markers to get a clear diagnosis of small-cell lung cancer (SCLC) and/or non-small-cell lung cancer (NSCLC) and TPSA (sum of free PSA and PSA bound to proteins) which is a tumor marker for prostate cancer. As FRET is highly distance dependent, the choice of F(ab)<sub>2</sub> conjugation to QDs would result in a shorter separation distance between the QDs and Tb in sandwich immunoassays, hence higher FRET efficiencies and sensitivities than when using IgGs. Furthermore, the small size of the F(ab)<sub>2</sub> together with its 2 binding sites for more binding opportunity, would be beneficial to the increasing

biomarker sizes (32 kDa to 180 kDa) in the FRET immunoassays. Photophysical characterizations of the FRET-pairs (Tb-donor and QD-acceptor) were performed and the labeling ratio of Tb per AB and QD per AB were estimated by UV/Vis absorption spectroscopy. As the first study suggested that for different clinical cut-off values QD705 should be used for the biomarker with the lowest cut-off and QD605 for the one with the highest cut-off, antibodies against CEA, NSE and TPSA have been conjugated to eBioscience QDs eQD650, eQD605 and Life Technologies QDs iQD705 respectively. Our multiplexed homogeneous Tb-QD FRET immunoassay has been able to simultaneously detect 3 differently sized tumor markers from a single serum sample of CEA (180 kDa), NSE (95 kDa) and PSA (32 kDa) using Tb and QD probes conjugated to their respective monoclonal antibodies conferring no biological crosstalk. Taking advantage of the narrow and Gaussian emission spectra of the QDs and the well separated Tb emission bands together with the appropriate optical bandpass filters, allowed negligible optical crosstalk. Therefore no matrix correction was necessary to determine the tumor markers concentration. LODs calculated in 50  $\mu$ L volume samples were all below the clinical cut-off levels of the tumor markers, where higher LODs we observed for the triplexed format as compared to the singleplex format except for TPSA. The contamination of the eQD605/650 detection channels from the 3 times more Tb signal resulted in an increase in LOD whereas virtually no Tb emission can be detected in the iQD705 detection channel. A “worst-case scenario” assay was performed where we challenged our immunoassay with a combination of high and low target concentrations. Overall, CEA and TPSA could be detected with high precision with minor deviations from known concentrations except for NSE which presented an underestimation in its concentrations in a specific range of concentration with a combination of high and low concentrations of CEA and low concentrations of TPSA. Detection limits of the tumor markers in the sub-nanomolar range (few ng/mL) within a complex environment as in serum and containing 9 different biomolecules proves the immediate applicability to diagnostic applications for sensitive multiplexed measurements.

The forth study comprised the investigation of new generation of fluorophores, known as upconversion nanoparticles (UCNPs). Upconversion is a process where low energy light (near-infrared (NIR) or infrared (IR)) is converted to higher energies (ultraviolet or visible) by means of multiple absorptions or energy transfers in a non-linear process [27,28]. This property (among others) allow them to possess great potential for imaging and biodetection assays in both *in vitro* and *in vivo* applications [27]. Similar to lanthanide complexes, lanthanide-doped UCNPs possess very narrow emission bands in the visible wavelength region allowing them to function as energy donors with an assortment of acceptors in FRET-based biosensing. Three

types of UCNPs were analyzed in this thesis so as to choose the best candidate as FRET-donor. Core and core/shell UCNPs were synthesized by our collaborators from Institut National de la Recherche Scientifique (INRS), Québec Canada, which were  $\text{NaGdF}_4:\text{Er}^{3+},\text{Yb}^{3+}$  (core-doped),  $\text{NaGdF}_4:\text{Er}^{3+},\text{Yb}^{3+}/\text{NaGdF}_4$  (core-doped/shell) and  $\text{NaGdF}_4/\text{NaGdF}_4:\text{Er}^{3+},\text{Yb}^{3+}$  (core/shell-doped). These UCNPs were rendered ligand-free and surface functionalization with amino-PEG-COOH was performed through electrostatic interaction in order to generate functional groups on the surface of UCNPs for possible biomolecule attachment. TEM measurements of the UCNPs showed rather spherical particles and XRD patterns showed that they are highly crystalline and comparison with the reference pattern revealed a hexagonal  $\beta$ -structure of  $\text{NaGdF}_4$ . FTIR spectra confirmed presence of the amino-PEG-COOH polymer on the surface of the UCNPs. DLS measurements showed that the three types of PEGylated-UCNPs were not at all stable in various buffers including physiological buffers where aggregation was observed. Hence, optimized surface functionalization strategies should be envisaged in order to produce good dispersibility in buffers as conjugation to biomolecules often requires using buffers of different pH. Upconversion emission in the visible range of the electromagnetic spectrum was observed for core-doped, core-doped/shell and core/shell-doped nanoparticles upon excitation at 980 nm. Green emissions occurred at the following transition states:  $(^2\text{H}_{11/2}, ^4\text{S}_{3/2}) \rightarrow ^4\text{I}_{15/2}$  and red emission from  $^4\text{F}_{9/2} \rightarrow ^4\text{I}_{15/2}$ . As compared to the core/shell UCNPs, the lifetime of the core-doped nanoparticles are smaller and can be attributed to surface-quenching effect of  $\text{Er}^{3+}$  ions at the core surface by high vibrational energy modes of OH groups from the surrounding solvent. Growing a shell around the doped-core, greatly suppresses surface-quenching effects as the shell brings a better protection between the core and the surrounding environment. The core/shell-doped nanoparticles showed unexpected long luminescent lifetimes as compared to the core-doped/shell nanoparticles, favoring them to be suitable FRET-donors as the presence of  $\text{Er}^{3+}$  ions on the surface would result in efficient FRET to an acceptor molecule in close distance.

After this introduction, a theoretical background on biomarkers (protein tumor markers in this thesis), FRET, lanthanides and quantum dots will be presented as well as their application as FRET-donors and FRET-acceptors. Four experimental studies will follow in a paper-style with an introduction, materials and method, results and discussion, and a conclusion. A summary addressing the results obtained from the experimental studies will be discussed and an outlook on future research. Appendix and bibliography follow at the end of the thesis.

## 2. Background

### 2.1 Biomarkers

Interaction of chemicals with biological systems is recognized by the analysis of tissues and body fluids for chemicals, metabolites of chemicals, enzymes and other biological substances. These substances known as biomarkers, short for “biological markers”, have been defined in 1988 by the National Institutes of Health Biomarkers Definitions Working Group as “a characteristic that is objectively measured and evaluated as an indicator of normal biological processes, pathogenic processes, or pharmacologic responses to a therapeutic intervention” [29–31]. Biomarkers which can also reflect the entire spectrum of a disease from its early to terminal stage, play therefore a vital role in understanding the prediction, cause, diagnosis, progression, regression, or outcome of disease treatments [32]. Biomarkers can be classified into the following categories: 1) predisposition, 2) diagnostic, 3) prognostic and 4) predictive biomarkers. Predisposition biomarkers give an increased probability of developing a health disorder based on someone’s genetic family history, whereas diagnostic biomarkers confirm whether or not a patient has a certain disease. Prognostic biomarkers, on the other hand, indicate how a health disorder will evolve after primary diagnosis and treatment of a disease, thus predicting recurrence. Predictive biomarkers help to foretell which specific treatment would be beneficial to a patient [33,34]. Examples of biomarkers can include everything from the recording of blood pressure, electrocardiogram, imaging tests to more complex laboratory tests from blood, urine or tissues [29,35]. One type of biomarker which is secreted in tissues, blood, and other body fluids are tumor biomarkers (or tumor markers) that are produced by cancer or by other cells of the body in response to cancer or certain benign conditions [36]. Most tumor markers are secreted by normal cells as well as by cancer cells but in the case of cancerous conditions, these markers are produced in higher levels. Therefore, the early diagnosis of tumor markers is crucial at such stage as they offer the high probability of successful treatment. These tumor markers include a large variety of molecules such as peptides, proteins, DNA, micro-RNA, metabolites and circulating tumor cells among others [35,37–40].

Normal cells in the body age and die, and are replaced by new cells in a controlled and orderly manner. When this routine breaks down, cancer begins. Cancer is the malignant growth or tumor resulting from an uncontrolled abnormal division of cells which can invade neighborhood tissues and also spread to other parts of the body [40,41]. A tumor is said to be benign when the

tumor cells clustered in a single mass stays in one spot of the body. A complete cure is usually achieved by surgical removal of the mass. In the case of malignant tumors, their cells break off from the cancer and have the ability to invade and destroy surrounding healthy tissues by moving throughout the body using the bloodstream or lymphatic vessels, forming secondary tumors, or metastases at different sites in the body (**Figure 2.1**). This process called metastasis is a very severe condition that is hard to eradicate [42]. Among the large variety of tumor markers, circulating tumor cells (CTC) and protein markers could be measured to detect cancer activity in the body from a simple blood sample. CTC detection, a relatively new technique for early metastasis detection has been able to provide independent prognostic information and has shown a direct correlation of its presence in the blood of tumor patient with poor survival rate of patients suffering from metastatic prostate, breast, and colon cancers [43–45]. In comparison to *ca.*  $5 \times 10^6$  white blood cells and *ca.*  $5 \times 10^9$  red blood cells per mL of blood, the typical concentration of CTC (1 CTC in 1 mL) of blood is extremely low. To date the only method, Food and Drug Administration (FDA) approved, for the enumeration of CTC that has been cleared for clinical use in breast, colorectal and prostate cancer patients, is the CellSearch™ CTC Test by Veridex [45–49]. Protein tumor markers are specific proteins often produced by cancer tumors that can serve as a marker for a cancer. These protein tumor markers are predominantly found in blood and sometimes in urine [40]. In this thesis, we will focus exclusively in the detection of cancer protein markers (or tumor markers/biomarkers).

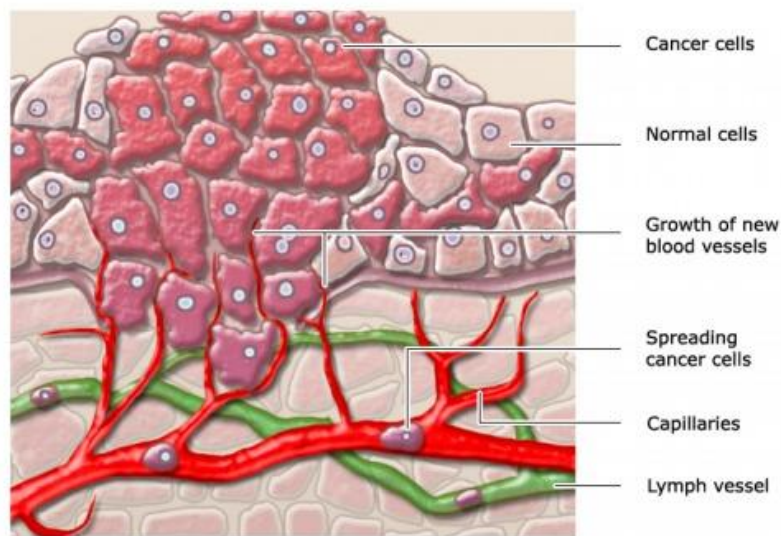


**Figure 2.1.** Representation of malignant cancer propagation. The tumors grow by creating their own blood vessels to get the necessary supply to keep them from surviving and getting bigger. Metastasis occurs when the cancer cells spreads through the bloodstream or lymphatic system to other parts of the body forming tumor somewhere else [50].

Cancer protein biomarkers are among the commonly used biomarkers for cancer detection as they can be used for early cancer detection, determine whether a particular treatment is working and/or to detect recurrence or progression during follow-up after treatment [40]. Despite their usefulness, no tumor marker could be identified to date to be sensitive or specific enough to be used on its own to screen for cancer. In most cases, tumor markers are used in combination with imaging, biopsy and associated clinicopathological information before a clinical decision is made. For example, carcinoembryonic antigen (CEA) which is used to detect colon cancer recurrence is produced only in 70-80 % of colon cancer cases and elevated levels of CEA are present only in 25 % of cases that are limited to the colon [51]. Although many strategies exist for new biomarker discoveries, among which we find, gene-expression profiling, peptidomics, cancer-biomarker-family approach, secreted protein approach, cancer researchers are turning to proteomics which is a strategic technology for the development and discovery of new protein biomarkers [41,52,53]. Mass-spectrometry-based methods of proteomic analysis, through its improved and including more-advanced technology, enables increased throughput and more reliable data for new protein biomarker profiling [52]. As the majority of current drug targets are proteins, most of the biomarkers used in clinical studies are based on proteomic applications as studying protein-protein interactions can be an innovative and an efficient way to find novel cancer biomarkers [54,55]. Furthermore, the majority of licensed tests available for disease detection are protein-based assays [56]. We can however note that even though an enormous number of publications on tumor biomarkers have been published in these recent years, only a handful have entered clinical use due to the absence of a clearly defined validation pathway for advancing a newly discovered biomarker into the clinic. The five phases of biomarker developments, which are preclinical exploratory studies, assay development and validation, retrospective longitudinal clinical repository studies, prospective screening and randomized control trials, should therefore undergo rigorous and effective validation for adoption in clinical practice [52,57]. **Table 2.1** lists some of the protein tumor markers FDA-approved which are currently used in clinical practice [58].

Protein biomarkers are often interrogated and quantified by the immunoassay method (further explained in **section 2.5**), which depends on the reaction of an antibody and an antigen. Detection of the amount of antigen present in a sample is achieved by detection of the antibody-antigen (immuno) complex [10,59]. In order to quantify the signal from the immuno-complex, there exists a wide range of labels such as radioisotopes, enzymes, and fluorophores. Among the widely used heterogeneous enzyme-linked immunosorbent assay (ELISA), many other immunoassay methods are applied in pharmaceutical analysis such a radio-, fluoro-, and chemiluminescence-immunoassays [59]. They will be discussed in **section 2.5**.

## 2.2 Antibodies

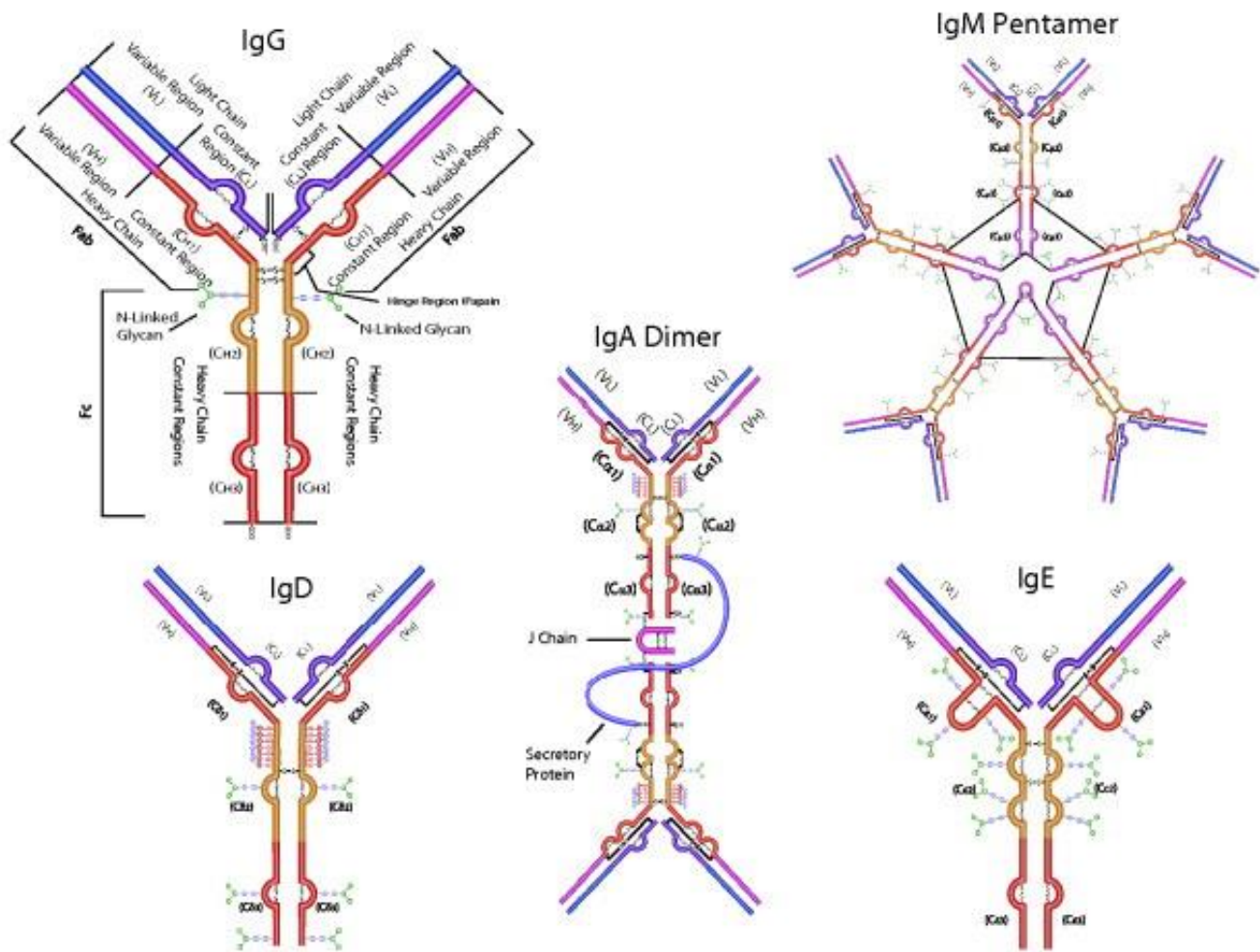


**Figure 2.2.** Structure of the 5 classes of antibodies based on number of Y units and type of heavy chain [www.sigma-aldrich.com].

Antibodies are glycoproteins belonging to the “immunoglobulin supergene family” that are produced in response to an invading substance in the body. IgG, IgM, IgA, IgD, and IgE (**Figure 2.2**) are the five classes of immunoglobulin in most higher mammals and they differ in size, charge, amino acid composition, and carbohydrate content. Antibodies exist as one or more copies of a Y-shaped molecule with each Y-shape consisting of four polypeptide chains: two identical heavy chains which are linked to each other by disulfide bonds and two identical light chains where each light chain is linked to a heavy chain by disulfide bonds. The light chain has two domains namely variable ( $V_L$ ) and constant ( $C_L$ ). The heavy chain is composed of four domains, which consists of one variable ( $V_H$ ) and three constant ( $C_{H1}$ ,  $C_{H2}$  and  $C_{H3}$ ). The Y-shaped unit of the antibody can be divided into three fragments: two identical fragments which

contain the antigen-binding activity (F(ab) fragments) and another fragment that contains no antigen-binding activity called Fc fragment short for Fragment crystallizable. The structure of the Y-shape of an antibody is represented in **Figure 2.2** top left. IgGs with an approximate molecular weight of 150 kDa, consist of one Y-shape unit and are the most abundant class of antibodies in blood, totaling up to 80 % of the total serum antibodies [10,60–62]. IgGs are also found in plasma which is a mixture of serum with clotting factors and fibrin. Measurement of antibodies is usually done in serum as compared to plasma because serum lacks clotting factors and large fibrinogen proteins, hence more specific detection of antibodies [63]. IgGs are almost exclusively used in immunoassays and can be covalently modified to accommodate labels (**see section 2.4.3**) [10]. Antigens are substances (*e.g* foreign proteins) that the body is trying to eliminate by provoking an immune response [64]. Antibodies specific to the antigen can be generated by vaccinating animals with the antigen of interest through the process called immunization [10]. Two distinct processes by which antigens are recognized in the body are by 1) B cells and their surface antibodies and 2) by the T cell receptor on T cells [65]. Antibodies produced by B cells due the presence of an antigen can bind specifically to a small site on the antigen called an epitope. The antibodies produced can be polyclonal or monoclonal. A polyclonal antibody has the ability to recognize multiple epitopes on an antigen while a monoclonal antibody is restricted to only one epitope. The antigen-antibody binding reaction is reversible and follows the basic principles of thermodynamic for any reversible biomolecular interaction. At equilibrium:

$$K_{eq} = \frac{k_a}{k_d} = \frac{[\text{antibody} - \text{antigen complex}]}{[\text{antibody}] \times [\text{antigen}]} \quad (2.1)$$

where  $K_{eq}$  is the equilibrium constant and is equal to the ratio between the association ( $k_a$ ) and dissociation ( $k_d$ ) rate constants;  
 $[\text{antibody-antigen complex}]$  is the molar concentration of the antibody and antigen complex;  
 $[\text{antibody}]$  and  $[\text{antigen}]$  are the molar concentrations of the reactants.

$K_{eq}$  cannot be determined for polyclonal antibodies due to their heterogenic binding properties with their antigens. Factors affecting the antibody-antigen reaction include temperature, pH, and ionic strength of the solvent [10,66].

In this thesis, we will use serum-based homogeneous fluoroimmunoassays in a sandwich format where monoclonal antibodies (IgGs) labelled with fluorophores bind to specific epitopes of the tumor marker. The antigens (tumor markers) used in this thesis are carcinoembryonic

antigen (CEA), neuron-specific enolase (NSE) and total prostate specific antigen (TPSA) (*cf* **Table 2.1**, highlighted in red). CEA is a glycoprotein with an approximate molecular weight of 180 kDa and is essentially secreted and excreted by digestive tract glandular cancers (colon, rectum, pancreas, stomach) and their metastases can be found in the lung, breast, bladder, ovary, and thyroid. CEA is mainly assayed in the field of colorectal cancers but when its level is related to metastatic propagation in breast and lung, its variation can be a useful indicator when monitoring patient response to therapy [67]. NSE is a glycolytic enzyme with a molecular weight that is approximately 95 kDa and is normally present in neurons, peripheral nerve tissues and neuroendocrinal tissues, and also in cells of the amine precursor uptake decarboxylation (APUD) system. NSE is not a specific tumor marker and was found to be frequently overexpressed in patients with small cell lung carcinoma (SCLC) and neuroblastoma. Its clinical use is in the follow up and therapy control for neuroblastoma and SCLC, and includes differential diagnosis for SCLC [68–70]. PSA is a glycoprotein of the kallikrein group with an approximate molecular weight of 32 kDa and is found almost exclusively in the prostate. PSA plays a major role in the liquefaction of seminal fluid and circulates simultaneously in two forms in serum: free PSA (fPSA) and complexed PSA (TPSA, which is the sum of fPSA and PSA complexed to anti-proteases). Increased concentrations of TPSA can result in men with malignant as well as benign prostatic diseases such as hyperplasia or prostatitis. To improve specificity it has been reported that the two forms of PSA can be measured where a low ratio of fPSA to TPSA is an indication of malignant prostatic diseases. Free PSA testing has mostly been used as additional test along with TPSA, particularly in men who have already undergone a negative prostate biopsy and have a PSA that remains elevated [71,72]. As soon as prostate cancer has been diagnosed, TPSA assays are used to establish the cancer stage, the tumor response after therapy for early detection of any relapse.

**Table 2.1.** Modified list of protein tumor markers, FDA-approved, currently used in clinical practice [58].

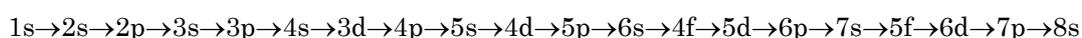
<b>Biomarker</b>	<b>Clinical use</b>	<b>Cancer type</b>	<b>Specimen</b>	<b>Year first approved or cleared</b>
Pro2PSA	Discriminating cancer from benign disease	Prostate	Serum	2012
ROMA (HE4 CA-125)	Prediction of malignancy	Ovarian	Serum	2011
OVA1 (multiple proteins)	Prediction of malignancy	Ovarian	Serum	2009
AFP-L3%	Risk assessment for development of disease	Hepatocellular	Serum	2005
Circulating Tumor Cells (EpCAM, CD45, cytokeratins 8, 18+, 19+)	Prediction of cancer progression and survival	Breast	Whole blood	2005
c-Kit	Detection of tumors, aid in selection of patients	Gastrointestinal stromal tumors	FFPE tissue	2004
CA19-9	Monitoring disease status	Pancreatic	Serum, plasma	2002
CA-125	Monitoring disease progression, response to therapy	Ovarian	Serum, plasma	1997
Free PSA	Discriminating cancer from benign disease	Prostate	Serum	1997
Alpha-fetoprotein (AFP)	Management of cancer	Testicular	Serum, plasma, amniotic fluid	1992
Neuron-specific Enolase (NSE)	Aid in management and prognosis	Small cell lung cancer, neuroblastoma	Serum	1987
Total PSA	Prostate cancer diagnosis and monitoring	Prostate	Serum	1986
Carcino-embryonic antigen (CEA)	Aid in management and prognosis	Colon,rectum,stomach, lungs	Serum, plasma	1985

## 2.3 Lanthanides

### 2.3.1 Introduction

Lanthanides (Ln) are a series of 15 metal elements, which are listed separately at the bottom of the periodic table and are also referred as the f-block elements. The name comes from lanthanum, which is the first element of this series and lutetium being the last element. The Ln series with scandium and yttrium are called rare earth elements as they were once thought to be present in small quantity in the Earth's crust. Today we actually know that these elements are not actually rare in terms of abundance. Yttrium is among the 30 most abundant elements with thulium and lutetium 100 times more abundant than gold in the Earth's crust. Rare earth elements were originally discovered in 1787 in the form of a mineral called Ytterbite which came from a quarry in the village of Ytterby in Sweden. The mineral was studied by the Finnish chemist Johan Gadolin and in 1794 found that it contained an oxide that he named yttria. From yttria, the pure element yttrium was obtained and later revealed to contain several lanthanide elements. The discovery of lanthanides took a long time period since the extraction of cerium (Ce) from its mineral cerite in 1803 and the last Ln element to be discovered was promethium (Pr) in 1938, more than 100 years later. Similarity in their chemical properties, particularly in their oxidation states, is responsible for such delay in their discovery. This can be explained by the electronic configuration of the Ln ions [73,74].

Ln in the electronic ground state are characterized by the progressive filling of their 4f orbitals and share the electronic configuration of xenon. Xenon has an electronic configuration of  $1s^2 2s^2 2p^6 3s^2 3p^6 4s^2 3d^{10} 4p^6 5s^2 4d^{10} 5p^6$  and is abbreviated as [Xe]. The lowest energy orbitals are filled first with electrons and follow the sequence:



Ln have the general electronic configuration [Xe]  $4f^n 6s^2$  with the exception of lanthanum (La), Ce, gadolinium (Gd) and lutetium (Lu) for which the ground electronic configuration is [Xe]  $4f^n 5d^1 6s^2$ , with  $n=0$  for La and  $n$  ranging from 1 to 14 for the rest of the Ln elements. In the case of  $\text{Ln}^{3+}$  ions where the +3 oxidation state is the most stable for all lanthanide cations in aqueous solutions, the filling of electrons is perfectly regular from  $4f^1$  to  $4f^{14}$  [75,76]. Through these specific electronic configurations, Ln show similar physical and chemical properties, such as in their oxidation states, and ionic radii [75].  $\text{Ln}^{3+}$  ions possess magnetic properties arising from unpaired 4f electrons and are said to be paramagnetic in nature with the exception of  $\text{La}^{3+}$  and  $\text{Lu}^{3+}$ , which are diamagnetic due to the cancellation of the opposite spins of the electrons as a

result of pairing [77]. The particularities of Ln elements result in the shielding of 4f orbitals by the filled  $5p^6 6s^2$  sub-shells allowing for very weak perturbations of the spectroscopic and magnetic properties of Ln ions by the surrounding microenvironment. Additionally, this shielding effect causes the interaction between Ln ions (the Ln ion being the central ion) with ligands to form complexes to be electrostatic in nature rather than covalent. The coordination of ligands to a central  $\text{Ln}^{3+}$  ion will depend on the steric demand of the ligand and the strength of electrostatic interaction between the  $\text{Ln}^{3+}$  ions and the ligand [14,74,78]. The coordination number in aqueous solution is usually in the range of 8 to 10 depending on their ionic radii. Another important feature of the Ln is the lanthanide contraction which leads to a smooth decrease of ionic radii of the ions with increasing charge density. This contraction arises because of the poor shielding ability of the inner 4f orbitals to the nuclear charge, thus the nucleus charge contracting and stabilizing the outer 5p, 5d and 6s orbitals. All these phenomena contribute to the similarities in chemical and physical properties of lanthanides [14,74,75].

## 2.3.2 Lanthanide chelates

### 2.3.2.1 Luminescence of lanthanide ions

The luminescence of  $\text{Ln}^{3+}$  ions is related to its forbidden parity intra-shell 4f-4f transitions within their partially filled 4f orbitals. The electronic energy levels generated by the  $4f^n$  configuration are determined in order of importance (selection rule), by the Coulombic interaction and the spin-orbit coupling between the f orbital electrons. The mutual repulsion of electrons represented by the Coulombic interaction generates the total spin angular momentum (S), and the total orbital angular momentum (L), with the spin-orbit coupling defining the total angular momentum (J) of the f electrons.

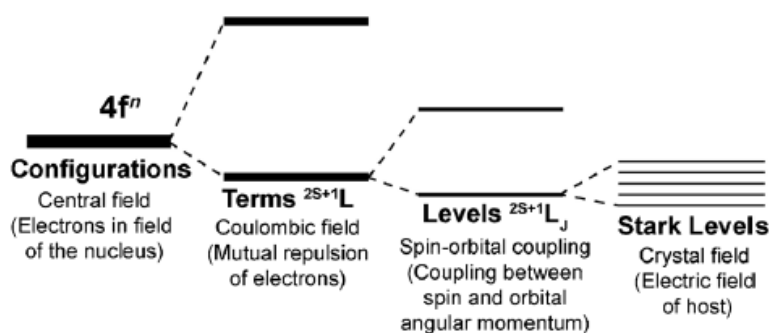


**Figure 2.3.** Simplified representation of the electronic transition within the 4f orbitals governed by the selection rules of spin (S), orbital (L) and total angular momentum (J) [79].

L, S and J are the quantum numbers that define a particular energy level and the distribution of the 4f electrons. The electronic levels generated by the  $4f^n$  configuration and characterized by the aforementioned quantum numbers S, L and J, can further be split by weak ligand field effects as shown in **Figure 2.3** [79,80].

The transitions can be described by the Russell-Saunders coupling scheme and denoted as  $(2S+1)L_J$ , with  $(2S+1)$  the spin-multiplicity and  $L=0,1,2,3,4,5,6,7,8$  designated in spectroscopy by the letters S, P, D, F, G, H, I, K, L respectively. **Figure 2.4** represents the ground and excited state energy levels of the  $Ln^{3+}$  ions, where radiative transition between the energy levels occurs to give rise to luminescent lanthanide ions. As it can be observed for  $Gd^{3+}$ , the large energy gap without intermediate energy states between  $^8S_{7/2}$  and  $^6P_{7/2}$ , results in radiation at shorter wavelength in UV. A consequence of the shielding of the 4f orbitals is that the f-f emission lines exhibit narrow line-like emission bands and cover the entire spectrum from UV ( $Gd^{3+}$ ) to visible (for *e.g.*,  $Pr^{3+}$ ,  $Sm^{3+}$ ,  $Eu^{3+}$ ,  $Tb^{3+}$ ) and NIR ( $Pr^{3+}$ ,  $Nd^{3+}$ ,  $Er^{3+}$ ,  $Yb^{3+}$ ) with the exception of  $La^{3+}$ ,  $Lu^{3+}$  [14,81,82].

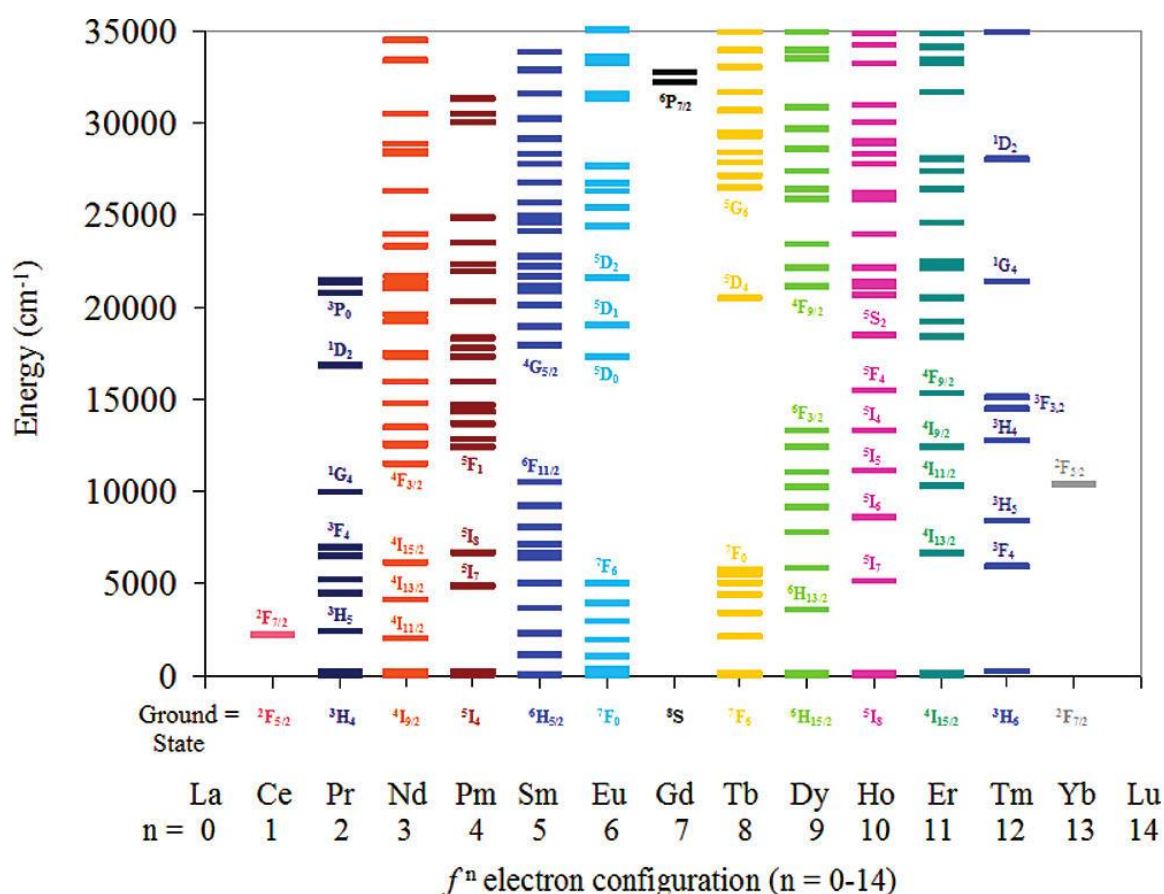


**Figure 2.4.** Ground and excited energy levels of  $Ln^{3+}$  ions where transitions results in f-f narrow line-like emission bands except for  $La^{3+}$  and  $Lu^{3+}$  [83].

Other consequences of the parity forbidden 4f transition dictated by the spin and Laporte rule are their extremely long luminescent lifetimes (an asset for bioassays) and very low direct absorption of photons by the  $\text{Ln}^{3+}$  ions causing the absorption cross-sections of the f-f transitions to have very low molar absorption coefficients (typically  $< 3 \text{ M}^{-1} \text{ cm}^{-1}$ ) [76]. Actually luminescence of  $\text{Ln}^{3+}$  ions exhibit fluorescence (transitions which occur without change of electron spin from singlet excited state), phosphorescence (transitions which occur with a change of electron spin from triplet excited state) or, often both. Direct excitation using intense light sources are needed to populate the excited states of the  $\text{Ln}^{3+}$  ions and therefore limit their practical usage. One way to circumvent this limitation is by chelating the  $\text{Ln}^{3+}$  ions to some ligands which acts as a light-harvesting antenna that can further transfer its excitation energy to the Ln ion followed by emission of characteristic line-like luminescence [78,81]. This “antenna effect” or “luminescence sensitization” was first discovered by Weissman in 1942, when he observed an increased photoluminescence of  $\text{Eu}^{3+}$  in the presence of some UV absorbing organic aromatic ligands [84]. Another way of enhancing luminescence of lanthanide ions is by doping of  $\text{Ln}^{3+}$  ions (one being a sensitizer – light absorber - and another being an activator – light emitter) in a crystal lattice structure which serves as a host material. As suggested in 1966 by F. Auzel, energy transfer can take place between neighboring  $\text{Ln}^{3+}$  ions by a sequential two-step absorption process where a sensitizer is excited by two (or more) low-energy photons and energy is transferred non-radiatively to an activator resulting in higher-energy photon emission, known as upconversion emission [80]. Photon upconversion was also demonstrated by Hyppänen et al. in an  $\text{Er}^{3+}$  complex which was chelated with an organic dye serving as an efficient NIR photon-harvesting antenna and upon excitation at 808 nm, upconversion energy transfer occurred between the antenna and the  $\text{Er}^{3+}$  ion. This resulted in a sequential two-step excitation of the  $\text{Er}^{3+}$  ion followed by the characteristic Er emission [85].

### 2.3.2.2 Antenna effect on lanthanide complexes

During the past two decades, a large variety of multidentate ligands have been synthesized and used as antennas to complex  $\text{Ln}^{3+}$  ions. Luminescence of  $\text{Ln}^{3+}$  ions in such complexes is a three step process where 1) photons are absorbed by the ligands coordinated to the  $\text{Ln}^{3+}$  ion, 2) energy is transferred onto one or several excited states of the  $\text{Ln}^{3+}$  ion and 3) light is emitted. These processes are quite intricate as they involve several energy migration mechanisms such as Dexter type and dipole-dipole or dipole-multipole (Förster) type [76,81]. The main energy migration paths imply permissible Laporte and spin rules, and are often modelled in terms of a simplified energy flow from ligand singlet state  $\rightarrow$  ligand triplet state  $\rightarrow$   $\text{Ln}^{3+}$  excited state followed by  $\text{Ln}^{3+}$  ion centered emission. **Figure 2.5** represents A) a simplified Jablonski

diagram for the antenna effect and B) the electronic transitions from excited  $^5D_J$  state to  $^7F_J$  ground state of europium (Eu) and terbium (Tb) complexes. Light is absorbed ( $h\nu^*$ ) by the surrounding ligand and reaches a short-lived first singlet excited state ( $S_0 \rightarrow S_1$ ), and is generally assumed to first undergo intersystem crossing to longer-lived triplet excited state ( $S_1 \rightarrow T_1$ ) followed by population of  $Ln^{3+}$  excited states through energy transfer from  $T_1$  state of the ligand and finally characteristic radiative emission ( $h\nu$ ) of the centered lanthanide ion after suitable internal conversion. A large energy gap, often called ligand-induced Stokes shift, should exist between ligand absorption and lanthanide emission in order to prevent back energy transfer which results in low quantum yields and short, temperature-dependent lifetimes [78,81,86]. **Figure 2.6** represents the Tb complex (Lumi4-Tb) based on 2-hydroxyisophthalamide ligands we used in this thesis bearing NHS functional groups for biomolecules' coupling with the ligand having a molar absorption coefficient of *ca.* 26000  $M^{-1} cm^{-1}$  at 340 nm [87]. Examples of other ligands and lanthanide complexes are found in these selected references [14,74,75,81,83,86–88].

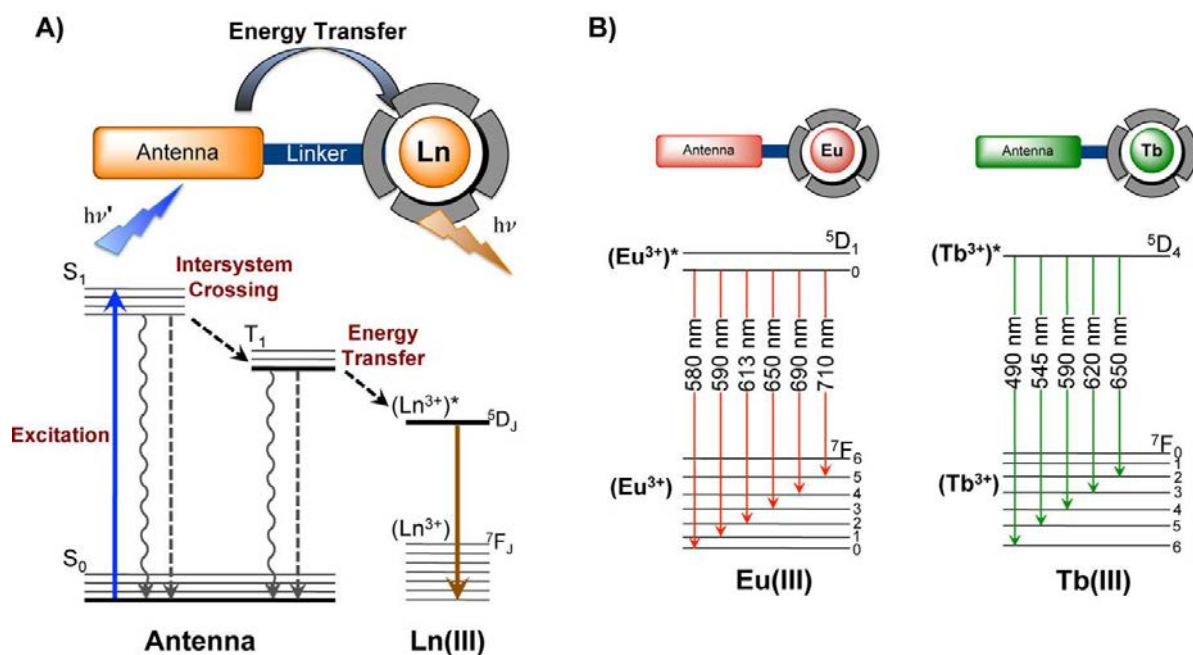


**Figure 2.5.** Simplified Jablonski diagram of the antenna effect. (A)  $h\nu^*$  is absorbed by the antenna which goes to the singlet excited state  $S_1$ .  $S_1$  undergoes intersystem crossing to triplet excited state  $T_1$  and populates the  $Ln^{3+}$  excited states. Finally characteristic radiative emission ( $h\nu$ ) of the centered lanthanide ion after suitable internal conversion occurs. (B) Commonly observed emission wavelengths of Eu (red) and Tb (green) complexes from the  $^5D_J$  excited state to  $^7F_J$  ground state [86].

The overall quantum yield,  $Q_{Ln}^L$ , of a lanthanide complex is given by **Equation 2.2**:

$$Q_{Ln}^L = \frac{I_{Ln}(E)}{I_L(A)} = \eta_{sens} Q_{Ln}^{Ln} \quad (2.2)$$

where  $I_{Ln}(E)$  is the number of photons emitted by the Ln metal ion;

$I_L(A)$  is the number of photons absorbed by the ligand;

$Q_{Ln}^{Ln}$  is the intrinsic quantum yield of the Ln metal ion when excitation has been carried-out directly on the 4f excited state;

$\eta_{sens}$  represents the sensitization efficiency.

Based on **Equation 2.2**, enhancing the overall quantum yield of lanthanide complexes requires tuning the following two parameters:  $\eta_{sens}$  and  $Q_{Ln}^{Ln}$ . The sensitization efficiency can be determined experimentally if both overall and intrinsic quantum yields are known, but  $\eta_{sens}$  is generally more difficult to calculate.  $Q_{Ln}^{Ln}$  can be improved by considering the energy gap between the lowest lying excited state of the Ln ion and the highest sublevel of its ground multiplet. A small energy gap will result in non-radiative deactivation processes for example, through vibrational quenching by high O-H energy vibrations. The overall quantum yield can be further improved using antennas which have a high energy gap between the triplet excited state of the ligand and the lowest emitting levels of the Ln<sup>3+</sup> ions, at least 2500 cm<sup>-1</sup> difference. A low energy gap will limit the overall quantum yield due to thermal deactivation caused by back energy transfer and quenching effects to the triplet state. The ligand should be multidentate, have a high absorption coefficient, possess kinetic and thermodynamic stability, be biocompatible with activated functional groups for biolabeling, and be able to shield the lanthanide ion from its surrounding environment. Coordination with water molecules quenches the long lifetime of the Ln<sup>3+</sup> through non-radiative vibrational energy transfer to the O-H oscillator [14,75,81].

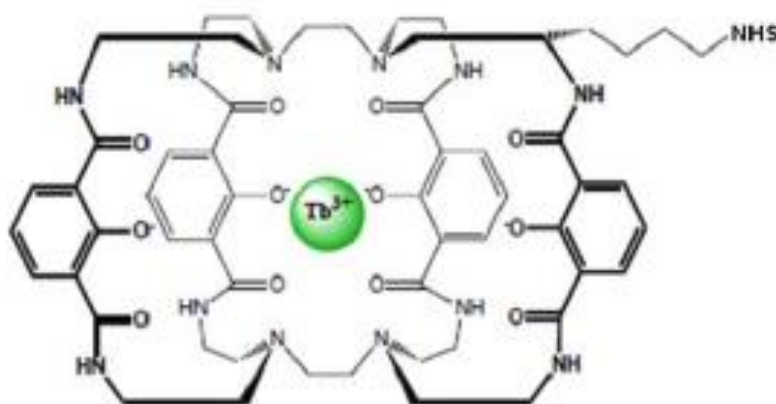


**Figure 2.6.** Cage-like structure of the ligand for photon harvesting of the Lumi4-Tb complex used in this thesis and provided by Lumiphore Inc. (Berkeley, CA, USA) based on 2-hydroxyisophthalamide ligands.

### 2.3.3 Upconversion nanoparticles

Luminescence of lanthanide chelates in most cases relies on energy downconversion where excitation usually occurs in the UV and luminescence generated at lower energies. In biological applications, excitation in the UV/Vis is generally accompanied by strong scattering and absorption in tissues, and is limited to penetration depths. Furthermore, sample autofluorescence causes low signal-to-noise ratio (SNR) and prolonged illumination at these excitation wavelengths may cause cell death and damage to the biomolecules being investigated [89]. Due to the long luminescence lifetimes of lanthanides, time-gated measurements can be performed to increase the SNR. An alternative to circumvent UV/Vis excitation of lanthanide chelates is by using upconversion nanoparticles (UCNPs) in which optically active  $\text{Ln}^{3+}$  ions are doped in an optically inactive inorganic crystal lattice structure that serves as a host material. Upconversion refers to non-linear optical processes capable of converting low energy excitation photons into high energy emission (anti-Stokes shift). Lanthanide ions-doped UCNPs offer the unique property of being able to emit visible/NIR light followed by excitation with a NIR laser. NIR excitation allows detection of signals with the significant minimization of background autofluorescence and scattered excitation light, and provides deeper and non-invasive penetration of photons in the tissue due to their NIR transparency (also known as the biological window). The measurement of upconversion luminescence in the red and downconversion luminescence in the NIR region also provides high sensitivity detection in the “second transparent biological window”. Even if a single  $\text{Ln}^{3+}$  ion allows upconversion emission, the low absorption cross-section results in weak emission and by co-doping with a different  $\text{Ln}^{3+}$  ion, upconversion efficiency is enhanced. In the latter, one Ln ion acts as a sensitizer that absorbs light and the other Ln ion is an activator responsible for upconversion emission [89–91].

Upconversion processes can be roughly divided into three classes: 1) excited state absorption (ESA), 2) energy transfer upconversion (ETU), and 3) photon avalanche (PA). These upconversion mechanisms involve sequential absorption of two or more photons resulting in the population of highly excited long-lived metastable energy states from which upconversion emission occurs and are represented in **Figure 2.7**. For ESA, at least two photons of sufficient energy are sequentially absorbed by the emitting ions to reach the emitting level (**Figure 2.7 (a)**). ETU is similar to ETA as they both employ sequential absorption of photons to populate the metastable excited states of the emitting ion but in ETU the excitation is performed by energy transfer to the neighboring ions where both ions are in the excited states and energy is transferred non-radiatively to the emitting ion leading to emission of light at a

shorter wavelength (**Figure 2.7 (b)**). In PA (**Figure 2.7 (c)**), a pump intensity above a certain threshold value is required that will populate the level E1 by non-resonant weak ground state absorption, followed by the population of visible emitting E2 energy level by resonant ESA. Cross-relaxation energy transfer between a neighboring ion in its ground state and the excited ion occurs, resulting in building up of population in the excited state E1 from which a resonant absorption occurs to a higher level E2 to further initiate cross-relaxation and exponentially increase level E2 population by ESA, thus causing an upconversion emission as an avalanche process [90,92].

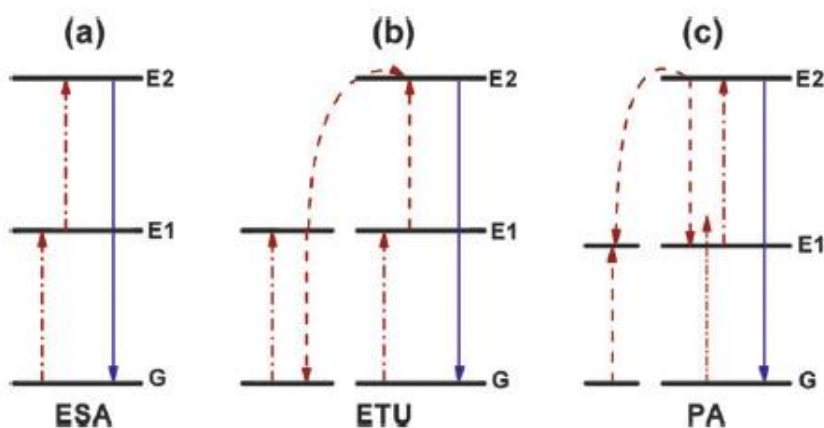


**Figure 2.7.** UC mechanisms for lanthanide-doped crystals. (a) excited state absorption, (b) energy transfer upconversion, and (c) photon avalanche. The dashed-dotted arrows represent photon excitation, dashed arrows correspond energy transfer and full arrows are radiative emission upconversion [90].

Ln-doped UCNPs that follow the ETU mechanism usually consist of a host lattice, sensitizers and activators.  $\text{Yb}^{3+}$  is often used as the sensitizer due to its larger absorption cross-section in the NIR (980 nm) region, only one large energy gap of *ca.*  $10000 \text{ cm}^{-1}$  and long luminescence lifetimes of about 1 ms. Upon 980 nm excitation,  $\text{Yb}^{3+}$  can effectively transfer its energy to activator ions such as  $\text{Er}^{3+}$ ,  $\text{Tm}^{3+}$ ,  $\text{Pr}^{3+}$ , or  $\text{Ho}^{3+}$  by ETU which usually requires one activator in the presence of two or three  $\text{Yb}^{3+}$  ions.  $\text{Nd}^{3+}$  can also be used as a sensitizer when excited at its absorption maximum around 800 nm for  $\text{Er}^{3+}$  or  $\text{Tm}^{3+}$  activators. Shen et al. [93] showed that following excitation of  $\text{Nd}^{3+}$  at 800 nm initiated the energy transfer cascade to nearby  $\text{Yb}^{3+}$  ions ( $\text{Yb}^{3+}$  ions serves as a bridging sensitizer) that in turn activated  $\text{Er}^{3+}$  or  $\text{Tm}^{3+}$  following upconversion emission. Anti-Stokes emission efficiency of ETU is greatly dependent on the distance between the ions, which is related to their concentration. Upconversion enhancement can be obtained by varying dopant concentration but great care should be taken to avoid non-radiative quenching such as concentration quenching, which results from concentration dependent cross-relaxation processes. For the case of  $\text{Yb}^{3+}$ , a relatively high doping

concentration of 20%-30% is used for efficient energy transfer to neighboring ions and less than 2% doping rate of activators such  $\text{Er}^{3+}$ ,  $\text{Tm}^{3+}$  and  $\text{Ho}^{3+}$  are required to avoid concentration quenching. In the work of Shen et al.  $\text{Nd}^{3+}$  was doped only up to 1% [89,94,95]. **Figure 2.8** represents the upconversion processes involving  $\text{Yb}^{3+}$  when excited by a 980 nm diode laser and  $\text{Nd}^{3+}$  when excited at 800 nm.

The choice of the host lattice that accommodates the sensitizers and activators is essential for upconversion emission efficiency as they should have low phonon energies, bearing homogeneous doping, high chemical stability and show low non-radiative energy losses. Low phonon energies guarantee low non-radiative and multiphonon losses with enhanced luminescent lifetimes. Host lattice of chlorides, bromides and iodides having low phonon energies of *ca.* 144, 172 and 260  $\text{cm}^{-1}$  are more appropriate than fluorides (*ca.* 355  $\text{cm}^{-1}$ ) or oxides (*ca.* 600  $\text{cm}^{-1}$ ) for upconversion emission. However, upconversion may at times require phonon assistance. Fluoride-based lattices such as  $\text{LaF}_4$ ,  $\text{NaYF}_4$ ,  $\text{NaGdF}_4$  (a start for bi-modal analysis), and  $\text{BaYF}_4$  have been used as host lattices in lots of studies and  $\text{NaYF}_4$  was acknowledged to provide the most efficient host lattice for upconversion visible emissions and long lifetimes [89,92,95]. Crystal symmetry has also an impact on upconversion efficiency and hexagonal  $\beta$ -phase nanocrystals ( $\beta\text{-NaYF}_4$ ) provided better upconversion emissions than cubic  $\alpha$ -phase nanocrystals ( $\alpha\text{-NaYF}_4$ ) [89,95].

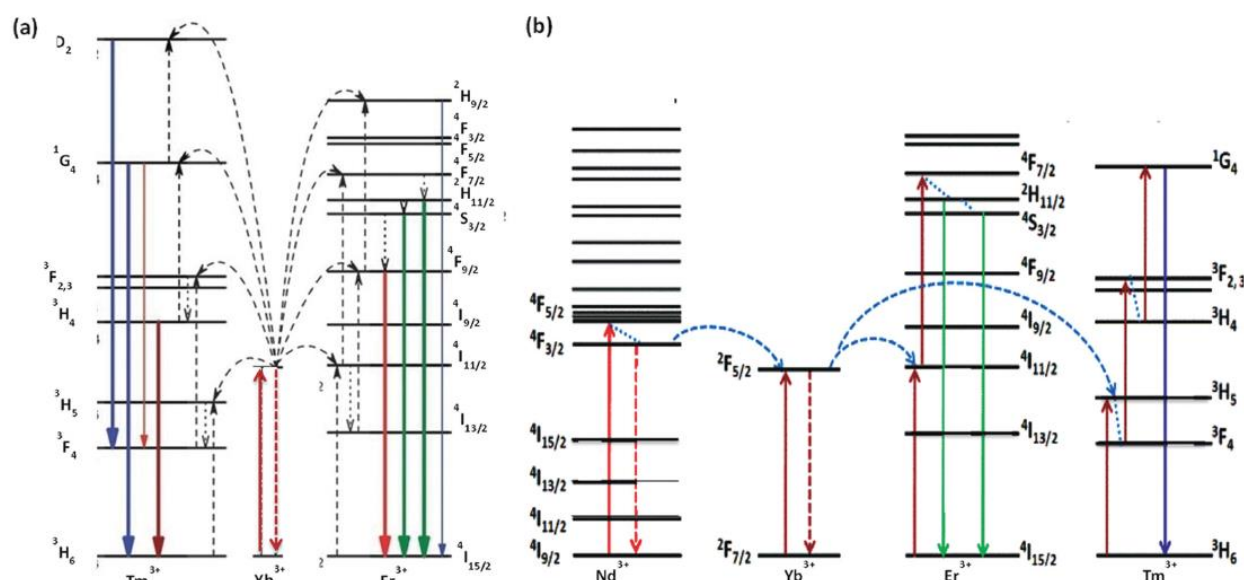


**Figure 2.8.** A simplified energy upconversion mechanism with (a) diode laser excitation of  $\text{Yb}^{3+}$  at 980 nm followed by energy transfer to neighboring  $\text{Tm}^{3+}$  or  $\text{Er}^{3+}$ , (b) diode laser excitation of  $\text{Nd}^{3+}$  at 800 nm followed by energy transfer to  $\text{Yb}^{3+}$  acting as a bridge for population of excited states of either  $\text{Er}^{3+}$  or  $\text{Tm}^{3+}$  [95].

Many preparation techniques of UCNPs have been reported in the literature, including coprecipitation, thermal decomposition, solvothermal synthesis, and high-temperature coprecipitation. These synthesis techniques are usually carried out in organic solvents but synthesis in aqueous media can also be performed by hydrothermal synthesis, and sol-gel processes. Wet-chemical approaches such as thermal decomposition and hydrothermal / solvothermal allow controlled, narrow sized distribution and dispersibility of the upconversion nanocrystals. After synthesis, depending on the route taken, UCNPs can be rendered hydrophilic by ligand exchange or by obtaining ligand-free UCNPs. The surface can be further functionalized to accommodate reactive functional groups such as NHS, maleimide,  $\text{NH}_2$ , and  $\text{COOH}$  for binding of biomolecules on the surface of UCNPs [96–99]. It is also important to confirm that surface modification did not have any negative impact on the upconversion efficiency and colloidal stability is retained for the UCNPs. Luminescent properties of lanthanide-doped UCNPs are known to be affected by the size of the nanocrystallites. The surface to volume ratio increases as the inverse of the NPs diameter ( $1/D$ ), and as the size is decreased to reach nanometric scales (in order to be compatible with the infinitely small biological world), there is a high percentage of optically active dopant ions that are distributed on the surface of the nanoparticle. Despite the shielding of the f electrons, it is known that lanthanide ions are affected by surface defects, surface ligands and are quenched by water molecules, thus causing a drop in the overall upconversion efficiency. Arppe et al. studied the influence of water on the upconversion luminescence intensity and decay of bare and silanized  $\text{NaYF}_4:\text{Yb}^{3+},\text{Er}^{3+}$  and  $\text{NaYF}_4:\text{Yb}^{3+},\text{Tm}^{3+}$  UCNPs in  $\text{H}_2\text{O}$  and  $\text{D}_2\text{O}$ . They found out that the main quenching mechanism was a result of multiphonon deactivation of the  $\text{Yb}^{3+}$  sensitizer ion caused by OH-vibrations on the surface of the UCNPs instead of non-radiative relaxation of the activators ( $\text{Er}^{3+}$ ,  $\text{Tm}^{3+}$ ) and the silica shell around the UCNPs did not provide much protection against the quenching effect of water. Hence better surface passivation is necessary in order to eliminate most of the quenching effects and enhance the upconversion luminescence [100]. UCNPs possess generally quantum yields ranging from 0.1% to 1% [101], energy loss and surface quenching effects can be greatly minimized by coating the UCNPs with a uniform shell which can be active (doped with  $\text{Ln}^{3+}$  ions) or inactive to reduce non-radiative decays causing an increase in quantum yields. Many studies reported a several fold enhancement of the anti-Stokes emission by growing a shell around the UCNPs [102–108]. Vetrone et al. demonstrated that core/shell strategies also cause a change in the energy distribution in the nanoparticle. They synthesized core-only, active-core/inert-shell and active-core/active-shell UCNPs, and observed an enhancement of the upconversion emission yield of *ca.* 3 in the green and *ca.* 10 in the red when comparing active-core/active-shell to active-core/inert-shell respectively. A

comparison with active-core/active-shell and core-only showed a more intense factor of *ca.* 13 and 20 for the green and red emissions respectively. By increasing Yb<sup>3+</sup> concentration in relation to Er<sup>3+</sup> ions there was enhanced population of the red emitting state <sup>4</sup>F<sub>9/2</sub> and concentration quenching was reduced due to spatial separation of the ions by placing them in either the core or the shell [107].

### 2.3.4 Applications of lanthanides

Lanthanide luminescence is implicated in a wide variety of technologies ranging from photovoltaics, optical imaging to biomedical and sensing areas. The NIR luminescence of the Nd<sup>3+</sup>, Yb<sup>3+</sup> and Er<sup>3+</sup> are used as optical signal amplifier in telecommunication network and Nd<sup>3+</sup> has since a long time been used in laser systems such as the Nd:YAG laser with its main emission wavelength at 1064 nm. Ln ions emitting in the visible region when coupled to suitable antennas can be used in various lighting applications such as LEDs, security inks and bioprobes [75]. Lanthanide complexes and UCNPs have found their place as labels on biological compounds, in bioanalytical detection and in luminescence microscopy. Due to their unique photophysical properties such as microsecond to millisecond lifetimes and characteristic narrow emission bands and large Stokes shift / anti-Stokes shift, they provide a higher SNR as compared to organic dyes or QDs. Visible emitting Ln complexes are widely used in bioassays and microscopy while NIR emitting Ln complexes are becoming good candidates for optical microscopy and time-resolved imaging as their emission is in the 650-1350 nm region where light penetration in tissues is maximum with minimum autofluorescence and scattering. When used in fluorescence-based bioassays or microscopy imaging, Ln complexes allows the suppression of short-lived sample autofluorescence and light scattering when combined with pulsed excitation and time-gating. The introduction of a delay with is typically in the range of 10-100 μs after UV pulsed excitation, allows acquiring the PL signal of the Ln complexes background-free during a detector integration time of for *e.g.* 100-1000 μs [109]. The use of UCNPs in biomedical applications are of growing interest as the emission of upconversion light under 980 nm or 800 nm excitation falls in the so-called biological window resulting in an increased transparency of biological tissue towards NIR light as compared to UV or visible light excitation. Penetration of light with UV in the tissue is of a few μm to 1 mm whereas NIR radiation penetrates deeper several millimeters to centimeters with minimal photodamage. Detection of UCNPs can therefore be performed sensitively in steady-state or time-resolved mode with high SNR [110,111]. **Figure 2.9**, (left) represents the absorption spectrum of a human skin where three biological windows are defined and (right) a comparison of the penetration depth in tissue when exposed to 800 nm and 980 nm radiation.

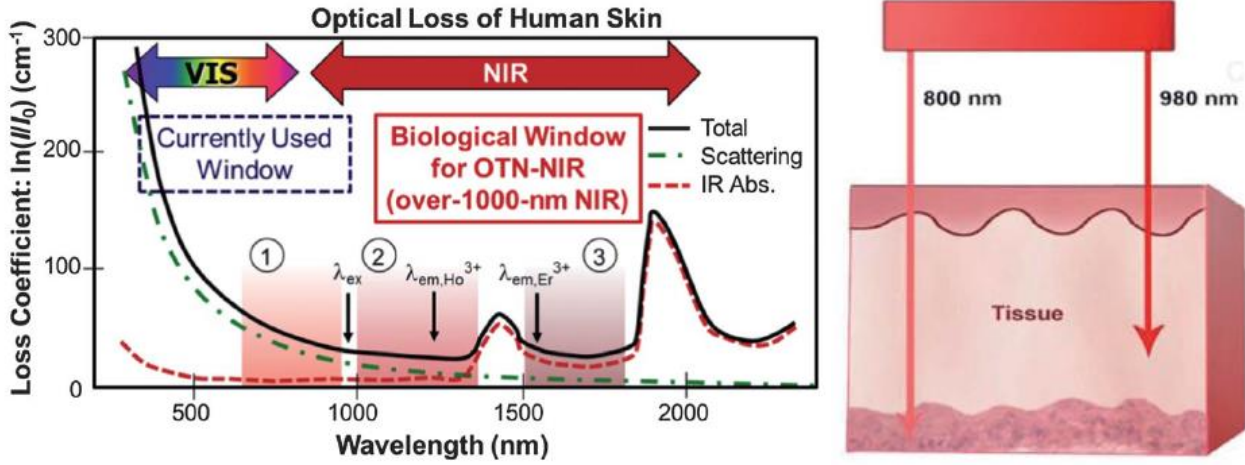


**Figure 2.9.** (Left) Absorption spectrum of human skin where the 1<sup>st</sup> biological window is observed in the range ca. 650 nm - 950 nm; sensitive spectral range for *in vivo* imaging found in the 2<sup>nd</sup> biological window ranging from 1 to 1.35  $\mu\text{m}$  and a 3<sup>rd</sup> biological window between 1.5 and 1.8  $\mu\text{m}$  [110]. (Right) Comparison of penetration depth in tissue upon excitation at 800 nm and 980 nm [94].

## 2.4 Quantum dots

### 2.4.1 Introduction

Quantum dots (QDs) are highly stable and brightly luminescent inorganic nanoparticles composed of semiconductor materials from II-VI (CdS, CdSe, CdTe, ZnO, ZnS), III-V (GaAs, GaN, GaP, InAs, InP), or IV-VI (PbS, PbSe) groups of the periodic table, and are also composed of their alloys (CdSeS, CdSeTe, InGaAs, etc.), or core/shell structures of these materials. QDs are roughly spherical in shape and sizes of these semiconductor nanocrystals range between *ca.* 1 – 10 nm. Quantum mechanical behavior is observed due to their small nanometric sizes where their fluorescence is directly related to the sizes of the QDs resulting in a blue color shift in the emitted light as the size decreases. QDs have extensively been used for biological applications after two seminal studies in 1998 reported the potential of colloidal CdSe/ZnS core/shell as fluorescent labels for cellular imaging [112,113]. The most popular QD fluorophores for biological applications are composed of CdS, CdSe, and CdTe overcoated with a layer of ZnS is because of their already established chemistry and conjugation strategies [109,114,115]. However, due to the high toxicity of these heavy metals, QDs made of alternative materials have to be developed for *e.g.* indium phosphide (InP) which is one of the most promising compounds as a result of its low intrinsic toxicity [116]. Compared to conventional fluorophores, such as organic dyes or fluorescent proteins, which have narrow excitation spectra, small Stokes shifts, broad fluorescence band and more prone to photobleaching, QDs present several technical advantages, such as photostability, high brightness, and size-tunable absorption and narrow emission wavelengths. These unique properties of QDs have attracted more and more attention in biotechnology and medical applications where they have become important fluorescent probes for *in vitro* and *in vivo* bioimaging and clinical diagnostics research [117]. **Figure 2.10** represents the spectral range of emission for the most widely studied types of semiconductor nanocrystals.

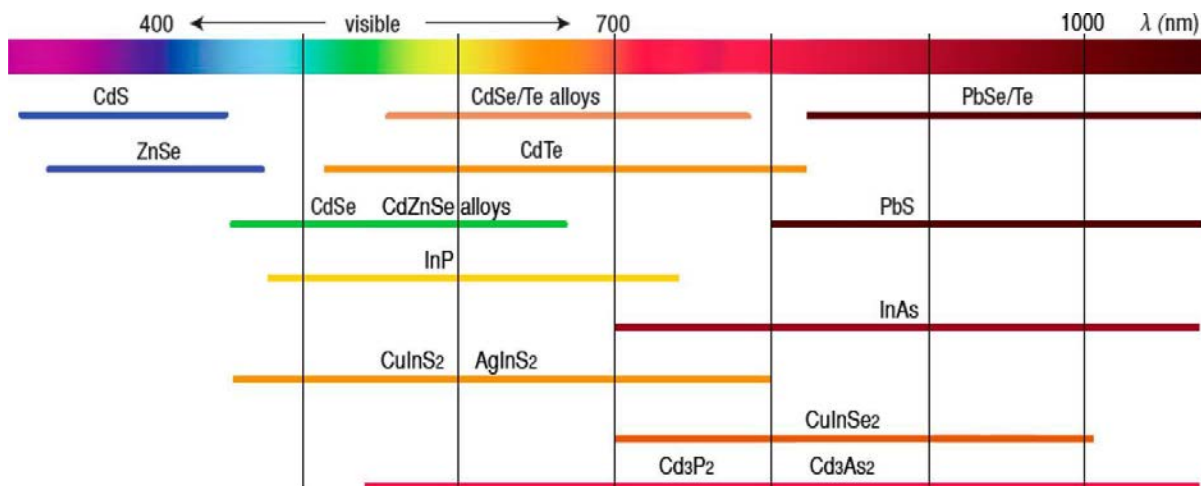


**Figure 2.10.** Spectral range of the photoluminescent emission for the most widely studied types of semiconductor nanocrystals [118].

### 2.4.2 Optical properties of QDs

Quantum dots possess electronic properties that are intermediate between those of bulk semiconductors and discrete molecules. Semiconductors are electronically characterized by having a filled valence band separated from the empty conduction band by an energy bandgap of *ca.* 0.5 to 3.5 eV (where  $1 \text{ eV} = 1.602 \times 10^{-19} \text{ J}$ ) [119]. When a bulk semiconductor is excited by photons of energy  $h\nu > \text{bandgap}$ , an electron is promoted into the quasi-continuum conduction band leaving in the valence band a positively charged hole with the average separation distance between the electron and hole referred to as the exciton Bohr radius and electron-hole pair regarded as an exciton. When an exciton is created and that the size of the bulk semiconductor approaches the exciton Bohr radius, the density of electronic states is not enough to form complete band structures and quantization of the energy levels is observed at the band edges. The physical dimensions of the particle therefore confine the exciton as in a particle-in-box problem forcing the electron-hole pair to be closely together thus increasing the exciton binding energy. This phenomenon known as the quantum confinement has a direct effect on the boundaries of the bandgap (**Figure 2.11**) where the relative positions of the highest occupied state and lowest unoccupied state equivalent in 1) bulk semiconductor: top of valence band and bottom of conduction band, and 2) molecular dyes: highest occupied molecular orbital (HOMO) and lowest unoccupied molecular orbital (LUMO)) are controlled by the size of the QD. The magnitude of this energy spacing is inversely proportional to the number of atoms in the semiconductor nanocrystal. Due to the quantum confinement effect, there is an increase in the inter-bandgap energy as the size of the QD decreases, meaning that for a QD composed of the same material the emission frequency (from UV to NIR range for some QDs), which results from the radiative recombination of an exciton, is size dependent. The smaller the QD

the more blue shifted will be its photoluminescence (PL). Another characteristic of QDs is their narrow and symmetrical emission, which approximates a Gaussian profile and depends on the quality and size distribution of the QDs. High quality and monodisperse QDs yield emission profiles with FWHM which are typically in the range of 25-35 nm [109,119,120]. The broad absorption spectra are caused by an increase absorption probability at shorter wavelengths, which has the advantage of being able to excite different QDs with a single light source. QDs generally have multi-exponential lifetimes and absorption coefficients in the range of  $10^5 - 10^6 \text{ M}^{-1}\cdot\text{cm}^{-1}$  that increase with shorter excitation wavelengths and larger nanocrystal sizes. It has also been reported of QD's two-photon absorption cross-sections that are about two orders of magnitude larger than the best organic dyes [109,121]. In an aqueous environment for biological applications core nanocrystals suffer from surface defects and cause the formation of temporary trap states for the electron or hole preventing their radiative recombination and resulting in blinking at the single-molecule level and low quantum yield. A shell of a higher bandgap can be coated around the core which helps confine the exciton to the core of the nanocrystal therefore minimizing trap states, improving quantum yield, preventing leeching of the core materials and protecting the core from oxidation and other chemical reactions from its surrounding environment. Core/shell QDs are especially required in biological applications.

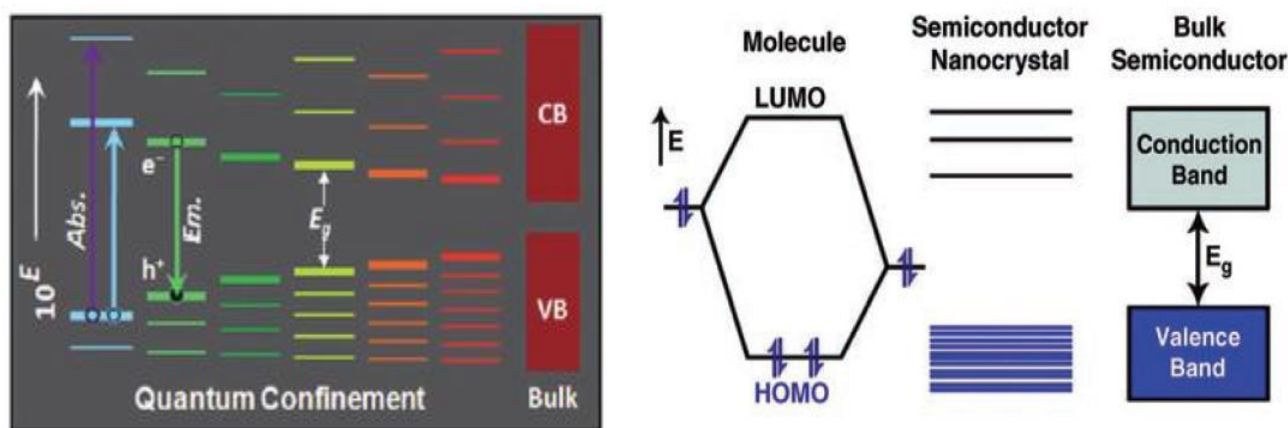
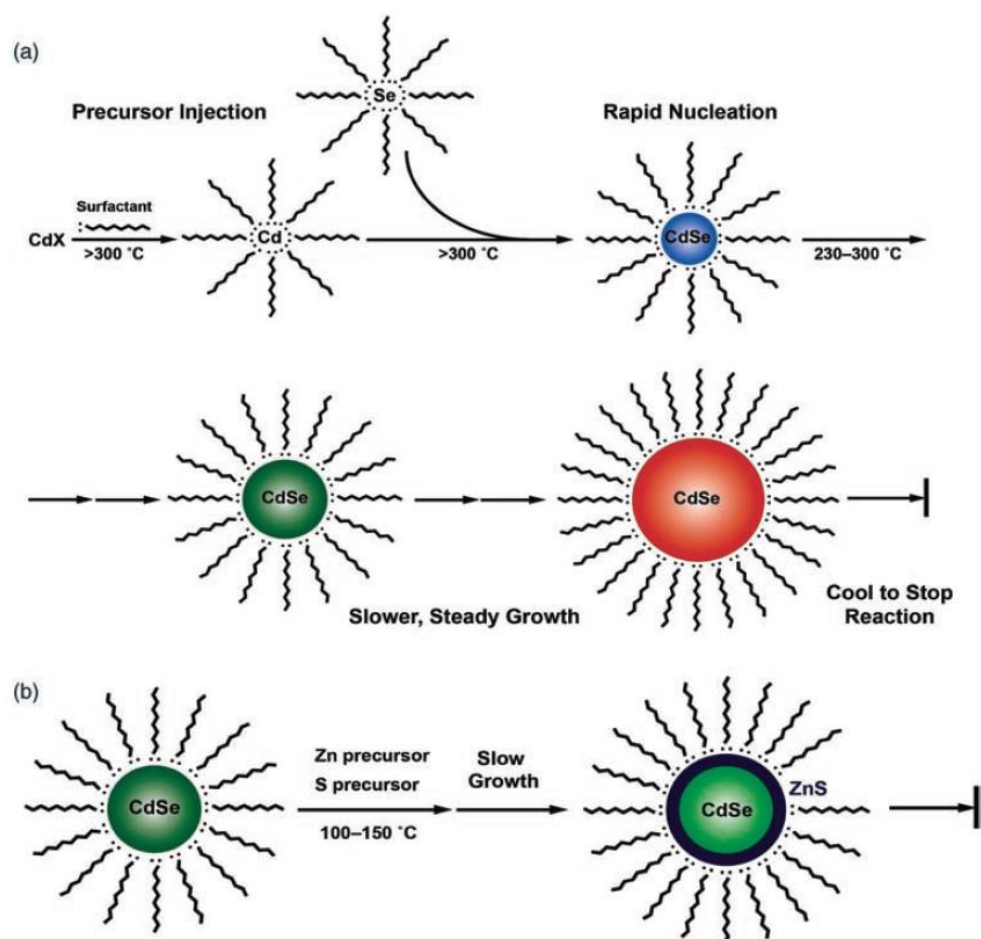


**Figure 2.11.** (Left) Quantization of the energy level as a result of the quantum confinement effect in a QD.  $E_g$  represent the bandgaps energies,  $E_m$  the radiative emission of a photon upon recombination of electron ( $e^-$ ) and hole ( $h^+$ ). Energy levels are color coded: The smaller the QD the more blue shifted will be its photoluminescence. Continuous conduction band (CB) and valence band (VB) of bulk semiconductor shown as comparison. (Right) Diagrams illustrating that the electronic structure of a QD is intermediate between a bulk semiconductor and a molecule [109].

### 2.4.3 Biofunctionalization

QDs need to be exceptionally water-soluble, biocompatible, highly luminescent and monodisperse for use in biological applications. Synthesis of QDs can be carried-out using the top-down method or the bottom-up approach. In the top-down method the semiconductor

material is thinned to form QDs using the following processing methods: molecular beam epitaxy, ion implantation, e-beam lithography, and X-ray lithography. Synthesis of QDs via the bottom-up approach consists of preparing colloidal QDs by self-assembly in a solution following a chemical reduction [122]. The most common technique to yield high quality colloidal QDs is by the bottom-up approach where monodisperse QDs are synthesized in non-polar organic solvents by pyrolysis of organometallic precursors in the presence of hydrophobic coordinating ligands. The size of the QDs can be tuned by changing temperature, pH, or growth time. QDs have also been directly synthesized in aqueous solutions yielding immediate hydrophilic QDs for bio-applications but have so far not been equivalent as those prepared in hot organic solvent [123]. A schematic generic synthesis of a typical CdSe/ZnS core/shell QDs is presented in **Scheme 2.1**.



**Scheme 2.1.** Typical synthesis of colloidal CdSe/ZnS core/shell QDs. (a) Cadmium precursor is generally dimethyl cadmium or cadmium oxide and selenium precursor is usually trioctylphosphine selenide (TOPSe). The growth time determines the size of the QDs and the solution is cooled to stop the reaction growth of the nanocrystals. (b) A solution of bis(trimethylsilyl)sulfide and either dimethyl or diethyl zinc is added to the core nanocrystals and heated at different temperatures between  $100\text{--}150\text{ }^{\circ}\text{C}$  to slowly grow the ZnS shell around the core CdSe [109].

The resulting QDs prepared in organic solvents are hydrophobic in nature and need to be rendered water soluble for further bio-use, which can be done by different strategies of surface modifications such as ligand exchange, or encapsulation. Ligand exchange involves the substitution of hydrophobic ligands present on the QDs' surface with bifunctional ligands that have the ability to anchor on the QDs at one end, generally through thiol based molecules, and on the other end provide solubility with a hydrophilic end group, which can be carboxylates, amines or PEGs. Small hydrodynamic diameters can be obtained using this method but yield usually a lower quantum yield as the surface state is modified [117,123]. It has been reported that ligand exchange using PEGylated-dihydrolipoic acid (PEG-DHLA) ligands produced small hydrodynamic sized QDs with low non-specific binding, high quantum yield and the ability of incorporating reactive functional groups for bioconjugation [124]. Recently, ligand exchange with zwitterionic penicillamine resulted in compact QDs with small hydrodynamic diameters and colloidal stability for at least two years, which could further be functionalized with reactive bearing functional groups for biomolecule attachment [125]. Encapsulation does not modify the QDs surface as assembly with amphiphilic molecules, such as polymers or phospholipids, are driven by the hydrophobic interactions, which intercalate within the alkyl chains terminated by the native ligands while the hydrophilic part (which can incorporated functional reactive groups towards biomolecules) faces outwards and interact with the aqueous environment [126]. The encapsulation method with polymer coating is known to provide QDs with high stability in aqueous solutions and retaining their optical properties as compared to ligand exchange method, but also yield QDs with large hydrodynamic diameter, which is not optimal for FRET applications.

Once QDs have been rendered water soluble they can be further bio-functionalized with proteins, peptides, nucleic acids or any other biomolecules for their use in biological applications. When conducting bioconjugation, several parameters such as retaining activity of biomolecule, functionality of the QD, orientation of the biomolecule and reproducible and stable bioconjugation, should be carefully considered [115]. Different approaches for labeling of biomolecules on QD surfaces can be separated into chemistry- and biology inspired techniques. Biology inspired techniques include labeling based on receptor-ligand (biotin/avidin), fluorescent proteins, enzymatic (SNAP<sup>TM</sup>, HALO<sup>TM</sup>-tag, etc.), non-natural amino acids, and peptide recognition (tetracysteine, polyhistidine, etc.). Chemistry inspired techniques include non-covalent (electrostatic, encapsulation) and covalent attachment (amine reactive, cysteine reactive, ketone/aldehydes, tyrosine, tryptophan, cycloaddition reactions, etc.). Covalent attachment of biomolecules to their probes is the most popular and traditional group of chemistries used to date. For protein labeling, four major functional groups have been

identified as primary amines (-NH<sub>2</sub>), carboxyls (-COOH), sulfhydryls (-SH) and carbonyls (-CHO), which can be targeted by a number of chemical reactive groups. **Figure 2.12** illustrates the bioconjugation and surface coating strategies that can be performed on a QD [117], and **Table 2.2** summarizes some of the functional groups and their representative reaction mechanism for bioconjugation [127,128]. DNA and peptides can be directly synthesized with site-specific amine or thiol groups for subsequent bioconjugation with QDs [127]. Polyhistidine tags affixed to biomolecules spontaneously coordinate via metal-affinity interactions directly to the QDs surface [120]. In this thesis, we mainly targeted free thiol groups and primary amines using maleimide reactive groups and succinimidyl ester (NHS) respectively, and involved crosslinking using heterobifunctional crosslinkers (heterobifunctional crosslinkers possess different reactive groups at either end of a short spacer arm).

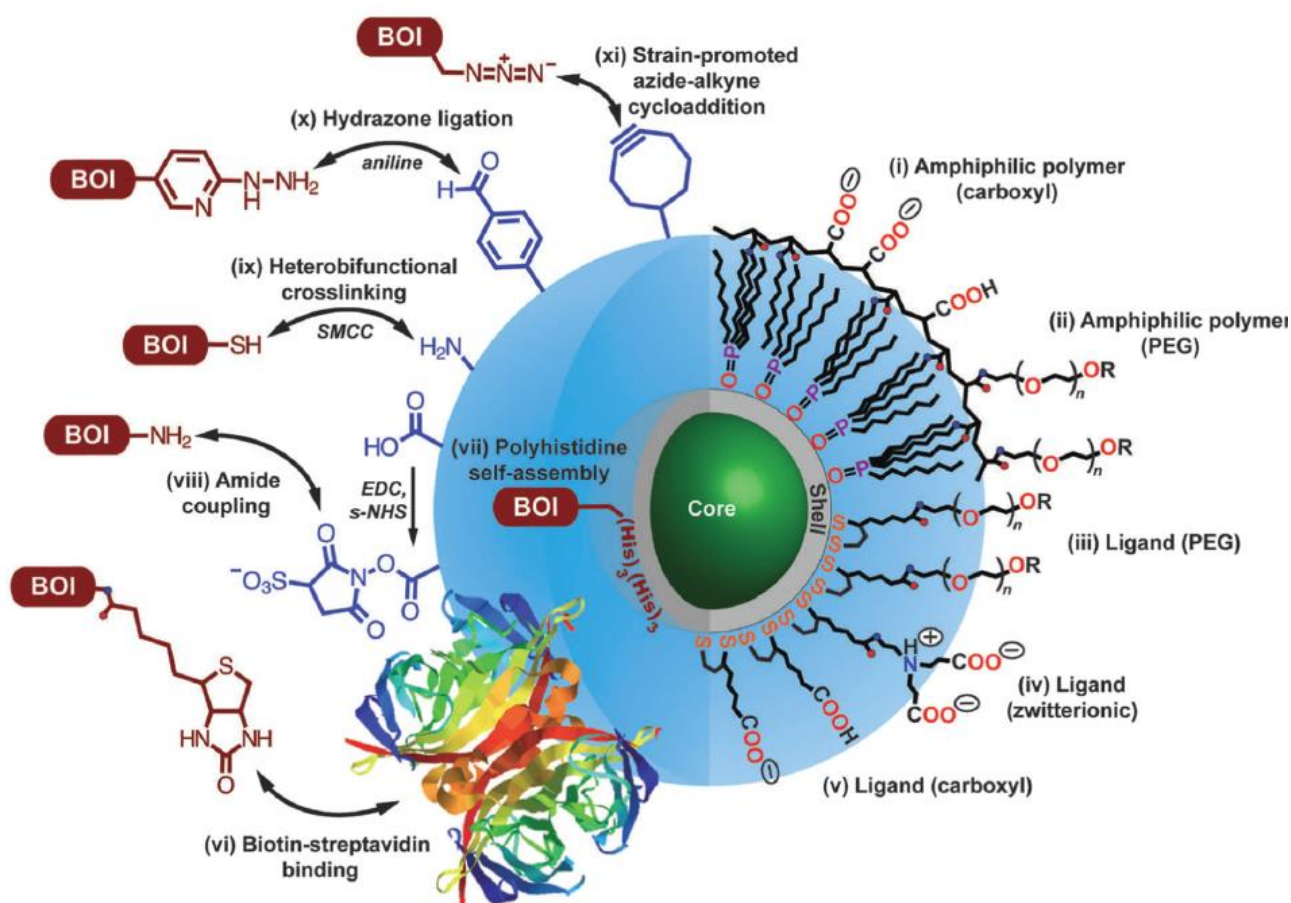


**Figure 2.12.** Illustration of selected bioconjugation (left, BOI stands for biomolecule of interest) and surface coating (right) strategies. Left side represents mostly covalent and receptor-ligand labeling strategies and right side (i,ii) represents encapsulation with amphiphilic polymers and (iii-v) hydrophobic ligand exchange to hydrophilic ligands take advantage of the thiol-affinity to anchor on the ZnS shell of the QD [117].

**Table 2.2.** Selected biological target functional groups and representative reaction mechanisms with their reactive group [153].

Target	Reactive Group	Product	Example Mechanism <sup>4</sup>
Free Thiol	Maleimide <sup>1</sup> Haloacetyl/Alkyl Halide Arylating agents Aziridine Acryloyl derivatives Disulfide Exchange <sup>1</sup> – pyridyl disulfides, 5-thio-2-nitrobenzoic acid (TNB)	Thioether Thioether Thioether Thioether Thioether Mixed disulfides	
Aldehyde/ Ketone	Hydrazine <sup>1</sup> Amines	Hydrazone Schiff's base (iminc) <sup>2</sup>	
Free Amine	<i>N</i> -hydroxysuccinimide ester (NHS) <sup>4</sup> Acyl azides Isocyanates, Isothiocyanates Sulfonyl chlorides Aldehydes, Glioxals Epoxides, Oxiranes Carbonates Arylating agents Imidoesters Carbodiimides, anhydrides	Amide Amide Urea, thiourea Sulfonamide Imine, secondary amine <sup>3</sup> Secondary amine Carbamate Arylamine Amidine Amine <sup>4</sup>	
Carboxylate	Carbodiimides <sup>1</sup> , Carbonyldiimidazole Diazoalkanes, Diazoacetyl	Amides <sup>4</sup> Ester	
Hydroxyl	Epoxides, Alkyl halogens Periodate Isocyanates <sup>1</sup> , Carbonyldiimidazole, <i>N,N'</i> -disuccinimidyl carbonate, <i>N</i> - hydroxysuccinimidyl chloroformate	Ether Aldehyde Carbamate or urethane <sup>4</sup>	
Reactive Carbon (On a phenol <i>e.g.</i> tyrosine)	Diazonium <sup>1</sup>	Diazo bond	

## 2.5 Immunoassays

Immunoassays can be considered to provide a sophisticated biochemical toolbox to quantitatively, selectively and sensitively detect an analyte (antigen), a recognition that depends on the reaction of an antigen and an antibody. These assets of immunoassays come from three important properties of antibodies which are 1) their enormous diversity of antibody paratopes to bind to an exceptionally wide range of natural and synthetic chemicals, biomolecules, cells and viruses; 2) the specificity of each antibody for the substance they bind to; and 3) the binding strength between an antibody and its target allowing precise and accurate detection of the target even at low concentrations in biological fluids. Immunoassays can be classified into heterogeneous or homogeneous assays and require signal-generating labels such as radioactive isotopes, enzymes, fluorescent probes, chemiluminescent substances, metals and metal chelates, for detection [10]. Heterogeneous and homogeneous assays can be performed in either competitive or immunometric (non-competitive) design. Competitive immunoassays are preferred when the target analytes are small molecules with the binding to only one antibody. The analyte is marked with a suitable signal-generation label and the exact concentration of analyte and antibodies should be known parameters. During reaction of analyte and antibody, competition reaction arises between unlabeled analyte and labeled analyte to a limited amount of antibody sites. The measured signal of the label is indirectly proportional to the concentration of the analyte in the sample. Immunometric designed immunoassays (also known as two-site or sandwich immunoassays) are usually used for large molecules (analytes) which possess several recognition epitopes and where two antibodies can bind to different locations on the molecule. One antibody has the role to capture an analyte and the other antibody is labeled and used for detection upon biological reaction. The measured signal from the labeled antibody in the form of antibody-antigen-antibody complex is in this case directly proportional to the concentration of the analyte in the sample. As signal-generating labels we can find: iodine 125 is the commonly used radioisotope with a half-life of 60 days and less commonly employed radioactive atoms are tritium ( $^3\text{H}$ ) with a half-life of 12.26 years, and carbon 14 ( $^{14}\text{C}$ ) with a half-life of *ca.* 5730 years according to the National Institute of Standards and Technology (NIST). Labeled antigen allows the bound or free fractions to be estimated in a competitive assay, whilst labeled antibody in a sandwich assay allows the detection of the bound analyte. In enzyme immunoassays, the label is an enzyme which is marked on either antigen or antibody and can be carried out in competitive or non-competitive formats by analyzing the enzyme's catalytic properties. Alkaline phosphatase and HRP (a 44 kDa glycosylated hemoprotein) are the two frequently used enzymes in immunoassays.

Following immuno-reaction between antibody and antigen, the enzyme activity is monitored by observing color, fluorescence or luminescence, and chemiluminescence generation from a “neutral” substrate. The recorded signal is then correlated to the antigen’s concentration. Fluorescent probes such as organic dyes, quantum dots or metal chelates can be directly labeled on the immunoanalytical reagents through functional reactive groups and used in a competitive or immunometric format. During antibody-antigen reaction and upon excitation of the fluorophores by an external light source, fluorescence or luminescence signals are generated and the signal intensity directly correlates with the antigen’s concentration. Time-resolved fluorescence immunoassays using metal chelates have the advantage of overcoming background interference by measuring in a time-window after pulsed excitation. This technique will be discussed in the next section. Chemiluminescent immunoassays do not require external light excitation to emit photons for detection. They rather depend on chemiluminescent compounds as labels such as acridinium esters/sulphonamides, and isoluminol, where light is emitted during a chemical reaction using an alkaline solution of hydrogen peroxide as an oxidizing agent [10,59].

To establish the relationship between the response (in our case luminescent signal from FRET) and concentration of the measured analyte in an immunoassay, a calibration curve needs to be constructed. Known concentrations of the samples are necessary and these specific samples are called calibrators or standards. The calibrators can come in a high known concentration and are diluted to different lower concentrations covering the desired range of measurements. A calibration curve is thus obtained and fitted to the responses of the calibrators, which is used to determine the limit of detection of the system and estimation of unknown sample concentrations. Unknown sample concentrations are usually assayed together with the calibrators and the concentration of the unknown samples are directly read and estimated on the linear fitted calibration curve due to the proportionality of the signal strength to the concentration of the analyte. The important parameters which characterize an immunoassay are the dynamic and linear range of detection, followed by the limit of detection (LOD) and sensitivity. Dynamic range corresponds to the maximum range where an accurate measurement can be made and ranges between the limit of quantification (LOQ) and limit of linearity (LOL). LOQ is defined as the concentration of the analyte that can be calculated with a high degree of confidence and LOL is the concentration of the analyte that deviates 5% from linearity. LOD is the minimum concentration that can be detected at a known confidence limit and can be calculated using **Equation 2.3**. The  $3\times SD$  is equivalent to 99.7% confidence limit. The slope of the calibration curve determines the sensitivity of the immunoassay.

$$LOD = \frac{3 \times SD}{slope} \quad (2.3)$$

*where SD corresponds to the standard deviation from a set of samples;  
3 × SD is equivalent to 99.7% confidence limit;  
slope determines the sensitivity of the immunoassay.*

## 2.6 Förster resonance energy transfer

### 2.6.1 Introduction

Förster resonance energy transfer (FRET), reabsorption, complex formation, and collision quenching are among the main mechanisms where excitation energy can be transferred from a donor molecule to an acceptor molecule. To differentiate between these transfer mechanisms, we can approximate a donor as a group of electrical oscillators close together that produce an electric field in the space around the donor. The space around the donor can be divided into four concentric zones (**Figure 2.13**) named as the contact or Dexter zone, the near zone or near field, the intermediate zone, and the far zone or far-field/radiation zone. Complex formation and collision quenching require molecular contact to occur which happen when an acceptor is in the Dexter zone (0 - 1 nm) of the donor. Reabsorption, where an emitted photon by a donor gets absorbed by an acceptor, occurs in the radiation zone of the donor which spans from 1  $\mu\text{m}$  to infinity. FRET happens only in the near zone which is approximately around 1 – 20 nm of the donor where the ideal dipole approximation can be applied. The ideal dipole approximation is valid in the near field when the distance separating the donor and acceptor is much larger than the radius of the donor and acceptor. As a result the electromagnetic interaction between the donor and acceptor is a dipole-dipole interaction, and all interactions due to higher multipoles can be ignored [129]. As verified and supported by a number of publications and citations, FRET appears to be among the most popular and important tools in biology and biochemistry. FRET is a non-radiative process involving an excited donor molecule and an acceptor molecule in its fundamental ground state. During this process, energy is transferred non-radiatively from the excited donor molecule to an acceptor molecule in close proximity. As a result, the fluorescence intensity (and decay time) of the donor decreases and the fluorescence intensity (or decay time) of the acceptor increases provided the acceptor is fluorescent. The rate of energy transfer is strongly distance dependent between the two molecules. Based on its intrinsic sensitivity to small variations in molecular distance and orientation, scientists were able to apply FRET as an optical technique to gain information in molecular conformation with nanometer resolution, structure elucidation, measuring of intermolecular/intramolecular interactions, and in *in vivo/in vitro* diagnostics [6,130,131]. In this chapter, FRET theory is mainly extracted from references [6,129,132].

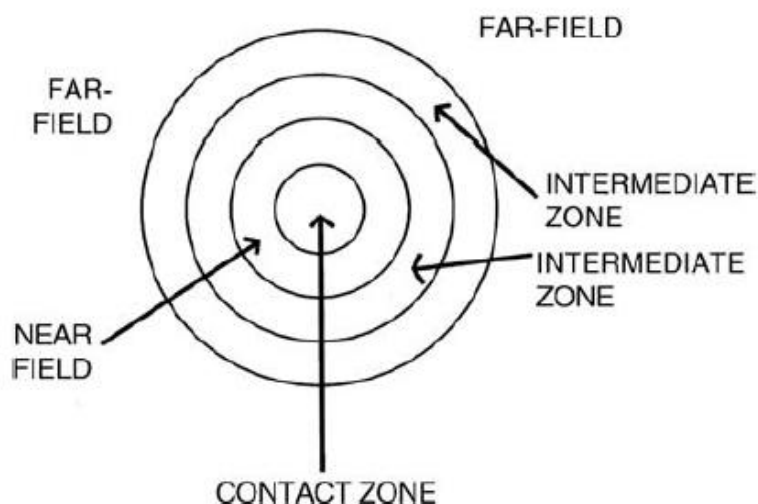


**Figure 2.13.** Space around a donor fluorophore visualized as a group of electrical oscillators, divided into four zones: contact zone, near field, intermediate zone and far-field [129].

### 2.6.2 FRET theory

The theory behind resonance energy transfer was developed by Theodor Förster back in the 40's from his knowledge of classical [133] and quantum [134] theory. In honor of his contribution, the effect was named after him. Förster was able to link theory and experiment by explaining the relationship between spectral overlap, energy transfer, and proximity, thereby showing the inverse proportionality to the sixth power of the distance between two molecules to FRET efficiency [129]. FRET is the non-radiative energy transfer between a donor molecule (D) in the excited state to an acceptor molecule (A) in the ground state, which are in close proximity, and is based on the approximation that dipole-dipole coupling can be represented by Coulombic coupling. The donor must be a fluorophore and the acceptor should be able to absorb light at the emission wavelength(s) of the donor but does not necessarily have to emit photons. In order for energy transfer to take place, the resonance condition must be fulfilled. When the donor or acceptor molecule is treated as a group of coupled electrical oscillators, the oscillators in the donor will oscillate and generate their own electromagnetic field as a result of the donor oscillators being in an external electromagnetic field caused by light exciting the donor. Often, the acceptor oscillators will not respond to the external electromagnetic field, but may be sensitive to the electric field from the donor oscillators. The resonance phenomenon appears when the acceptor oscillators sensitive to the donor oscillators' electric field, oscillate in phase with the donor oscillators at a distance. With the sharing of this electric field, in other words when the donor and acceptor share the same electronic transitions, resonance energy transfer occurs. These electronic transitions are presented in a simplified Jablonski diagram in

**Figure 2.14** (left) showing the basic principle of FRET. In spectroscopic terms, there should be a spectral overlap between the donor emission and the acceptor absorption spectra (**Figure 2.14** right).

The degree of spectral overlap, the quantum yield of the donor, the relative transition dipoles orientation of the donor and acceptor, and the distance between the donor and acceptor molecules, directly affect the rate of energy transfer. The rate of energy transfer (or FRET transfer rate),  $k_{FRET}$ , is given by **Equation 2.4** and we can observe a strong distance dependency which is proportional to  $r^{-6}$ .

$$k_{FRET} = \frac{1}{\tau_D} \left( \frac{R_0}{r} \right)^6 \quad (2.4)$$

where  $\tau_D$  is the excited-state lifetime of the donor in absence of the acceptor;  
 $R_0$  is the Förster distance representing a transfer efficiency of 50 %;  
 $r$  is the donor-to-acceptor distance.

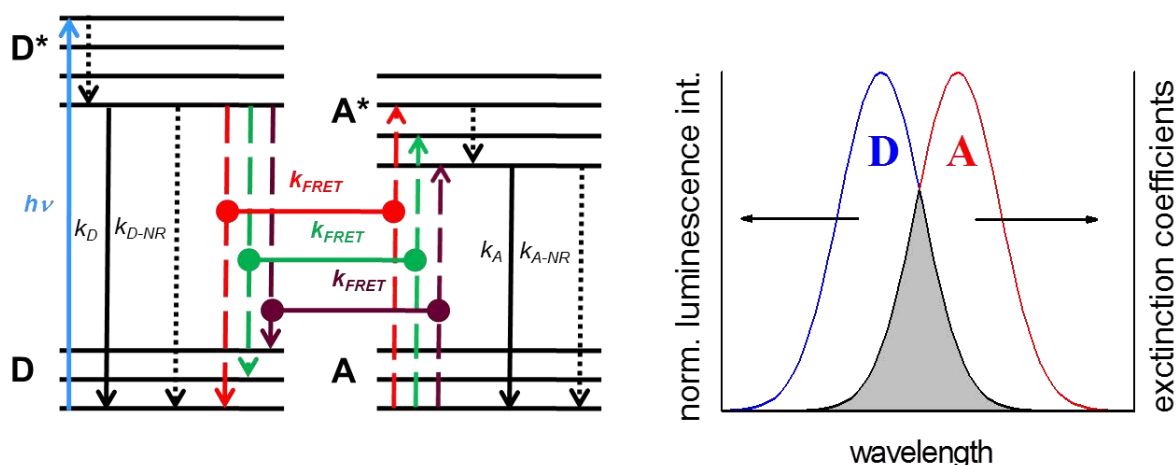


**Figure 2.14.** (Left) Simplified Jablonski diagram representing the energy levels of the donor (D) and acceptor (A) molecules. The donor is brought to an excited state ( $D^*$ ) from an electronic ground state (D) by light excitation ( $h\nu$ ), followed by inner relaxation (dotted arrows) to an excited electronic ground state and finally to the ground state by radiative decay ( $k_D$ ), non-radiative decay ( $k_{D-NR}$ ) or FRET ( $k_{FRET}$ , dashed lines referring to possible resonant transitions). FRET (horizontal lines with dots on each end) occurs when the energy levels of  $D^*$  and A are in resonance. After FRET, the acceptor is in an excited state ( $A^*$ ), followed by radiative decay ( $k_A$ ) and non-radiative decay ( $k_{A-NR}$ ) to its ground state. (Right) Spectral overlap (grey) between the donor emission (blue) and the acceptor absorption (A). The integral of this overlap is calculated using **Equation 2.6**.

From **Equation 2.4**,  $R_0$  expressed in nm, which is characteristic to a donor-acceptor pair, can be calculated at equilibrium where the FRET efficiency ( $\eta_{FRET}$ ) = 50%, giving rise to **Equation 2.5** which encompasses several crucial variables including the overlap integral  $J(\lambda)$ .

$$R_0 = \left( \frac{9(\ln 10) \kappa^2 \Phi_D}{128 \pi^5 N_A n^4} J(\lambda) \right)^{\frac{1}{6}} \quad (2.5)$$

where  $\kappa^2$  is the orientation factor describing the relative orientation of the transition dipoles of the donor and acceptor. Usually assumed to be 2/3;

$\Phi_D$  is the quantum yield of the donor in absence of energy transfer (ie, the no. of photons emitted / no. of photons absorbed);

$N_A$  is Avogadro's number ( $6.023 \times 10^{23} \text{ mol}^{-1}$ );

$n$  is the refractive index of the medium. Assumed to be  $\sim 1.4$  for biomolecules in aqueous media;

$J(\lambda)$  is the spectral overlap between the donor emission and acceptor absorption profiles.

The overlap integral (**Equation 2.6**),  $J(\lambda)$  expressed in  $\text{M}^{-1} \cdot \text{cm}^{-1} \cdot \text{nm}^4$ , is an important variable of **Equation 2.5** as it describes the degree of spectral overlap (resonance) between the donor emission and acceptor absorption. The donor emission and acceptor absorption spectra are obtained through spectroscopic measurements by recording the spectra every 0.5 or 1.0 nm. Same wavelength steps are recommended for acquiring both spectra. It is important to note that because of  $\lambda^4$  in **Equation 2.6**, the peak of the overlap curve will always be at a larger wavelength than where the donor emission and acceptor extinction coefficient intersect. Overlap integral function will not correspond exactly to the spectral overlap curve and calculation of  $R_0$  from  $J(\lambda)$  will thus lead to an approximation.

$$J(\lambda) = \int \bar{I}_D(\lambda) \varepsilon_A(\lambda) \lambda^4 d\lambda \quad (2.6)$$

where  $\bar{I}_D$  is dimensionless and represents the area normalized emission spectrum of the donor;

$\varepsilon_A(\lambda)$  is the molar extinction coefficient spectrum of the acceptor;

$\lambda$  is the wavelength range of the spectral overlap in nm.

The orientation factor,  $\kappa^2$ , describes the relative orientation of the transition dipoles in space of the donor and acceptor. In **Equation 2.7**,  $\theta_{DA}$  is the angle between the donor and acceptor transition moments and is defined by **Equation 2.8**.  $\theta_D$  and  $\theta_A$  are the angles between the donor and acceptor transition dipole moments and the donor-acceptor connecting vector  $\mathbf{r}$ , and  $\phi$  is the azimuth between the planes  $(\mathbf{M}_D, \mathbf{r})$  and  $(\mathbf{M}_A, \mathbf{r})$ . **Figure 2.** illustrates the angles involved in the definition of  $\kappa^2$  and the different values of  $\kappa^2$ .

$$\kappa^2 = (\cos\theta_{DA} - 3\cos\theta_D \cos\theta_A)^2 \quad (2.7)$$

$$\cos\theta_{DA} = \sin\theta_D \sin\theta_A \cos\phi + \cos\theta_D \cos\theta_A \quad (2.8)$$

Kappa square,  $\kappa^2$ , can range from 0 to 4 depending on the relative orientation of donor and acceptor transition dipole moments. A value of 0 corresponds to perpendicular transition

moments, collinear transition moments results when  $\kappa^2 = 4$  and  $\kappa^2 = 1$  for transition moments that are parallel (**Figure 2.15 right**). We assume an average  $\kappa^2 = 2/3$  when the orientations of the donor and acceptor transition dipole moments randomize within the lifetime of the excited state (dynamic averaging regime). In other words when the donor and acceptor molecules undergo fast isotropic motion all orientations are equally probable and the dynamic isotropic average of  $\kappa^2 = 2/3$ . However, we can also assume static averaging regime when the rates of rotation are small compared to the rate of donor decay in the presence of the acceptor. In this case,  $\kappa^2$  can take values ranging between 0 and 2/3. In most biological FRET experiments the orientation factor is assumed to be 2/3 and since the sixth root is taken to calculate  $R_0$ , an error not exceeding 35 % results.

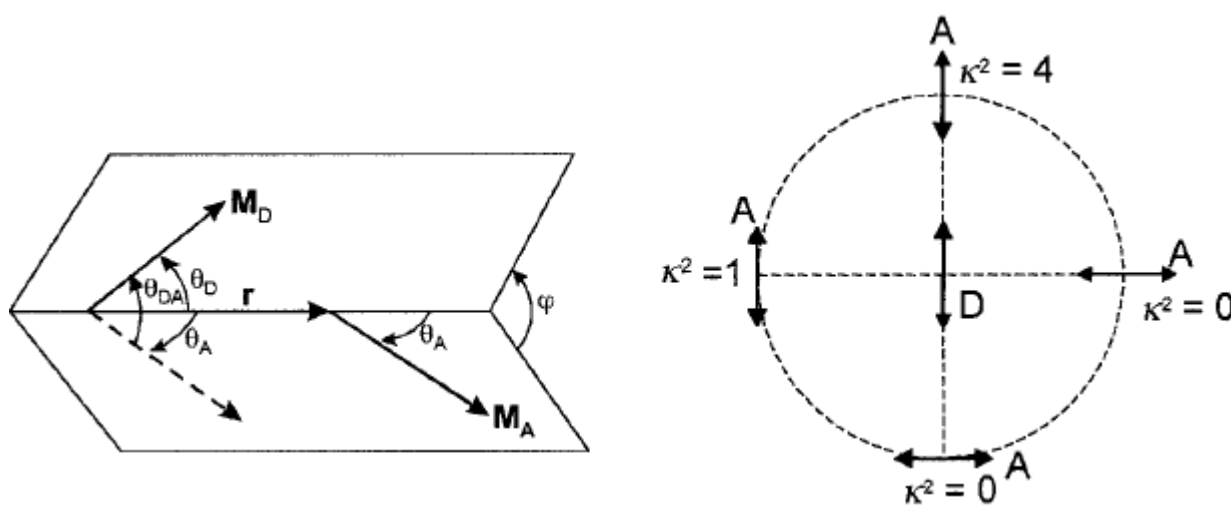


**Figure 2.15.** (Left),  $\theta_{DA}$  is the angle between the donor and acceptor transition moments and is given by Equation 6.  $\theta_D$  and  $\theta_A$  are the angles between the donor and acceptor transition dipole moments and the donor-acceptor connecting vector  $r$ , and  $\phi$  is the azimuth between the planes ( $M_D, r$ ) and ( $M_A, r$ ). (Right) Values which  $\kappa^2$  can take depending on the orientation of the donor and acceptor transition dipoles [132].

The efficiency of energy transfer (or FRET efficiency) denoted as  $\eta_{FRET}$ , can be calculated by using the FRET transfer rate and the decay time  $\tau_D$  of the donor. The faster the transfer rate as compared to the decay rate, the more efficient will be the energy transfer. First part of **Equation 2.9** shows the relationship of FRET transfer rate to the total decay rate of the donor in presence of an acceptor. Substituting **Equation 2.4** into  $\kappa_{FRET}$ , we obtain the right side of **Equation 2.9** which shows that FRET efficiency is greatly dependent as sixth power of the distance between the donor and acceptor molecules. Determination of  $r$  using  $\eta_{FRET}$  and  $R_0$ , allows FRET to be used as a spectroscopic molecular ruler. As it can be observed in **Figure 2.16**, due to this sixth power dependency, FRET efficiency is mostly sensitive in the region  $0.5R_0 \leq r \leq 2.0R_0$  with a sharp efficiency at  $r = R_0$  (high dynamic range).

$$\eta_{FRET} = \frac{\kappa_{FRET}}{\tau_D^{-1} + \kappa_{FRET}} = \frac{R_0^6}{R_0^6 + r^6} \quad (2.9)$$

where  $r$  is the distance separating the donor and acceptor

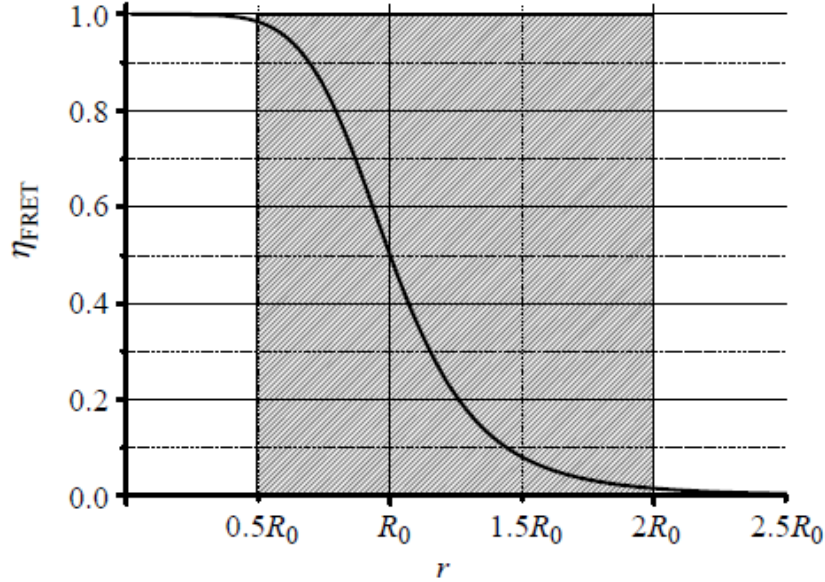


**Figure 2.16.** FRET efficiency  $\eta_{FRET}$  variation as a function of the donor-acceptor distance ( $r$ ) shows the sixth power dependency and a measurable range of the FRET efficiency between  $0.5R_0$  and  $2.0R_0$  with a steep curve around  $R_0$  [135].

FRET efficiency can also be calculated using intensities and lifetimes of the donor in absence and presence of an acceptor (**Equation 2.10**). During FRET process, quenching of donor intensity and lifetime occur causing  $I_{DA} < I_D$  and  $\tau_{DA} < \tau_D$  hence leading to efficiency values between 0 and 1.

$$\eta_{FRET} = 1 - \frac{I_{DA}}{I_D} = 1 - \frac{\tau_{DA}}{\tau_D} \quad (2.10)$$

where  $I_D$  is the fluorescence intensity of the donor in absence of the acceptor;  
 $I_{DA}$  is the fluorescence intensity of the donor in presence of the acceptor;  
 $\tau_D$  is the donor decay time in absence of the acceptor;  
 $\tau_{DA}$  is the donor decay time in presence of the acceptor.

### 2.6.3 FRET applications

The ability of FRET to detect near field interaction between two molecules at the nanometer scale enables numerous applications for the study of molecular dynamics in biophysics and in molecular biology. Some examples include monitoring of protein-protein / protein-DNA interactions, receptor/ligand interactions, and protein conformational changes. Recently, more and more FRET-based biosensors are being developed for use in the medical field as a simple,

rapid, and sensitive transduction mechanism [130,136]. FRET is not restricted to the biological field and can also be used as the basis for pH and cation sensors [6]. FRET happens when a donor and acceptor fluorophore are in close proximity and the examples mentioned earlier allow doing so. FRET can be triggered upon attachment of a donor fluorophore and an acceptor fluorophore to a single protein, and due to environmental constraints the protein is forced to alter its conformation thus bringing donor and acceptor close together [136]. In the case of monitoring of cellular dynamics, donor and acceptor fluorophore are labelled to a molecule at close positions to continuously observe FRET. Upon cleavage by a cellular process on the binding site of one of the fluorophores, they are separated and FRET decreases [137]. Single-molecule FRET (sm-FRET) is another FRET technique that allows the sensitive detection at the single-molecule level. Compared to an ensemble of measurements that provide average FRET data of a whole population of molecules, sm-FRET gives conformational changes in a single biomolecule or association/dissociation dynamics in a single complex of interacting partners [138]. Biosensors using FRET as a signal transduction mechanism are gaining popularity in the medical field such as in medical diagnostics, prognostics and personalized medicine based on their improved sensitivity, specificity and performance. Biomolecules target of interest include proteins, metabolites, drugs, toxins, nucleic acids, human cells, microbes, and other pathogens such as viruses, parasites and are often found in blood, urine, saliva, urine and other bodily fluids [130,139]. Conjugation/labeling of donor and acceptor fluorophores to biomolecules such as on antibodies, proteins and peptides, nucleic acids, and aptamers, results in measurable FRET signals when the donor and acceptor are brought close together during sensing/recognition process [130]. pH probes based on FRET are optical sensors for pH determination, for *e.g.* in intracellular pH sensing and imaging, and have the advantages of being non-invasive, can be miniaturized to the nanoscale level and are shielded from electrical or magnetic field interferences as compared to pH sensors based on electrodes. One method of designing a highly sensitive FRET-based pH probe is by using a europium chelate which is coupled to a fluorescent near-infrared emitting pH indicator via a dodecyl spacer, resulting in a FRET system that is sensitive to pH changes covering a dynamic range of pH from 9 to 3 [140]. There exist a tremendous amount of fluorophores which can be used as donor and acceptor (FRET-pairs) and great care should be taken while choosing the appropriate FRET-pairs for the successful design of the experiments. Among the most often used fluorophores we can find organic dyes, fluorescent proteins, lanthanide chelates (terbium/europium complexes), quantum dots, and carbon nanomaterials. These materials may function as FRET donor and/or acceptors depending on the experimental design [9].

### 2.6.3.1 FRET-based immunoassays

A competitive homogeneous FRET-based assay was first demonstrated by Ullman et al. in 1976 by labeling fluorescein (donor dye) to an antigen and an antibody with rhodamine (acceptor dye) [141] and since then, FRET-based immunoassays have been greatly improved. Immunoassays based on FRET using fluorescent labels provide high selectivity and sensitivity by measuring the donor quenched luminescence or sensitized acceptor emission when the FRET-pairs are brought in close proximity due to biological recognition from large or small analytes (antigens) with their corresponding antibodies. Other sensing and recognition molecules include polymers, carbohydrates, nucleic acids, and aptamers [130]. FRET is a spectroscopic tool that allows measuring distances in the 1-20 nm range; hence FRET-pairs having large  $R_0$  should be wisely selected in order to achieve sufficient energy transfer for sensitive detection of biomolecules especially when large analytes are involved. As discussed in **section 2.2**, proteins contain a wide range of functional groups, and there exists many donor/acceptor probes modified with reactive functional groups for bioconjugation. The probes' position and stoichiometry should also be considered when designing FRET experiments in order to be consistent in terms of reproducibility [9]. Even though sandwich assays are the conventional format for antigen detection, the relatively large immuno-complex can be an inconvenient from a FRET perspective bringing decreased energy transfer efficiency, hence sensitivity of the immunoassay is impacted. By using "non-traditional" FRET materials ("traditional" materials being organic dyes) such as colloidal QDs or lanthanide complexes, unique labeling strategies, or using fragmented antibodies, have been reported to improve energy transfer efficiency. QDs known for their high quantum yields have been used in combination with an Alexa Fluor dye to improve  $R_0$  for the sensitive detection of estrogen receptor  $\beta$  using monoclonal IgGs in a sandwich assay format [142]. Sub-nanomolar concentrations of prostate-specific antigen [25] and alpha-fetoprotein [143] were detected using FRET combinations of QDs and lanthanide complexes. QDs and a terbium complex in a homogeneous sandwich format has been recently designed for the duplexed measurement of EGFR/HER2 from a single sample using nanobodies and antibodies with sub-nanomolar detection limits [144]. Multiplexed sensitive detection, without any amplification steps, of micro-RNA using terbium complexes to QDs FRET was also reported [145]. Oligonucleotide antibody-labeling system has also been used to detect several target analyte types also in a homogeneous sandwich assay. Short complementary oligonucleotides (single-stranded DNA, ssDNA) were labeled with either a donor or an acceptor which were in turn conjugated to specific antibodies. Addition of the target analyte and binding of the antibodies to the epitopes of the target resulted in hybridization of the two ssDNA due to their close proximity [146,147].

### 2.6.3.2 Lanthanides as FRET-donor

LLCs and UCNP make ideal FRET-donors due to their unique photophysical properties. In 1993, Mathis presented for the first time the use of LLCs as energy donors in a homogeneous FRET immunoassay [148] and since then terbium- and europium-based LLCs have been used greatly as FRET-donors. With extremely narrow emission bands of LLCs and UCNP it is fairly easy to discriminate their luminescence from other PL signals and they are relatively less prone to photobleaching as compared to organic fluorescent dyes. Depending on the designed FRET experiments, luminescent acceptor fluorophores such as fluorescent proteins, organic dyes, and QDs can be paired with LLCs as donor in order to achieve large Förster distance,  $R_0$ , (*ca.* 11 nm for a Tb-QD FRET-pair [125]) [149]. However, UCNP-QD (or any suitable acceptor) FRET-pairs yield smaller Förster distance due to the low quantum yield of UCNP as compared to LLCs ( $R_0 < 5$  nm). Lanthanide ions possess long luminescence lifetime of up to a few millisecond and when paired with traditional acceptor fluorophores which have generally very short nanosecond range lifetimes, a detector gating after pulsed excitation can efficiently suppress nanosecond to microsecond lifetimes of directly excited acceptors and sample autofluorescence, hence improving measurement accuracy and SNR. Furthermore, due to large difference in donor and acceptor excite-state decay times,  $\tau_{DA} = \tau_{AD}$  in the case the acceptor is excited by FRET via the donor. This particularity provides the same decay time analysis on the quenched donor and sensitized acceptor and also allows detection of sensitized emission of the acceptor caused by FRET. Two lanthanide ions that have been commonly used in LLCs are terbium and europium as a result of their strong luminescence in the visible range and detection with standard spectroscopy and microscopy equipment [149,150]. These Eu and Tb complexes have been employed in several FRET experiments for conformational changes study, biological binding events, DNA hybridization, and as spectroscopic ruler [149–151]. Spectral multiplexing is possible with LLCs as a result of their narrow and well-separated emission bands, and multiplexed detection of tumor markers or micro-RNA using Tb complexes as donor with organic dyes or QDs as acceptors in a homogeneous TR-immunoassay have been successfully demonstrated [11,144,145,152]. LLCs had a major impact on homogeneous and heterogeneous time-resolved immunoassays for biomarker detection. In commercially available assays we find dissociation-enhanced lanthanide fluorescence immunoassay (DELFLIA) from PerkinElmer which is a heterogeneous TR-assay based on luminescence of europium, samarium and terbium chelates [153]. Among the TR-homogeneous assays we find HTRF (homogeneous time-resolved fluorescence) from Cisbio [154], TRACE (time-resolved amplified cryptate emission) from B.R.A.H.M.S and Cezanne [155], LANCE (lanthanide chelate excitation) from PerkinElmer [156], and LanthaScreen from ThermoFisher Scientific [157].

Today, HTRF and TRACE are the routinely used technologies in medical diagnosis and high-throughput-screening applications for the detection of different biomarkers [149].

UCNPs donors in most cases are coupled to organic dyes as acceptors for biosensing. UCNPs-based DNA sensor was firstly designed by Zhang et al. in 2006 using DNA hybridization with a complementary DNA labeled with dye TAMRA as FRET-acceptor for the detection of target DNA [158]. Zhu et al. in 2014, developed a novel aptasensor for the detection of lysozyme and DNA based on FRET between  $\text{NaYF}_4:\text{Yb}^{3+},\text{Er}^{3+}$  UCNPs as donor and a dye labeled aptamer as acceptor which provided nM detection limit [159]. UCNPs coupling with QDs have also been reported where UCNP-to-QD FRET was successfully designed for biosensing [13]. Doughan et al. in 2015 developed a paper-based FRET nucleic acid hybridization assay where core/shell UCNPs were immobilized on a paper substrate and then conjugated to ssDNA, which was complementary to one part of the target ssDNA. Formation of UCNP-QD FRET pairs occurred when solutions containing QD-ssDNA and target DNA were added on the paper substrate. Upon NIR excitation,  $\text{Tm}^{3+}$  transferred non-radiative energy to the QDs and QD PL could be observed due to FRET. The test was able to detect three different ssDNAs with fmol detection limits [160]. Another FRET bioassay involving UCNPs and QDs were designed by Mattsson et al. in 2016 where they used UCNP-streptavidin-biotin-QD recognition as a biological model system. Such model system allowed the quantification of biotin in a competitive replacement assay and upon 980 nm excitation, QD PL could be detected due to FRET from  $\text{Er}^{3+}$  ions to QDs having a maximum emission at 605 nm. The detected QD PL intensity was relatively low due to the relatively large distance between  $\text{Er}^{3+}$  donors and QD acceptors and low PL quantum yields of UCNPs but could nevertheless return very sensitive measurements of biotin in the nM range due to no sample autofluorescence or no PL from direct excitation of QDs at 980 nm [161]. Another attractive system which has great potential for sensing and imaging applications was reported by Lahtinen et al. in 2015, where they used NIR excitation to generate long-luminescence of an  $\text{Eu}^{3+}$ -chelate (which is normally excited in UV to luminescence) by using  $\text{Tm}^{3+}$ -doped UCNPs as donors which have their emission in the UV range. The functionality of the pair was demonstrated in a homogeneous back-titration assay for biotin and upon excitation at 980 nm,  $\text{Tm}^{3+}$  ions could transfer their energy by resonance energy transfer to the neighboring excited singlet state of the  $\text{Eu}^{3+}$  chelate antenna which further populated the excited energy levels of  $\text{Eu}^{3+}$  after intersystem crossing to the triplet state of the antenna. Relaxation of the excited energy levels of  $\text{Eu}^{3+}$  was accompanied by characteristic emission wavelengths of the metal ion [162]. Monitoring of pH inside cells is crucial as an abnormal acidic pH is usually assigned to cellular dysfunctions such as cancer [163]. Optical pH sensors combining UCNPs and pH-sensitive dyes represent a good alternative

to available pH-sensitive sensors (which are prone to photobleaching and background autofluorescence) for sensing and imaging of pH in biological applications. Meier et al. demonstrated an easy-to-fabricate pH sensor film consisting of NaYF<sub>4</sub>:Er<sup>3+</sup>,Yb<sup>3+</sup> upconversion phosphors (UCP) and pH indicator neutral red (absorbing at the UCP's green emission) incorporated in a hydrogel matrix. The red emission of the UCP is unaffected by the pH indicator and was used as a reference signal for ratiometric measurements. A hand-held digital camera based on a CMOS chip containing red-green-blue channels was utilized as a simple spectrometer for recording the green and red peak of the UCP. Upon 980 nm excitation of the pH sensor film, ratiometric measurement of the red to the green channel data allowed measuring pH in the range of 5 – 8.5, background-free, which enabled the sensor to be applied in strong scattering and highly autofluorescent samples such as milk and human serum. Maximum sensitivity with this pH sensor was observed in the pH range of 6.0 to 7.5 with a resolution of 0.06 pH units [164]. Arppe et al. developed a much more sensitive nanoprobe for sensing and imaging of intracellular pH compared to common luminescent pH indicators, with a dynamic pH-range of 2.5 to 7.2, and a resolution of 0.3 pH units. Their pH nanosensor was based on the upconversion resonance energy transfer between an aminosilane-coated NaYF<sub>4</sub>:Yb<sup>3+</sup>,Er<sup>3+</sup> UCNPs and a fluorescent NHS red pH-dependent dye. Upon conjugation of both probes and excitation at 980 nm, ratiometric measurement could be performed by determining the ratio of the green upconversion emission and the sensitized emission of the indicator, which increased with decreasing pH. They also demonstrated the applicability of their pH nanosensor as a probe for ratiometric pH imaging in HeLa cells using a confocal fluorescence microscope [165].

### 2.6.3.3 QDs as FRET-donor/acceptor

The unique photophysical properties of QDs make them ideal FRET donors and when paired with appropriate donors make them excellent FRET acceptors. As FRET donors, their emission can be size (or composition) fine-tuned due to the confinement effect and hence optimize the spectral overlap and FRET efficiency with an acceptor, for *e.g.* an inorganic dye, yielding larger Förster distance. Their narrow emission spectra allow minimizing the optical crosstalk in both acceptor and donor PL detection channels. Furthermore, QDs have broad absorption wavelength range and excitation wavelength can be chosen in order to avoid direct excitation of the acceptor. Different QDs can be excited at a single wavelength and their narrow PL emission which can be more readily deconvoluted, make them serious candidates for multiplexing. QDs are suitable acceptors only for a very few donor molecules. Considering that PL decay times of QDs (>10 ns) are usually longer than that of most organic dyes (< 5ns) and in a FRET

experiment upon light excitation when they are in close proximity, there will be only a very small population of QDs, which remain in the ground state for accepting non-radiative energy from a short-lived donor dye. This FRET configuration shows that QDs as acceptors are limited to donors having long-lived decay times ( $> \mu\text{s}$ ) [120].

Potential donors having long luminescent lifetimes are lanthanide based complexes or UCNPs. When used as donors to QD acceptors, upon pulsed excitation both donor and acceptor will be excited and due to their large decay time difference the majority of the lanthanide donors will remain in the excited state longer than the nanosecond short-lived QDs which have already decayed to their ground state thus enabling FRET if they are close to one another. Some applications of lanthanide as donors and QDs as acceptors for FRET have already been discussed in **section 2.6.3.2**.

#### 2.6.4 Measurement techniques

Once suitable FRET-pairs have been selected with known photophysical properties and  $R_0$  determined, detection of luminescence intensities from donor and acceptor probes during FRET can be measured by steady-state and/or time-resolved spectroscopy [6,135]. It should also be noted that the photophysical characterization of the FRET-pairs are also performed using steady-state and time-resolved measurements. **Steady-state** measurements are performed by continuous excitation (generally with a xenon arc lamp) at a fixed wavelength and recording of the emission intensities of the FRET-pairs as a function of wavelength. Full emission spectra measurement is achieved by scanning over the wavelength range of their emission spectra using usually monochromators and detection with a photomultiplier tube (PMT) in selected wavelength steps. The smaller the wavelength steps, the more resolute the emission profile. Emission (also applies to excitation) spectra need spectral correction in order to obtain the “true” emission profiles of a sample. The raw spectra are affected by the output of the excitation source, monochromator efficiency and spectral response from the detector. The corrected spectra are obtained by using calibration files that are unique for each spectrometer, monochromator, and detector which are usually built in the acquisition software by the manufacturer. From the corrected spectra, we can extract donor only intensities ( $I_D$ ), acceptor only intensities ( $I_A$ ), donor in presence of acceptor intensities ( $I_{DA}$ ) and acceptor in presence of donor intensities ( $I_{AD}$ ). In order to yield quantitative information, the individual spectra of the donor only and acceptor only (**Figure 2.17 (a)**) should be deconvoluted (separated) (**Figure 2.17 (c-d)**) from the FRET spectra (**Figure 2.17 (b)**), which can be performed by using

a fitting procedure by identifying the proportional contribution of the donor and acceptor to the donor-acceptor spectrum during FRET. In this way we obtain correct values for  $I_D$ ,  $I_A$ ,  $I_{DA}$ , and  $I_{AD}$ , which can be substituted in **Equation 2.10** for FRET efficiency and hence determination of distances from **Equation 2.9**. For spectrally well separated emission, we can use the peak values of  $I_D$ ,  $I_A$ ,  $I_{DA}$ , and  $I_{AD}$  for FRET parameters calculation [135].

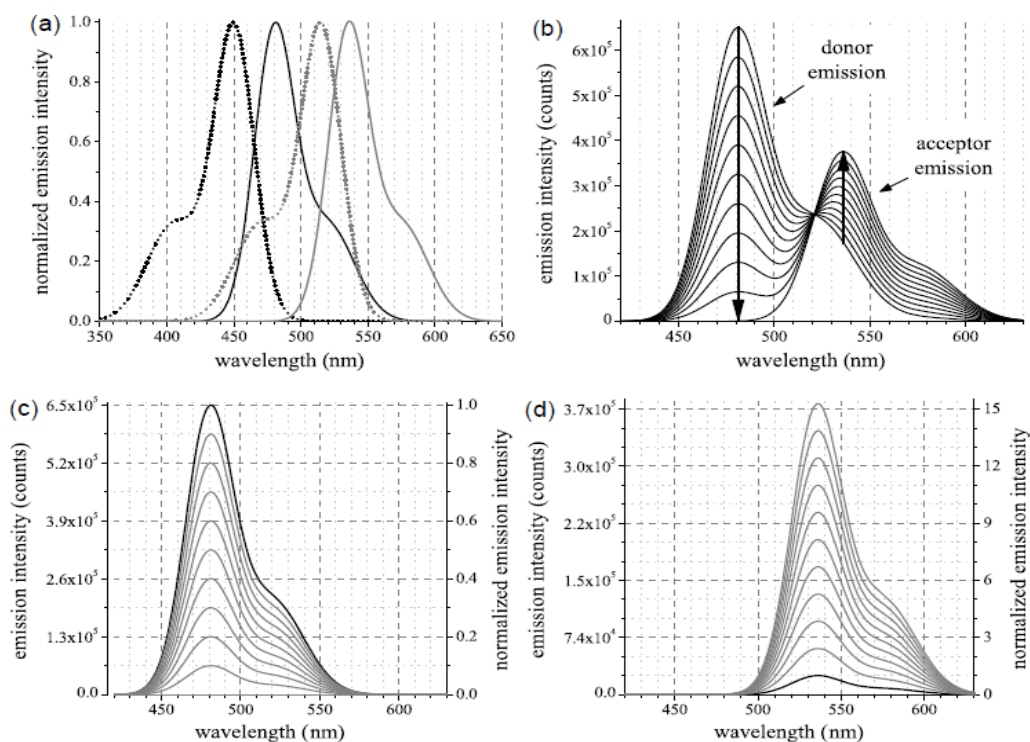


**Figure 2.17.** Representative steady-state FRET experiments involving dyes. (a) Peak normalized absorption (dotted) and emission (continuous) spectra of donor and acceptor. (b) Emission spectra of different mixtures of donor-acceptor during FRET. Excitation of donor at 420 nm. Luminescence of donor is quenched by acceptor and luminescence of acceptor is sensitized in presence of donor as indicated by the arrows. (c) represents the deconvoluted spectra of the donor in presence of the acceptor and (d) the deconvoluted spectra of the acceptor in presence of the donor [135].

**Time-resolved** measurements are performed to measure luminescence decay-times or lifetimes of a fluorophore and represent the average time for a molecule to remain in an excited state before emission of a photon. Time-domain and frequency-domain measurements are the two dominant methods employed in time-resolved luminescence spectroscopy. After presenting both methods for lifetime determination and the techniques involved for photon counting involved in this thesis, time-resolved FRET (TR-FRET) will be presented. In time-domain measurements, time-dependent intensities are measured following short pulsed excitation of light. The pulse width should be very short and depending on the lifetime of the sample excitation pulse can be in nanosecond range for lasers and up to microsecond range for flash

lamps. Single or multiple luminescence decay times  $\tau_i$  are determined by exponential fitting of the photoluminescence decay curves based on **Equation 2.11**:

$$I = \sum_i A_i e^{-\frac{t}{\tau_i}} \quad (2.11)$$

where  $I$  is the luminescence intensity;

$A_i$  is the amplitude for different  $\tau_i$ ;

$\tau_i$  is the different decay times.

When luminescence decay is multi-exponential, each decay time is weighted by the corresponding fractional intensity or amplitudes and are referred as intensity-averaged or amplitude-average lifetime respectively. Depending on the phenomenon under study, intensity-average lifetime ( $\langle \tau \rangle_{Int}$ , **Equation 2.12**) is used for the calculation of an average collisional quenching constant, whereas amplitude-average lifetime ( $\langle \tau \rangle_{Amp}$ , **Equation 2.13**) is used for the calculation of FRET efficiency in FRET experiments.

$$\langle \tau \rangle_{Int} = \frac{\sum A_i \tau_i^2}{\sum A_i \tau_i} \quad (2.12)$$

$$\langle \tau \rangle_{Amp} = \frac{\sum A_i \tau_i}{\sum A_i} \quad (2.13)$$

**Frequency-domain** method relies on the excitation of a sample with intensity-modulated light, which is typically a sine-wave modulation, at a frequency  $f$ . The light emitted from the sample follows the modulation frequency, which is defined as  $= \frac{\omega}{2\pi}$ , with  $\omega$  being the angular modulation frequency, but with a time delay usually called phase shift or phase angle and partially demodulated with respect to the excitation. Suppose the sample is excited by an intensity-modulated light source,  $I = I_{av}(ex) + I_p(ex) \cos(\omega t)$ , then the emitted light will be  $I = I_{av}(em) + I_p(em) \cos(\omega t - \phi)$ ; where  $I_{av}(ex)$  and  $I_{av}(em)$  are the average intensity of excitation and emission, respectively.  $I_p(ex)$  and  $I_p(em)$  are the amplitude or peak of the intensity oscillations of excitation and emission, respectively, and  $\phi$  the phase shift. The

demodulation is expressed as modulation ratio  $M = \frac{I_p(em)}{\frac{I_{av}(em)}{I_p(ex)} \frac{I_{av}(ex)}}{I_{av}(ex)}$ , and both  $\phi$  and  $M$  characterize the

harmonic response of the fluorophore which can be used to calculate single or multiple lifetimes. The mathematical relation between phase shift, modulation ratio and lifetimes are defined by **Equations 2.14 and 2.15** with  $\alpha_i$  being the pre-exponential factors (or amplitudes):

$$\phi = \tan^{-1} \left( \frac{\sum_i (\alpha_i \omega \tau_i^2) / (1 + \omega^2 \tau_i^2)}{\sum_i (\alpha_i \tau_i) / (1 + \omega^2 \tau_i^2)} \right) \quad (2.14)$$

$$M = \sqrt{\frac{\left[ \left( \sum_i (\alpha_i \omega \tau_i^2) / (1 + \omega^2 \tau_i^2) \right)^2 + \left( \sum_i (\alpha_i \tau_i) / (1 + \omega^2 \tau_i^2) \right)^2 \right]}{\left( \sum_i \alpha_i \tau_i \right)^2}} \quad (2.15)$$

Response curves (decay curves) generated for the time-domain and frequency-domain are fitted using the least-square method by varying the fitting parameters  $A_i$ ,  $\alpha_i$  and  $\tau_i$  in **Equations 2.11-2.15** until a best fit is obtained between the experimental data and the mathematical fit values. In the case of short lifetimes (in the nanosecond range), a deconvolution of the instrument response function (IRF) to the measured fluorescence decay curve is necessary in time-domain measurements in order to extract the “true” lifetime of the sample whilst no deconvolution is necessary for frequency-domain measurements as the data are directly analyzed in the frequency domain [6,132,135]. IRF depends on the shape of the excitation pulse and the instrumentation used to detect the pulse. The IRF is recorded under the same measuring conditions as the fluorescence decay curve by using a scattering solution such as Ludox which is a colloidal silica solution or water [6,132]. The measured IRF is thus the convolution of the response from the detector, the electronic response time of the acquisition system and the laser pulse duration. Similarly, the acquired fluorescence decay curve is the convolution of the real exponential decay with the IRF. A deconvolution process is then performed using the least-square method in order to obtain the best fit to the model decay and then comparing the fit to the experimental decay curve hence extracting the “true” lifetimes of the sample. It should be noted that the term “deconvolution” is not mathematically exact in this context as the fitting procedure used by most fitting programs is achieved using iterative reconvolution with least-square analysis [6,166]. The model for performing the multi-exponential fits with reconvolution is given by **Equation 2.16**:

$$I(t) = \int_{-\infty}^t IRF(t') \sum_i A_i e^{-\frac{t-t'}{\tau_i}} dt' \quad (2.16)$$

where  $t'$  is the fitting starting point

**Figure 2.18** and **Figure 2.19** show the measurement of decay curves in the time-domain and frequency-domain. A “deconvolution” is needed in time-domain in order to extract the lifetimes of the fluorophore whereas in frequency-domain no deconvolution is necessary.

Measurements of lifetime in the frequency domain are compatible with tunable continuous-wave excitation sources and lifetimes in the ps range can be rapidly determined. In time-

domain, the decay curves are acquired by excitation with pulsed sources such as pulsed diode lasers. Depending on the lifetime of the fluorophore, the photons arriving at the detector can be counted by several techniques such as steady-state photon counting, gated photon counting, multichannel scalers (MCS), and time correlated single photon counting (TCSPC) [167]. In this thesis we chose to use the time-domain method for temporal characterization of the FRET-pairs using MCS and TCSPC as counting techniques.

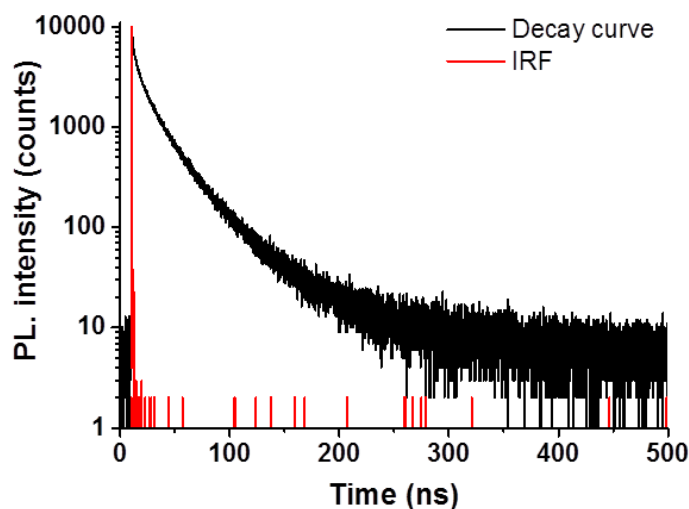


**Figure 2.18.** (Black) Multi-exponential decay curve of a QD sample emitting at 605 nm when excited by a pulsed laser at 405 nm. (Red) Instrument response function (IRF) measured at excitation wavelength of 405 nm. "Deconvolution" of the 2 curves resulted in a typical lifetime of QDs with  $\langle\tau\rangle_{\text{amp}} = 4.8$  ns.

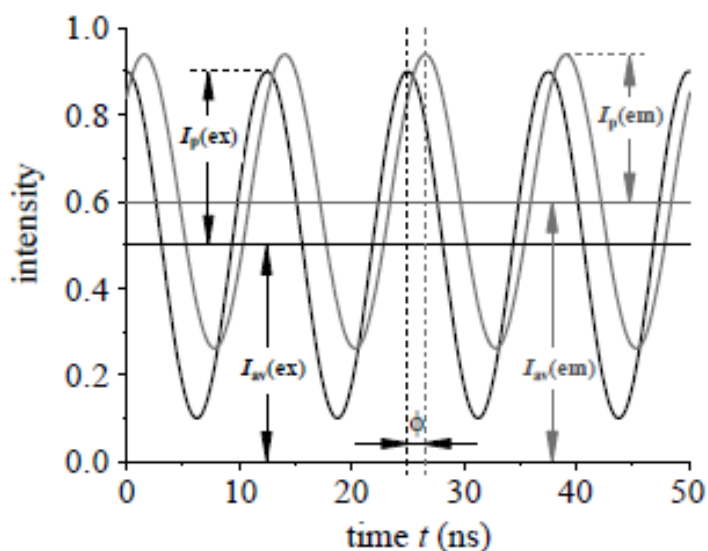


**Figure 2.19.** Frequency domain measurements for the determination of luminescence lifetimes. In this simulated graph, the sample is excited at an intensity modulated frequency of 80 MHz (black curve). The emission profile is displayed in grey and calculation of  $\phi$  and  $M$  gives an average lifetime of 2 ns [135].

**Multichannel Scalers (MCS)** are able to count several photons per signal period. All incoming photons are counted within subsequent time intervals and stored in channels of a fast data memory. Each sequence or sweep is started in the memory by a trigger pulse and is synchronized with the period of the optical signal. A waveform is generated as a result of the numerous photons arriving at the photomultiplier tube (PMT) and the waveform of repetitive emitted signals can therefore be accumulated over many signal periods to improve data quality. A histogram of counts as a function of time is constructed (**Figure 2.20**). MCS however are not fast enough to record fluorescence lifetimes which are in the ns range due to its channel width but are excellent solution for long luminescence lifetime measurements in the microsecond to second range [168]. We will use this counting technique for TR-FRET experiments and characterization of our donor, which is a lanthanide complex of Tb. **Figure 2.20** represents the principle of a multichannel scaler.

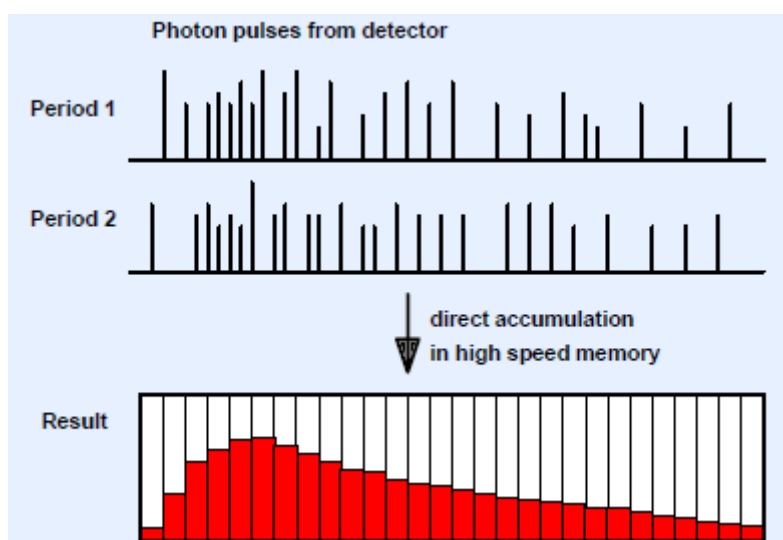


**Figure 2.20.** Principle of a multichannel scaler where several photons per signal period are recorded and the direct accumulation of the photons in high speed memory allows the creation of a histogram of counts versus time [167].

**Time correlated single photon counting (TCSPC)** is another counting technique for the counting of single photons per excitation pulse. The probability of detecting one photon at time  $t$  after pulsed excitation is directly proportional to the fluorescence intensity at that time. The generation of a single photon or an empty cycle is a completely random process and is described in terms of probabilities (**Figure 2.21**). This counting technique can be compared to a stopwatch where the reference for the timing (start time) is the excitation pulse and when a single photon is detected (stop time) by a single photon sensitive PMT (or by micro channel plate detector; single photon avalanche diode detector), this photon count is stored in one memory cell of the TCSPC electronics card for one corresponding time bin. The recording of

numerous single photons after timing is performed over a large number of exciting pulses and a histogram of counts versus time is constructed (**Figure 2.22**). **Figure 2.21** represents the timing technique for recording a single photon per excitation pulse.

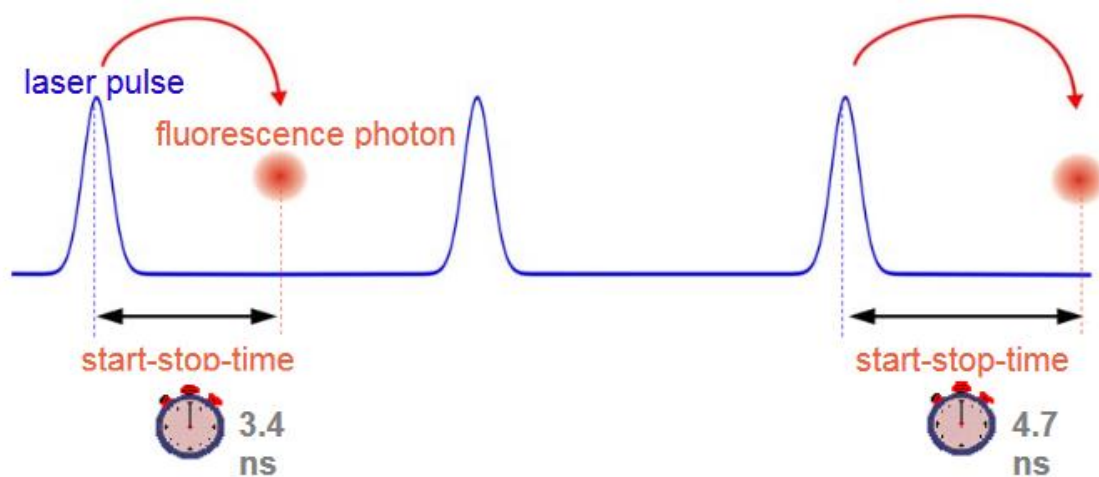


**Figure 2.21.** Analogy to a stopwatch with start/stop times, which represents the timing technique for recording a single photon per excitation pulse. Laser pulse triggers a start condition, and generation with detection of a photon per laser pulse produce the stop condition [169].

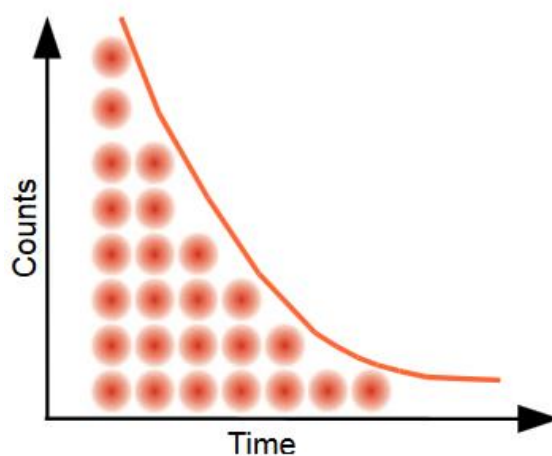


**Figure 2.22.** A histogram of counts in function of time is created when sufficient counts have been collected and is used for lifetime analysis [169].

In order to build a histogram based on single photon counting, the average count rate at the detector must be in the range between 1 to 5% of the excitation rate, if not more than one photon can occur during one excitation cycle and the detector will record the first photon but will miss the following ones due to most of single photon counting detectors and TCSPC electronics have a “dead-time” after recording a photon. This “dead-time” usually lasts pico to nanoseconds where no events can be processed and a pileup effect would appear if more than one photon is generated in one excitation cycle which would distort the counting statistics,

thereby leading to an over-representation of early photons in the histogram and causing the decay times to be shorter [168,169]. This pileup effect is represented in **Figure 2.23**. For TCSPC measurements we used a compact single photon sensitive PMA Hybrid -40 detector, based on a fast hybrid photomultiplier tube, from PicoQuant with a spectral response ranging between 300-720 nm and a dead-time of typically 600 ps.

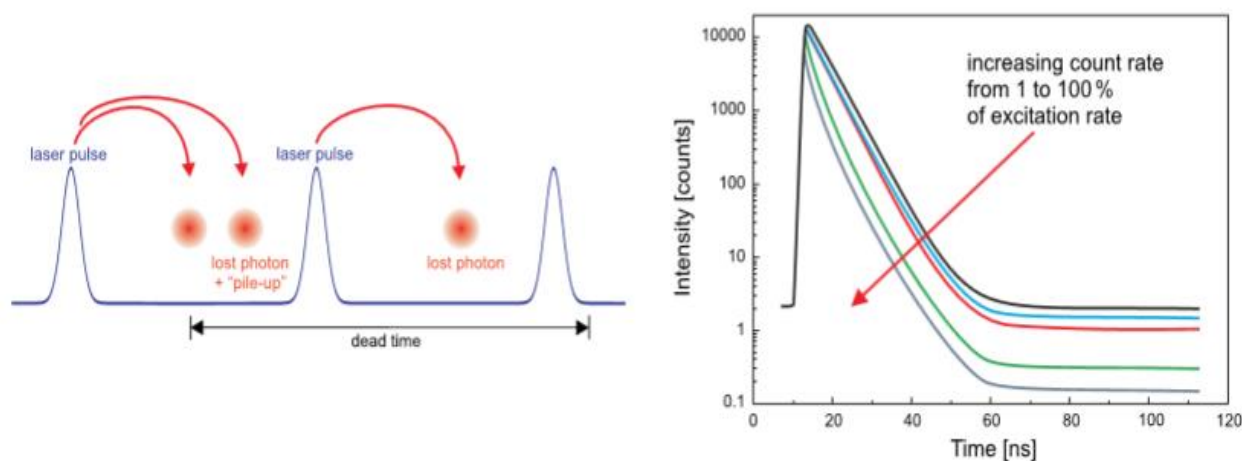


**Figure 2.23.** (Left) Representation of the pileup effects with the occurrence of more than one photon per excitation rate and dead time of the detector and TCSPC electronics. (Right) Distortion of the decay curves due to the pileup effect causing shorter decay than it actually is [169].

TCSPC makes use of high repetition signal rates and with their time bin in the ps range, fluorescence lifetimes can be measured in the nanosecond range. We will use this technique to measure the lifetimes of the acceptor molecules which are quantum dots.

## 2.6.5 Time-resolved FRET

The development of fluorescence FRET assays with time-resolved measurements provided great improvement in normal fluorescence immunoassays. Time-resolved measurements were made possible in FRET assays due to the utilization of rare-earth lanthanides as FRET-donors with long-lived emission decay times which are usually of the order of millisecond as compared to traditional donor dyes which have nanosecond fluorescence lifetimes. When engaged in TR-FRET after a short pulsed excitation, the excited long-lived donor will transfer energy non-radiatively to a short-lived acceptor in close proximity, resulting in donor lifetime quenching and a long-lived fluorescence (sensitization) of the acceptor. The signals can be integrated for a period of time by applying a time-gated window after pulsed excitation, hence measuring fluorescence associated only with the emission of the donor and only from the acceptor that participated in FRET. This time-gated window can be varied depending on the experiment in order to optimize the signal-to-noise ratio. In an assay involving biomolecules and complex

matrix like serum, TR-FRET significantly allows performing highly sensitive detection of the analyte as by delaying the time (*ca.* between 50-150  $\mu$ s) between light excitation and fluorescence measurement, we are able to eliminate any short-lived autofluorescence from the biological media/samples and from directly excited acceptor molecules not participating in FRET. **Figure 2.24** shows the principle of time-gated FRET detection after pulsed excitation. Furthermore, the ratiometric format (FRET-ratio), by analyzing the time-gated photoluminescence (PL) intensities of the FRET-pairs in presence of FRET at two different wavelengths, can be very advantageous for analytical applications as they offer an instantaneous suppression of sample and excitation source fluctuations. The FRET-ratio is proportional to the concentration of the analyte. In our TR-FRET immunoassays, we will use a lanthanide complex of terbium (Tb) as FRET-donor with a decay time of *ca.* 2.6 ms and quantum dots as FRET-acceptor with lifetimes ranging from 6 to 90 ns. The time-gated PL intensities obtained from 100 flashes for Tb ( $I_{TG}(Tb)$ ) and QDs ( $I_{TG}(QD)$ ) when engaged in FRET were used to calculate the FRET-ratio (**Equation 2.18**) using a temporal detection window of 800  $\mu$ s after a time delay of 100  $\mu$ s after pulsed excitation. In this particular FRET case with  $\eta_{FRET} < 90$  %, the quenched PL lifetime of the Tb donor is still much longer than the fluorescence lifetime of the QDs, and therefore the decay time of the donor in presence of the acceptor and the lifetime of the acceptor in presence of the donor are equal ( $\tau_{DA} = \tau_{AD}$ ) [10,135,170]. **Equation 2.10** can then be written as **Equation 2.17**:

$$\eta_{FRET} = 1 - \frac{\tau_{DA}}{\tau_D} = 1 - \frac{\tau_{AD}}{\tau_D} \quad (2.17)$$

$$FRET - ratio = \frac{I_{TG}(QD)_{100-900 \mu s}}{I_{TG}(Tb)_{100-900 \mu s}} \quad (2.18)$$

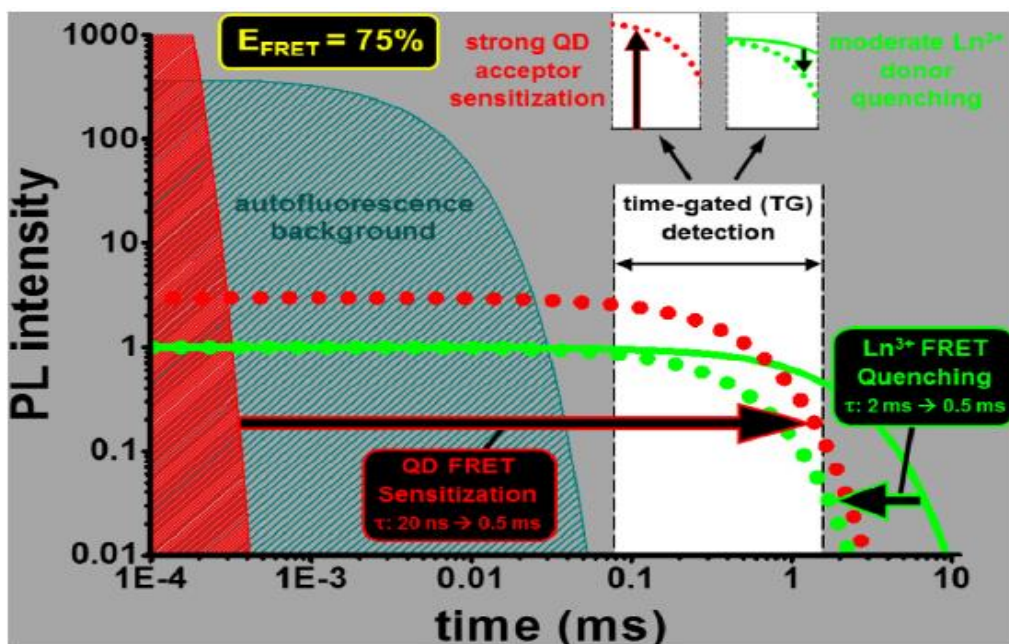


**Figure 2.24.** Principle of time-gated FRET detection. PL intensity after pulsed excitation is plotted as a function of time (logarithmic scale). FRET quenching of Ln donor results in a reduced decay time (green dots) and FRET sensitization of the QD acceptor results in an increased decay time (red dots), which equals the one of FRET-quenched Ln PL (0.5 ms in this example). Time-gated detection allows for measuring both PL signals (Ln and QD) in two spectrally separated detection channels (green and red) to completely suppress autofluorescence background and QD PL from direct light excitation. Decay time ( $\tau$ ) and FRET-efficiency ( $E_{\text{FRET}}$ ) values were arbitrarily chosen but are representative values for Ln-to-QD FRET [13].

## 3. Terbium to commercial QDs FRET immunoassays for PSA detection

S. Bhuckory, O. Lefebvre, X. Qiu, K. D. Wegner, and N. Hildebrandt. Evaluating quantum dot performance in homogeneous FRET immunoassays for prostate specific antigen. *Sensors* **2016**, 16(2), 197.

### 3.1 Introduction

Over the last two decades QDs have become one of the most attractive nanomaterials for fluorescence-based biosensing [23,24]. Despite the advantages mentioned in **section 2.4**, QDs have still not become standard fluorophores for diagnostic applications. Toxicity issues have been largely resolved by the application of appropriate surface coatings so that their application in *in vitro* diagnostics is not hampered by that issue. However, one of the main problems remains a widely applicable, reproducible and stable bioconjugation that allows a full exploitation of both the photophysical advantages of the QDs and the complete functionality of the biological recognition molecule. In particular for homogeneous immunoassays (in which two different fluorescently labeled primary antibodies bind to a biomarker of interest to induce a close proximity between the antibodies and a concomitant FRET between their respective fluorophores) the relatively large dimensions of the biological recognition system that contains antibodies, biomarkers, and a QD nanoparticle have limited the application of QDs [10]. One possibility to overcome the large distances in homogeneous FRET immunoassays and to provide at the same time high sensitivity and multiplexing capability is the use of luminescent terbium complexes as FRET donors for QD acceptors (**section 2.6.3.2 & 2.6.3.3**, respectively).

Oligonucleotide-based hybridization assays for the detection of DNA or RNA have the advantage that the hybridization strategy allows the design of shorter donor-acceptor distances and recent results have demonstrated the sensitive and multiplexed detection of different microRNAs using Tb-to-dye and Tb-to-QD FRET [145,152]. As the binding sites of antibodies to their antigens are well-defined and the Y-shaped IgG antibodies have a length of ca. 10 nm, the design of efficient FRET systems using QDs is significantly more difficult. To date, Tb-to-dye FRET immunoassays have been demonstrated for the multiplexed detection of up to five different tumor markers [11], but the application of Tb-to-QD FRET has so far been limited to the detection of single antigens using self-synthesized QDs for the detection of alpha-fetoprotein (AFP) and carcinoembryonic antigen (CEA) in buffered solution [143,171] or commercial QD-antibody conjugation kits (eFluor nanocrystal antibody conjugation kits, Affymetrix/eBioscience, which are unfortunately not available anymore) for the detection of prostate specific antigen (PSA) or the epidermal growth factor receptor (EGFR) [25,172].

Probably the most frequently applied types of QDs are Qdots from Life Technologies, but so far only one study showed their use in Tb-to-QD FRET immunoassays for the detection of CEA [150]. Within that study only a single QD color was used and the QD-antibody conjugates were prepared by a costly custom labeling performed at the Invitrogen laboratories.

In this contribution, we demonstrate the general applicability of multicolor Tb-to-QD FRET immunoassays using standard in-stock Qdot ITK amino PEG QDs (Life Technologies) with PL maxima at 605, 655, and 705 nm, respectively, and a commercial Lumi4-Tb complex (Lumiphore). We have developed a standard procedure of conjugating these QDs via sulfo-EMCS crosslinkers to sulfhydryl groups of F(ab) antibodies (ABs) and show the successful application of these different QD-AB conjugates in homogeneous Tb-to-QD FRET assays against PSA. We also present a detailed photophysical analysis of the QD-AB and Tb-AB bioconjugates and their FRET properties and show that the Tb-QD FRET-pair with the largest Förster distance and the lowest Tb PL background (Qdot705) also provides the highest sensitivity (lowest limit of detection) compared to the FRET-pairs using Qdot655 (second best) and Qdot605. Multiplexing capability was shown by a duplexed detection of PSA using the Tb-Qdot655 and Tb-Qdot705 FRET-pairs. Our results will be of high importance for the development of QD-FRET acceptor-based immunoassays against different biomarkers (**Chapter 5**).

## 3.2 Materials and Methods

### 3.2.1 Materials

Qdot® ITK™ amino PEG 605, 655, and 705 (QD605, QD655, and QD705) were purchased from Life Technologies/Thermo Fisher Scientific and possess amine-derivatized polyethylene glycol (PEG) ligands covalently attached to the amphiphilic coating rendering them water soluble and compatible for the attachment of biomolecules. The reactive amino groups of the ligand allow for the attachment of biomolecules via N-hydroxysuccinimide (NHS) ester conjugation. The NHS-activated terbium complex Lumi4-Tb was kindly provided by Lumiphore in lyophilized form. Prostate specific antigen (PSA) and monoclonal primary antibodies against PSA (IgGs “PSR222” and “PSS233”) were provided by Cezanne/Thermo Fisher (Nîmes, France). IgGs were fragmented to F(ab) using a Pierce™ Mouse IgG F(ab')<sub>2</sub> preparation kit and following the instructions provided by the supplier (Thermo Fisher Scientific) and the SDS-PAGE of the fragmentation is shown in **Appendix 8.2.3**. Bovine calf serum was provided by

Cezanne/Thermo Fisher Scientific. Sulfo-EMCS (a water-soluble heterobifunctional amine-to-sulfhydryl cross-linker that contains NHS ester on one end and a maleimide reactive group on the other end) used to transform the amino-reactive QDs into maleimide-reactive QDs was purchased from Sigma-Aldrich. Bovine serum albumin (BSA), Tris(hydroxymethyl)aminomethane (TRIS/Cl), sodium tetraborate (borate), phosphate buffer saline (PBS) and Tris(2-carboxyethyl)phosphine (TCEP) were also purchased from Sigma-Aldrich.

### 3.2.2 Methods

#### 3.2.2.1 Tb-AB conjugation

Lumi4-Tb-NHS was reacted in molar excess to available primary amines of the IgG (“PSR222”) antibodies by mixing both solutions in carbonate buffer (pH 9). The mixtures were incubated for 2 h at room temperature while rotating at 30 rpm using an ELMI Intelli-Mixer. The IgG-Tb conjugates (**Figure 3.1**) were purified and washed 4 times with 100 mM TRIS/Cl pH 7.4 using 50 kDa molecular weight cut-off (MWCO) spin columns from Millipore, to remove the unbound Tb-complex. The purified conjugate was stored at 4 °C.

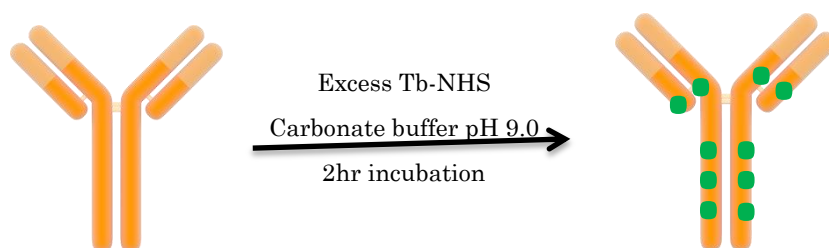
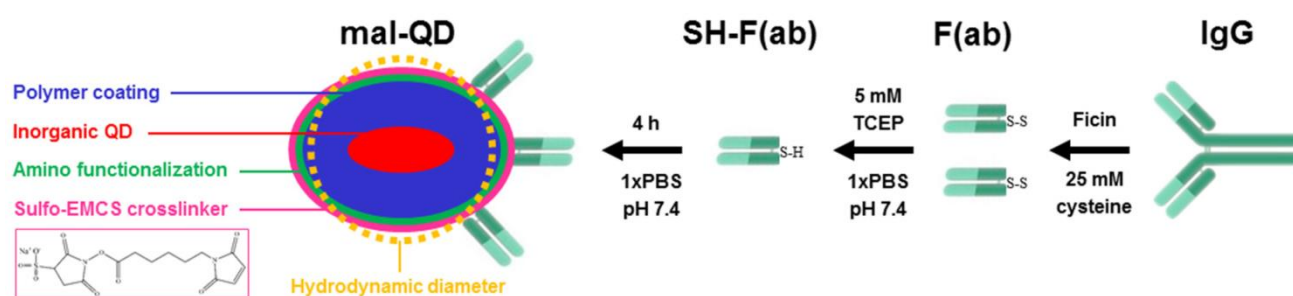


**Figure 3.1.** Random labeling via NHS coupling of Lumi4Tb-NHS to available primary amines of PSR222 in carbonate buffer pH 9.

#### 3.2.2.2 QD-AB conjugation

Conjugation of F(ab) to the QDs was performed using sulfo-EMCS crosslinkers. To receive maleimide-reactive QDs a several-fold molar excess of sulfo-EMCS was mixed and incubated in 1xPBS buffer (pH 7.4) with the QDs for 30 min at room temperature while rotating at 30 rpm using an Intelli-Mixer. Disulfide bonds (S-S) on the F(ab) were reduced to sulfhydryls (S-H) using 30 min of incubation (rotating at 30 rpm) with 5 mM of Tris(2-carboxyethyl)phosphine (TCEP) in 1x PBS buffer (pH 7.4). Maleimide-activated QDs and F(ab)-SH were purified using Zeba 7K desalting columns to remove excess cross-linkers and reducing agent, respectively. For the final F(ab)-QD conjugation step both desalted solutions were mixed and incubated for 4 h at room temperature in the dark while rotating at 30 rpm. Unbound F(ab) was separated from the conjugation mixture using a 100 kDa MWCO spin column from Millipore by washing four times

with 100 mM borate buffer (pH 8.4). Purified conjugates were centrifuged at 4000 g and supernatants were taken and stored at 4 °C. The QD-antibody conjugation procedure is presented in **Scheme 3.1**.



**Scheme 3.1.** F(ab) conjugation of QD605, QD655, and QD705 was performed by transferring the amine-reactive QDs to maleimide-reactive QDs (mal-QD) using a sulfo-EMCS crosslinker (left). IgG was fragmented to F(ab) using a commercial fragmentation kit. The available disulfides on the F(ab) were reduced to sulfhydryls, which allowed a conjugation to the mal-QDs.

### 3.2.2.3 Photophysical characterization

Absorption spectra were acquired using a Lambda 35 UV/Vis spectrophotometer from Perkin Elmer. Photoluminescence (PL) spectra and decay curves were recorded on a FluoTime 300 lifetime fluorescence spectrometer from PicoQuant using as excitation sources a continuous-wave Xe lamp for spectra acquisition, a Xe flash lamp (100 Hz repetition rate) for Tb decay curves, and a 405 nm diode laser (Edinburgh Instruments) for QD decay curves. Tb-conjugates and QD-conjugates were measured in 100 mM TRIS/Cl buffer (pH 7.4) and 100 mM borate buffer (pH 8.4) respectively.

### 3.2.2.4 FRET characterization and immunoassays

The Förster distances ( $R_0$ , distance at which FRET efficiency is 50%) of the different Tb-QD FRET-pairs were calculated using **Equations 2.5** and **2.6**. All homogeneous Tb-QD FRET immunoassays were measured on a modified KRYPTOR Compact Plus (Cezanne/Thermo Fisher) clinical fluorescence plate reader. Time-gated PL intensities of the Tb donor (donor detection channel ChD) and the QD acceptors (accepter detection channel ChA) were collected simultaneously in a time window from 100 to 900  $\mu$ s after pulsed excitation using an integrated nitrogen laser operating at 20 Hz. Spectral separation in the detection channels was performed by optical bandpass filters:  $494 \pm 10$  nm (Semrock) for Tb,  $607 \pm 4$  nm (Delta) for QD605,  $660 \pm 6.5$  nm (Semrock) for QD655 and  $707 \pm 8$  nm (Semrock) for QD705. The time-gated PL intensities from ChD ( $I_{TG}(Tb)$ ) and ChA ( $I_{TG}(QD)$ ) were used to calculate a time-gated FRET-ratio by **Equation 2.18**.

Within all immunoassays the Tb-AB and QD-AB were dissolved in 10 mM TRIS/Cl buffer (pH 7.4) containing 0.5% BSA and their concentrations were kept constant (3 nM) while the antigen (PSA) concentrations were increased. This induced an increase in Tb-to-QD FRET-pairs with increasing PSA concentration and lead to a typical FRET immunoassay calibration curve for which the FRET signal increased with biomarker concentration.

### 3.3 Results and discussion

In a previous study (using eBioscience QD-AB conjugation kits) we showed that sulfhydryl-based conjugation to maleimide-reactive QDs led to functional QD-AB conjugates that could be successfully used in homogeneous immunoassays [25,172]. Because the eBioscience QD-AB-conjugation kits are unfortunately not sold anymore and maleimide-reactive QDs are not sold by Life Technologies either, we transferred the amine-reactive QDs into a maleimide-reactive form using a sulfo-EMCS crosslinker (NHS-to-maleimide). The maleimide-reactive QDs could then be conjugated with F(ab) antibody fragments, which had shown to be advantageous for FRET immunoassays due to their smaller size and the higher amount of ABs per QD [25]. Nevertheless, IgGs were conjugated to QD705 using the same conjugated method as for F(ab) and tested in a FRET immunoassay against PSA but yielded no exploitable calibration curves for quantitative analysis due to the almost negligible FRET signal as it can be witnessed in **Figure 3.2**.

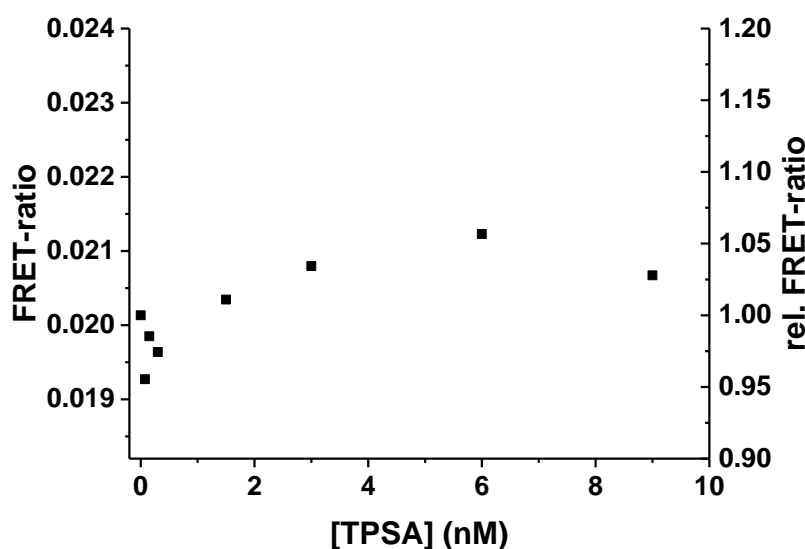


**Figure 3.2.** PSA immunoassay calibration curve for the detection of TPSA using Tb-QD705 IgG conjugates. Although a small increase in FRET-ratio is observable at higher concentration of TPSA, the data are not exploitable for statistical analysis due to the negligible FRET-ratio increase.

Another important aspect of our investigation was the performance evaluation of QDs with different PL emission wavelengths (QD605, QD655, and QD705). This evaluation is very important for their application as acceptors in FRET assays with Tb donors because the variations in shapes, sizes, spectral overlap (QD absorption with Tb emission), and PL wavelength range lead to differences in FRET and detection efficiencies, which can result in significant differences in sensitivity. Therefore a careful photophysical characterization and sensitivity evaluation within comparable immunoassays for the same antigen are indispensable for designing and optimizing such homogeneous FRET immunoassays, in particular for multiplexed detection with different QD colors. The following paragraphs will discuss the photophysical properties of the assay constituents (Tb and QD AB-conjugates) and show their performance in Tb-QD FRET immunoassays for the detection of PSA in low volume serum samples.

### 3.3.1 Tb and QD AB conjugates and Tb-QD FRET-pairs

Tb concentrations were calculated using Beer-Lambert's law with a molar absorptivity (extinction coefficient) of  $26,000 \text{ M}^{-1} \cdot \text{cm}^{-1}$  at the absorption maximum of 340 nm. AB concentration was determined at 280 nm using a molar absorptivity of  $210,000 \text{ M}^{-1} \cdot \text{cm}^{-1}$ . A labeling ratio of 6 Tb per PSR222 IgG was determined by linear combination of the respective absorbance spectra of Tb and AB to fit the spectrum of the Tb-AB conjugate **Figure 3.3 A**. Excitation of the Tb-AB conjugates in the absorption band of Tb (between ca. 300 and 400 nm) led to the typical  $\text{Tb}^{3+}$  PL spectrum (**Figure 3.3 A**) and a nearly mono-exponential PL decay with an average decay time of  $2.6 \pm 0.2 \text{ ms}$  (**Figure 3.3 B**).

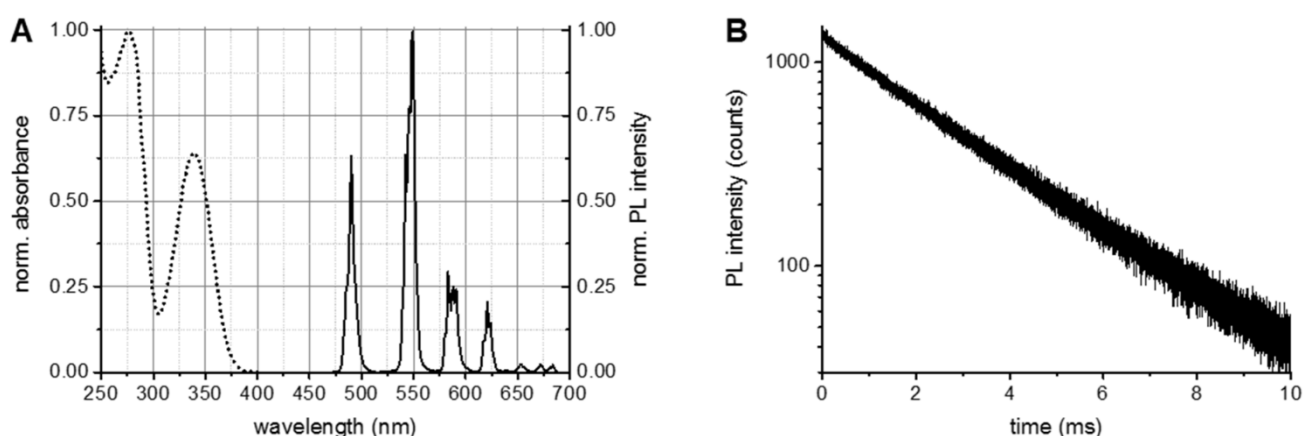


**Figure 3.3.** Optical characterizations of Tb-AB conjugates. (A) Absorption spectrum (dotted line) of the Tb-AB conjugate, of which the Tb peak at 340 nm and the AB peak at 280 nm were used to calculate the Tb per AB labeling ratio. The PL spectrum (solid line) was acquired upon excitation in the Tb absorption band ( $365 \pm 2 \text{ nm}$ ); (B) Pulsed (Xe flash lamp at 100 Hz) excitation ( $360 \pm 2 \text{ nm}$ ) was used to measure the

PL decay at  $490.0 \pm 0.5$  nm. The slightly bi-exponential decay curve ( $\tau_1 = 0.4 \pm 0.3$  ms,  $\tau_2 = 2.70 \pm 0.02$  ms) gave an amplitude-averaged decay time of  $\tau(\text{Tb}) = 2.6 \pm 0.2$  ms.

QD concentrations were calculated using the QDs' molar absorptivities at 405 nm ( $\epsilon_{405}(\text{QD605}) = 2.8 \times 10^6 \text{ M}^{-1} \cdot \text{cm}^{-1}$ ,  $\epsilon_{405}(\text{QD655}) = 5.7 \times 10^6 \text{ M}^{-1} \cdot \text{cm}^{-1}$ ,  $\epsilon_{405}(\text{QD705}) = 8.3 \times 10^6 \text{ M}^{-1} \cdot \text{cm}^{-1}$ ). ABs per QD labeling ratios of 5 PSS233 F(ab) per QD605, 8 PSS233 F(ab) per QD655, and 6 PSS233 F(ab) per QD705 were determined by linear combination of the respective absorbance spectra of QDs and AB to fit the spectrum of the QD-AB conjugates (molar absorptivity of ABs used to calculate labeling ratios was  $\epsilon_{280}(\text{ABs}) = 70,000 \text{ M}^{-1} \cdot \text{cm}^{-1}$ ). The different QD absorption and PL spectra as well as their PL decay curves are shown in **Figure 3.4**.

The QD PL spectra were selected to fit in between (for QD605 and QD655) or beyond (for QD705) the Tb PL bands. This allows a detection of the QD PL with a low PL background of Tb. The PL decays of all QDs are multi-exponential with amplitude averaged decay times of  $6.3 \pm 1.2$  ns for QD605,  $14.0 \pm 0.9$  ns for QD655, and  $80.0 \pm 3.0$  ns for QD705. Due to the large difference in excited-state lifetimes of Tb and QD (ca. 50,000 times longer for Tb) the FRET-quenched PL decay time of Tb equals the FRET-sensitized PL decay time of the QD [2,12]. Therefore time-gated FRET detection can be performed using the different QD PL wavelengths. The spectral overlap integrals (**Equation (2.6)**) and the Förster distances (**Equation (2.5)**) were calculated using the QD molar absorptivity spectra and the Tb PL spectrum. As expected from the spectral overlaps in **Figure 3.4 A** the Tb-QD705 FRET-pair provided the largest Förster distance ( $R_0 = 11.2 \pm 0.6$  nm), followed by the Tb-QD655 FRET-pair ( $R_0 = 10.5 \pm 0.5$  nm), and the Tb-QD605 FRET-pair ( $R_0 = 8.8 \pm 0.4$  nm). Considering that FRET should still be detectable at distances of up to ca.  $2R_0$ , all Tb-QD systems should be able to provide at least measurable QD-FRET sensitization within the [QD-AB]-PSA-[Tb-AB] binding system, even with the thick QD polymer coatings, which extend the QDs to diameters of ca. 16, 20, and 21 nm for QD605, QD655 and QD705, respectively (as provided by the supplier).

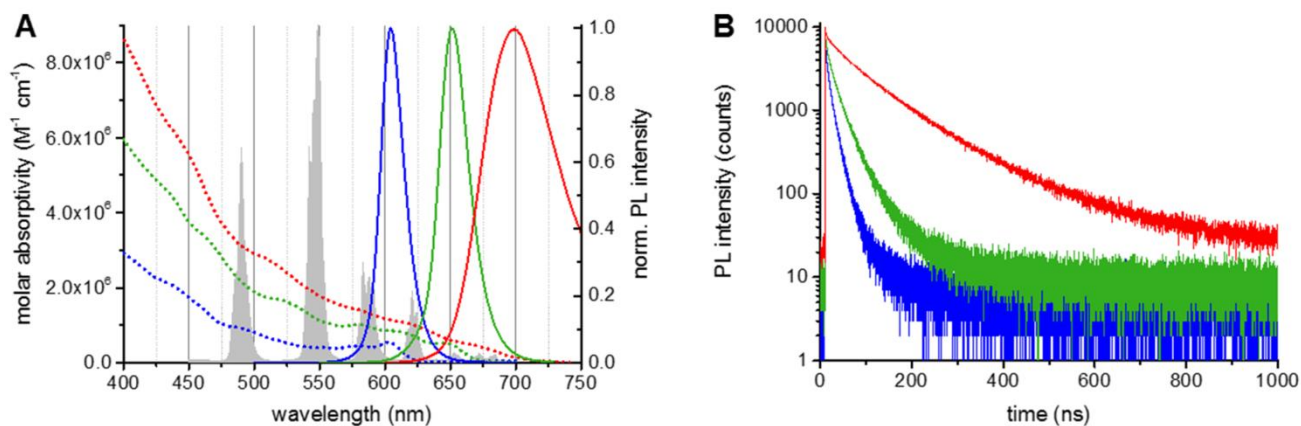


**Figure 3.4.** Optical characterizations of QD-AB conjugates. (A) Absorption (dotted lines) and PL (solid lines) of QD605 (blue), QD655 (green) and QD705 (red). To show the spectral overlap between Tb emission and QD absorption and the differences in PL wavelengths also the Tb PL spectrum is shown (gray spectrum in the background). Förster distances were calculated as  $R_0(\text{QD605}) = 8.8 \pm 0.4$  nm,  $R_0(\text{QD655}) = 10.5 \pm 0.5$  nm, and  $R_0(\text{QD705}) = 11.2 \pm 0.6$  nm; (B) Pulsed (405 nm diode laser at 1 MHz) excitation was used to measure the PL decay curves at the respective PL peaks of the QDs. The multi-exponential decay curves (same colors as in (A) gave amplitude-averaged decay times of  $\tau(\text{QD605}) = 6.3 \pm 1.2$  ns,  $\tau(\text{QD655}) = 14.0 \pm 0.9$  ns, and  $\tau(\text{QD705}) = 80.0 \pm 3.0$  ns.

### 3.3.2 Homogeneous Time-Resolved FRET immunoassay

To compare the performance of the different Tb-QD FRET-pairs for homogeneous immunoassays, fixed volumes of serum samples spiked with increasing concentrations of PSA (from 0.05 to 4.0 nM) were added to fixed volumes of assay solutions containing constant concentrations of Tb-AB and QD-AB conjugates. Both the time-gated Tb and QD PL intensities were measured and the FRET-ratio (**Equation (2.18)**) was plotted as a function of PSA concentration as shown in **Figure 3.5**. Although the FRET-ratio increases were relatively small (ca. 1.2, 1.3, and 3.5 from 0 to 4 nM PSA for Tb-QD605, Tb-QD655, and Tb-QD705, respectively) they were still very significant and the many different concentrations measured showed a clear increase of FRET ratio over PSA concentration, as expected for an assay calibration curve. Also the expected saturation becomes visible at PSA concentrations corresponding to those of the Tb-ABs (3 nM). The absolute values of the FRET-ratio are smallest for the Tb-QD705 pair, followed by Tb-QD605 and Tb-QD655. This was expected as the Tb PL background in the different QD detection channels follows a similar trend (QD705 < QD605 < QD655). The strongest relative increase is again measured for the Tb-QD705 FRET-pair, due the most efficient FRET. Tb-QD655 and Tb-QD605 have similar relative FRET-ratio increases although the Förster distance is smaller for QD605. In this case, the significantly smaller size of the QD605 compared to the QD655 compensates the smaller Förster distance.

To compare the sensitivity of the Tb-to-QD FRET pairs the limits of detection (LODs) were calculated using the calibration curves in **Figure 3.5**, the standard deviation of 30 measurements of samples without any PSA (zero concentration) and **Equation 2.3**. All three FRET systems provide sub-nanomolar LODs and as expected from the previous performance results the Tb-to-QD705 FRET assay yields the lowest LOD. Although the relative increase of the Tb-QD605 and Tb-QD655 calibration curves is very similar, the QD655 system has an almost 6-fold lower LOD. This is caused by the larger relative errors of the time-gated PL intensities in the QD605 channel compared to the QD655 channel. The LODs for PSA (and also the conjugation ratios and Förster distances) are summarized in **Table 3.1**. Taking into account a clinical cut-off concentration of 4 ng/mL for PSA [173], QD655 and QD705 provide sufficiently low LODs, whereas the QD605 LOD is too high for clinically relevant PSA concentrations. Nevertheless, the comparison of LODs for the same biomarker (PSA) is highly important because the relative comparison provides an important guidance for the development of multiplexed diagnostic kits. As most biomarkers have different clinical cut-off values QD705 should be used for the biomarker with the lowest cut-off and QD605 for the one with the highest cut-off. An important finding is that all Tb-QD FRET pairs provide LODs in a concentration range that is clinically relevant and that the 50  $\mu$ L serum samples present clinically relevant solutions. Therefore our results present an important step toward the development of QD-based multiplexed homogeneous FRET immunoassays for their application in clinical diagnostics.

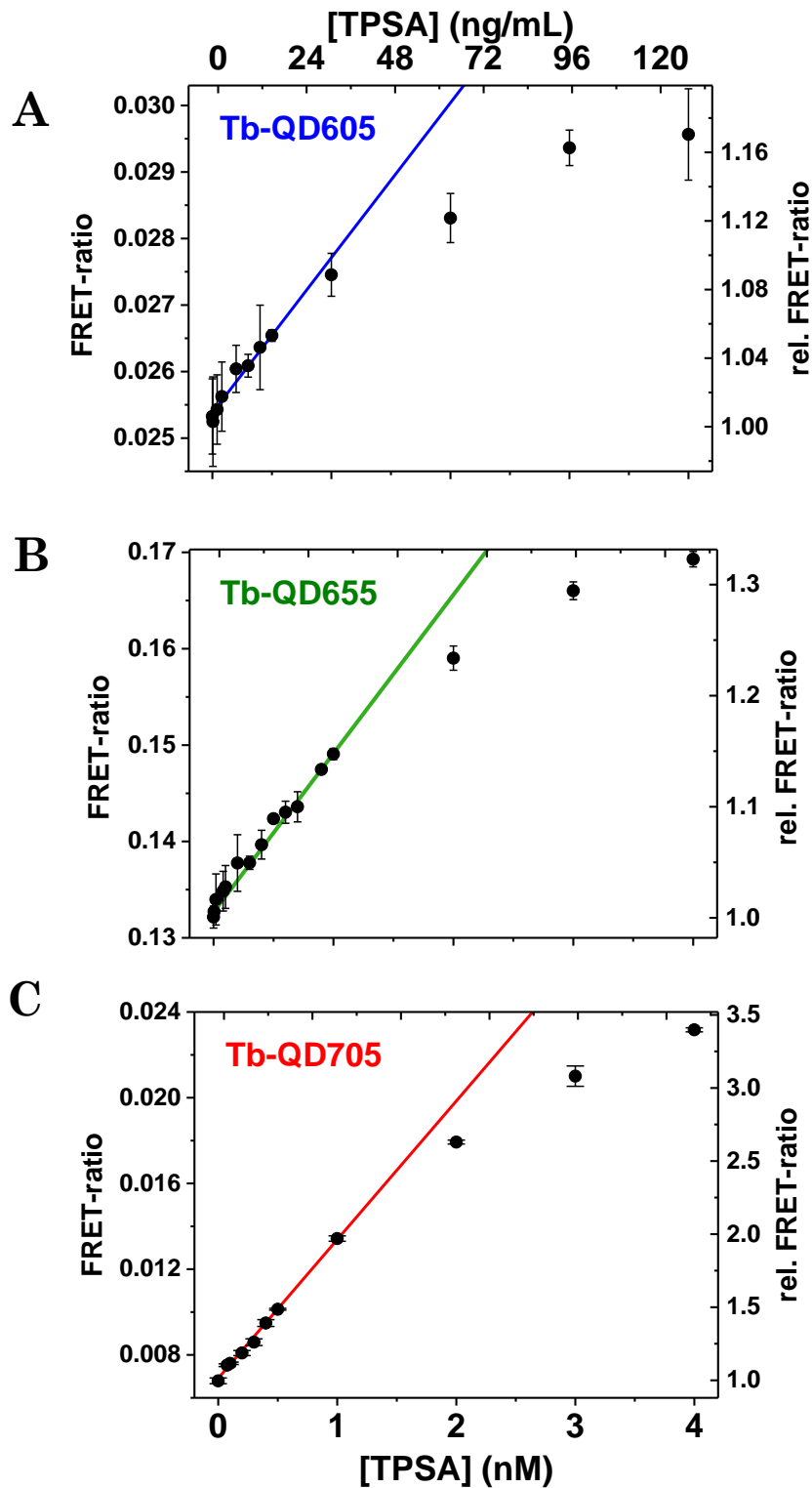


**Figure 3.5.** PSA immunoassay calibration curves of the different Tb-QD FRET systems using QD605 (A); QD655 (B); and QD705 (C). Bottom abscissae give total PSA (TPSA) concentrations in nM, top abscissae give TPSA concentration in ng/mL. LODs were determined using the linear parts of the calibration curves (solid lines) and the standard deviation of the FRET-ratio at zero TPSA concentration (Equation (2.3))

**Table 3.1.** Overview of Tb and QD AB conjugation ratios, Förster distances  $R_0$ , and limits of detection (LOD) of PSA immunoassays using the three different FRET pairs.

Donor-AB	Tb/AB	Acceptor-AB	AB/QD	$R_0$ (nm)	LOD (nM)	LOD (ng/mL)
Tb-IgG	$6 \pm 1$	QD605-F(ab)	$5 \pm 2$	$8.8 \pm 0.4$	$0.71 \pm 0.07$	$23 \pm 2$
		QD655-F(ab)	$8 \pm 3$	$10.5 \pm 0.5$	$0.12 \pm 0.01$	$3.7 \pm 0.4$
		QD705-F(ab)	$6 \pm 2$	$11.2 \pm 0.6$	$0.06 \pm 0.01$	$2.0 \pm 0.3$

### 3.3.3 Duplexed Tb-to-QD FRET immunoassay

In order to demonstrate the ability of multiplexed detection using different Tb-QD FRET-pairs we prepared a duplexed PSA immunoassay that contained the two QD-AB conjugates with the lowest LODs (Tb-QD655 and Tb-QD705). Conjugation ratios for these Tb and QD AB conjugates were 7 Tb per PSS233 IgG, 49 PSR222 F(ab) per QD655, and 48 PSR222 F(ab) per QD705. A high labeling ratio for these two QD-AB conjugates, as compared to those mentioned in **Table 3.1**, can be due to the larger molar excess of F(ab) that were conjugated to the QDs. The same experimental parameters and concentration of the QD-AB and Tb-AB conjugates were used as within the singleplex assays. However, for the duplexed assays the FRET ratios of both Tb-QD FRET-pairs were measured from the same samples for each PSA concentration. **Figure 3.6** shows the assay calibration curves (relative FRET ratios as a function of PSA concentration) for both Tb-QD655 (green) and Tb-QD705 (red) FRET-pairs. These calibration curves show the same trends as the single Tb-QD FRET-pair assays in **Figure 3.5**, namely a linear increase of the FRET-ratios until ca. 3 nM PSA, after which the FRET-ratio levels off because of a saturation of Tb-AB conjugates (3 nM). These similar trends of the single and duplexed calibration curves demonstrate the capability of using our Tb-QD FRET immunoassays for multiplexed detection.

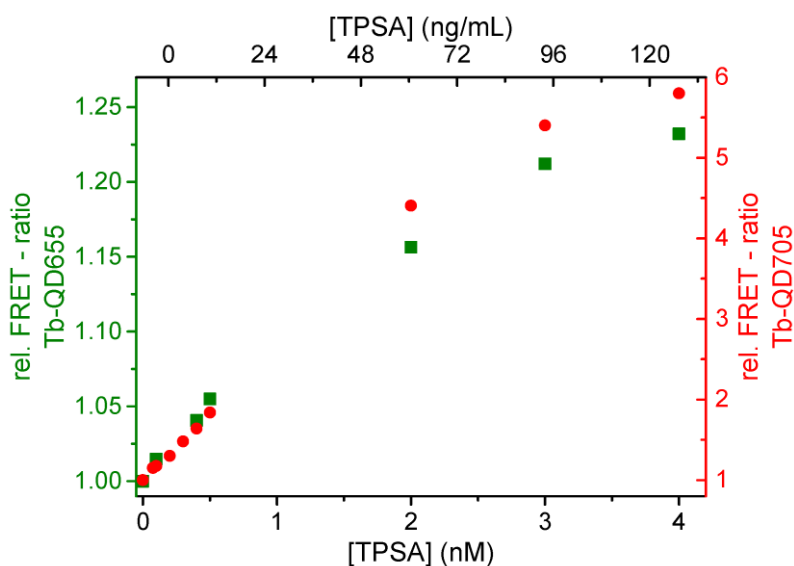


**Figure 3.6.** PSA immunoassay calibration curves for the detection of TPSA in a duplexed detection format using the Tb-QD655 (green) and Tb-QD705 (red) FRET-ratios measured from the same samples (for each concentration) that contained both QD655 and QD705 AB conjugates.

### 3.4 Conclusions

We have successfully tested the performance of three commercially available QDs – from Life Technologies – possessing a thick polymer PEG coating and surface amino functionalized in homogeneous FRET immunoassays. The development of a generic and easily applicable AB-conjugation method to the QDs yielded successful labeling with fragmented F(ab) ABs against PSA, which were used in combination with Lumi4-Tb-AB conjugates for Tb-to-QD FRET assays. All three Tb-to-QD FRET systems showed increasing time-gated FRET signals with increasing PSA concentrations and immunoassay calibration curves could be successfully recorded. The LODs for PSA in 50  $\mu$ L serum samples were in the sub-nanomolar concentration range and below the clinical cut-off value of 4 ng/mL for the QD655 and QD705 based FRET-pairs. Duplexing capability was demonstrated in PSA assays containing both QD655 and QD705 AB conjugates. Our results provide important information concerning the development of QD-based FRET immunoassays for multiplexed clinical diagnostics because the AB-conjugation method is applicable to any commercially available amino-functionalized Qdot, which exist in many other colors than the three used in this study. Our results show a direct relation between the FRET parameters and the analytical performance of the FRET-pairs. The comparison of LODs for the same biomarker (PSA) is an important tool for a relative comparison of the FRET-pairs in order to adapt the FRET-probes to the required concentration range of different biomarkers in a multiplexed assay. Our proof-of-concepts for three-color

Tb-to-QD FRET and two-color duplexed Tb-to-QD FRET detection for biomarker immunoassays in serum samples present highly important steps toward the development of multiplexed QD-based FRET immunoassay kits for clinical use.

In reference to these results, the next two chapters will be consecrated to the influence of a compact surface coating of QDs (same core-shell QDs from Life Technologies used in this study) on the sensitivity of such FRET immunoassays and to the development of multiplexed assays against different biomarkers.

## 4. Terbium to compact QDs FRET immunoassay for PSA detection

L. Mattera, S. Bhuckory, K.D. Wegner, X. Qiu, F. Agnese, C. Lincheneau, T. Senden, D. Djurado, L.J. Charbonnière, N. Hildebrandt, and P. Reiss. Compact quantum dot-antibody conjugates for FRET immunoassays with subnanomolar detection limits. *Nanoscale* **2016**, 8, 11275-11283.

S. Bhuckory, L. Mattera, K. D. Wegner, X. Qiu, Y-T. Wu, L. J. Charbonnière, P. Reiss, and N. Hildebrandt. Direct conjugation of antibodies to the ZnS shell of quantum dots for FRET immunoassays with low picomolar detection limits. *Chemical Communications* **2016**, 52, 14423-14425.

### 4.1 Introduction

Involving QDs with thick polymer PEG coating and surface amino functionalized from Life Technologies, and sulfhydryl bioconjugation chemistry for Tb-to-QD FRET immunoassays reported in the previous chapter showed that it was possible to detect PSA in the sub-nanomolar range. Therefore, the development of QD-AB conjugates with compact surface functionalization for aqueous phase transfer and high-performance photophysical properties for efficient FRET immunoassays in serum samples would present a milestone of the utmost importance for the integration of QDs into clinical *in vitro* diagnostics. They would allow overcoming the major limitations for developing QD-FRET immunoassays with LODs competitive to commercial kits which are: (i) insufficient colloidal stability of compact QDs in biological media, (ii) thick QD surface coatings (e.g., PEG, polymer, or lipid coatings that protect the inorganic QD from the biological environment and render them hydrosoluble), and (iii) insufficient AB-conjugation strategies for QDs with thinner organic capping. The latter two QD surface related aspects result in long FRET donor-acceptor distances and unfavorable binding conditions, respectively. This leads to lower sensitivities compared to conventional time-resolved (TR)-FRET immunoassays that use lanthanide donor and dye acceptor AB conjugates [174]. Here we present a novel QD functionalization and bioconjugation approach, which yielded stable compact QDs and highly luminescent QD-AB conjugates for improved TR-FRET immunoassay. This work was jointly carried out with the INAC-SyMMES laboratory in CEA Grenoble, where they performed phase transfer of the QDs from organic to aqueous solvent and their characterization. Post-functionalization of the QDs with a bifunctional ligand was carried-out by both groups, and bioconjugation with fragmented antibodies as well as optical characterization and FRET immunoassays were done by our group.

Aqueous phase transfer of lab-synthesized (by INAC-SyMMES laboratory) InPZnS/ZnSe/ZnS QDs emitting at 530 nm and commercial CdSe/ZnS and CdSeTe/ZnS QDs (Life Technologies) emitting at 605 and 705 nm was achieved by surface ligand exchange with penicillamine (Pen). These wavelengths have been selected as they result in minimal interference with the emission of the Tb-complexes used as the FRET donor. Under optimized conditions, ligand exchange with Pen results in a very compact (~1 nm) organic surface layer while preserving high PL quantum yields. The zwitterionic Pen also provides low non-specific binding with serum proteins and very high colloidal stability of several years in aqueous buffers. For sulfhydryl-reactive QD-AB conjugation, we further functionalized the QD surface with a bifunctional ligand (Mal1) containing a lipoic acid anchoring function and a maleimide group, spaced by three poly(ethylene) glycol (PEG) moieties. The bidentate (reduced) lipoic acid function is able to substitute Pen molecules and provides excellent stability of the Mal1 ligand on the QD surface. Successful conjugation of the prepared QDs with fragmented antibodies F(ab), further reducing the size of the sandwich immunocomplexes, was characterized by optical spectroscopy, dynamic light scattering (DLS), agarose gel electrophoresis, and FTIR. These QD-AB conjugates will be further referred as **QD-Mal1-AB**. To demonstrate the advantages of the ultra-compact (hydrodynamic diameter <13 nm), stable, and strongly fluorescent QD-AB conjugates for clinical diagnostics, we performed Tb-to-QD FRET immunoassays for the detection of prostate specific antigen (PSA) in 50  $\mu$ L serum samples on a commercially available clinical fluorescence plate reader (KRYPTOR). The FRET results being consistent with those obtained in **Chapter 3**, we further challenged our sulfhydryl conjugation strategy by showing for the first time the direct attachment of ABs (IgG, F(ab')<sub>2</sub>, F(ab)), via free sulfhydryl groups, to the surface of the compact QDs (metal-affinity of thiols to zinc) emitting at 705 nm (largest R<sub>0</sub>, highest sensitivity) without using any linker or crosslinker. This would allow for more efficient FRET immunoassays due to the close proximity of the donor and acceptor molecules. The direct conjugation of the ABs to the QDs will be further referred as **QD-d-AB** conjugates, with “d” corresponding to direct conjugation. The achieved LODs down to 0.8 ng/mL (Mal1 ligand conjugation) and 0.08 ng/mL (direct conjugation) are 2.5 fold and 25 fold lower than the best Tb-to-QD PSA FRET immunoassays reported so far, which were performed under identical conditions but with the commercially available ITK-Qdots (Life Technologies) as reported in **Chapter 3** [175]. The latter differ from our QDs only by their surface coating: a comparably thick organic layer composed of amphiphilic polymers, which yields QDs with hydrodynamic radii of more than 26 nm (without conjugated biomolecules) [151]. Our results are the first demonstration of using compact surface-ligand capped QDs for homogeneous FRET immunoassays that can outperform the commercial QD “gold standard”

and function under clinically relevant conditions (50  $\mu$ L serum samples measured on a clinical plate reader). Comparing the 0.08 ng/mL LOD with the clinical cut-off level of PSA (4 ng/mL) [173] clearly shows the immediate applicability of the compact QD nanoprobe for PSA diagnostics.

## 4.2 Materials and Methods

### 4.2.1 Materials

#### 4.2.1.1 Chemicals

D-Penicillamine, tetramethylammonium hydroxide (TMAOH), phosphate-buffered saline solution (10x PBS), 0.5 M tris(2-carboxyethyl)phosphine hydrochloride solution (TCEP), tris(hydroxymethyl)aminomethane (TRIS/Cl), bovine serum albumin (BSA), agarose powder, indium acetate (99.99%), myristic acid (>99%), tris(trimethylsilyl)phosphine (95%), 1-dodecanethiol (97%), and 1-octadecene (90%) were purchased from Sigma-Aldrich. Zinc stearate (90%) was acquired from Riedel de Haën. MAL-dPEG3-lipoic acid (Mal1) was purchased from Quanta Biodesign. QD CdSe/ZnS 605 and QD CdSeTe/ZnS 705 were purchased from Life Technologies/Thermo Fisher Scientific [176] while the NHS-activated terbium complex (Lumi4-Tb) was provided by Lumiphore in lyophilized form. Prostate specific antigen (PSA) and monoclonal primary antibodies against PSA (IgGs: “PSR222” and “PSS233”) were provided by Cezanne/Thermo Fisher. IgGs were fragmented to F(ab)<sub>2</sub> and F(ab) using a Pierce™ Mouse IgG F(ab') F(ab)<sub>2</sub> preparation kit and following the instructions provided by the supplier (Thermo Fisher Scientific). SDS-PAGE of the fragmentation is shown in **Appendix 8.2.3**. Solvents were purchased from Aldrich, Fluka, and Acros, and used without further purification. All water solutions were prepared from ultrapure laboratory grade water (resistivity 18 M $\Omega$  cm) that was filtered and purified using a Millipore MilliQ cartridge system and autoclaved.

#### 4.2.1.2 Instruments

Absorption and emission spectra were recorded on the following spectrometers: HP 8452A and Perkin Elmer Lambda 35 for UV-Vis absorption; Hitachi F-4500 fluorescence spectrophotometer equipped with a 150 W xenon lamp and an excitation monochromator as well as a PicoQuant Fluotime 300 for photoluminescence (PL). Decay curves were acquired on the Fluotime 300 and fitted using EasyTau (PicoQuant). The hydrodynamic diameter (by dynamic light scattering) and zeta potential of the NCs dispersed in water were measured using a Malvern Zetasizer (NanoZS). Fourier transform infrared (FTIR) spectra were taken on

a Perkin Elmer Paragon 500 spectrometer equipped with an attenuated total reflection (ATR) setup. Gel images were acquired using a Gel Doc XR system (Bio-Rad, Hercules, CA). HRTEM analyses were performed on a JEOL 3010 working at 300 kV, equipped with a LaB<sub>6</sub> gun and a Gatan Orius SC 200 2k × 2k CCD camera. The homogeneous FRET immunoassays were measured on a modified “KRYPTOR compact plus” clinical fluorescence plate reader using 500 detection bins of 2μs integration time from Cezanne/Thermo Fisher Scientific and a prototype fluorescence plate reader (developed during a joint project) from Edinburgh Instruments (EI) using 4000 bins of 2μs integration time for FRET decay curves.

## 4.2.2 Methods

### 4.2.2.1 InPZns/ZnSe/ZnS QD synthesis

The synthesis of InPZnS/ZnSe/ZnS alloy core gradient shell nanocrystals is based on reported procedures [116,177]. All procedures except for nanocrystal purification have been carried out under an inert atmosphere.

#### Preparation of precursor solutions

For the preparation of the indium myristate (In(MA)<sub>3</sub>) stock solution (0.1 M), 1 mmol of anhydrous indium acetate was mixed with 3 mmol of myristic acid (MA) and 10 mL of 1-octadecene (ODE) in a 50 mL three-neck flask equipped with a condenser. The mixture was heated to 100–120 °C for 1 h under vacuum until an optically clear solution was obtained. After backfilling the flask with Ar and cooling to room temperature, the turbid solution of indium myristate was stored in a glovebox. For the zinc oleate (Zn(OA)<sub>2</sub>) stock solution (0.4 M), 5 mmol of zinc acetate, 10 mmol of oleic acid (OA) and 9.35 mL of ODE were loaded into a 50 mL three-neck flask and the same procedure as for the preparation of In(MA)<sub>3</sub> was followed. The zinc stearate (Zn(St)<sub>2</sub>) stock solution (0.1 M) was prepared by heating 1 mmol of Zn(St)<sub>2</sub> with 10 mL of ODE at 120 °C for 1 h. A 0.4 M TOPSe stock solution was prepared by the dissolution of 2 mmol Se powder in 5 mL of trioctylphosphine (TOP) under stirring for 24 h. A TOPS stock solution was prepared with the same procedure using elemental sulfur.

#### Synthesis of InPZnS alloy nanocrystals

In a glovebox, 1 mL of the In(MA)<sub>3</sub> stock solution (0.1 mmol In(MA)<sub>3</sub>), 1 mL of the Zn(St)<sub>2</sub> stock solution (0.1 mmol), 0.1 mmol of 1-dodecanethiol (DDT) and 7.5 mL of ODE were added to a 50 mL three-neck flask. Afterwards the flask was equipped with a condenser and connected to a Schlenk line. Next, the mixture was heated under vigorous stirring to 300 °C with a ramp of around 60 °C min<sup>-1</sup> using a molten salt bath. When the temperature inside the flask reached

100 °C, 0.1 mmol of tris(trimethylsilyl)phosphine (P(TMS)<sub>3</sub>), diluted with 1 mL of ODE, were injected. During the heating, NC formation is visible by the color change of the reaction mixture to dark yellow/orange. After 30 min, the reaction mixture was cooled to below 220 °C to stop growth.

### **Growth of a ZnSe/ZnS gradient shell**

For the ZnSe/ZnS gradient shell growth, a 10 fold excess of precursors was used with respect to the core synthesis, and a Se:S ratio of 0.2. Briefly, Zn(OA)<sub>2</sub> (1 mmol, 2.5 mL of the 0.4 M stock solution) was added dropwise to the reactive mixture at 220 °C. This was followed by the successive injection of TOP-Se (0.2 mmol, 0.5 mL of the 0.4 M solution) and TOP-S (0.8 mmol, 2 mL of the 0.4 M solution). The resulting mixture was heated to 300 °C within 10 minutes and then kept at this temperature for 20 min. After cooling down to room temperature, purification of the QDs was performed via three cycles of precipitation/redispersion. First, 10 mL of a 1 : 1 (v/v) mixture of chloroform/methanol and 100 mL of acetone was added. Then the resulting suspension was centrifuged (8000 rpm for 5 minutes), the supernatant discarded and the obtained solid dispersed in 5 mL of chloroform. Finally, the QDs can be dispersed and stored in a variety of organic solvents, like hexane, toluene or chloroform.

### **Purification before phase transfer**

Thorough purification of the initial QDs, enabling the complete removal of excess surface ligands or side-products is crucial for successful phase transfer. 1 mL of the InPZnS/ZnSe/ZnS QDs in chloroform was mixed with anhydrous ethanol (1 mL) and centrifuged at 10 000 rpm for 2 minutes. The clear solution of supernatant was discarded and the precipitate was dispersed in 1 mL of chloroform. This cycle was repeated three times. For the commercial CdSe/ZnS-based QDs in decane the solvent was changed to chloroform prior to phase transfer. 4 mL of a methanol/isopropanol (3 : 1 v : v) mixture were added to 1 mL of the QD colloidal solution and centrifuged for 2 min at 10 000 rpm. The supernatant was discarded and the resulting pellet dispersed in 1 mL of chloroform.

### **Phase transfer**

A 0.2 M solution of penicillamine (containing 200 µL of 0.5 M TCEP) was prepared in 1 mL of degassed MilliQ water (18 MΩ cm). The pH was adjusted to 9 by drop-wise addition of 0.5 M TMAOH. 500 µL of the phase transfer solution was mixed with 1 mL of a 3–5 µM colloidal solution of QDs in chloroform. The biphasic mixture was stirred vigorously at ~1400 rpm for 2 h at room temperature. At the end of the transfer, affording QD–Pen, the biphasic mixture

results either in a clear separation of two phases or in an emulsion. In the latter case, the mixture is centrifuged at 5200 rpm for 1 min to obtain a clear phase separation. The QDs in the (upper) aqueous phase are separated from the (lower) organic phase.

### **Purification and storage**

A NAP™-5-10,-25 size exclusion column (Sephadex™ G-25 DNA Grade from GE Healthcare) was vertically clamped and equilibrated according to the manufacturer's protocol. QDs in water were added and after being adsorbed on the gel bed, they were eluted using 1x PBS buffer and kept at 4 °C in the dark for storage.

### **Post-functionalization**

Solutions of Mal1 (1 mL, 10 mM) and TCEP (0.046 mL, 0.5 M) in degassed water were added to a suspension of QD–Pen (0.5 mL, 5.2 μM in degassed water) and the pH was adjusted to 7.0 by dropwise addition of 0.5 M TMAOH. The mixture was vortexed at 800 rpm overnight at room temperature. The resulting fine suspension was purified by size exclusion chromatography with NAP™-10,-25 columns (Sephadex™ G-25 DNA Grade from GE Healthcare). The obtained QD-Mal1 were then concentrated under vacuum or by using a 30 kDa molecular weight cut-off (MWCO) spin column from Millipore, centrifuging at 4000g for 4 min with a final volume of 400 μL. Storage at 4 °C in the dark.

#### **4.2.2.2 Preparation of Tb-AB conjugate**

The same conjugation protocol as described in **Section 3.2.2.1** was applied to prepare the Tb-IgG conjugate.

#### **4.2.2.3 Preparation of QD-AB conjugates**

IgGs were fragmented to F(ab')<sub>2</sub> and F(ab) using a Pierce™ Mouse IgG F(ab') F(ab')<sub>2</sub> preparation kit following the instructions provided by the supplier. QD-Mal1 were conjugated to F(ab) whilst QD-Pen (QD705) were conjugated to IgGs, F(ab')<sub>2</sub> and F(ab). Prior to conjugation of the QDs to the ABs in a molar ratio of 1 : 20, disulfide bonds of the latter were reduced to sulfhydryls with 5 mM of TCEP in 1x PBS by mixing for 30 minutes at 30 rpm at room temperature (RT). Purification from excess TCEP was performed using Zeba 7K spin columns (Thermo Fisher Scientific) according to the manufacturer's protocol. The resulting purified ABs were then mixed with the QDs in 1× PBS and incubated for 4 hours while rotating at 30 rpm at RT. Conjugates were washed from unbound ABs 4 times with 1 mL 1× PBS pH 7.5

using a 100 kDa MWCO spin column from Millipore at 1000g. Supernatants were taken after a final centrifugation at 4000g for 5 minutes.

#### 4.2.2.4 QD photoluminescence quantum yields

The absolute fluorescence QYs of the QDs were determined by comparison with a standard of known QY (freshly prepared solution of Fluorescein 548 in 0.1 M NaOH; QY = 93%, Rhodamine 6G in ethanol; QY = 95% [178] or QD705 in chloroform; QY = 92% [176]). The QY was calculated with the following formula:

$$\Phi_{NC} = \Phi_{Standard} \left( \frac{a_{NC}}{a_{Standard}} \right) \left( \frac{n_{NC}^2}{n_{Standard}^2} \right) \quad (4.1)$$

where  $\Phi$  is the QY,  $a$  the gradient (slope) of the plot of the integrated fluorescence intensity vs. absorbance and  $n$  the refractive index of the solvent (1.375 for hexane, 1.446 for chloroform, 1.333 for water and buffer and 1.360 for ethanol [178]). All spectra were corrected for the instrumental response with calibration curves furnished by the supplier and the estimated errors on QY are  $\pm 15\%$  of the calculated values. Aliquots or purified samples of the QDs in hexane, chloroform or water were put into 1 cm quartz cuvettes and diluted until the absorbance at the excitation wavelength was around 0.1. At least four samples of different concentrations were prepared and measured for determining the slopes. Both the sample and the reference were excited at 460 nm for InP based QDs and at 480 nm for CdSe based QDs.

#### 4.2.2.5 Hydrodynamic size and dispersibility of QDs

The hydrodynamic diameter of the water-soluble QDs was measured by dynamic light scattering (Malvern Zetasizer NanoZS). Multiple runs ( $>3$ ) were performed and averaged, and the QDs in 1x PBS buffer were filtered (0.22  $\mu\text{m}$ ) prior to the measurements. The spectra have been corrected by the instrument software for viscosity (0.882 mPa s at 25 °C), absorption (0.01), solvent (water) refractive index (1.33) and material refractive index (assumed as 2.7 and 2.45 for In- and Cd-based QDs, respectively [179]). The data were collected in automatic mode and expressed in number %. The zeta potential was measured using the same instrument under zeta potential settings.

#### 4.2.2.6 Gel electrophoresis

A 1% gel was prepared in 25 mM Hepes buffer (pH 7.4) and poured in a 10.7  $\times$  5.2 cm gel tray levelled in a gel caster (RunOne System). A comb (12 wells) was placed into the gel. The gel was allowed to cool down to room temperature and to solidify within at least 1 hour. The comb was removed and the gel was taken out of the casting device and placed into the electrophoresis

device which was filled with 25 mM Hepes buffer pH 7.4 until the whole gel was covered. The samples were mixed with about 20% of their volume with the loading buffer (30% glycerol in 25 mM Hepes buffer with 0.3% Orange G) and carefully filled into the wells. The electrophoresis devices were run at a constant voltage of 100 V. After 5, 10, 15 and 30 min an image was taken placing the gel on a UV transilluminator (Gel Doc XR system, Bio-Rad).

#### **4.2.2.7 FRET immunoassays**

All FRET assays contained 50  $\mu$ L of each AB-Tb and QD-AB conjugate (in 10 mM TRIS/HCl; 0.5% BSA pH 7.4) at constant concentrations, to which 50  $\mu$ L of serum with increasing concentrations of TPSA was added. The homogeneous FRET immunoassays were measured on a modified “KRYPTOR compact plus” clinical fluorescence plate reader from Cezanne/Thermo Fisher Scientific and the EI plate reader with a 20 Hz nitrogen laser as excitation source operating at 337.1 nm. The KRYPTOR simultaneously detects the time-gated PL intensities, in a time window from 0.1 ms to 0.9 ms, in the Tb donor and QD acceptor channels fitted with the appropriate bandpass filters. The same bandpass filters were fitted on the EI plate reader.

### **4.3 Results and discussion**

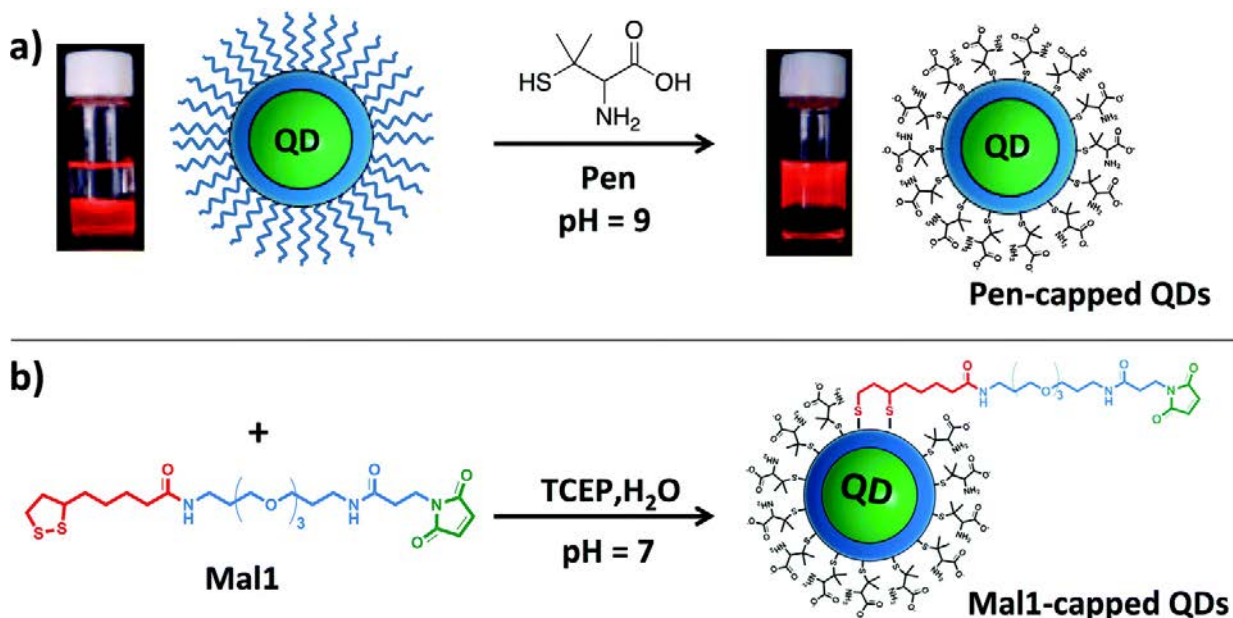
#### **4.3.1 Surface functionalization of the QDs**

Initially the strongly fluorescent InP-based or CdSe-based QDs were capped with hydrophobic organic surfactants rendering them soluble in non-polar media. Aqueous phase transfer is a critical step to make these QDs usable in biological studies. Two factors are of prime importance with regard to the phase transfer protocol: first, the procedure needs to guarantee a minimum loss of fluorescence quantum yield; second, it should provide high colloidal stability preventing the aggregation of QDs. Many literature protocols and commercial products rely on the encapsulation of the QDs with bulky amphiphilic polymers, which leads to hydrodynamic diameters in the range of 15–20 nm or more. Here, we focus on direct ligand exchange, which yields a much more compact surface coating beneficial for FRET applications. In the first step, the QDs were transferred from the organic to the aqueous phase by means of penicillamine (Pen), following a procedure we reported earlier [180]. It relies on the use of a biphasic mixture of QDs in chloroform and Pen in an aqueous solution of precisely controlled pH in the presence of the mild reducing agent TCEP. Basic pH is required for achieving the deprotonation of the Pen thiol group, which results in stronger binding to the surface of the different ZnS-coated QDs, while TCEP prevents Pen disulfide formation. Quantitative phase transfer was visible by

the mutual color change of both phases (**Figure 4.1**). In a second step, post-functionalization with the bifunctional ligand Mal1 was carried out under reduction of the disulfide group by means of TCEP (**Scheme 4.1**) [128]. The bidentate lipoic acid group provides stronger binding to the QD surface than Pen molecules, facilitating introduction of Mal1 [124]. The short PEG chain improves hydrosolubility and adds a spacer, which makes the maleimide functions stick out of the Pen corona and hence easily available for subsequent antibody conjugation. The full structural and photophysical characterization of the Pen- and Mal1-functionalized QDs is presented below and in the next section. Though we succeeded in conjugating directly antibodies on the QD-Pen emitting at 705 nm surface, full photophysical characterizations of all the QD-d-AB conjugates were not possible due to the low concentration recovery after purification for QD-d-F(ab')<sub>2</sub>. Absorption measurements were carried out in order to perform FRET immunoassays and only absorption and PL spectra of QD705-d-IgG will be shown.



**Figure 4.1.** Yellow sample corresponds to QD530 and brown sample to QD705. Mutual colour change from (left) chloroform phase (bottom) to (right) aqueous phase (top).



**Scheme 4.1.** Schematic representation of (a) the aqueous phase transfer of QDs with Pen, (b) post-functionalization with Mal1.

Surface functionalization of the QDs with Pen and post-functionalization with Mal1 did not lead to significant modifications of the PL and UV-Vis spectra as shown in **Figure 4.2**. On the other hand, a decrease of the PL QY was observed, from 0.40 (QD530), 0.60 (QD605), and 0.92 (QD705) in chloroform to 0.27, 0.30, and 0.66, respectively.

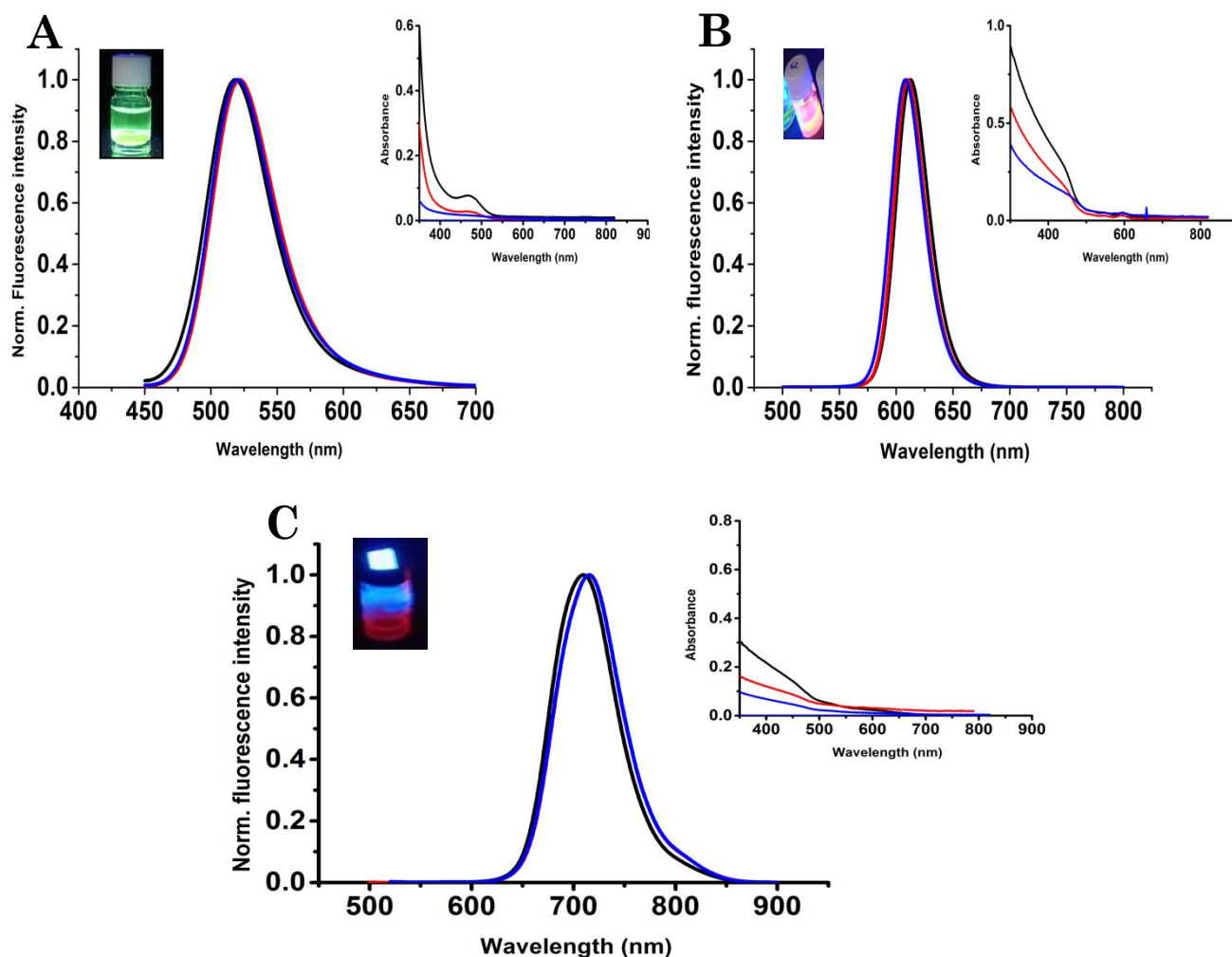


**Figure 4.2.** PL and UV-vis (inset) spectra of (A) InPZnS/ZnSe/ZnS QD530, (B) CdSe/ZnS QD605, (C) CdSeTe/ZnS QD705, in chloroform (black), after functionalization with penicillamine (red) and with the bifunctional ligand Mal1 (blue) in 1× PBS buffer. No significant alteration of their spectra could be observed after surface functionalization and post-functionalization.

### 4.3.2 Tb-AB and QD-AB conjugates

#### Tb-AB conjugate

NHS-functionalized Tb complexes (Lumi4-Tb) were directly labeled to available primary amines of anti-PSA IgG ABs (Tb-AB). A Tb per IgG (**Table 4.2**) conjugation ratio of  $11 \pm 3$  was determined by UV-Vis absorption spectroscopy using the molar absorptivities of Lumi4-Tb ( $\epsilon(340 \text{ nm}) = 26\,000 \text{ M}^{-1} \text{ cm}^{-1}$ ) and IgGs ( $\epsilon(280 \text{ nm}) = 210\,000 \text{ M}^{-1} \text{ cm}^{-1}$ ) and Beer-Lambert's law (**Figure 4.3 left**). The comparison of Tb-AB with the unconjugated complex shows no

alteration of the PL properties after AB-conjugation. Upon excitation at 365 nm the PL spectrum of Tb–AB shows the characteristic Tb emission lines and the obtained decay curve had an almost single exponential decay with an average PL lifetime of ca. 2.6 ms (Figure 4.3 right).

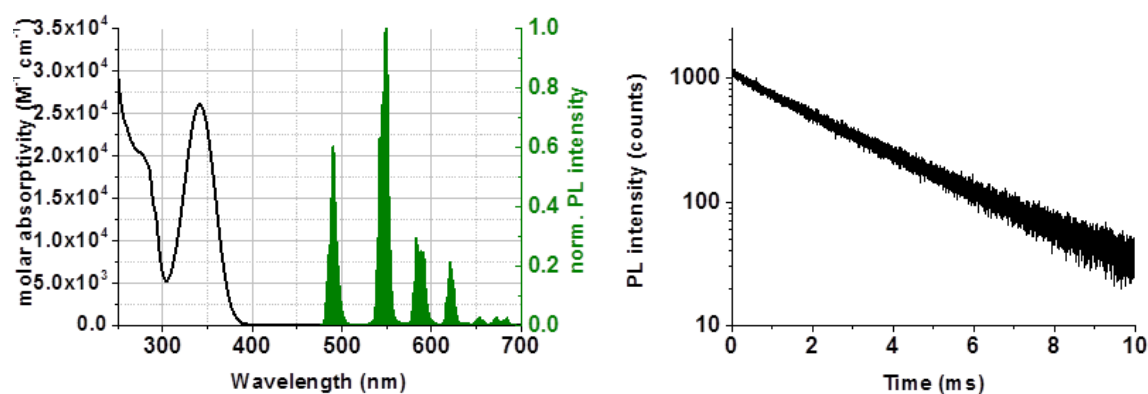
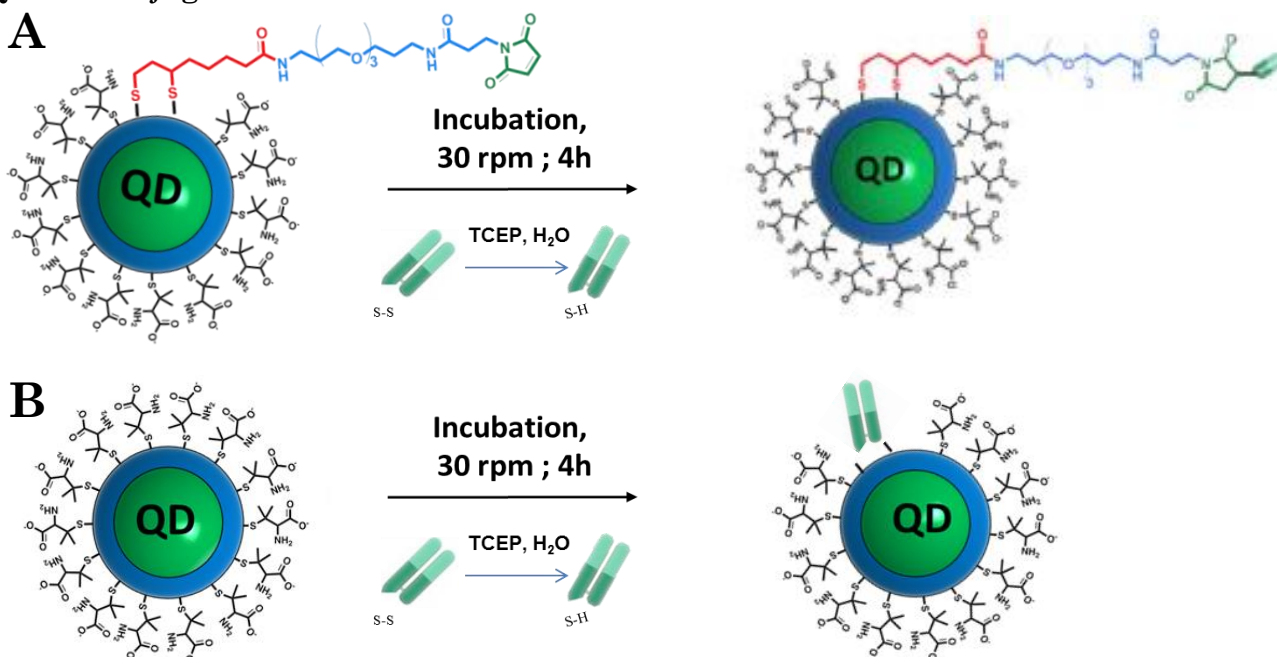


**Figure 4.3.** Left: absorption (black line) and PL (green, excitation wavelength 365 nm) spectra of Tb–AB conjugate. Right: Tb–AB PL decay curve ( $490 \pm 0.5$  nm) upon pulsed excitation at 365 nm with a repetition rate of 100 Hz. Amplitude-averaged decay time:  $\tau(\text{Tb}) = 2.6 \pm 0.3$  ms.

#### QD-AB conjugates



**Scheme 4.2.** (a) Indirect conjugation of QD-Mal1 to reduced F(ab) forming a covalent thio-ether bond, (b) direct conjugation to QD-pen surface with reduced F(ab) through metal affinity coordination of thiol on F(ab) to  $\text{Zn}^{2+}$  on QDs surface.

The conjugation of ABs to the QDs was performed by two different methods: referred in this thesis as indirect conjugation and direct conjugation. F(ab) were indirectly conjugated to QD-Mal1 through sulfhydryl chemistry [128,181]. IgG, F(ab')<sub>2</sub> and F(ab) were directly conjugated to

QD705-Pen (coming from a different batch of QD705-Pen) through metal affinity. The choice of direct conjugation of ABs to the QD-Pen emitting at 705 nm was based on the results obtained in **Chapter 3** (largest  $R_0$ , highest sensitivity). For both indirect and direct conjugation, the ABs prior to coupling with the QDs, were first activated through reduction of the S–S bond by TCEP (

**Scheme 4.2**) as described in **section 3.2.2.2**

The absorption and PL spectra of the three QD–Mal1-F(ab) conjugates are shown in **Figure 4.4 A-D left**. QD concentrations (**Table 4.2**) were determined using the molar absorptivities of  $\epsilon_{450\text{ nm}}(\text{QD530}) = 4.2 \times 10^5 \text{ M}^{-1} \text{ cm}^{-1}$  (experimentally determined),  $\epsilon_{405\text{ nm}}(\text{QD605}) = 2.8 \times 10^6 \text{ M}^{-1} \text{ cm}^{-1}$  and  $\epsilon_{405\text{ nm}}(\text{QD705}) = 8.3 \times 10^6 \text{ M}^{-1} \text{ cm}^{-1}$  (provided by the supplier) [176]. The estimation of the labeling ratio of AB/QDs could not be determined here due to the high background of the QD's absorption at 280 nm interfering with the absorption of the ABs at this wavelength. The photophysical properties of the QDs were slightly altered by the F(ab) conjugation, as summarized in **Table 4.1**, compared to the Pen-capped QDs. A PL red shift of 4 nm could be detected for the CdSe-based QD605 and QD705, while a blue shift of 3 nm was found for the InP-based QD530. Further experiments are needed to unequivocally elucidate the origin of these shifts; we tentatively ascribe them to the quantum confined Stark effect, induced by the change of the dielectric environment of the QDs upon conjugation with F(ab) [182]. On the other hand, no emission maxima shifts could be observed for the QD705-d-IgG, although a slight broadening of the spectra towards the red spectrum resulted. We believe to have similar results upon direct conjugation with F(ab)<sub>2</sub> and F(ab) due to the same conjugation protocol. F(ab)-conjugation through Mal1 also led to changes in the PL lifetimes (**Table 4.1**) from 24 to 18 ns for QD530, from 4.6 to 10 ns for QD605, and from 79 to 41 ns for QD705 and direct conjugation of IgGs to QD705, from 93 ns to 84 ns. These changes are attributed to the generation or filling of electronic trap states acting as competing deexcitation channels upon AB attachment.

**Table 4.1.** Optical characterization of QD-Mal1-F(ab) and QD-d-IgG conjugates were performed by excitation at 405 nm using as excitation sources a continuous-wave Xe lamp and a pulsed diode laser from Edinburgh Instruments for steady-state and time-resolved measurements respectively. *\*coming from a different batch of QD-Pen emitting at 705 nm*

<u>Sample</u>	InPZnS/ZnSe/ZnS 530		CdSe/ZnS 605		CdSeTe/ZnS 705		CdSeTe/ZnS 705*	
	-Pen	-F(ab)	-Pen	-F(ab)	-Pen	-F(ab)	-Pen	-IgG
Emission wavelength maxima (nm)	505 ± 1	502 ± 1	602 ± 2	606 ± 0.5	699 ± 2.5	703 ± 0.5	707 ± 0.5	707 ± 0.5
Lifetime (ns)	24.3 ± 6.1	17.7 ± 2.8	4.6 ± 0.4	10.4 ± 1.1	79.4 ± 20.8	40.7 ± 6.4	93.0 ± 9.6	83.6 ± 8.1

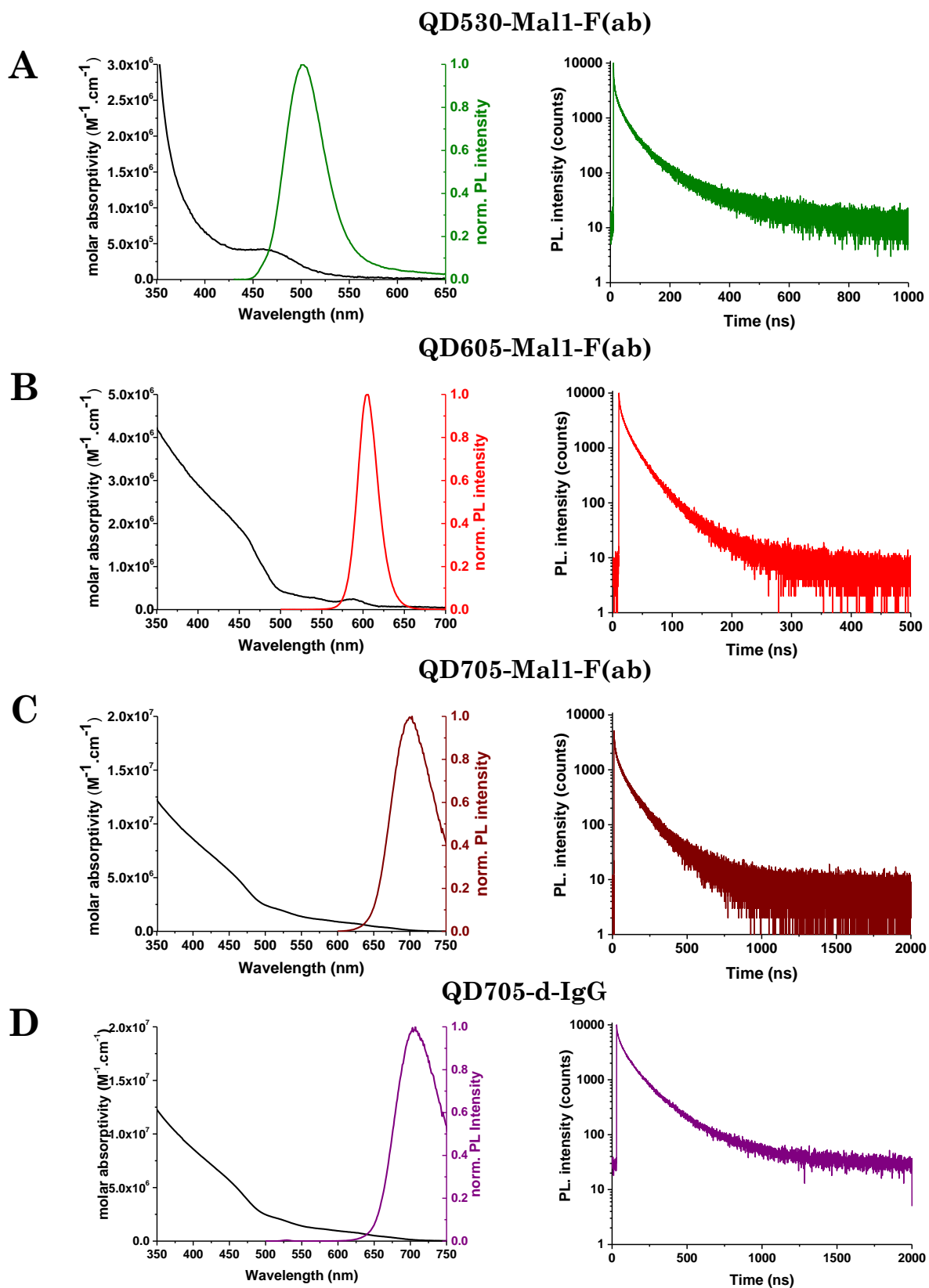


**Figure 4.4.** Absorption and PL spectra (left) and PL decay curves (right) of (A-C) F(ab)-conjugated through Mal1 InPZnS/ZnSe/ZnS (QD530-Mal1-F(ab)), CdSe/ZnS (QD605-Mal1-F(ab)), CdSeTe/ZnS (QD705-Mal1-F(ab)) and (D) CdSeTe/ZnS (QD705-d-IgG) QDs in  $1\times$  PBS buffer. Amplitude-averaged PL lifetimes:  $\tau(\text{QD530-Mal1-F(ab)}) = 17.7 \pm 2.8$  ns,  $\tau(\text{QD605-Mal1-F(ab)}) = 10.4 \pm 1.1$  ns,  $\tau(\text{QD705-Mal1-F(ab)}) = 40.7 \pm 6.4$  ns and  $\tau(\text{QD705-d-IgG}) = 83.6 \pm 8.1$  ns

**Table 4.2.** Overview of concentration and labeling ratios of the FRET-pairs.

Tb-AB	[Tb] ( $\mu\text{M}$ )	[AB] ( $\mu\text{M}$ )	Tb/AB	QD-AB	[QD] (nM)
Tb-IgG	2.6	27.6	$11.0 \pm 2$	QD530-Mal-F(ab)	480
				QD605-Mal-F(ab)	207
				QD705-Mal-F(ab)	120
				QD705-d-IgG	60
				QD705-d-F(ab') <sub>2</sub>	11
				QD705-d-F(ab)	132

Sizes and morphologies of the inorganic parts of the QDs were characterized using transmission electron microscopy (TEM), which revealed nearly monodisperse spherical (QD530 and QD605) and elongated (QD705) nanocrystals (**Figure 4.5**).

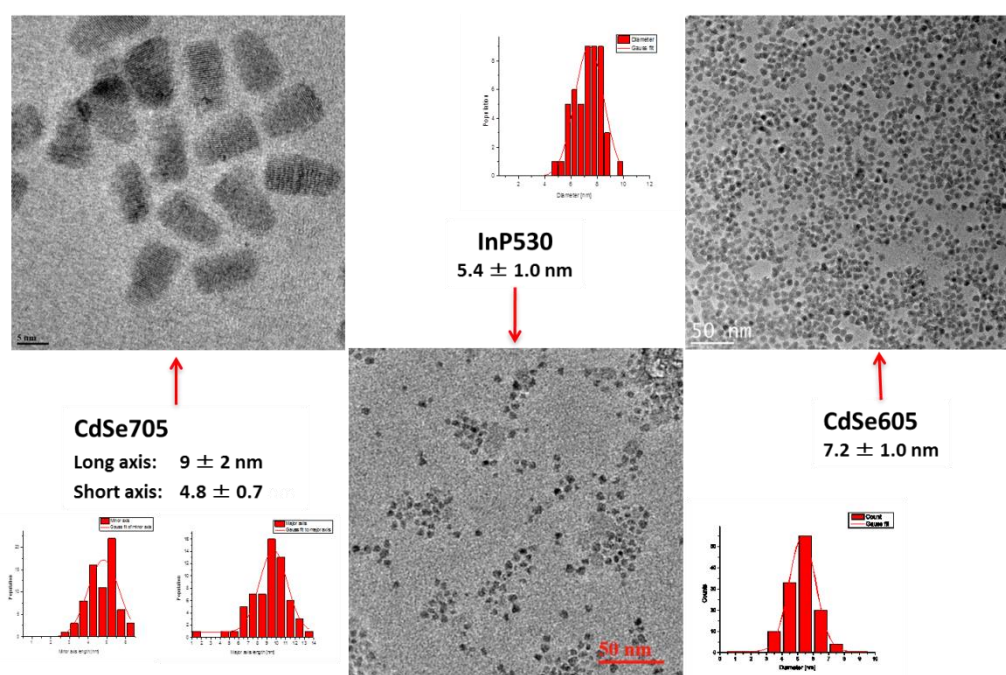


**Figure 4.5.** TEM image of CdSe705- (left) InP-based QDs (middle) after post-functionalization with Mal1 and CdSe605-based QDs after functionalization with Pen.

The hydrodynamic diameters of the QDs were evaluated by dynamic light scattering (DLS) and are presented in **Figure 4.6**. These measurements confirmed the narrow size distribution observed with TEM and revealed small hydrodynamic diameters, which slightly increase with each functionalization step. As exemplified by QD705, introduction of the Mal1 ligand led to a size increase from 8 to 10 nm with respect to QD705-Pen, which was in the expected range for a

ligand with an approximate length of 3.0 nm. Conjugation with F(ab) led to a further increase to 13 nm as the total hydrodynamic diameter, which makes this QD–Mal1-AB conjugate one of the smallest AB-functionalized near-infrared (NIR) emitting nanoprobe ever reported.

**Table 4.3.** Polydispersity index (PDI) and zeta potentials of QD-Pen and QD-Mal1.

Sample	PDI-Pen	PDI-Mal1	Zeta potential-Pen (mV)	Zeta potential-Mal1 (mV)
QD530	0.33	0.58	-31	-24
QD605	0.15	0.23	-33	-28
QD705	0.08	0.23	-36	-24

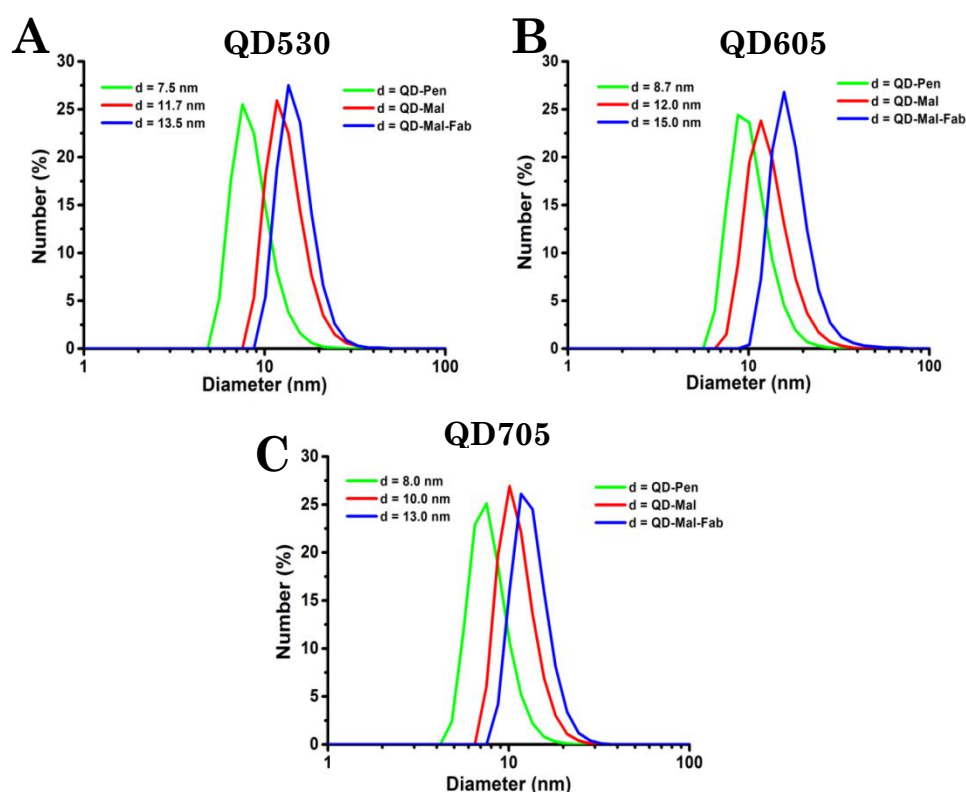


**Figure 4.6.** Size distribution of (A) QD530 (B) QD605 (C) QD705 after each functionalization step (Pen-capping: green, Mal1-functionalization: red, and F(ab)-conjugations: blue) obtained by DLS measurements. The average hydrodynamic diameter  $d$  (nm) of each measurement is given in the legend.

Zeta potential of both Pen-capped and Mal1-capped were measured in order to understand the state of the QDs surface and prediction of long term stability. The magnitude of zeta potential is therefore predictive of the QDs colloidal stability. Generally, zeta potential values greater than +25 mV or less than -25 mV result in high degrees of stability [183]. Zeta potential values (Table 4.3) of both Pen-capped and Mal1-capped QDs display values between -36 mV and -24 mV, respectively, and together with low polydispersity indices, high colloidal stability is confirmed. The negative charge on the carboxylate group of the Pen ligands guarantees

stability by electrostatic repulsion between the QDs. After post-functionalization with Mal1, the zeta potential decreases due to the reduction of negatively charged Pen ligands on the QDs' surface in favor of neutral Mal1 ligands. The short PEG moieties of Mal1 are expected to contribute in colloidal stability of the QDs in aqueous media.

Colloidal stability of the QDs in water or relevant buffer solutions is of crucial importance for biological detection. The obtained Pen- and Mal1-functionalized QDs showed no sign of aggregation after storage of more than two years (**Figure 4.7**) at 4 °C in the dark in 1× PBS buffer (pH = 7.4), as confirmed by combined periodical DLS and UV-Vis measurements. After indirect F(ab) conjugation and direct AB conjugation the colloidal stability was determined to be at least 2 and 1 month respectively, which is the current limit of our measurements.

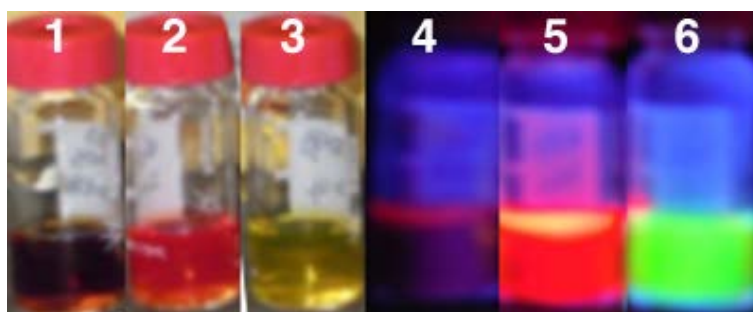


**Figure 4.7.** Photographs of Pen-functionalized QD705 (1/4), QD605 (2/5) and QD530 (3/6) taken two years after aqueous phase transfer with Pen. 1-3 under room light, 4-6 under UV light.

The photophysical and morphological characterization results show that our approach of using an optimized ligand exchange with Pen, followed by post-functionalization with Mal1, is an efficient and simple way of obtaining highly luminescent, stable, and compact QDs ready for further functionalization with small F(ab)s to yield very small fluorescent AB-nanoprobes. Gel electrophoresis (**Figure 4.8**) and FTIR (**Figure 4.9**) measurements further confirmed successful post-functionalization with Mal1 and F(ab) conjugation of the QDs. For all QDs, the bands on the agarose gel corresponding to the QD–Mal1-F(ab) conjugates were the most retarded due to the larger sizes of the QD–AB conjugates. FTIR spectra (**Figure 4.9**) clearly revealed, by comparison to the free, i.e. not QD-bound, molecules, peaks corresponding to the carbonyl stretch vibrations of the maleimide function in QD-Mal1 (**Figure 4.9 left, green**) centered around 1000  $\text{cm}^{-1}$  and to the N–H stretch vibration of F(ab) in QD-Mal1-F(ab) centered around 3300  $\text{cm}^{-1}$ . In these characterizations all three types of QDs behaved in the same way, which was expected as they mainly differ in the inorganic core composition but all possess an identical ZnS outer shell and the same first ligand exchange procedure with Pen has been used.

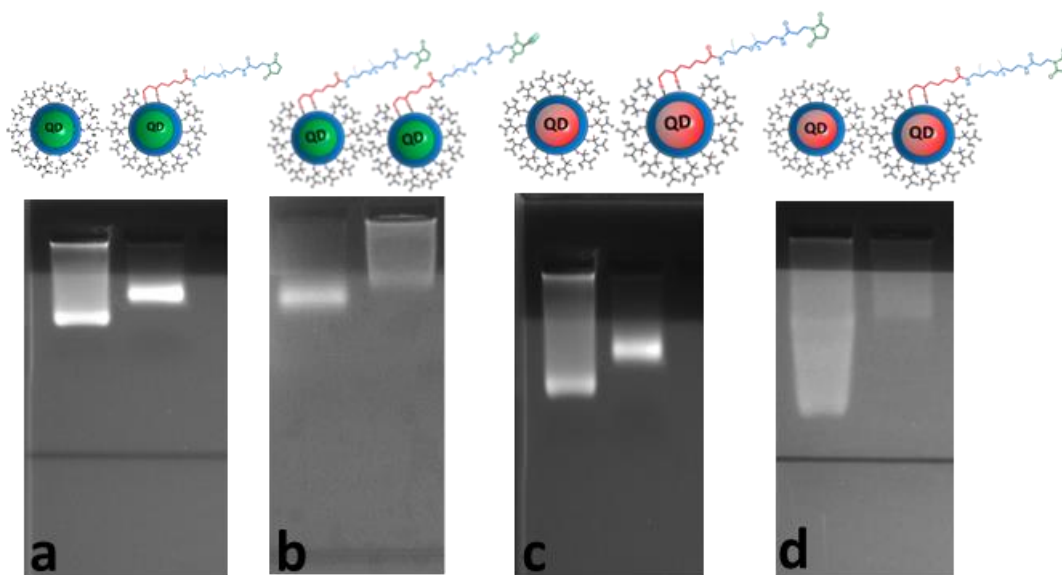


**Figure 4.8.** Gel electrophoresis characterization of the sample InP530 (a, b), QD705 (c) and QD605 (d) at different stages of functionalization was carried out on 1% agarose gel in 25 mM Hepes buffer at 100 V on a RunOne System. Prior to gel electrophoresis, to each sample a solution corresponding to 20% of the sample volume and containing Orange G and 30% glycerol in 6% loading buffer was added. For visualization, the gel was placed on a UV transilluminator, and an image was captured with a Gel Doc XR system (Bio-Rad, Hercules, CA). In the case of InP-based QDs (a-b) the image shown here was acquired after 10 min while for the Cd-based QDs after 20 min. The label a, c and d refers to the sample functionalized with Pen and Mal1, while b refers to the sample functionalized with Mal1 and bioconjugated with F(ab).

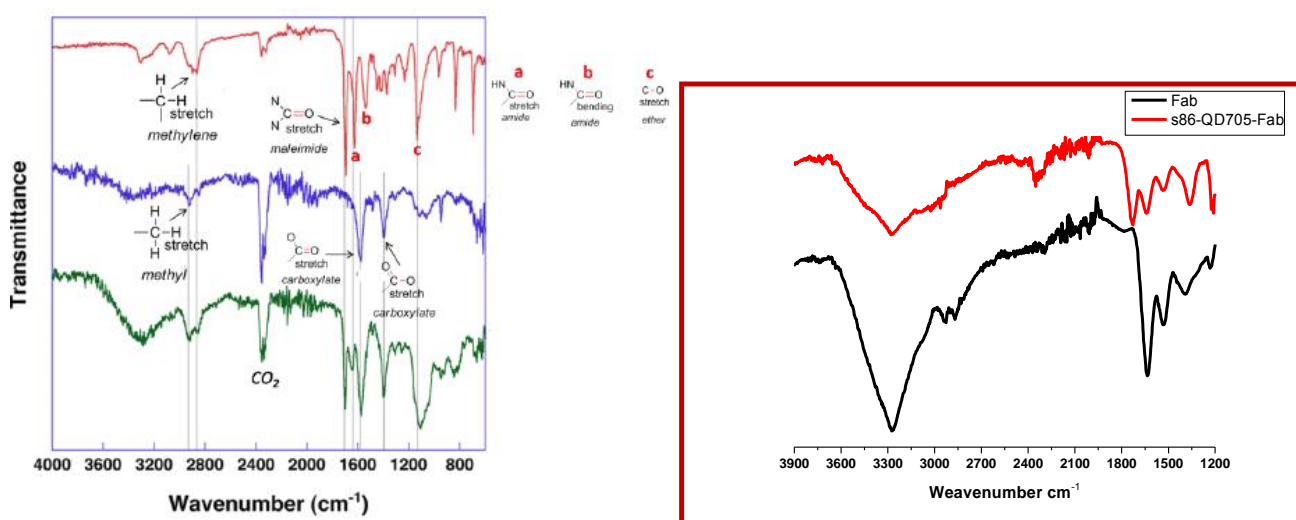


**Figure 4.9.** FTIR characterization showing the successful functionalization of the QDs with the Mal1 ligand and subsequent conjugation of the fragmented antibody F(ab). Left: FTIR spectra of Mal1 (red), QDs functionalized with Pen (blue) and post-functionalized with Mal 1 (green); right: FTIR spectra of F(ab) and of CdSe/ZnS QD705 after F(ab) conjugation.

### 4.3.3 FRET immunoassays

To demonstrate the functionality of the compact QD–AB conjugates, we performed homogeneous Tb-to-QD FRET immunoassays against PSA on the KRYPTOR compact plus clinical fluorescence plate reader (Cezanne/Thermo Fisher). PL intensities of Tb ( $I_{\text{Tb}}$ ) and QDs ( $I_{\text{QD}}$ ) were acquired simultaneously in a time-gated detection window between 100  $\mu\text{s}$  to 900  $\mu\text{s}$  after pulsed excitation at 337 nm using a nitrogen laser operating at 20 Hz. Due to the extremely long PL lifetimes of Tb (ms) compared to QDs (ns), the time-gating allows efficient suppression of short-lived sample autofluorescence and direct excitation of the QDs. This allows for solely obtaining the pure FRET signals (FRET-quenched Tb PL and FRET-sensitized QD PL). Optical bandpass filters (Delta and Semrock) for the Tb donor and QD acceptor detection channels were  $(494 \pm 10)$  nm for Tb and  $(522 \pm 6)$  nm,  $(607 \pm 4)$  nm, and  $(707 \pm 8)$  nm for QD530, QD605 and QD705, respectively. The FRET-ratio was defined as **Equation 2.18**.

Within all the FRET-assays the Tb–AB and QD–AB concentrations were kept constant. Concentrations of 3 nM Tb–AB with 3 nM QD605-Mal1-F(ab) or QD705-Mal1-F(ab), and 9 nM Tb–AB with 9 nM QD530-Mal1-F(ab) were used. For direct conjugation with the QDs, 3 nM Tb–AB with 3 nM QD-d-IgG, QD-d-F(ab)<sub>2</sub> or QD-d-F(ab) were used. PSA concentrations, prepared in serum, ranged from 0.05 nM (for QD605 and QD705) or 0.1 nM (for QD530) to 9 nM and to 24 nM for QD705-d-IgG/F(ab)<sub>2</sub>. 50  $\mu\text{L}$  of each AB-conjugate (Tb–AB and QD–AB) were mixed with 50  $\mu\text{L}$  of serum for a total working volume of 150  $\mu\text{L}$ . The immunoassay calibration curves (FRET-ratio over total PSA concentration) are presented in **Figure 4.11**. Assays **A-C** from **Figure 4.11** showed a steep FRET-ratio increase with increasing PSA concentration up to ca. 2 to 4 nM, which was expected due to the saturation of Tb–QD FRET complexes (in the concentration range of Tb–AB or QD–AB). Assays **D-F** from **Figure 4.12** yielded even steeper FRET-ratio increase as compared to its QD-Mal1 conjugate counterpart indicating better sensitivity of these assays. It should be noted that the FRET-ratio increase was very small (only ca. 5% at the maximum) for the Tb–QD530 assay, which was most probably related to the lower Förster distance of Tb–QD530 ( $R_0 = 6.1$  nm) compared to the values of Tb–QD605 ( $R_0 = 7.7$  nm) and Tb–QD705 ( $R_0 = 11$  nm). These findings can be understood by analyzing the overlap integrals of the different D–A pairs (**Figure 4.10**). Therefore, only the FRET systems B-C could be used for a quantitative evaluation of PSA immunoassays using QDs-Mal1 (**Figure 4.11 B and C**).

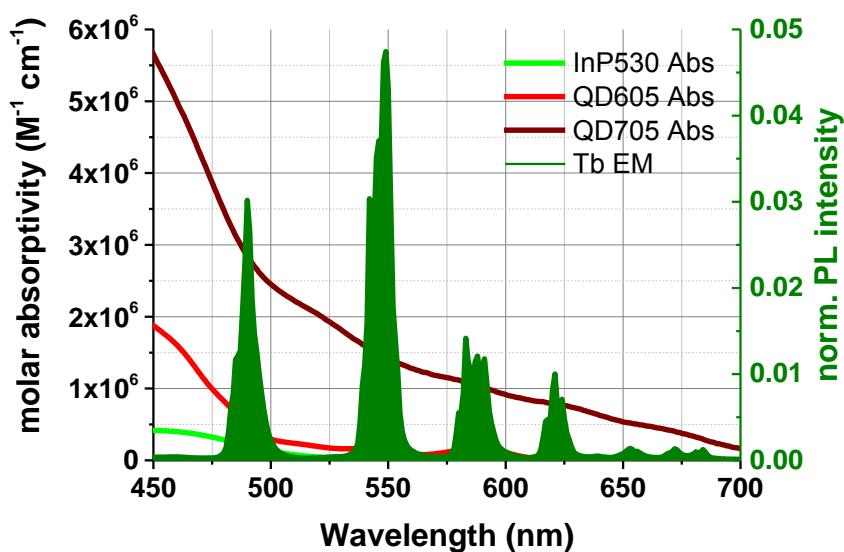


**Figure 4.10.** Overlap between QDs absorption spectra (QD530: green; QD605: red; QD705: brown)) and area-normalized Tb emission spectra (olive green). Förster distances: Tb-QD530 = 6.1 nm, Tb-QD605 = 7.7 nm and Tb-QD705 = 11 nm.

### Tb-to-QD-Mall immunoassays

Calibration curves (A-C) over a concentration range of 0 to 9 nM (black squares) revealed a linear FRET-ratio increase, followed by saturation and a FRET-ratio decrease. This decrease is due to the so-called Hook-effect, describing the increase of the fraction of single fluorophore (Tb-AB-PSA and QD-AB-PSA) binding complexes compared to FRET (Tb-AB-PSA-QD-AB) binding complexes. Homogeneous FRET assays are usually designed for the detection of very low concentrations without any washing or separation steps. To access the very low concentration range, high signal-to-background ratios are required and therefore the Tb-AB concentrations are selected in a low nM range (in our case 3 nM) to keep the Tb PL background at a minimum intensity level. As a consequence, the dynamic detection range becomes relatively narrow (ca. 0.05 to 2 nM in our case). On the KRYPTOR clinical plate reader used in our study, this drawback is overcome by a kinetic sample detection and automated dilution of too highly concentrated samples,[25] which can increase the dynamic detection range by several orders of magnitude. A second calibration curve, with many more PSA concentrations in the linearly increasing parts of the assay curves (red circles), was used to determine the LODs (Table 4.5). The same method for determining the LODs as in the previous chapter was used.

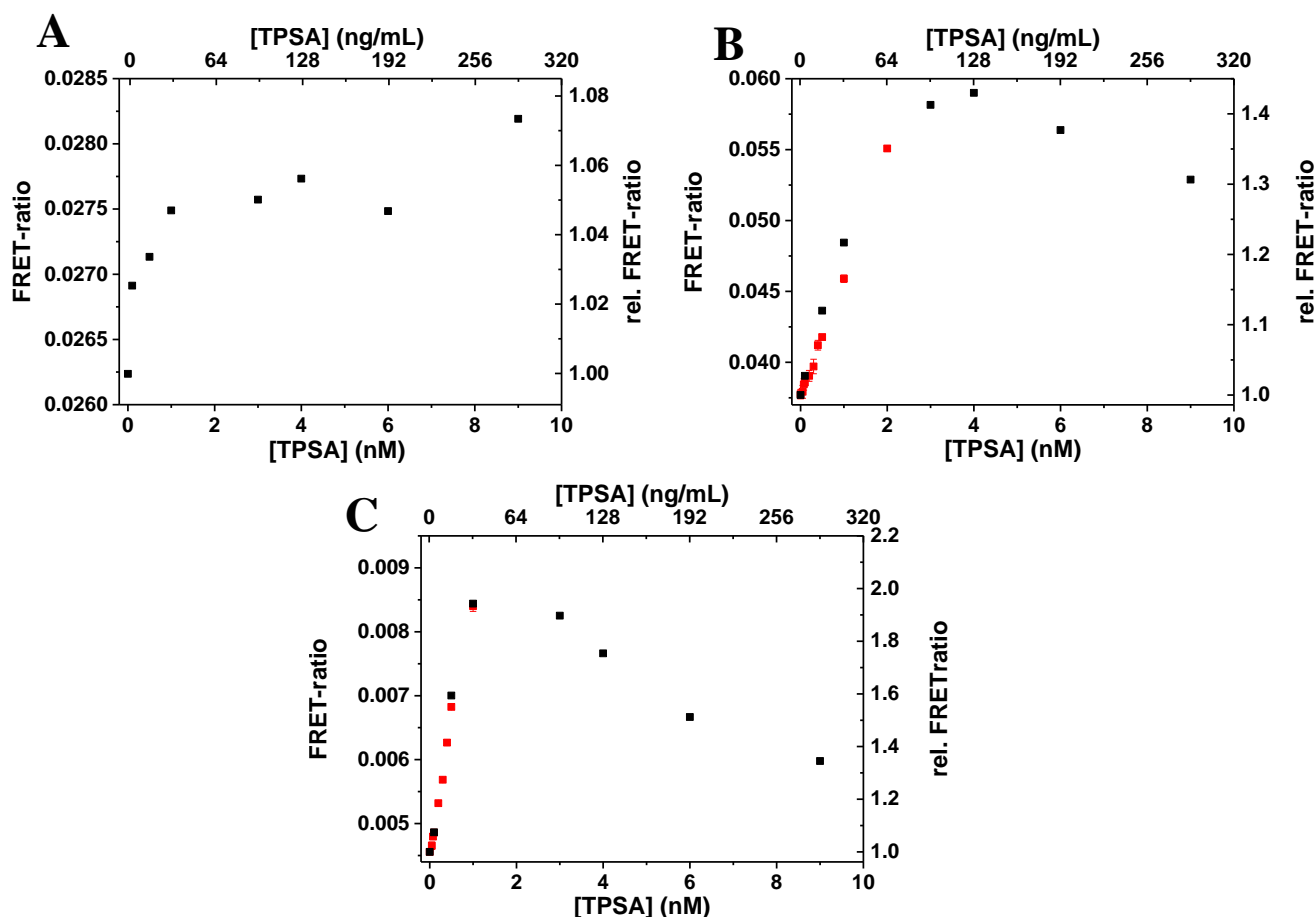


**Figure 4.11.** Calibration curves for total PSA (TPSA) homogeneous FRET immunoassays using the (A) Tb-QD530-Mal1, (B) Tb-QD605-Mal1, and (C) Tb-QD705-Mal1 FRET pairs. Assays (B) and (C) could be used for quantitative analysis. Black data points (squares) were from a first set of experiments using PSA concentrations between 0 and 9 nM. Red data points were taken in a second set of experiments for a statistical analysis of LODs in the linearly increasing parts of the assay curves. The inset corresponds to the linear part used for LOD calculation.

### Tb-to-QD-d immunoassays

The FRET calibration curves Tb-to-QD705 (**Figure 4.12**) (D) IgG, (E) F(ab')<sub>2</sub> and (F) F(ab) show a remarkable increase of the time-gated FRET-ratio with a linear detection range of *ca.* 1 order of magnitude as compared to the calibration curves obtained when using the QD-Mal1 conjugates. One reason could be of direct conjugation of the ABs on the surface of the QDs bringing the Tb donors closer to the QDs upon biological recognition of PSA, hence more efficient energy transfer. As  $\eta$  is directly proportional to  $r^{-6}$ , Mal1 ligand, as observed by DLS, brings another *ca.* 3 nm before conjugation to F(ab), which greatly influences the energy transfer efficiency. The LODs were calculated using the linear increasing slope and are summarized in **Table 4.5**. Calibration curve (E) could not be used for quantitative analysis because of the low concentration of the QD-F(ab')<sub>2</sub> conjugate obtained and only a test assay (*i.e.* one data point corresponding to a single concentration) could be performed. However,

comparison of the sensitivities of the calibration curves as summarized in (G), suggest comparable sensitivity of the  $F(ab')_2$  to the IgG in the linear range (0 to 2 nM). So, we could expect similar LOD when using  $F(ab')_2$ . Furthermore, graph (G) shows that the highest sensitivity is obtained using  $F(ab)$ .

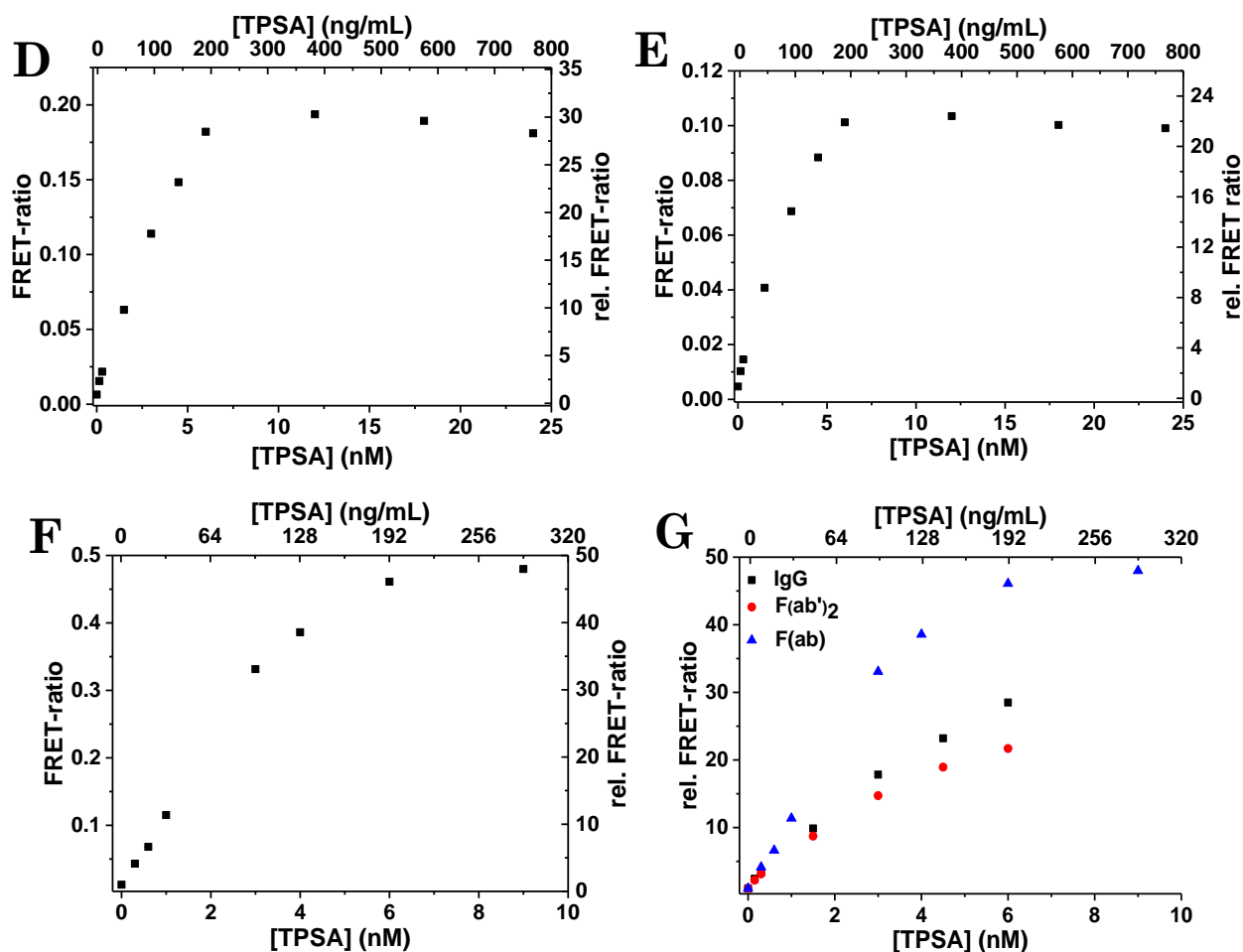


**Figure 4.12.** Calibration curves using the direct conjugated QDs to ABs. Assays with Tb-to- (D) QD705-d-IgG, (E) QD705-d- $F(ab')_2$  and (F) QD705-d- $F(ab)$  FRET pairs. Calibration curves (D) and (F) could be used for LOD calculation while (E) correspond to a test assay. (G) Relative FRET-ratio curves of the FRET assays with the different ABs showing the highest sensitivity achieved using  $F(ab)$ .

PL FRET decay curves could be acquired for the Tb-to-QD705-d-IgG/ $F(ab)$  systems, revealing obvious FRET-sensitization in the QD channel and more obvious FRET-quenching for Tb-QD705-d- $F(ab)$  than for Tb-QD705-d-IgG. For the FRET-pairs involving IgGs, we mainly observe stable and unquenched Tb signals which can be attributed to long distance between donor and acceptor. Unbound Tb-IgG and the random labeling of Tb on the IgG (only close Tb near the IgG binding sites can participate in efficient energy transfer) in the FRET experiments also cause a high background of unquenched Tb signals thus making it difficult for an observable FRET quenching. As the Tb PL background is weaker in the acceptor channel,

FRET-sensitization can be observed more easily and allows a more precise fitting of the acceptor channel for distance determination between the FRET-pairs. **Figure 4.13** represents the PL decays curves for the Tb-to-QD705-d-IgG/F(ab) where we can distinguish in the QD channel the appearance of new decay components in the  $\mu\text{s}$  range and higher PL intensities with increasing TPSA concentration as compared to the 0 nM black curve where only Tb-QD FRET-pairs ( $\mu\text{s}$  decay component from QD and long decay component from Tb originating from PL background in the QD detection channel) are present, which indicates sensitization of the QDs by FRET. The PL decay curves measured in the Tb channel reveal differences in FRET-quenching when QD-IgG or QD-F(ab) was used. For the Tb-QD-d-IgG immunoassay, stable and undistinguishable FRET-quenching of Tb PL decay curves could be observed whereas the combination of QD-d-F(ab) and Tb-IgG showed a decrease of the Tb PL intensities with increasing TPSA concentration. These observations are direct evidence of non-radiative energy transfer from Tb to QD in the presence of TPSA (target) and use of F(ab) brings the FRET-pairs closer together where FRET-quenching of Tb and FRET-sensitization of QD could be observed.

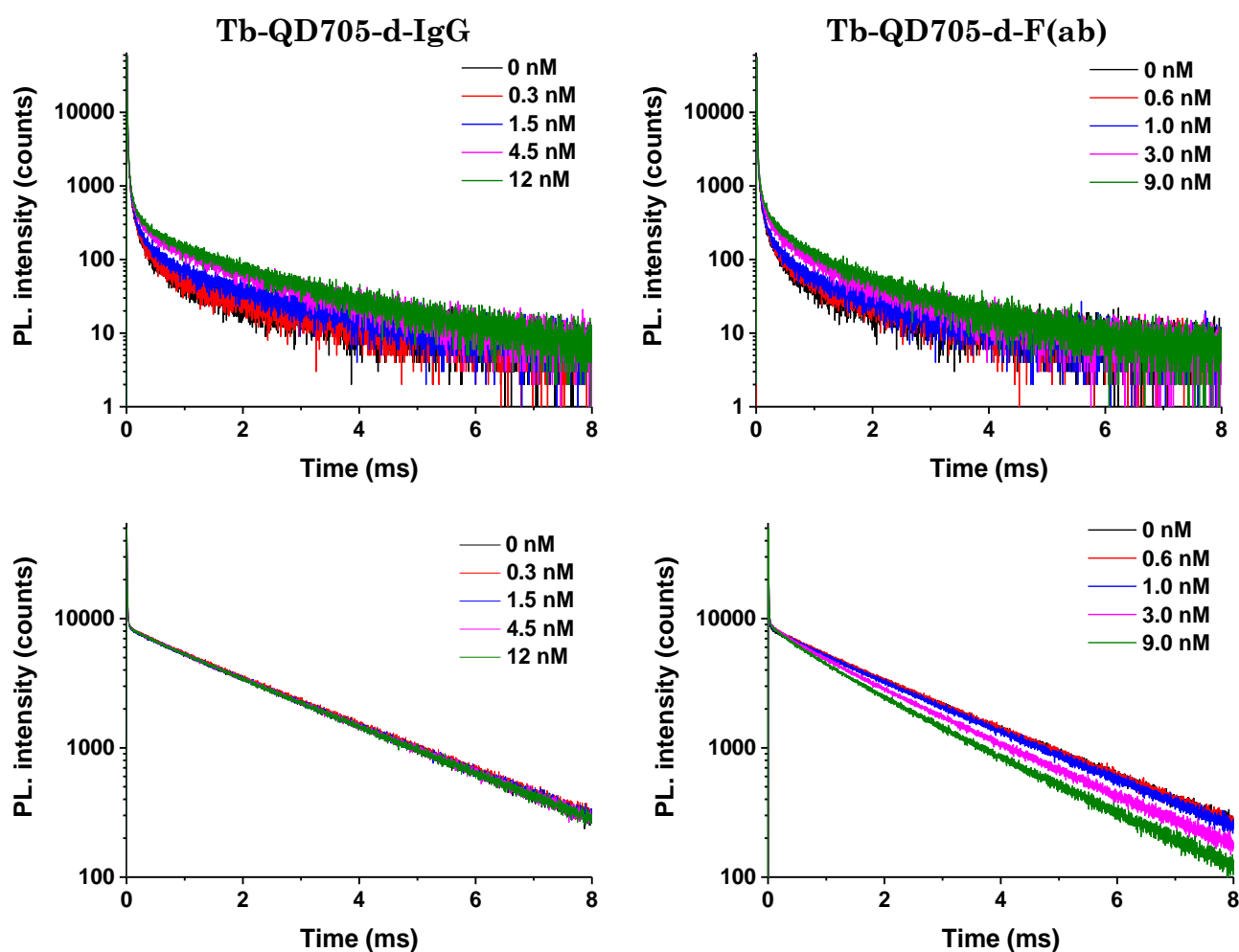


**Figure 4.13.** PL decay curves of the IgG and Fab system. Top curves correspond to acceptor channel showing sensitization of QDs due to FRET and below (bottom curves) their respective Tb decay curves in the donor channel.

As it was mentioned before, both acceptor and donor channels contain signals from unquenched donor (**Figure 4.13**). Decay time fitting in the two channels of the Tb-to-QD FRET system to estimate the pure FRET decay time, for FRET efficiency and distance analysis, involves decay time correction of free Tb not participating in FRET. A detailed description of LLC-to-QD FRET decay time analysis of donor quenching and acceptor sensitization is available in reference [135]. The pure donor can be fitted with a double-exponential resulting in a short  $\tau_{D1}$  and a long dominant decay time  $\tau_{D2}$  with amplitude fractions  $\alpha_{D1}$  and  $\alpha_{D2}$  respectively. FRET-quenched donor and FRET-sensitized acceptor can be fitted with triple-exponential and quadruple-exponential fit functions respectively. Due to sample autofluorescence and direct excitation of QDs in the short time range, and contribution of donor crosstalk within the QD channel in the long time range, a delay of around 10 - 50  $\mu$ s can be applied to the fits to avoid such disturbances. Such fits with a delay in the starting point of the fit which is different from  $t_0$  are called tail fits and although they do not change the different single decay times, the single amplitudes  $A_{i-FIT}$  have to be corrected from  $t_0$  to the actual correct start at 0 to yield the correct amplitudes ( $A_i$ ) of the complete decay function:

$$I = A_{i-FIT} \cdot e\left(-\frac{t-t_0}{\tau}\right) = A_i e\left(-\frac{t}{\tau}\right) \rightarrow A_i = A_{i-FIT} e\left(-\frac{t_0}{\tau}\right) \quad (4.2)$$

The FRET-quenched donor decay curves can be fitted with three exponents with amplitude fractions  $\alpha_{DA*1}$ ,  $\alpha_{DA*2}$  and  $\alpha_{DA*0}$  for decay times  $\tau_{DA1}$ ,  $\tau_{DA2}$  and  $\tau_{DA0}$  where  $\tau_{DA0}$  fixed to  $\tau_2$  to account the emission of the unquenched donor. Therefore, only  $\tau_{DA1}$  and  $\tau_{DA2}$  are used for estimation of FRET decay time and as such necessitates the redefinition of the amplitude fractions of these two decay times as follows:

$$\alpha_{DA1} = \frac{\alpha_{DA*1}}{\alpha_{DA*1} + \alpha_{DA*2}} \quad \text{and} \quad \alpha_{DA2} = \frac{\alpha_{DA*2}}{\alpha_{DA*1} + \alpha_{DA*2}} \quad (4.3)$$

The unquenched donor has two decay time components  $\tau_{D1}$  and  $\tau_{D2}$ , and  $\langle\tau_{DA}\rangle$  should be corrected from the short  $\tau_{D1}$  as it falls within the FRET decay time but fixing  $\tau_{D1}$  by addition of an extra exponential fit will lead to inconsistent fit. Hence a correction factor  $z_D$ , which corresponds to the fraction of unquenched donors in the short time components, has to be involved and corresponds to the ratio of amplitude fractions of  $\tau_{D2}$  and  $\tau_{DA0}$  multiplied by the amplitude fraction  $\alpha_{D1}$  :

$$z_D = \left(\frac{\alpha_{DA*0}}{\alpha_{D2}}\right) \cdot \alpha_{D1} \quad (4.4)$$

The average FRET-quenched decay can then be calculated using the redefined amplitudes ( $\alpha_{DA1} + \alpha_{DA2} = 1$ ) and  $z_D$  with the **Equation 4.3** and substituting  $\langle \tau_{DA} \rangle$  in **Equation 2.9** and **Equation 2.10** results in estimation of FRET efficiency and distance between the FRET-pairs:

$$\langle \tau_{DA} \rangle = \frac{\alpha_{DA1} \tau_{DA1} + \alpha_{DA2} \tau_{DA2} - z_D (\alpha_{DA1} + \alpha_{DA2}) \tau_{D1}}{\alpha_{DA1} + \alpha_{DA2} - z_D (\alpha_{DA1} + \alpha_{DA2})} = \frac{\alpha_{DA1} \tau_{DA1} + \alpha_{DA2} \tau_{DA2} - z_D \tau_{D1}}{1 - z_D} \quad (4.5)$$

Fitting of the FRET-sensitized acceptor is performed by four exponential fit function where only the first three components ( $\alpha_{AD*1}$ ,  $\alpha_{AD*2}$  and  $\alpha_{AD*3}$  for decay times  $\tau_{AD1}$ ,  $\tau_{AD2}$  and  $\tau_{AD3}$ ) are used to calculate the FRET decay time and the fourth component  $\tau_{AD0}$  is fixed to account for free and unquenched donor. The amplitudes  $\alpha_{AD*i}$  should therefore be corrected by the FRET rates  $k_{FRETi} = \tau_{ADi}^{-1} - \langle \tau_D \rangle^{-1}$  for  $i=1-3$  which considers the FRET efficiency dependent excitation of the acceptors using **Equation 4.6** and from the short component of the donor crosstalk in the acceptor channel by the correction factor  $z_A$  (**Equation 4.7**):

$$\alpha_{ADi} = \frac{\alpha_{AD*i}/k_{FRETi}}{(\alpha_{AD*1}/k_{FRET1}) + (\alpha_{AD*2}/k_{FRET2}) + \alpha_{AD*3}/k_{FRET3}} \quad (4.6)$$

$$z_A = \left( \frac{\alpha_{AD*0}}{\alpha_{D2}} \right) \cdot \alpha_{D1} \quad (4.7)$$

The FRET-sensitized decay time can as a result of these corrections be calculated by **Equation 4.8**:

$$\langle \tau_{AD} \rangle = \frac{\alpha_{AD1} \tau_{AD1} + \alpha_{AD2} \tau_{AD2} - z_A \tau_{A1}}{1 - z_A} \quad (4.8)$$

The average FRET-efficiency and distances can be calculated using  $\langle \tau_{AD} \rangle$  in **Equations 2.9** and **2.17**

Following the above corrections to account for unquenched donor emission and therefore the determination of pure FRET from quenching and sensitization of the FRET-pairs from **Figure 4.13**, we find for the Tb-to-QD-d-IgG and Tb-to-QD-d-F(ab) immunoassay, a FRET-efficiency (acceptor channel fitting) of 34 and 38 % with an estimated donor to acceptor distance of 12.3 and 11.9 nm respectively. The donor channel fitting for Tb-to-QD-d-IgG is not convenient as the Tb decay curves are all stable and no quenching could be observed resulting to an almost similar lifetime of Tb alone and Tb in presence of QD. Donor channel fitting for Tb-to-QD-d-Fab resulted in a FRET-efficiency of 47 % with an estimated donor to acceptor distance of 11.2 nm. The results are summarized in **Table 4.4**. The similar FRET-efficiencies of

the IgG and F(ab) Tb-to-QD FRET systems indicate that the average donor-acceptor distances are similar for both systems. Intuitively, this is surprising because a F(ab) fragment is significantly smaller than an IgG. However, this finding confirms previous results [144] and could be related to the orientation of the antibodies on the QDs' surface and the flexibility of the antibodies. IgGs and F(ab) were conjugated via sulfhydryl groups to the surface of the QDs leading to less random orientation as compared to labeling via primary amino groups on lysine residues, hence allowing for similar orientation of IgG and F(ab) on the QD. From the distance-point-of-view, there is no reason to favor IgG *vs* F(ab) but using F(ab) bring more Tb per QD causing a higher FRET-sensitization, hence higher sensitivity. On the other hand, the average donor-acceptor distances of *ca.* 12 nm are very large when taking into account the size of QD705 (*ca.* 10x5 nm in TEM – **Figure 4.5**, and *ca.* 9 nm in diameter in DLS – **Figure 4.6**) and the direct surface labeling approach. Further investigations are necessary to explain this relatively long distance.

**Table 4.4.** FRET efficiencies and donor-acceptor distance calculated from the decay times of the acceptor sensitization.  $\langle \tau_D \rangle$  corresponds to the average lifetime of Tb in absence of QD and  $\langle \tau_{AD} \rangle$  is the average lifetime of QD in presence of Tb

FRET system	$\eta_{FRET}$ (acceptor channel)	D-A distance (acceptor channel)	$\langle \tau_D \rangle$	$\langle \tau_{AD} \rangle$
Tb-to-QD-d-IgG	34 %	12.3 nm	2.20 ms	1.45 ms
Tb-to-QD-d-F(ab)	38 %	11.9 nm	2.19 ms	1.36 ms

**Table 4.5** summarizes the Förster distances and LODs obtained for the Tb–QD605 and Tb–QD705 FRET pairs, as well as LOD values obtained for the same Tb-to-QD FRET immunoassays against PSA using the readily surface-coated (thick PEG/polymer coating) hydrophilic QD605 and QD705 from the same supplier (Life Technologies). Tb–QD assays with compact QDs provide LODs below the clinical cut-off value for PSA (4 ng/mL) [184], and these LODs are also 6.2 (Tb-QD605) and 25 (Tb-QD705) fold lower compared to the same assays using the larger commercial QDs. It should be noted that the FRET assays, performed on a clinical plate reader, use ratiometric time-gated PL detection, which is known to provide very low coefficients of variation [148]. The 6.2 and 25 fold improvements are therefore very significant, particularly when taking into account the very low and clinically relevant concentrations, and the results confirm the superior performance of our compact QD–AB conjugates for homogeneous FRET immunoassays using serum samples.

**Table 4.5.** Förster distances  $R_0$  and LODs of Tb-QD FRET immunoassays against PSA. Acceptor-AB with “Mal1” corresponds to indirect conjugation via Mal1 ligand. Acceptor-AB with “d” corresponds to direct conjugation on the QDs’ surface.

Donor-AB	Acceptor-AB	$R_0$ (nm)	LOD compact QDs (ng/mL)	LOD* Qdot ITK™ amino PEG (ng/mL)	Clinical cut-off level of PSA
Tb-IgG	QD605-Mal1-F(ab)	7.7	3.7	23	<b>4 ng/mL</b>
Tb-IgG	QD705-Mal1-F(ab)	11.0	0.8	2.0	
Tb-IgG	QD705-d-IgG	11.0	0.3	--	
Tb-IgG	QD705-d-F(ab') <sub>2</sub>	11.0	--	--	
Tb-IgG	QD705-d-F(ab)	11.0	0.08	2.0	

\* From Chapter 3. Same Tb-QD FRET immunoassays against PSA, which used same commercial QDs but with a thick PEG/polymer coating.

## 4.4 Conclusions

In this study we presented a technique for the preparation of compact, highly luminescent, and colloiddally stable QDs. These QDs were further used for the simple and functional conjugation with ABs via Mal1 ligand and directly on the surface of the compact QDs, yielding one of the smallest fluorescent AB-nanoparticle conjugates to be used for FRET reported to date. Aqueous phase transfer was achieved by ligand exchange with the zwitterionic penicillamine and post-functionalization with Mal1 bifunctional ligand containing reactive maleimide functions allowed conjugation with free sulfhydryl containing groups of ABs. Another post-functionalization strategy involved was the direct conjugation of ABs containing free sulfhydryl groups on the surface of the compact QDs. Although these bioconjugation strategies were demonstrated only with InPZnS/ZnSe/ZnS, CdSe/ZnS, and CdSeTe/ZnS core/shell QDs and F(ab) antibodies via Mal1 and direct attachment of ABs on CdSeTe/ZnS core/Shell QDs, they

should be applicable to any kind of nanoparticle containing surface atoms with binding affinity for thiolate ligands and biomolecules containing sulfhydryl groups (e.g., on available cysteines). The immediate applicability of the compact QD–AB conjugates to biosensing was demonstrated in homogeneous FRET immunoassays against PSA, using Tb–ABs as FRET donors and the QD–ABs as FRET acceptors, both coupled by an immunological sandwich complex between the two ABs and the PSA biomarker. Detection of PSA in 50  $\mu$ L serum samples with subnanomolar (2 pM = 0.08 ng/mL) detection limits showed the clinically relevant concentration range, over which these FRET immunoassays can be applied. Not only were the LODs of two Tb–QD FRET immunoassays (using 605 nm and 705 nm emitting QDs) well below the clinical cut-off value of PSA (4 ng/mL), the utilization of the compact QD–AB conjugates also provided a 6.2 and 25 fold sensitivity improvement compared to the same commercially available QDs that were purchased with a standard PEG/polymer-based coating. These highly sensitive and homogeneous Tb-to-QD FRET immunoassays are suitable for any other biomarker against which two specific ABs exist. Our results show that the compact QD–AB conjugates have a large potential for improving diagnostic applications, and given the multiplexing capability of Tb–QD FRET [145,150], we are confident that these small nanoparticle–AB fluorescent probes will become important players in clinical *in vitro* diagnostics.

## 5. Multiplexed detection of tumor markers

### 5.1 Introduction

Tumor markers which may also be called biomarkers are produced by tumors or by the body in response to cancers or of benign conditions [36]. In 2012 worldwide, the International Agency for Research on Cancer recorded 14.1 million new cancer cases with estimates for cancer deaths to be 8.2 million with a mortality rate of 22000 deaths per day. Cancer which is responsible of one in seven deaths worldwide totaling more deaths than AIDS, tuberculosis, and malaria combined, is believed to raise to 21.7 million new cancer cases and 13 million cancer deaths by 2030 simply because of our growing and ageing population. The three most diagnosed cancers for both genders in economically developed countries were prostate (among males); breast (among females), lung and colorectal while in economically developing countries they were lung, liver, and stomach in males and breast, cervix uteri and lung in females [185,186]. Thus, for cancer diagnosis, drug choice, and their early detection for patients long-term survival, such biomarkers represent ideal markers. Today there is a clear need for the simultaneous detection of different tumor markers from a single sample in order to provide clinicians with a more accurate and detailed picture of a disease state thus providing high quality care, and at the same time decreasing the time and cost of such diagnostics. Among existing multiplexing technologies such as quantitative reverse transcription-polymerase chain reaction (qRT-PCR) and enzyme-linked immunosorbent assay (ELISA), recent results have demonstrated the sensitive and multiplexed detection of different microRNAs using Tb-to-dye and Tb-to-QD FRET [145,152]. Despite the fact that qRT-PCR and ELISA are highly sensitive, they are time-consuming, limited concerning high-throughput (qRT-PCR) and require washing and separating steps (ELISA).

Up to now, LLC-to-dye FRET immunoassays have been demonstrated for the multiplexed detection of five different tumor markers in a single 50  $\mu$ L serum sample. The authors were faced to biological crosstalk between the antibodies and the tumor markers, and optical crosstalk due to the overlapping of the broad emission spectra of the dyes used. In order to decode the FRET signal corresponding to each FRET-pair, a complex mathematical matrix correction was required [11]. Here we attempt a multiplexed LLC-to-QD FRET immunoassay involving 3 color quantum dots with emission maxima at 605 nm (QD605), 650 nm (QD650) and 705 nm (QD705) for the detection of carcinoembryonic antigen (CEA), neuron-specific enolase (NSE) and PSA from a single serum based sample. CEA and NSE are among the tumor

markers, for which the levels are monitored in combination with other tumor markers to get a clear diagnosis of small-cell lung cancer (SCLC) and/or non-small-cell lung cancer (NSCLC) [187,188]. In addition to CEA and NSE, we propose to detect PSA which is a biomarker used for characterizing and risk-access of prostate cancer prior to therapy [173,184,189,190]. As results from **Chapter 3** suggested that for different clinical cut-off values QD705 should be used for the biomarker with the lowest cut-off and QD605 for the one with the highest cut-off, antibodies against CEA, NSE and PSA have been conjugated to QD650, QD605 and QD705 respectively. Among these antigens, NSE has the highest cut-off level (12.5 ng/mL) [191,192] followed by CEA (5.0 ng/mL) [190,192] and PSA (4.0 ng/mL) [173,184,190]. Monoclonal antibodies used for specific biological recognition to their antigens have been verified. QDs used have allowed fitting the narrow PL bands in between and beyond the well-separated Tb emission bands resulting in minimal optical crosstalk and requiring no matrix correction. Homogeneous FRET immunoassays using the QD conjugates have been performed in a time-gated mode achieving detection limits in 50  $\mu$ L volume samples in the subnanomolar concentration range of the differently sized antigens. All LODs were below their clinical cut-off levels, showing the capability of our system for the simultaneous detection of various tumor markers where their corresponding ABs exist.

## 5.2 Materials and Methods

### 5.2.1 Materials

Commercial eFluor quantum dots (discontinued) denoted as eQD605 and eQD650, emission maxima at 605 nm and 650 nm respectively, were kindly provided by the company Affymetrix/eBioscience as part of a sulfhydryl-reactive conjugation kit. Qdot<sup>®</sup> ITK<sup>™</sup> amino PEG 705, referred as iQD705, emission maxima at 750 nm, were purchased from Life Technologies/Thermo Fisher Scientific and possess amine-derivatized polyethylene glycol ligands covalently attached to the amphiphilic coating rendering them water soluble and compatible for the attachment of biomolecules. eQD605 and eQD650 possess maleimide functional groups on the surface which selectively bind to free sulfhydryl groups. The reactive amino groups of the ligand on the surface of the iQD705 allow for the attachment of biomolecules via N-hydroxysuccinimide (NHS) ester conjugation. The NHS-activated terbium complex Lumi4-Tb was kindly provided by Lumiphore in lyophilized form. Tumor markers/biomarkers/antigens carcinoembryonic antigen (CEA, 180kDa), neuron-specific

enolase (NSE, 95 kDa), prostate specific antigen (PSA, 32 kDa) and monoclonal primary antibodies against CEA (IgGs “GFR44” and “G15”), NSE (IgGs “E15” and “E20”), PSA (IgGs “PSR222” and “PSS233”) were provided by Cezanne/Thermo Fisher. IgGs were fragmented to  $F(ab)_2$  using a Pierce™ Mouse IgG  $F(ab)_2$  preparation kit and following the instructions provided by the supplier (Thermo Fisher Scientific). Bovine calf serum was provided by Cezanne/Thermo Fisher Scientific. Sulfo-EMCS (a water-soluble heterobifunctional amine-to-sulfhydryl cross-linker that contains NHS ester on one end and a maleimide reactive group on the other end) used to transform the amino-reactive QDs into maleimide-reactive QDs was purchased from Sigma-Aldrich. Bovine serum albumin (BSA), Tris(hydroxymethyl)aminomethane (TRIS/Cl), sodium tetraborate (borate), phosphate buffer saline (PBS) and Tris(2-carboxyethyl)phosphine (TCEP) were also purchased from Sigma-Aldrich.

## 5.2.2 Methods

### 5.2.2.1 Preparation of Tb-AB conjugates

Lumi4-Tb-NHS was dissolved to 8 mM in anhydrous DMF and reacted individually in molar excess to available primary amines of “GFR44”, “E15” and “PSR222” IgG antibodies by mixing the solutions in 100 mM carbonate buffer (pH 9). The mixtures were incubated for 2 h at room temperature while rotating at 30 rpm using an ELMI Intelli-Mixer. The IgG-Tb conjugates were purified and washed 4 times with 100 mM TRIS/Cl pH 7.4 using 50 kDa molecular weight cut-off (MWCO) spin columns from Millipore, to remove the unbound Tb-complex. The purified conjugate was stored at 4 °C.

Tb concentrations were determined by absorbance measurements at 340 nm using a molar absorptivity of 26 000  $M^{-1} cm^{-1}$  as provided by the manufacturer. Antibodies were quantified by absorbance measurements at 280 nm using a molar absorptivity of 210 000  $M^{-1} cm^{-1}$ . The labeling ratios were estimated by linear combination of the respective absorbance values of Tb and antibodies within the Tb-antibody conjugates.

### 5.2.2.2 Preparation of QD-AB conjugates

IgGs “G15”, “E20” and “PSS233” were fragmented to  $F(ab)_2$  using Pierce™ Mouse IgG  $F(ab)_2$  preparation kit following the instructions provided by the supplier. eQDs 605 and 650 provided in lyophilized form was reconstituted according to the conjugation kit protocol. The fragmented antibodies against CEA and NSE in 1× PBS buffer were mixed directly with eQD 650 and eQD605 respectively. Conjugation of  $F(ab)_2$  to iQD705 was performed using sulfo-EMCS where disulfide bonds (S-S) on the  $F(ab)_2$  against PSA were reduced to sulfhydryls (S-

H) using 45 min of incubation (rotating at 30 rpm) with 5 mM of TCEP in 1x PBS buffer (pH 7.4). Maleimide-activated iQD705 and reduced F(ab')<sub>2</sub>-PSS233 were purified 2 times with 1x PBS from excess sulfo-EMCS and TCEP using a 30 kDa MWCO spin column from Millipore at 1000 g and 4000g respectively. The resulting purified solutions were mixed and all QD conjugations were incubated for 6 h while rotating at 30 rpm in the dark at room temperature. The QD-conjugates were washed 4 times against unbound F(ab')<sub>2</sub> with 100 mM borate buffer (pH 8.4) at 1000g and the purified QD-conjugates were further centrifuged at 4000 g where supernatants were taken and stored at 4 °C.

QD-AB conjugates concentrations were calculated by absorbance measurements using molar absorptivities of  $2.5 \times 10^5 \text{ M}^{-1} \text{ cm}^{-1}$  (at 594 nm) for eQD605,  $1.1 \times 10^6 \text{ M}^{-1} \text{ cm}^{-1}$  (at 641 nm) for eQD650 and  $8.3 \times 10^6 \text{ M}^{-1} \text{ cm}^{-1}$  at (405 nm) for iQD705 [176,193]. F(ab')<sub>2</sub> concentrations were determined using a molar absorptivity of  $140\,000 \text{ M}^{-1} \text{ cm}^{-1}$  at 280 nm. The labeling ratios were estimated by linear combination of the respective absorbance values of QDs and ABs within the QD-AB conjugates.

### 5.2.2.3 Optical characterization

Absorption spectra were measured on a Lambda 35 UV/Vis spectrometer from PerkinElmer. PL spectra and decay curves were recorded on a FluoTime 300 lifetime fluorescence spectrometer from PicoQuant using as excitation sources a continuous-wave Xe lamp for spectra acquisition, a Xe flash lamp (100 Hz repetition rate) for Tb decay curves, and a 405 nm diode laser (Edinburgh Instruments) for QD decay curves. Tb-conjugates and QD-conjugates were measured in 100 mM TRIS/Cl buffer (pH 7.4) and 100 mM borate buffer (pH 8.4) respectively. PL decay curves were acquired directly from the FRET immunoassay samples on the modified “KRYPTOR compact plus” and the EI plate reader using as excitation source a 20 Hz nitrogen laser operating at 337.1 nm. Spectral separation in the detection channels was performed by optical bandpass filters, where the number after the center wavelength represents the guaranteed minimum bandwidth (GMBW) for Semrock filters and full-width-at-half-maximum (FWHM) for Delta filters: 494 / 20 nm (Semrock) for Tb, 607 / 8 nm (Delta) for eQD605, 660 / 13 nm (Semrock) for eQD650 and 707 / 16 nm (Semrock) for iQD705.

### 5.2.2.4 FRET immunoassays

All FRET assays were measured in black 96-well microtiter plates with an optimal working volume of 150  $\mu\text{L}$  after an incubation time of 180 min at 37°C. Tb-AB and QD-AB conjugates were each dissolved in 50  $\mu\text{L}$  of 10 mM TRIS/Cl buffer (pH 7.4) containing 0.5 % of BSA. To this 100  $\mu\text{L}$  solution of Tb-AB/QD-AB, 50  $\mu\text{L}$  of varying concentrations of CEA, NSE or PSA

(dissolved in serum) were added. All samples were prepared in triplicates except for the antigen-free samples, which were prepared 10 times and measured 3 times. Time-gated (100 – 900  $\mu$ s) and time-resolved PL intensity measurements were acquired on a modified “KRYPTOR compact plus” and EI plate reader respectively.

## 5.3 Results and discussion

### 5.3.1 Tb-AB and QD-AB conjugates characterization

#### Tb-AB characterization

Lumi4-Tb-NHS complexes were directly labeled to available primary amines of “GFR44”, “E15” and “PSR222” IgG ABs. Tb per IgG conjugation ratios of  $10 \pm 2$  (Tb-GFR44),  $13 \pm 3$  (Tb-E15) and  $10 \pm 2$  (Tb-PSR222) were determined by UV-Vis absorption spectroscopy using the molar absorptivities of Lumi4-Tb and IgGs as mentioned in the **Methods section 5.2.2.1** and Beer–Lambert's law (**Figure 5.1, left**). The results are summarized in **Table 5.1**. Upon excitation at 365 nm the PL spectrum of Tb–AB shows the characteristic Tb emission lines at 495 nm, 545 nm 585 nm and 625 nm which are more prominent than the emission lines ranging from *ca.* 650 nm to 700 nm. Due to the forbidden 4f-4f transitions, the obtained decay curves have an almost single exponential decay with an average PL lifetime of *ca.* 2.6 ms (**Figure 5.1, right**).

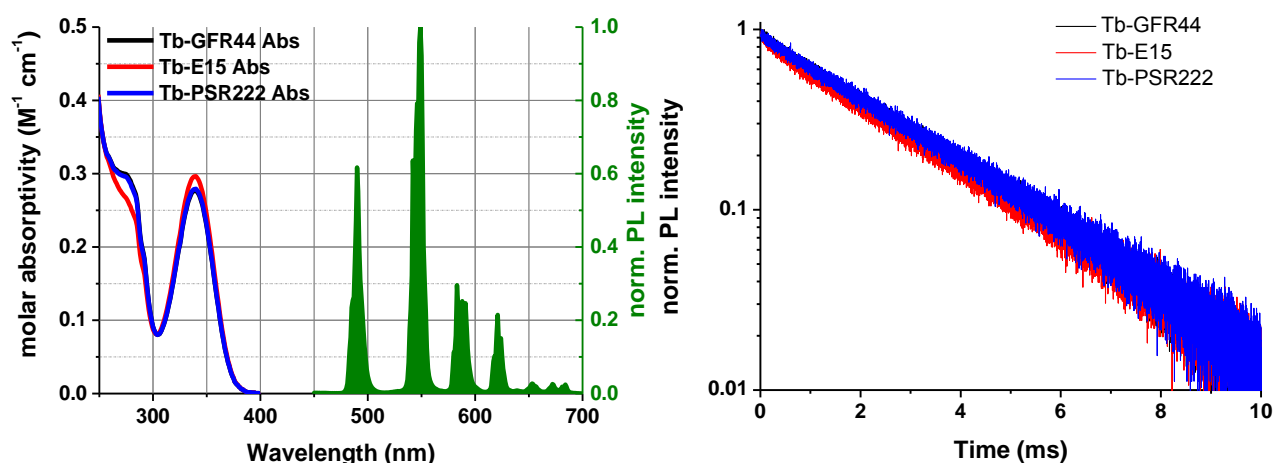


**Figure 5.1.** Left: absorption (black, red and blue lines) and PL (green, excitation wavelength 365 nm) spectra of Tb–AB conjugates. Right: Tb–AB conjugates normalized PL decay curves ( $490 \pm 0.5$  nm) upon pulsed excitation at 365 nm with a repetition rate of 100 Hz. Amplitude-averaged decay time *ca.*  $\tau(\text{Tb}) = 2.6$  ms.

## QD-AB characterization

As FRET is highly distance dependent, the choice of F(ab')<sub>2</sub> conjugation to QDs would result in a shorter separation distance between the QDs and Tb in sandwich immunoassays, hence higher FRET efficiencies and sensitivities than when using IgGs. Furthermore, the small size of the F(ab')<sub>2</sub> together with its 2 binding sites for more binding opportunity, would also be beneficial to the increasing biomarker sizes (32 kDa to 180 kDa) in the FRET immunoassays [25]. All QD-AB conjugations were performed through sulfhydryl chemistry. F(ab')<sub>2</sub> of “E20”, “G15” were conjugated to eQD605 and eQD650 respectively while F(ab')<sub>2</sub> of “PSS233” to iQD705. Fragmented ABs of “E20” and “G15” were not conjugated to iQD705 because of the relatively large size of their antigens and the thick polymer/PEG coating of the iQDs causing inefficient FRET for their detection. QD-AB conjugates concentrations were calculated by UV-Vis absorption spectroscopy using molar absorptivities of eQDs, iQD705 and F(ab')<sub>2</sub> mentioned in the **Methods section 5.2.2.2**. The calculated concentrations and labeling ratios are summarized in **Table 5.1**. Emission spectra and PL decay curves were measured upon excitation at 405 nm using a Xe-CW lamp and a 405 nm diode laser (Edinburgh Instruments) respectively and are shown in **Figure 5.2**.

The QDs emission spectra show narrow and Gaussian shape of the emission bands with a broader FWHM for iQD705 compared to the eQDs. Detection of the QD PL with a low PL background of Tb oriented our choice to QDs605/650/705 which allowed to fit the QDs PL spectra in between (for eQD605/650) or beyond (for iQD705) the Tb PL bands. The PL decays of all QDs are multi-exponential with amplitude averaged decay times of  $7.4 \pm 0.9$  ns for eQD605,  $17.4 \pm 2.5$  ns for eQD650, and  $63.5 \pm 10.8$  ns for iQD705. The spectral overlap integrals (**Equation (2.4)**) and the Förster distances (**Equation (2.3)**) were calculated using the QD molar absorptivity spectra and the normalized area Tb PL spectrum. Large  $R_0$  and spectral overlap resulted due to the high extinction coefficients and broad absorption range of QDs. As expected from the spectral overlaps in **Figure 5.3** the Tb-iQD705 FRET-pair provided the largest Förster distance ( $R_0 = 11.2 \pm 0.6$  nm), followed by the Tb-eQD650 FRET-pair ( $R_0 = 10.8 \pm 0.5$  nm), and the Tb-eQD605 FRET-pair ( $R_0 = 7.6 \pm 0.4$  nm).

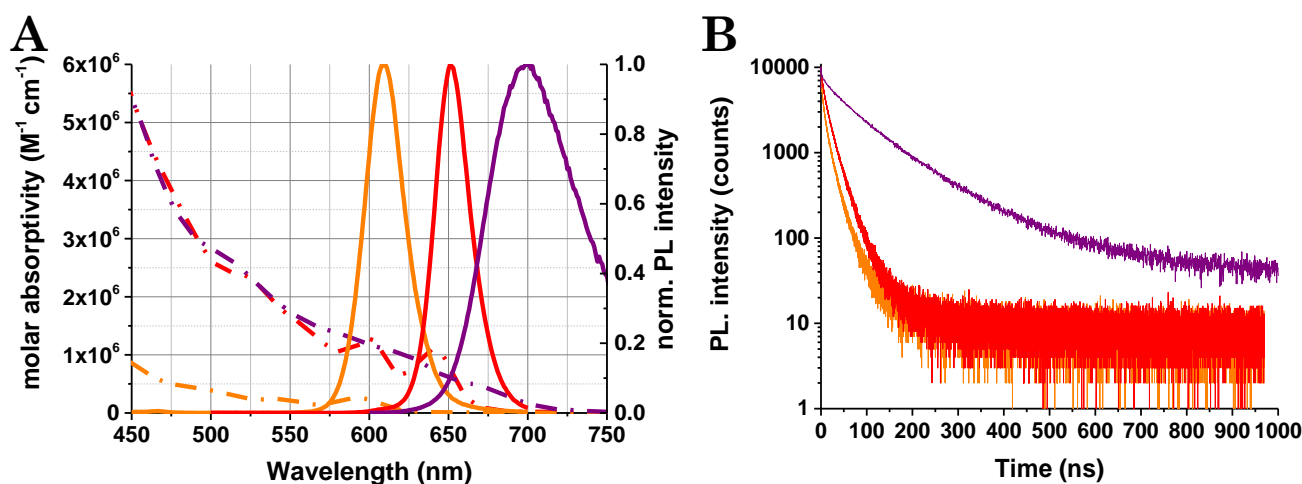


**Figure 5.2.** Optical characterizations of QD-AB conjugates. (A) Absorption (dash dotted lines) and PL (solid lines) of eQD605 (orange), eQD655 (red) and iQD705 (purple). (B) Pulsed (405 nm diode laser at 1 MHz for eQD605/650 and 0.5 MHz for iQD705) excitation was used to measure the PL decay curves at the respective PL peaks of the QDs. The multi-exponential decay curves (same colors as in (A)) gave amplitude-averaged decay times of  $\tau(\text{eQD605}) = 7.4 \pm 0.9$  ns,  $\tau(\text{eQD655}) = 17.4 \pm 2.5$  ns, and  $\tau(\text{QD705}) = 63.5 \pm 10.8$  ns.

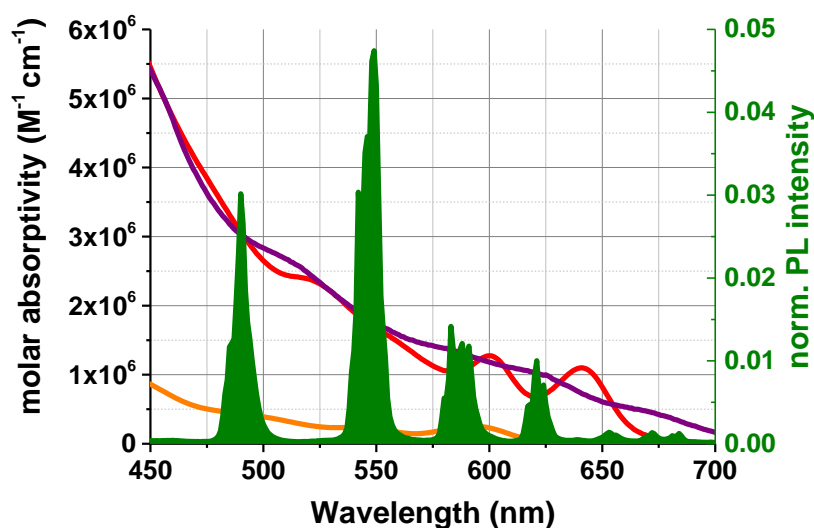


**Figure 5.3.** Overlap between QDs absorption spectra (eQD605: orange; eQD650: red; eQD705: purple) and area-normalized Tb emission spectra (olive green). Förster distances: Tb-eQD605 =  $7.6 \pm 0.4$  nm, Tb-eQD650 =  $10.8 \pm 0.5$  nm and Tb-iQD705 =  $11.2 \pm 0.6$  nm.

**Table 5.1.** Overview of the concentration of donor-AB and acceptor-AB conjugates with their respective labeling ratio.

Donor-AB	[Tb] ( $\mu\text{M}$ )	[AB] ( $\mu\text{M}$ )	Tb/AB	Acceptor-AB	[QD] (nM)	[AB] ( $\mu\text{M}$ )	AB/QD
Tb-GFR44	33.6	3.5	$9.7 \pm 2.0$	eQD650-F(ab') <sub>2</sub>	480	2.0	$4.2 \pm 2.0$
Tb-E15	43.8	3.5	$12.5 \pm 3.0$	eQD605-F(ab') <sub>2</sub>	200	0.7	$3.8 \pm 2.0$
Tb-PSR222	33.0	2.8	$9.9 \pm 2.0$	iQD705-F(ab') <sub>2</sub>	190	2.8	$14.9 \pm 7.0$

### 5.3.2 Single quantitative detection of tumor markers

The clinical cut-off level of CEA, NSE and PSA being 5 ng/mL, 12.5 ng/mL and 4 ng/mL respectively, our acceptor-AB conjugates were chosen as such, *i.e.* eQD605-G15; eQD650-E20; iQD705-PSS233, based on the results obtained in **Chapter 3** where we concluded that for different clinical cut-off values QD705 should be used for the biomarker with the lowest cut-off and QD605 for the one with the highest cut-off.

Within all FRET experiments the concentrations of the donor-AB and acceptor-AB were kept constant at 1.5 nM (for Tb-GFR44 and Tb-E15), 3 nM (for Tb-PSS233) and 1.5 nM (for all the QD-AB conjugates) while the antigens' concentrations were increased. 50  $\mu$ L of each donor-AB and acceptor-AB were mixed with 50  $\mu$ L of the antigen prepared in serum, totaling a working volume of 150  $\mu$ L. FRET immunoassays were measured on the "KRYPTOR compact plus" in a time-gated mode ranging from 100  $\mu$ s to 900  $\mu$ s and fitted with the appropriate bandpass filters for spectral separation in the Tb (494 / 10 nm) and QDs (607 / 8 nm for eQD605, 660 / 13 nm for eQD650 and 707 / 16 nm for iQD705) detection channels. As shown in **Figure 5.4**, the calibration curves correspond to the detection of the biomarkers using one FRET-pair and one biomarker at increasing concentrations. All three sensors exhibit significant FRET-ratio increase with increasing antigen concentration due to FRET sensitization of the QDs by Tb-donors. The dynamic range differs depending on the QDs used, ranging from 30 pM to *ca.* 3 nM for eQD605 and *ca.* 5 nM for eQD650, and 5 pM to *ca.* 6 nM for iQD705. One reason could be of the different labeling ratio of active AB per QDs. From **Figure 5.4**, we can observe the best sensitivity for the FRET sensor Tb-iQD705 where the FRET-ratio at maximum is *ca.* one order of magnitude higher than for the Tb-eQD605 FRET-pair. The PL decay curves (**Figure 5.5**) of the QDs and Tb measured on the EI plate reader show FRET sensitization of the QDs with increasing antigen concentration and a lower spectral crosstalk of Tb in the iQD705 detection channel. Stable Tb signals in the Tb detection channel reveal no obvious quenching due to FRET with increasing antigen concentration and are favorable for ratiometric measurements in multiplexing. Quenching of Tb signals in a mixture of Tb conjugates would make it difficult to perform ratiometric measurements as we would not be able to discriminate which FRET-pairs caused the quenching. The long decay component in the QDs detection channel comes from the optical crosstalk of Tb in these channels. Due to the biological recognition of the antibodies to its antigen, the close proximity of Tb and QD lead to a new decay time component (in the 10 to 100  $\mu$ s range) with increasing intensity generated by FRET.

To compare the sensitivity of the Tb-to-QD FRET pairs for the different antigens, LODs were calculated using the slope of the linear part (red data points for statistical analysis) of the

calibration curve (**Figure 5.4**), the standard deviation of 30 measurements of samples without any antigen and **Equation 2.3**. The LODs (summarized in **Table 5.2**) of the FRET immunoassays were all in the subnanomolar antigen concentration range and well below the clinical cut-off values of CEA, NSE and PSA.

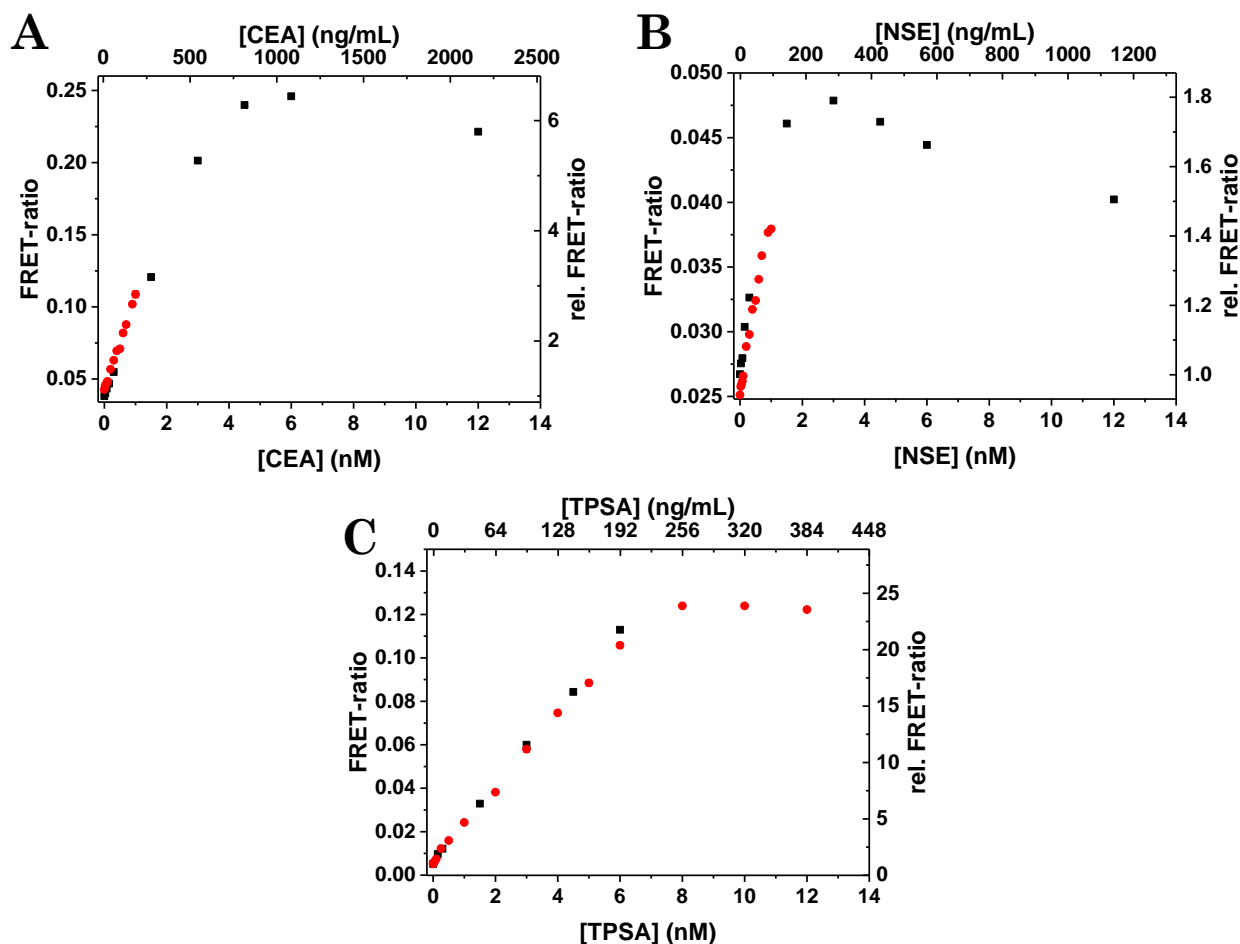


**Figure 5.4.** FRET-ratio and rel. FRET-ratio (normalized to unity at 0 nM antigen concentration) as a function of antigen concentration in a time-gated mode between 0.1 - 0.9 ms. The increase in FRET-ratio is caused by FRET until a saturation where no further FRET sensitization occurs. (A) Tb-eQD650 FRET-pair for the detection of CEA (B) Tb-eQD605 FRET-pair for the detection of NSE and (C) Tb-iQD705 FRET-pair for the detection of total PSA. Note: Only linear part of red data points were used for LOD for (C)

**Table 5.2.** Förster distance and LODs (in nM and ng/mL) for the single detection of the biomarkers CEA, NSE and PSA in homogeneous FRET immunoassays.

Donor-AB	Acceptor-AB	Antigen	$R_0$ (nm)	LOD (nM)	LOD (ng/mL)
Tb-GFR44	eQD650- F(ab') <sub>2</sub>	CEA	11	0.007	1.2
Tb-E15	eQD605- F(ab') <sub>2</sub>	NSE	8	0.016	1.5
Tb-PSR222	iQD705- F(ab') <sub>2</sub>	PSA	11	0.006	0.2

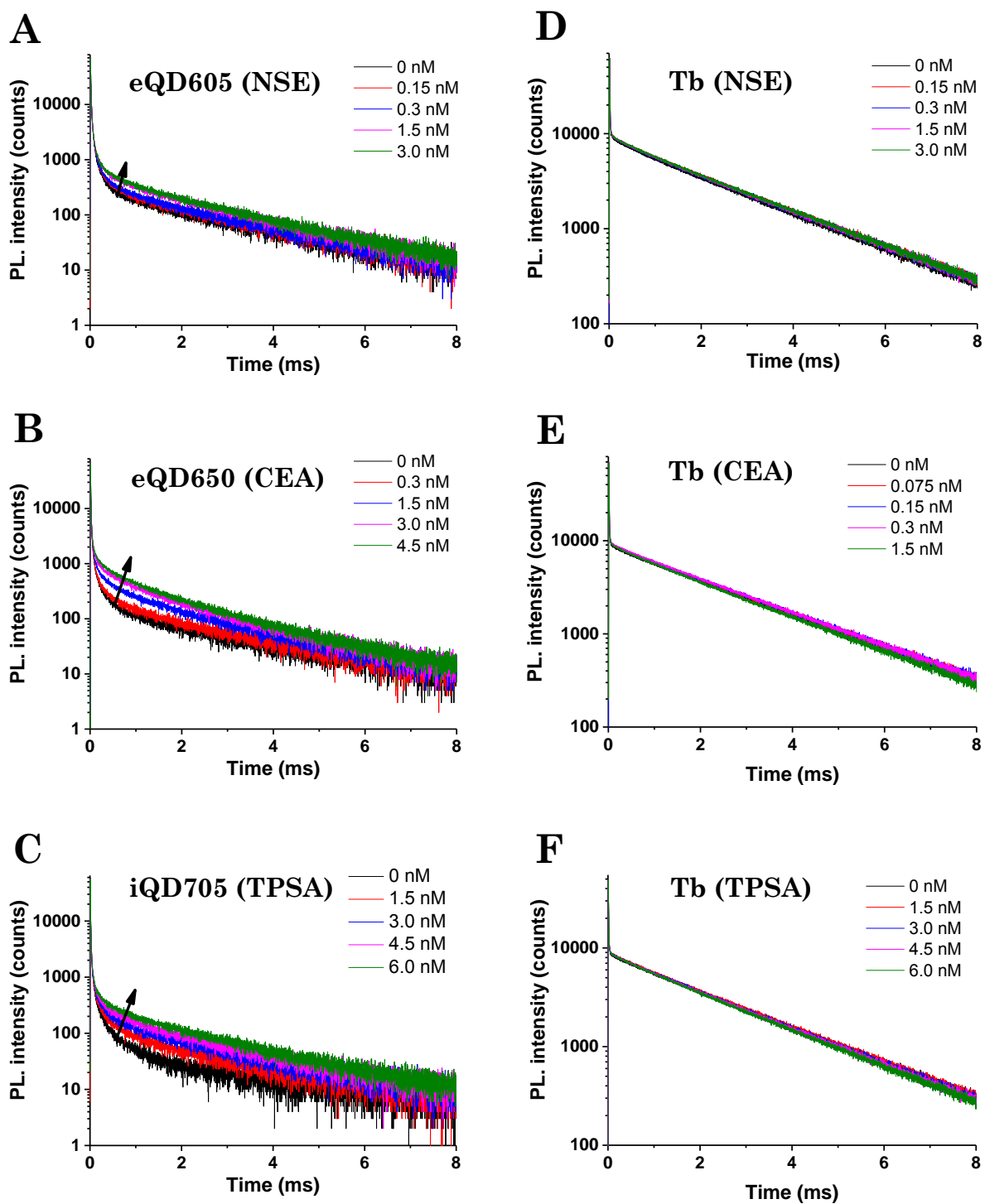


**Figure 5.5.** PL decay curves of the different QD channels and Tb of the singleplex FRET immunoassays showing sensitization of the QDs due to FRET with stable Tb intensities. PL decay curves of (A) eQD605 (607 / 8 nm filter) (B) eQD650 (660 / 13 nm filter) (C) iQD705 (707 / 16 nm filter) and (D-F) Tb (494 / 20 nm filter) with increasing concentration of NSE, CEA and TPSA respectively. Black curves represent the FRET-pairs containing no antigen in solution. (A-C) Short decay component (in the  $\mu\text{s}$  range) arise from the direct excitation of QDs and a long Tb component (in the ms range) from spectral crosstalk of Tb in the QDs detection channels. With increasing antigen concentration, a new FRET decay component in the tens to hundreds of  $\mu\text{s}$  range can be observed with increasing intensity as indicated by the black arrows. (D-F) Stable Tb signals show negligible quenching due to FRET which is favorable for ratiometric measurements when performing multiplexing.

### 5.3.3 Multiplexed quantitative detection of tumor markers

We challenged our singleplex FRET immunoassay which yielded LODs in the subnanomolar range, in an attempt to detect the three antigens from a single sample. The detection of multiple biomarkers from a single sample in FRET immunoassays requires careful testing for biological and optical crosstalk. These control measurements will give us an indication whether or not a spectral crosstalk correction has to be applied.

#### Biological crosstalk

Biological crosstalk may arise in our case when ABs for an intended antigen bind to another antigen, leading to a false response of the assay and an overestimation or underestimation of the concentrations. To investigate such possible crosstalk we designed immunoassays to test the specificity of CEA-AB FRET-pairs (in eQD650 detection channel), NSE-AB FRET-pairs (in eQD605 detection channel) and PSA-AB FRET-pairs (in iQD705 detection channel). As shown in **Figure 5.6**, the addition of CEA antigen with CEA-AB FRET-pairs resulted in a classical homogeneous FRET immunoassay with increasing FRET-ratio caused by the binding of CEA-ABs to CEA antigen, while the addition of NSE and PSA antigens caused no change in the FRET-ratio. The same results were obtained when using the other FRET-pairs to detect CEA and PSA. This proves that virtually no biological crosstalk exists between the ABs and the antigens if they were to be used in a multiplexed format. We could also expect these results since we are using monoclonal antibodies that were already optimized for FRET assays in commercial kits supplied by the company Cezanne/Thermo Fisher.

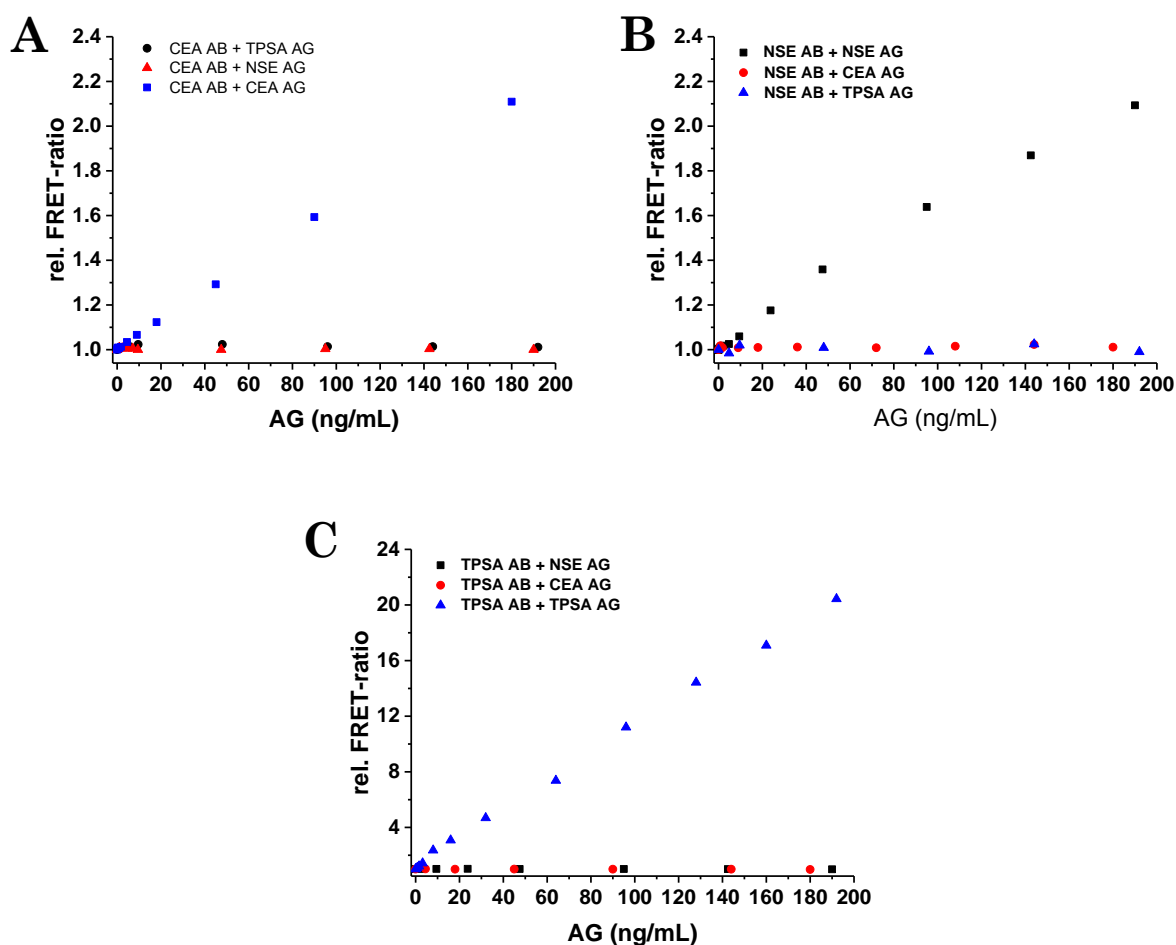


**Figure 5.6.** Biological crosstalk evaluation of different FRET-pairs for different antigens (AG). (A) CEA ABs used to detect CEA, NSE, and TPSA and measured in eQD650 detection channel. (B) NSE ABs used to detect CEA, NSE, and TPSA and measured in eQD605 detection channel. (C) TPSA ABs used to detect CEA, NSE, and TPSA and measured in iQD705 detection channel.

## Optical crosstalk

Optical crosstalk (or bleedthrough) is a phenomenon that can occur when the fluorescence of a fluorophore is detected in other detection channel because part of the photons goes through the “wrong optical” path, often caused by spectral overlap of 2 different fluorophores emission profiles and inefficient spectral separation. Here, we will test the optical crosstalk by inspecting the influence of: eQD605 in the eQD650 and iQD705 detection channel fitted with bandpass filters 660 / 13 nm and 707 / 16 nm; eQD650 in the eQD605 and iQD705 detection channel fitted with filters 607 / 8 nm and 707 / 16 nm; and iQD705 in the eQD605 and eQD650 detection channels fitted with filters 607 / 8 nm and 660 / 13 nm. We therefore devised immunoassays (**Figure 5.7**), in which all FRET sensors (CEA ABs, NSE ABs and PSA ABs) with one antigen (CEA, NSE or PSA) in increasing concentrations were present and detected in the QD detection channels. For example, to an increasing concentration of CEA antigen, CEA-

AB+NSE-AB+PSA-AB were added and the sensitized emission of the eQD650 was measured in eQD605, eQD650 and iQD705 detection channels. The same immunoassay was performed by changing the antigen from CEA to NSE and to PSA. In the eQD605 detection channel, we can observe a relatively low spectral crosstalk from eQD650 and no bleedthrough from iQD705. In the eQD650 detection channel we can observe a constant and low optical crosstalk from iQD705 and very low bleedthrough from eQD605. The iQD705 detection channel shows no crosstalk from eQD605 and negligible bleedthrough from eQD650. We can conclude from these findings that the low spectroscopic crosstalk arising from the choice of QDs with narrow and symmetrical wavelength spectra selected to fit in between and/or beyond the well separated Tb emission bands, requires no optical crosstalk or matrix correction for the determination of the antigens' concentration.

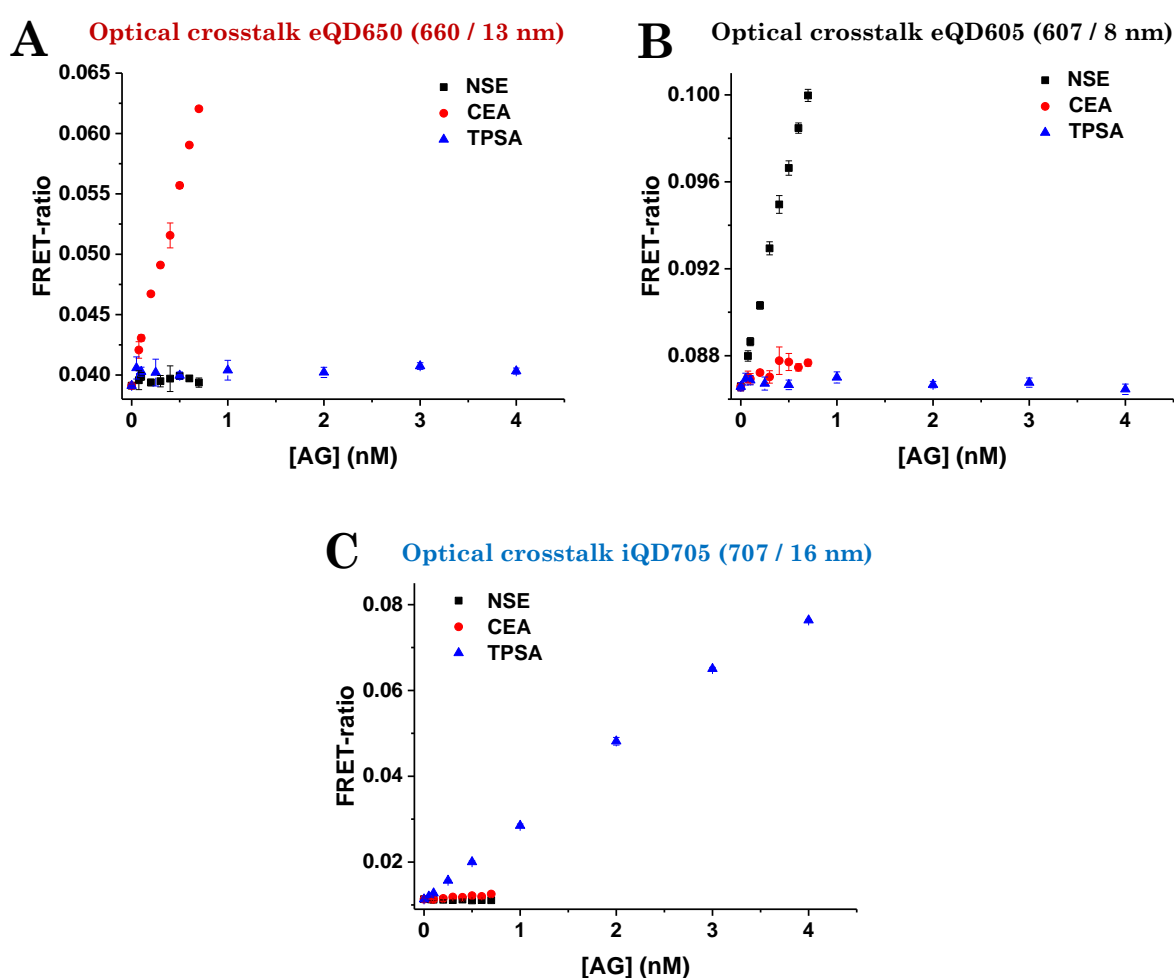


**Figure 5.7.** Spectral crosstalk: (A) eQD650 channel for detection of CEA with negligible bleedthrough from the other sensitized QDs (B) eQD605 channel for detection of NSE with low spectral crosstalk from the sensitized eQD650 and no bleedthrough from the sensitized iQD705 (C) iQD705 channel for detection of TPSA showing no crosstalk from sensitized eQD605 and negligible bleedthrough from sensitized eQD650.

## Multiplexing for the detection of CEA, NSE and PSA

From the calibration curves (**Figure 5.7** and reformatted **Figure 5.8**) we calculated the LODs in presence of all FRET-pairs and single antigen to compare with the singleplex immunoassays where only one FRET-pair and one antigen were present. The LODs (**Table 5.3**) determined when all FRET-pairs were present show an increase of LOD for CEA and NSE antigens from 1.2 ng/mL and 1.5 ng/mL in the singleplex format to 3.1 ng/mL and no deviation of LOD for PSA. One reason for these elevated LODs could be caused by the three times higher donor signal bleeding through the eQD605/650 channels conveying more noise in the measurements favoring a less steep slope as compared to the singleplex format. The iQD705 detection channel is spared from the influence of the Tb donor signal as there is negligible emission of Tb in the 700 nm wavelength range.

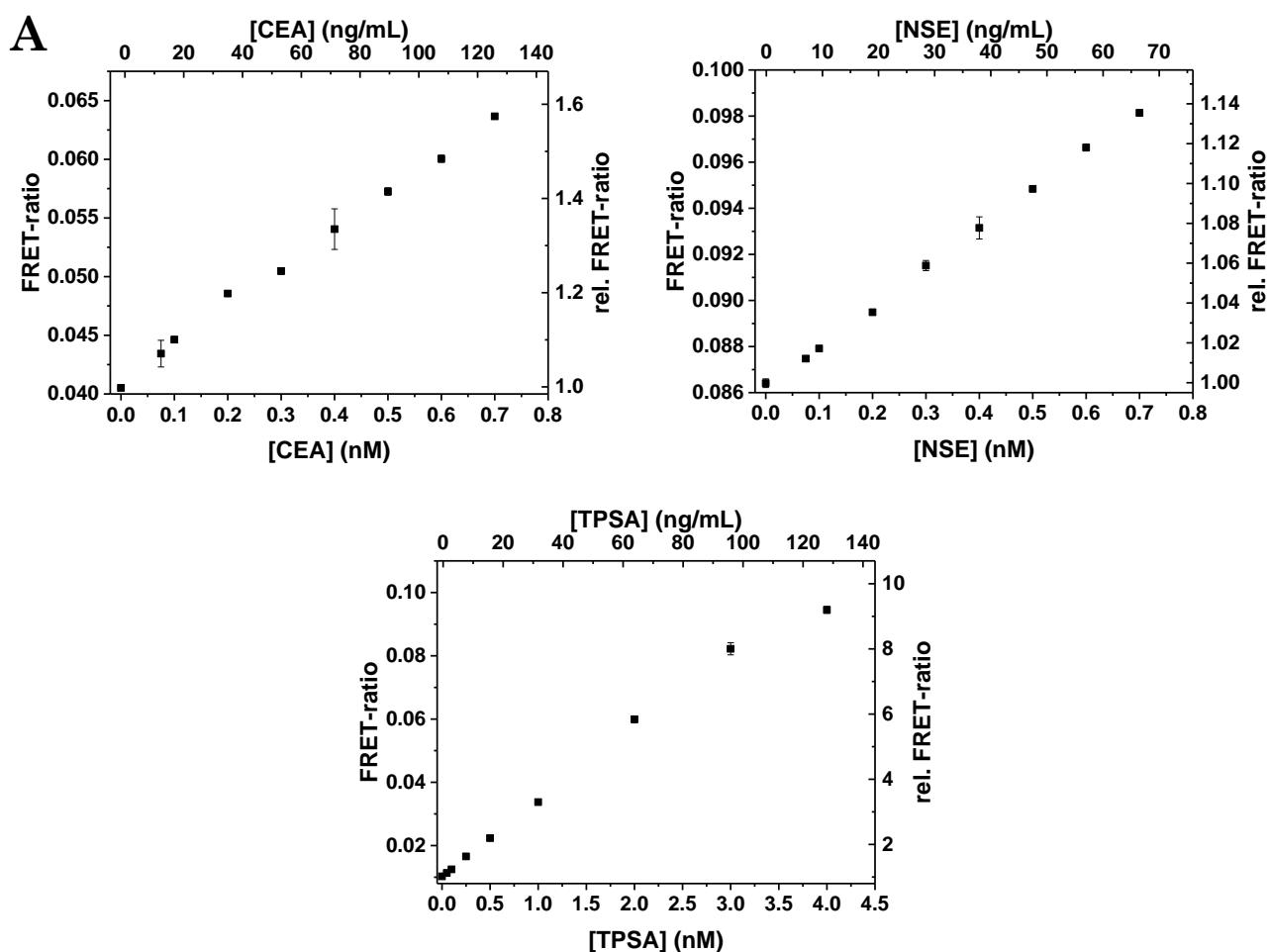


**Figure 5.8.** “Singleplex” FRET immunoassay calibration curves for (A) CEA; LOD: 3.1 ng/mL (B) NSE; LOD: 3.1 ng/mL (C) TPSA; LOD: 0.2 ng/mL, with all FRET-pairs and one antigen present in solution.

Following the control measurements, we proceed to the triplex detection of CEA, NSE and PSA from a single sample. For each measurement, 50  $\mu\text{L}$  of serum-based solutions containing increasing concentration of CEA, NSE and PSA were mixed to solutions of 100  $\mu\text{L}$  of the donor and acceptor ABs containing constant concentration of the probes, similar to the singleplex immunoassays. As it can be observed in **Figure 5.9**, the FRET-ratio increased as a result of the specific recognition of the ABs to their respective antigens, allowing close proximity of Tb and QDs, even though 6 different types of ABs were present in a single serum-based solution. In comparison to the “singleplex” format where all FRET-pairs and one antigen is present, the FRET-ratios for the triplex format is higher for the Tb-eQD605/650 FRET-pairs and a nearly perfect overlap of the calibration curves for the Tb-iQD705 FRET-pair. This intensity offset in the eQD605 and eQD650 calibration curves is caused by a lower Tb intensity when all the AGs are present (Tb intensity is quenched stronger than for singleplexed assay). The lower Tb intensity (in the denominator of the FRET-ratio) increases the FRET-ratio. This assumption was confirmed by comparing the delta ( $\Delta$ ) FRET-ratio curves ( $\Delta$  FRET-ratio reflects the specific signal, obtained by subtracting the background from the signal [194]) of the “singleplex” and triplexed format for which, we observed very similar slopes. The calculated LODs (**Table 5.3**) followed the steepness of the slopes with 3.6 ng/mL for CEA, 3.5 ng/mL for NSE and 0.3 ng/mL for PSA, which are all well below the clinical cut-off levels (5.0 ng/mL for CEA, 12.5 ng/mL for NSE and 4.0 ng/mL for TPSA) of the tumor markers.

The probability of measuring the same concentration of tumor markers in a single serum sample is usually low. We therefore performed a “worst-case scenario” assay where we challenged our immunoassay with a combination of high and low target concentrations. Seven different samples of the antigens at varying concentrations ranging from 0.2 nM to 2 nM were prepared and measured using the three FRET-ratio *vs* AG concentration curves of the triplexed immunoassay (**Figure 5.9 A-C**, black data points). For calculation of the prepared antigen concentrations from the calibration curves shown in **Figure 5.10**, calibration curves A and C were fit to a straight line and calibration curve B was fit to a quadratic function. Dashed lines in **Figure 5.11** represent known concentrations within the 7 samples containing the different antigens while the symbols with arrow bars are the estimated concentrations from the triplexing calibration curves of CEA, NSE and PSA. Overall, CEA, NSE and PSA could be detected with high precision with minor deviations from known concentrations. The concentration of the samples could be directly estimated from the calibration curves without the need of a matrix correction making our triplexing immunoassay easy and simple to produce.

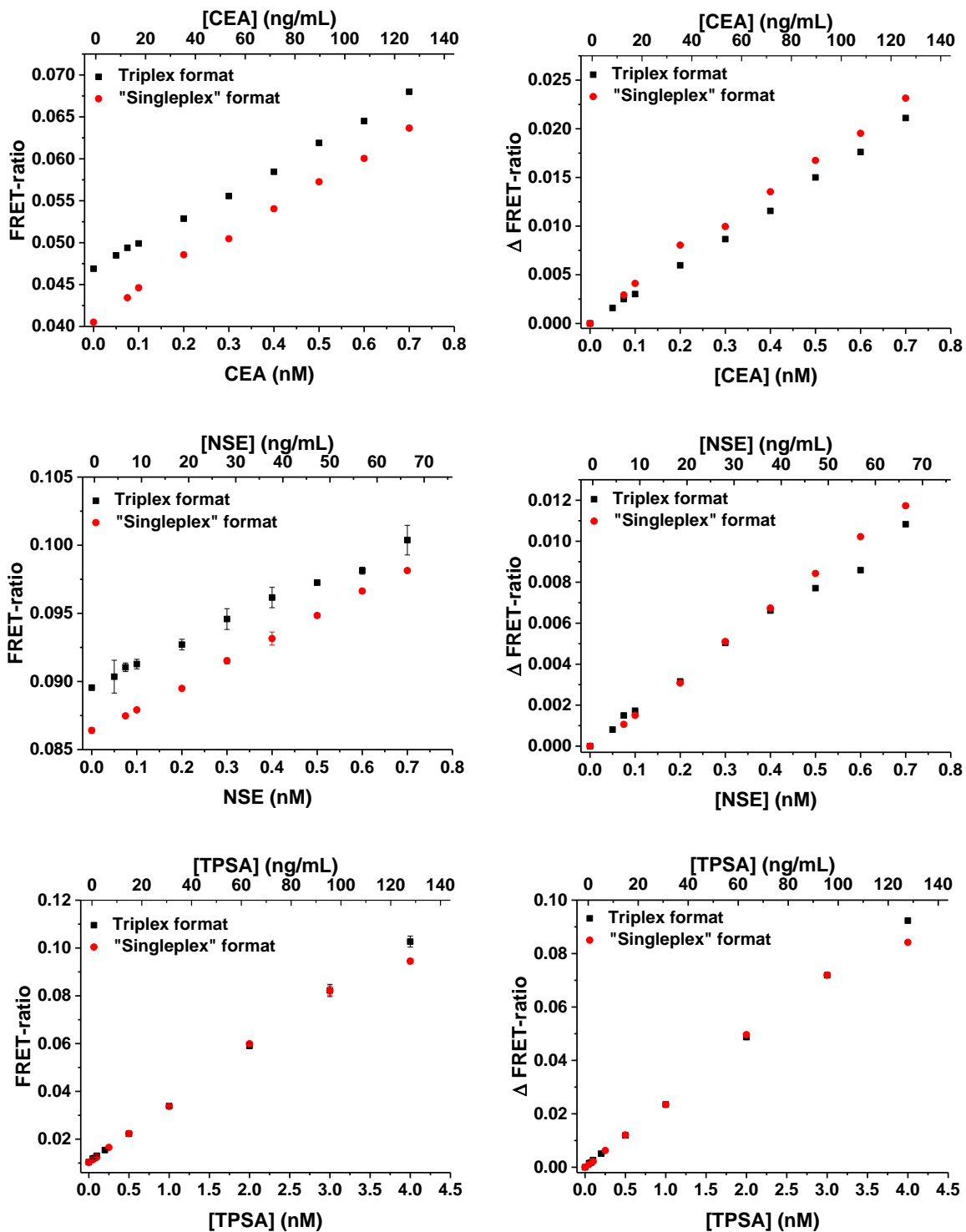


**Figure 5.9.** FRET-ratio and  $\Delta$  FRET-ratio curves for the “singleplex” format (all FRET-pairs with only one antigen) and triplexed format in function of their respective antigen concentrations. Red and black data points represent “singleplex” and triplexing FRET immunoassays respectively. We can observe an unusual high FRET-ratio between the 2 immunoassays (A-C). By plotting the specific signal in function of the antigens’ concentration, we find a less steep slope from the triplexing in comparison to the “singleplex” format (D-E). Negligible deviation of the sensitivity for TPSA (F).

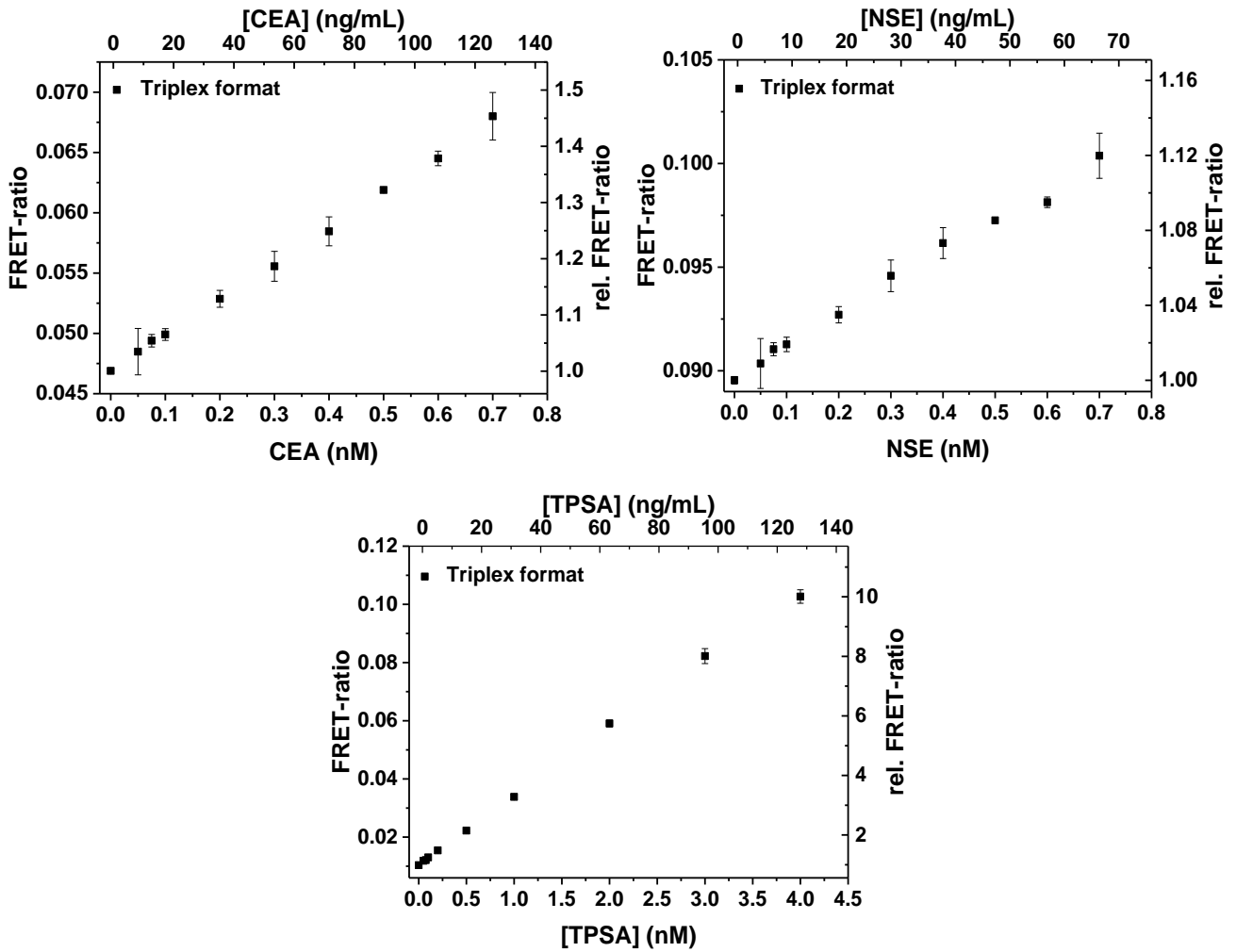


**Figure 5.10.** Triplexed FRET immunoassay calibration curves for (A) CEA; LOD: 3.6 ng/mL (B) NSE; LOD: 3.5 ng/mL and (C) TPSA; LOD: 0.3 ng/mL. Calibration curves (A) and (C) were fit to a straight line and calibration curve (B) was fit to a quadratic function, for the estimation of the calculated concentrations.

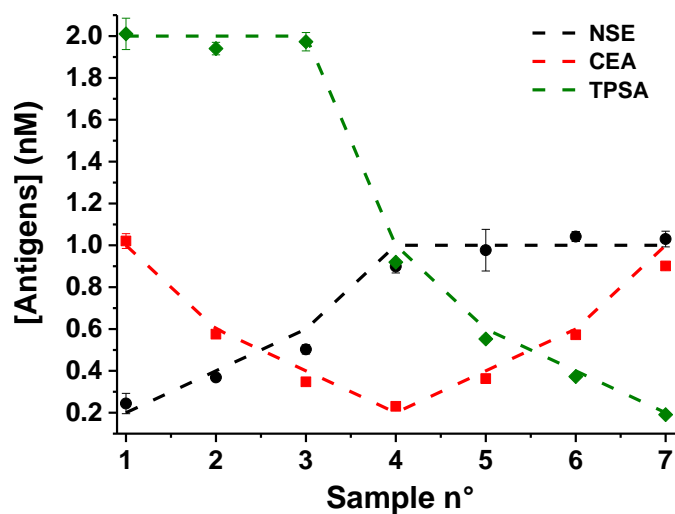


**Figure 5.11.** Triplexed "worst-case scenario" assay with a combination of high and low concentrations of antigens ranging from 0.2 nM to 2 nM. Dash lines and data points with error bars are color coded. Dash lines represent known prepared concentrations. Data points were estimated from triplexing calibration curves and error bars resulted from triplicate measurements.

**Table 5.3.** LODs overview of singleplex, “singleplex” and triplex format of the FRET immunoassays. All the LODs are below the clinical cut-off levels – 5.0 ng/mL for CEA, 12.5 ng/mL for NSE and 4.0 ng/mL for TPSA.

Donor-AB	Acceptor-AB	Antigen	LOD (nM)	LOD (ng/mL)
<b><u>Singleplex format</u></b>				
Tb-GFR44	eQD650-F(ab') <sub>2</sub>	CEA	0.007	1.2
Tb-E15	eQD605-F(ab') <sub>2</sub>	NSE	0.016	1.5
Tb-PSR222	iQD705-F(ab') <sub>2</sub>	TPSA	0.006	0.2
<b><u>“Singleplex” format – all FRET-pairs / 1 antigen only</u></b>				
Tb-GFR44	eQD650-F(ab') <sub>2</sub>	CEA	0.017	3.1
Tb-E15	eQD605-F(ab') <sub>2</sub>	NSE	0.033	3.1
Tb-PSR222	iQD705-F(ab') <sub>2</sub>	TPSA	0.006	0.2
<b><u>Triplex format</u></b>				
Tb-GFR44	eQD650-F(ab') <sub>2</sub>	CEA	0.020	3.6
Tb-E15	eQD605-F(ab') <sub>2</sub>	NSE	0.035	3.5
Tb-PSR222	iQD705-F(ab') <sub>2</sub>	TPSA	0.009	0.3

## 5.4 Conclusions

Our multiplexed homogeneous FRET immunoassay necessitating no washing or purification steps has been able to simultaneously detect 3 differently sized tumor markers from a single serum sample of CEA (180 kDa), NSE (95 kDa) and PSA (32 kDa) using Tb and QD probes conjugated to their respective monoclonal antibodies conferring no biological crosstalk. Taking advantage of the narrow and Gaussian emission spectra of the QDs and the well separated Tb emission bands together with the appropriate optical bandpass filters, allowed for negligible optical crosstalk. Therefore, no matrix correction was necessary to determine the tumor marker concentrations. Monoclonal antibodies used were able to detect specifically their respective targets bringing their FRET-pairs in close proximity and the excitation of Tb at 337 nm allowed the sensitization of multiple QDs at the same time due to FRET. After a delay of several  $\mu$ s, a time-gated window between 0.1 – 0.9 ms was applied to the measurements in order to eliminate background signals coming from the autofluorescence of the biological samples and the direct excitation of the QDs. LODs calculated in 50  $\mu$ L volume samples were all below the clinical cut-off levels of the tumor markers, where higher LODs we observed for the triplexed format as compared to the singleplex format except for PSA. The contamination of the eQD605/650 detection channels from the 3 times more Tb signal resulted in an increase in LOD

whereas virtually no Tb emission can be detected in the iQD705 detection channel. Detection limits of the tumor markers in the subnanomolar range (few ng/mL) within a complex environment as in serum and containing 9 different biomolecules demonstrated the immediate applicability to diagnostic applications for sensitive multiplexed measurements.

## 6. Upconverting nanoparticles for bio-sensing

### 6.1 Introduction

Upconversion is a process where low energy light (near-infrared (NIR) or infrared (IR)) is converted to higher energies (UV to NIR) by means of stepwise absorption and energy transfer processes. Similar to lanthanide complexes, lanthanide-doped upconversion nanoparticles (UCNPs) possess very narrow emission bands in the broad wavelength region spanning the UV, visible and NIR allowing them to function as energy donors with an assortment of acceptors in FRET-based biosensing [16–19]. The large anti-Stokes shift, long luminescence lifetime, extreme photostability and NIR excitation of UCNPs results in the efficient reduction of background fluorescence arising from cells and biomolecules normally occurring at higher energy excitation. Another advantage in addition to less autofluorescence is lower phototoxicity compared to UV or blue light used for the excitation of most common dyes [95,111,195].

In this work we performed a detailed structural and optical characterization of three types of PEGylated erbium and ytterbium doped NaGdF<sub>4</sub> UCNPs, namely NaGdF<sub>4</sub>:Er<sup>3+</sup>,Yb<sup>3+</sup> core only (core-doped) as well as core-shell nanostructures composed of either a NaGdF<sub>4</sub>:Er<sup>3+</sup>,Yb<sup>3+</sup> core and an undoped NaGdF<sub>4</sub> shell (core-doped/shell, NaGdF<sub>4</sub>:Er<sup>3+</sup>,Yb<sup>3+</sup>/NaGdF<sub>4</sub>) or an undoped NaGdF<sub>4</sub> core and a Er<sup>3+</sup>/Yb<sup>3+</sup> doped NaGdF<sub>4</sub> shell (core/shell-doped, NaGdF<sub>4</sub>/NaGdF<sub>4</sub>:Er<sup>3+</sup>,Yb<sup>3+</sup>). All UCNPs were synthesized via a thermal decomposition of trifluoroacetate precursors in 1-octadecene and oleic acid by our collaborators from Institut National de la Recherche Scientifique (INRS – Centre Energie Matériaux Télécommunication), Varennes (QC), Canada [73,97,107]. The characterization of morphological and photophysical properties, and in particular their photoluminescence (PL) decays are a prerequisite for selecting suitable FRET donor candidates [161]. The three types of PEGylated UCNPs were characterized by transmission electron microscopy (TEM), powder X-ray diffraction (XRD) and time-resolved spectroscopy to gain information on the PL decay times of the UCNPs. TEM images reveal rather spherical UCNPs of sizes ranging from *ca.* 11 nm to 23 nm while XRD patterns show a hexagonal ( $\beta$ -) phase of NaGdF<sub>4</sub>. PL decay analysis at the green (540 nm) and red (660 nm) upconversion emission of the Er<sup>3+</sup> ions was performed on a fluorescence plate reader with a 980 nm diode laser excitation. Intensity averaged decay times ranged from *ca.* 84 – 160  $\mu$ s at 540 nm and *ca.* 180 – 360  $\mu$ s at 660 nm. The longest lifetimes were observed for the core/shell-doped UCNPs. Combination of Er<sup>3+</sup> donor ions close to the UCNP surface and the long decay times suggest that these UCNPs may be highly interesting FRET donors with suitable FRET

acceptors for bio-sensing. As a proof-of-principle, we attempt a homogeneous UCNPs-to-dye FRET assay, which was based on the hybridization between oligonucleotides conjugated on the UCNPs and the complementary organic dye Cy3.5 labelled oligonucleotides.

## 6.2 Materials and Methods

### 6.2.1 Materials

Starting materials such as lanthanide oxides ( $Gd_2O_3$ , REacton®, 99.999 %, < 10 Micron Powder;  $Yb_2O_3$ , REacton®, 99.998 %, Powder;  $Er_2O_3$ , REacton®, 99.99 %, Powder, Alfa Aesar, Ward Hill, USA), sodium trifluoroacetate ( $CF_3COONa$ , 98 %, Sigma Aldrich, St. Louis, USA), trifluoroacetic acid ( $CF_3COOH$ , 99 %, Alfa Aesar, Ward Hill, USA), 1-octadecene ( $CH_3(CH_2)_{15}CH=CH_2$ , tech. 90 %, Alfa Aesar, Ward Hill, USA), oleic acid ( $CH_3(CH_2)_7CH=CH(CH_2)_7COOH$ , tech. 90 %, Alfa Aesar, Ward Hill, USA),  $N_2H$ -PEG-COOH ( $\alpha$ -amino  $\omega$ -carboxy terminated poly(ethylene,  $N_2H-CH_2CH_2O-[CH_2CH_2O]_n-CH_2CH_2COOH$ ,  $M_n = 700$ , Polymer Source Inc., Montreal, Canada), and hydrochloric acid (HCl, Reagent A.C.S., Fisher Scientific, Nepean, Canada) were used without further purification. Tris(hydroxymethyl)-aminomethane, bovine serum albumin, and HEPES were purchased from Sigma-Aldrich. Oligonucleotides were purchased HPLC purified from Eurogentec. The synthesis of the UCNPs was carried out in a well-ventilated fume hood as described previously in the references [107,196].

### 6.2.2 Methods

#### 6.2.2.1 Instruments

Analysis of size and shape was measured by TEM with a Philips CM200 high-resolution transmission electron microscope (HRTEM). XRD pattern for crystallinity and phase determination was performed on a Bruker D8 Advanced Diffractometer (Cu K $\alpha$  radiation). For FTIR spectroscopy, aqueous solutions of UCNPs were dropped on Real Crystal® NaCl IR cards (9.5 mm aperture, International Crystal Laboratories) and spectra were recorded after drying by use of a Nicolet 6700 FTIR spectrometer from Thermo Electron Corporation. The hydrodynamic diameter of the PEGylated UCNPs was measured by dynamic light scattering (DLS) on a Malvern Zetasizer NanoZS. Multiple runs (>3) were performed and the hydrodynamic diameters were averaged. The data were collected in automatic mode and expressed in number %. For upconversion emission measurements, dispersions of the nanoparticles were transferred into glass cuvettes and placed into a temperature-controlled cuvette holder (qpod 2e by Quantum Northwest, Washington, USA) allowing for wireless

temperature control through USB using the Q-Blue software (Quantum Northwest). Spectra were recorded under 980 nm excitation using a Thorlabs fibre-coupled laser diode (maximum power 330 mW). The laser was focused on the sample using a lens to obtain a spot with a Gaussian intensity distribution with a 0.4 mm diameter. The emitted light was collected by a lens in a 90° configuration, and then transferred to a spectrophotometer (Avaspec - 2048L - USB2) by use of an optical fibre. Decay curves were measured at the green and red upconversion emissions using bandpass filters 542 / 20 nm and 660 /13 nm (Semrock) on a prototype fluorescence plate reader (developed during a joint project) from Edinburgh Instruments (EI) equipped with a 2W 980 nm laser from Changchun New Industries (CNI) and a PM-1 laser modulator box from (EI) for controlling the pulsing parameters of the CNI laser.

### 6.2.2.2 Preparation of lanthanide trifluoroacetate precursors

For the synthesis of Er<sup>3+</sup>/Yb<sup>3+</sup> doped NaGdF<sub>4</sub>, lanthanide trifluoroacetate precursors were prepared in a 50 mL three-neck round-bottom flask (reaction vessel) by mixing 0.975 mmol of Gd<sub>2</sub>O<sub>3</sub> (353.4 mg), 0.25 mmol of Yb<sub>2</sub>O<sub>3</sub> (98.5 mg, corresponding to 20 mol % doping rate) and 0.025 mmol of Er<sub>2</sub>O<sub>3</sub> (9.6 mg, corresponding to 2 mol % doping rate), to 5 mL of distilled water and 5 mL of trifluoroacetic acid. The mixture was refluxed under magnetic stirring at 80°C until a clear solution was obtained. To slowly evaporate residual water and trifluoroacetic acid, the temperature was lowered to 60°C and the precursor was obtained as a white solid. For the synthesis of undoped NaGdF<sub>4</sub>, the amount of Gd<sub>2</sub>O<sub>3</sub> used was 453.22 mg and the same synthesis protocol was followed with no erbium or ytterbium oxide added. The chemical reaction taking place during the synthesis of the precursors are shown in **Figure 6.1**.

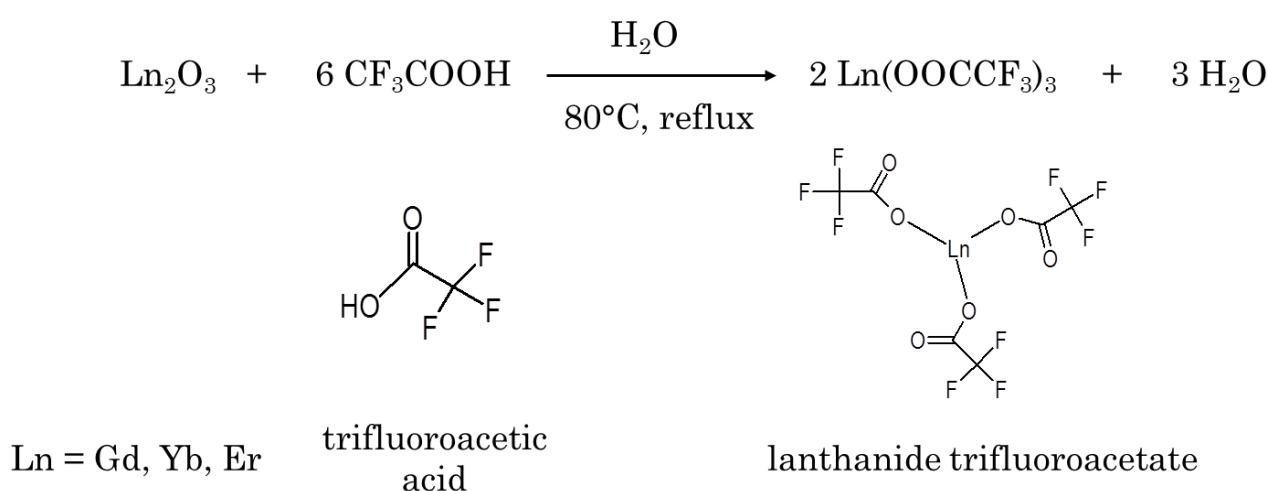


**Figure 6.1.** Chemical reaction taking place during synthesis of the precursors.

### 6.2.2.3 Synthesis of NaGdF<sub>4</sub>:Er<sup>3+</sup>,Yb<sup>3+</sup> nanoparticles (core-doped)

For the preparation of core (NaGdF<sub>4</sub>) doped UCNPs with 2 mol % Er<sup>3+</sup> and 20 mol % Yb<sup>3+</sup>, 12.5 mL of each the high boiling solvent 1-octadecene and of the coordinating oleic acid were mixed in a 100 mL three-neck round-bottom flask and degassed for 30 mins at 150°C under vacuum and magnetic stirring. Meanwhile, 2.5 mmol of sodium trifluoroacetate (340 mg) together with 7.5 mL of each 1-octadecene and oleic acid were added to the as-prepared precursor. The mixture was degassed at 125°C under vacuum and magnetic stirring. Next, the reaction vessel containing the degassed 1-octadecene and oleic acid was heated to 315°C under gentle argon flow. The hot precursor solution was then added dropwise to the reaction vessel using a syringe and pump system (Harvard Apparatus, Pump 11 Elite) at an injection rate of 1.5 mL/min. Following injection, the solution was maintained at 315°C and stirred for a further 60 mins under argon flow before allowing to cool to room temperature. The obtained nanoparticles were precipitated by addition of ethanol and recovered by centrifugation at 5500 rpm for 10 mins. The recovered white powder was washed twice with a mixture of hexane and ethanol (1:4 v/v) followed by centrifugation. The resultant oleate-capped core-doped nanoparticles were finally redispersed in hexane for storage.

### 6.2.2.4 Synthesis of NaGdF<sub>4</sub>:Er<sup>3+</sup>,Yb<sup>3+</sup>/ NaGdF<sub>4</sub> nanoparticles (core-doped/shell)

The synthesis of core-doped/shell UCNPs followed the same protocol as described for core-doped UCNPs with one additional injection step in order to grow the shell around the core-doped UCNP.

For the synthesis of doped-core/undoped shell UCNPs, in first step, the doped core was synthesized as described for the core-only UCNPs. Subsequently, instead of cooling the reaction mixture to room temperature after 60 min of reaction time, the shell precursor solution containing the previously synthesized lanthanide trifluoroacetates, 2.5 mmol of sodium trifluoroacetate (340 mg), and 4 mL each of 1-octadecene and oleic acid (degassed at 125°C for 30 min under vacuum and magnetic stirring) was added dropwise to the reaction vessel containing the core-doped (NaGdF<sub>4</sub>:Er<sup>3+</sup>,Yb<sup>3+</sup>) nanoparticles (injection rate of 1.5 mL/min). Following injection, the solution was maintained at 315°C and stirred for a further 60 mins under argon flow. The solution was then allowed to cool to room temperature and the obtained UCNPs were precipitation by addition of ethanol and recovered by centrifugation at 5500 rpm for 10 mins. The white powder obtained was washed 2 times with a mixture of hexane and ethanol (1:4 v/v) followed by centrifugation. The resultant oleate-capped core-doped/shell nanoparticles were finally redispersed in hexane for storage.



#### **6.2.2.6 Preparation of water-dispersible ligand-free UCNPs**

Oleate-capped UCNPs are hydrophobic in nature, and are therefore not dispersible in aqueous solvents, which is a requirement for biomedical applications. Water dispersibility is also essential for further surface modification (such as with PEG in this study) for subsequent biological functionalization. In order to obtain water-dispersible ligand-free UCNPs, typically 60 mg of the prepared oleate-capped UCNPs were dispersed in 5 mL of hexane and added to an aqueous solution of HCl which was adjusted to a *ca.* pH 4. The mixture was stirred at room temperature for 3 hours followed by separation of the aqueous phase containing the nanoparticles from the organic phase by use of a separation funnel. The UCNPs were collected by centrifugation at 5500 rpm for 15 mins after precipitation with acetone. The obtained particles were stirred for a further 2 hours in a 5 mL HCl aqueous solution maintaining the pH at 4. After the reaction, protonating of the carboxylate groups of the oleate ligand was completed and the ligand-free nanoparticles were recovered by centrifugation at 5500 rpm for 15 mins after precipitation with acetone. The precipitate was finally redispersed in distilled water.

#### **6.2.2.7 Surface modification by PEGylation**

Surface modification of the UCNPs with amino-PEG-COOH for biomolecule coupling was performed through electrostatic interaction between the negatively charged COO<sup>-</sup> of the polymer and the positively charged Ln<sup>3+</sup> on the surface of the UCNPs. An aqueous solution of amino-PEG-COOH was added to an aqueous dispersion of ligand-free UCNPs followed by stirring at room temperature overnight. The estimated concentrations that have been applied to prepare the PEGylated UCNPs were 50 mg/mL of a stock solution of PEG, 76 mg/mL of core-doped, 84 mg/mL of core-doped/shell and 60 mg/mL of core/shell-doped ligand-free UCNPs. The PEG-modified UCNPs were precipitated with acetone and collected by centrifugation at 7000 rpm for 25 mins. In order to remove excess PEG, the UCNPs were redispersed in water and precipitated with acetone before collection by centrifugation. The PEGylated UCNPs were finally redispersed in water with a final estimated maximum concentration of 50 mg/mL.

#### **6.2.2.8 UCNPs DNA conjugate**

As a proof-of-principle FRET immunoassay, only the core-doped UCNPs have been conjugated to thiolated-oligonucleotides (23 base pairs with thiol on the 3' position), due to the presence of Er<sup>3+</sup> ions close to the surface of the UCNPs. Conjugation of the oligonucleotides containing a thiol functional group to amino-PEGylated core-doped UCNPs was performed using sulfo-EMCS crosslinkers. A several-fold molar excess of sulfo-EMCS was added and mixed to an

aqueous solution (pH 7) of the UCNPs at 30 rpm for 1 hour in the dark using an Intelli-Mixer. Disulfide bonds (S-S) on the oligonucleotides were reduced to sulfhydryls (S-H) using 30 min of incubation (rotating at 30 rpm) with 5 mM of Tris(2-carboxyethyl)phosphine (TCEP) in 50 mM sodium phosphate, 150 mM NaCl buffer (pH 6.5). Maleimide-activated UCNPs were purified 2 times with pure water from excess sulfo-EMCS using a 100 kDa MWCO spin column from Millipore at 1000 g for 6 mins. SH-oligonucleotides were purified 2 times with 50 mM sodium phosphate, 150 mM NaCl (pH7.4) from excess TCEP using Zeba 7K desalting columns according to the manufacturer's protocol. The obtained purified maleimide-UCNPs and thiol-oligonucleotides were then mixed and incubated for 6 hours while rotating at 30 rpm. The core-doped UCNPs DNA conjugate was finally washed against excess unbound oligonucleotides 4 times with pure water using a 100 kDa MWCO spin column from Millipore at 1000g. The purified UCNPs conjugate was finally stored at 4°C.

### **6.2.2.9 FRET hybridization assay**

Within all hybridization assays, the UCNPs-oligo conjugate was kept at fixed concentration (*ca.* 2 mg/mL of core-doped UCNPs) to which increasing concentrations of the complementary oligo labeled to Cy3.5 in hybridization buffer (20 mM TRIS/Cl, 500 mM NaCl, 0.1% BSA, pH 8.0) was added. The solutions were then incubated at room temperature in a black 96-well microtiter plates for 30 minutes with an optical working volume of 150  $\mu$ L. Decay curves were measured on the EI plate reader equipped with a 2W 980 nm laser from Changchun New Industries (CNI) and a PM-1 laser modulator box from (EI) for controlling the pulsing parameters of the CNI laser. Emissions of UCNPs-oligo and Cy3.5 were measured using appropriate bandpass filters at 542 / 20 nm (Semrock) and 607 / 8 nm (Delta) respectively.

## **6.3 Results and discussion**

Sodium gadolinium fluoride ( $\text{NaGdF}_4$ ) was used in this study as host lattice for the doping of  $\text{Er}^{3+}$  and  $\text{Yb}^{3+}$  principally due to its relatively low multiphonon relaxation processes and low vibrational energies, as well as efficient upconversion emission [107,198,199]. It also possesses favorable bimodal properties for magnetic resonance and optical imaging [200].

### **6.3.1 Morphological characterization**

Morphologies and sizes of the core-doped, core-doped/shell and core/shell-doped UCNPs were characterized by transmission electron microscopy. We can observe from **Figure 6.3**, that all the prepared UCNPs have uniform sizes and shapes. UCNPs appear to be rather spherical in

shapes with average diameters (determined based on 150 particles by use of ImageJ software) of  $17 \pm 2$  nm for core-doped,  $24 \pm 3$  nm for core-doped/shell and  $15 \pm 3$  nm for core/shell-doped (**Table 6.1**). The X-ray diffraction patterns as shown in **Figure 6.4** for the three types of UCNPs clearly reveal that the particles crystallized in the hexagonal  $\beta$ - phase, which is believed to be the more efficient phase for upconversion emission for the  $\text{NaGdF}_4$  host material [201].

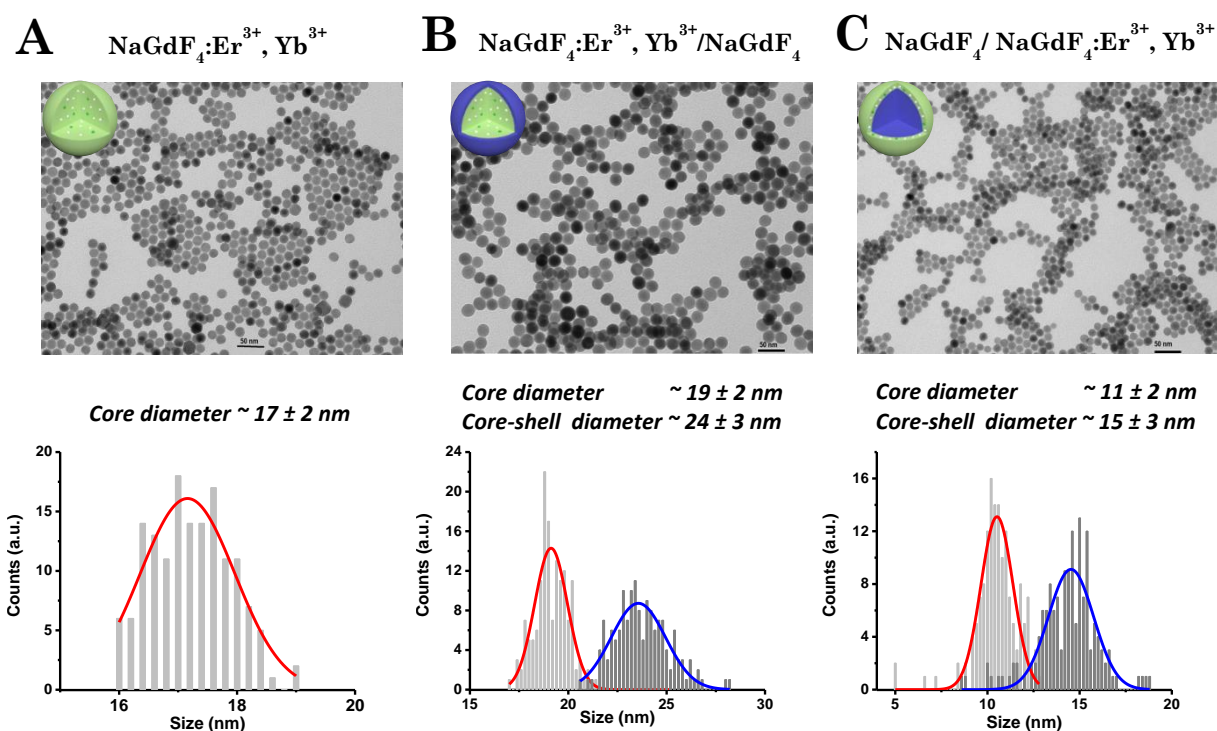


**Figure 6.3.** Top : TEM images of the synthesized UCNPs revealing uniform sizes and rather spherical shapes. Bottom: Histogram of the particle size distribution. (A) Core-doped samples:  $17 \pm 2$  nm; (B) Core-doped/shell samples:  $24 \pm 2$  nm total diameter and 2.5 nm shell thickness; (C) Core/shell-doped samples:  $15 \pm 3$  nm total diameter and 2 nm shell thickness.

**Table 6.1.** Overview of UCNPs' size and shell thickness as estimated from TEM measurements.

UCNPs	Core diameter (nm)	Core-shell diameter (nm)	Shell thickness (nm)
Core-doped	$17 \pm 2$	--	
Core-doped/shell	$19 \pm 2$	$24 \pm 3$	2.5
Core/shell-doped	$11 \pm 2$	$15 \pm 3$	2

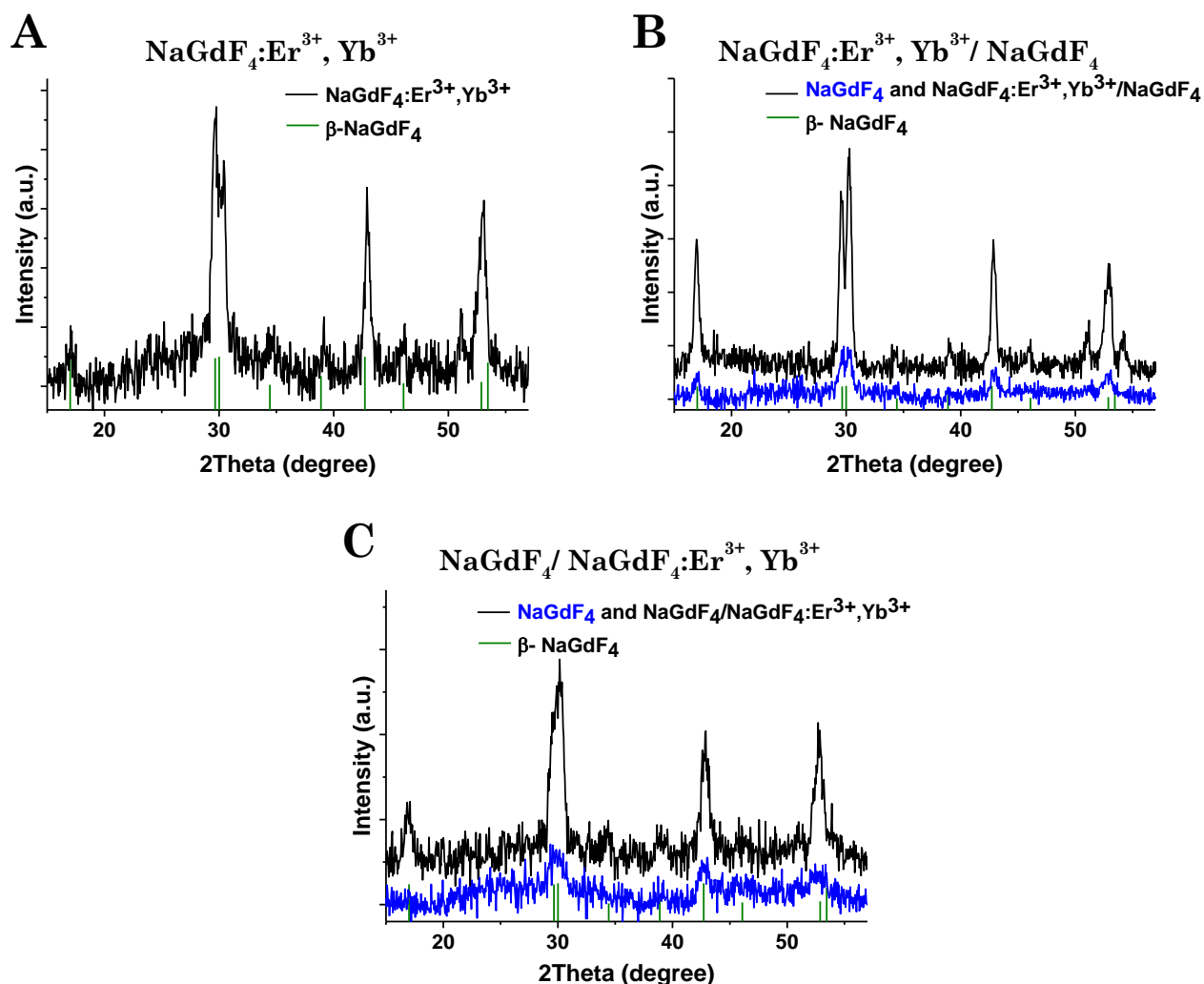


**Figure 6.4.** X-ray diffraction patterns of (A) core-doped (B) core-doped/shell (C) core/shell-doped UCNPs. In green: reference file for  $\beta\text{-NaGdF}_4$  [00-027-0699].

### 6.3.2 Optical characterization

The UCNPs were rendered hydrophilic by protonation of the carboxylate groups of the oleate ligand at low pH, which allows to detach them the UCNPs' surface. The resulting ligand-free UCNPs were soluble in water and were further functionalized with an amino-PEG-COOH polymer through electrostatic interaction between the negatively charged  $\text{COO}^-$  of the polymer and the positively charged lanthanide ions ( $\text{Ln}^{3+}$ ) on the surface of the UCNPs. The primary amines ( $-\text{NH}_2$ ) functional group now available on the UCNPs surface make it possible for biomolecules attachment through different conjugation strategies. FTIR measurements were performed on the UCNPs in order to verify the presence of the polymer on their surface. From the FTIR spectra (only core-doped/shell and core/shell-doped are presented here) shown in **Figure 6.5**, we can clearly observe the characteristic vibrational stretching of the O-H bond

and C=O bond of the carboxyl group at around 3400  $\text{cm}^{-1}$  and 1640  $\text{cm}^{-1}$  respectively. **Figure 6.5**, also reveals the presence of C-O-C bond from the PEG at 1119  $\text{cm}^{-1}$ .

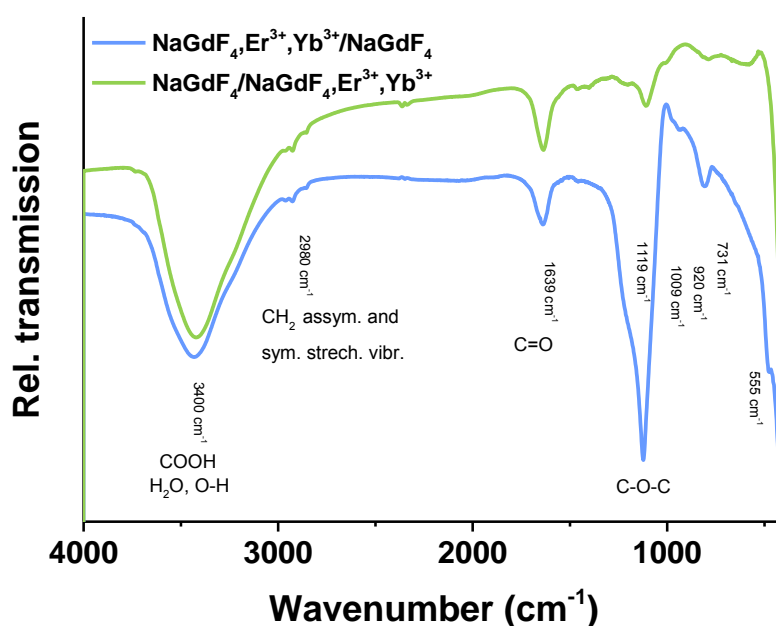


**Figure 6.5.** FTIR spectra of core-doped/shell (blue) and core/shell-doped (green) of the UCNPs. Characteristic bands of the carboxyl group are clearly visible, around 3400  $\text{cm}^{-1}$  for O-H bond and around 1640  $\text{cm}^{-1}$  for C=O bond. C-O-C bond corresponding to PEG at 1119  $\text{cm}^{-1}$  is also present on the spectra for the UCNPs.

The stability and dispersibility in various buffers of the PEGylated-UCNPs are important for their biological applications in bioconjugation (to proteins or DNA) and immunoassays, among other applications. Colloidal stability of the PEGylated-UCNPs was evaluated by dynamic light scattering (DLS) in water, 1× (10 mM) PBS pH 7.4 and 100 mM borate buffer pH 8.4. Both PBS and borate buffers are commonly used in biological research. The average hydrodynamic diameters were estimated from the analysis of three different measurements and are summarized in **Table 6.2**. Estimation of the hydrodynamic diameter of the PEGylated-UCNPs allows to assess aggregation behavior in different aqueous buffers as compared to TEM which provides only a picture of the nanoparticle's structure in dry state, yet does not provide any information about the hydrodynamic diameter or tendency to aggregate. From **Figure 6.6**, we can clearly observe aggregation with the increase in hydrodynamic diameters of the UCNPs as a result of change in media. The low stability of these nanoparticles in aqueous buffers is therefore not optimum for biomedical applications and will have to be improved in future work (e.g. by optimized surface modification).

**Table 6.2.** Hydrodynamic diameter of the PEGylated UCNP in different aqueous media indicating aggregation. Hydrodynamic diameters were estimated from a set of 3 measurements.

PEG-modified UCNPs	Hydrodynamic diameter (nm)		
	Water	1× PBS pH 7.4	100 mM borate pH 8.4
NaGdF <sub>4</sub> :Er <sup>3+</sup> ,Yb <sup>3+</sup> (Core-doped)	69 ± 20	1374 ± 237	1005 ± 208
NaGdF <sub>4</sub> :Er <sup>3+</sup> ,Yb <sup>3+</sup> /NaGdF <sub>4</sub> (Core-doped/shell)	66 ± 20	1080 ± 212	1122 ± 232
NaGdF <sub>4</sub> /NaGdF <sub>4</sub> :Er <sup>3+</sup> ,Yb <sup>3+</sup> (Core/shell-doped)	51 ± 17	3029 ± 478	1005 ± 178

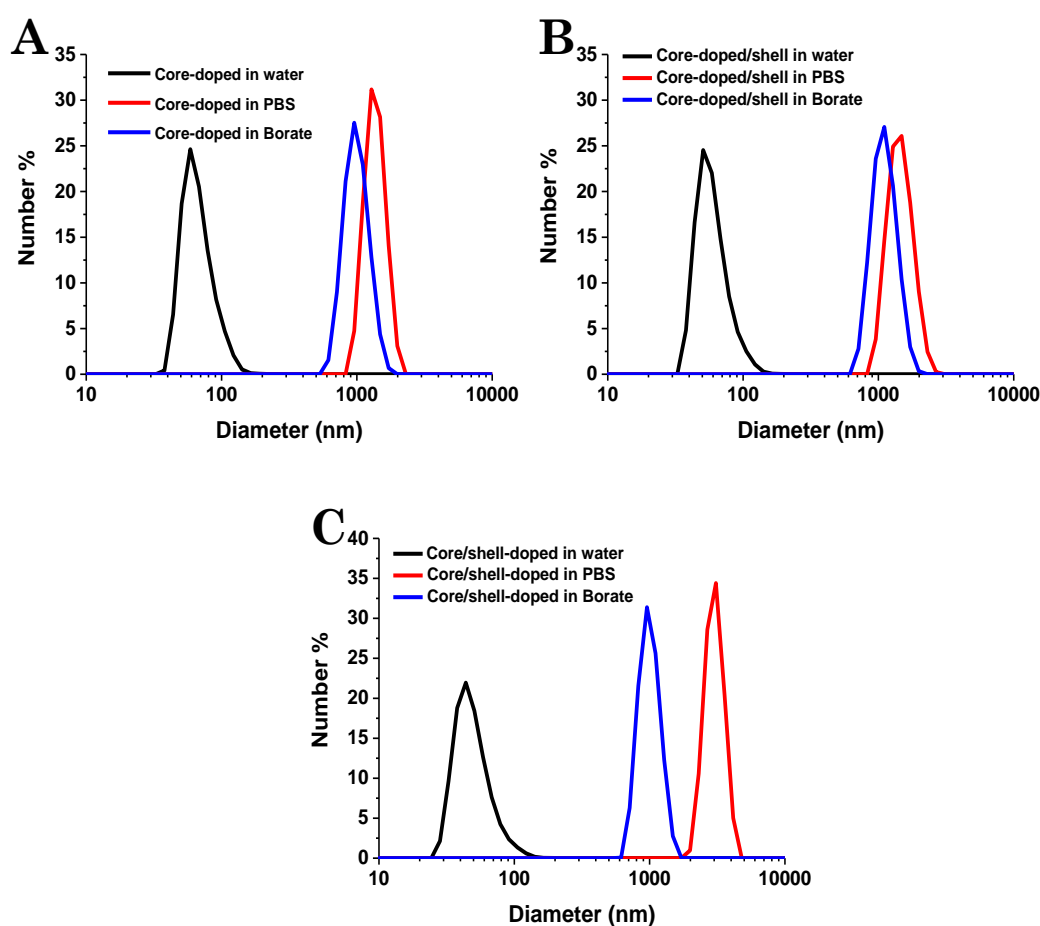


**Figure 6.6.** DLS measurement of (A) core-doped (B) core-doped/shell and (C) core/doped/shell PEGylated-UCNPs. UCNP were measured in (black) water, (red) PBS buffer and (blue) borate buffer.

Upon continuous excitation at 980 nm NIR radiation, the synthesized UCNP undergo upconversion emission in the visible range as it can be observed from **Figure 6.7**. The upconversion emission spectra normalized to the green peak emission for the core-doped, core-

doped/shell and the core/shell-doped display the typical  $\text{Er}^{3+}$  emission bands in the visible range and also suggest the influence of a core/shell structure on the UCNPs green and red light emission. Emissions in the green wavelength region between 512 nm and 535 nm as well as between 535 nm and 570 nm are assigned to the transitions  ${}^2\text{H}_{11/2} \rightarrow {}^4\text{I}_{15/2}$  and  ${}^4\text{S}_{3/2} \rightarrow {}^4\text{I}_{15/2}$  respectively. A red emission assigned to the transition state  ${}^4\text{F}_{9/2} \rightarrow {}^4\text{I}_{15/2}$  was also visible between 635 nm and 685 nm. Excitation with a 980 nm photon brings the  $\text{Yb}^{3+}$  ion from its  ${}^2\text{F}_{7/2}$  ground state to its single  ${}^2\text{F}_{5/2}$  excited state where energy transfer occurs to an  $\text{Er}^{3+}$  ion in close proximity bringing it from its  ${}^4\text{I}_{15/2}$  ground state to the  ${}^4\text{I}_{11/2}$  excited state. Simultaneously, the  $\text{Yb}^{3+}$  ion returns to its  ${}^2\text{F}_{7/2}$  ground state. Subsequently, another  $\text{Yb}^{3+}$  ion gets excited to its single excited state in the neighborhood of the excited  $\text{Er}^{3+}$  ion by a 980 nm photon. Energy is thus transferred to the  $\text{Er}^{3+}$  ion in the  ${}^4\text{I}_{13/2}$  excited state further promoting it to the  ${}^4\text{F}_{7/2}$  state, followed by the  $\text{Yb}^{3+}$  ion decaying back to its  ${}^2\text{F}_{7/2}$  state. Green emissions are thus obtained by non-radiative decay through the transitions  $({}^2\text{H}_{11/2}, {}^4\text{S}_{3/2}) \rightarrow {}^4\text{I}_{15/2}$ . The  $\text{Er}^{3+}$  ion in the  ${}^4\text{S}_{3/2}$  excited state can alternatively decay to the next lower-lying  ${}^4\text{F}_{9/2}$  state through non-radiative decay processes, which allows for red upconversion emission corresponding to the radiative  ${}^4\text{F}_{9/2} \rightarrow {}^4\text{I}_{15/2}$  transition (**Figure 6.8**) [199]. The upconversion spectra of the three types of UCNPs further reveal that the highest luminescence is observed from the core-doped/shell nanoparticle. In fact, the application of an undoped shell has previously been suggested in order to enhance the upconversion emission of UCNPs, which is based on the fact that the shell protects the optically active  $\text{Ln}^{3+}$  centers in the core from the environment, thus surface-related quenching effects are minimized [107].

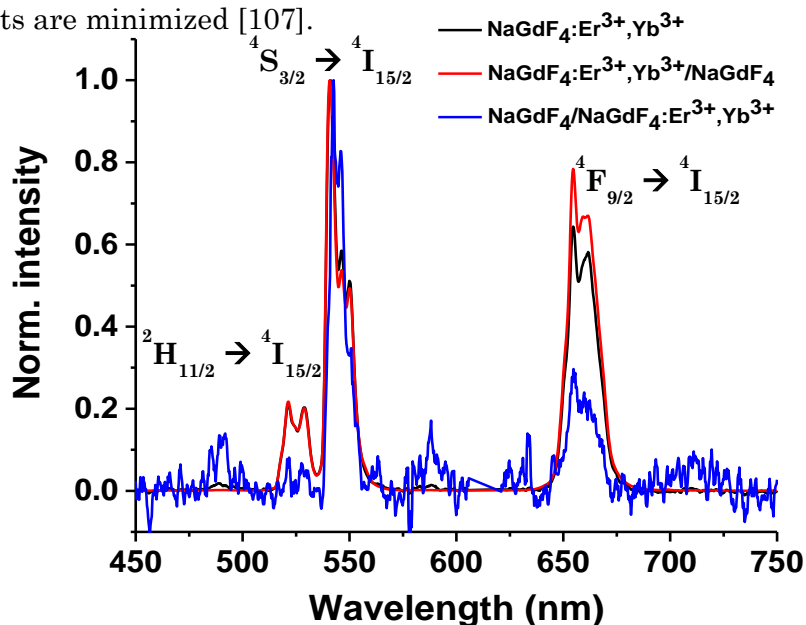


**Figure 6.7.** Upconversion emission spectra normalized at the green peak emission of (black) core-doped (red) core-doped/shell and (blue) core/shell-doped upon 980 nm excitation. Green emission occurred at the transition states  $({}^2\text{H}_{11/2}, {}^4\text{S}_{3/2}) \rightarrow {}^4\text{I}_{15/2}$  while red emission is assigned to the  ${}^4\text{F}_{9/2} \rightarrow {}^4\text{I}_{15/2}$  transition.

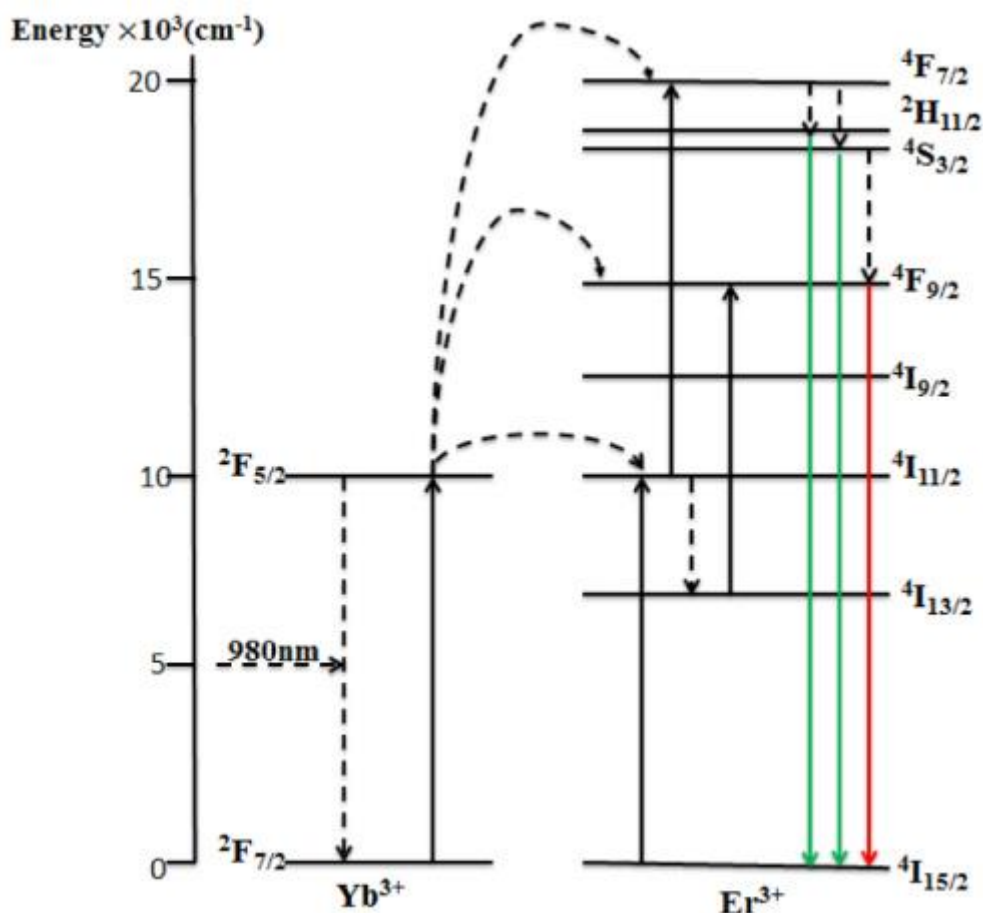


**Figure 6.8.** Relevant NaGdF<sub>4</sub>:Er<sup>3+</sup>, Yb<sup>3+</sup> energy levels with radiative (full arrows) and non-radiative (dashed arrows) processes. Curved dashed arrows represent energy transfer [202].

The average intensity and amplitude decay times have been determined for all the PEGylated UCNPs, measured in a 96-well microtiter plate with an optimal working volume of 150  $\mu$ L on the EI fluorescence plate reader. The obtained lifetimes are summarized in **Table 6.3**. The lifetimes of the nanoparticles were measured at the green and red upconversion emissions using bandpass filters 542 / 20 nm and 660 / 13 nm (Semrock) respectively by pulsed excitation at 980 nm and are represented in **Figure 6.9**. We can distinguish longer lifetimes for the core/shell-doped and the core-doped/shell as compared to the core-doped only UCNPs. In comparison to the core/shell UCNPs, the lifetime of the core-doped UCNPs is shorter, which can be attributed to surface-quenching effect of the Er<sup>3+</sup> based emission. For instance, high vibrational energy modes of OH groups from the surrounding solvent are effective quenchers of the upconversion emission. Growing a shell around the doped-core, greatly suppresses these surface-quenching effects as the shell brings a better protection between the core and the surrounding environment. From the lifetime analysis of the core-doped/shell and core/shell-doped UCNPs, we observe an unexpected increase in lifetime for the latter as we would assume quenching of Er<sup>3+</sup> ions on the shell surface by the surrounding aqueous environment. We can

exclude any protecting effect provided by the PEG coating against quenching effect of the aqueous media because the ligand-free UCNPs gave similar lifetimes (data not shown). One explanation could be that during the synthesis of the core/shell-doped nanoparticles a part of the sensitizer ( $\text{Yb}^{3+}$ ) and activator ( $\text{Er}^{3+}$ ) ions migrate into the superficial and/or inner part of the core, resulting in a non-homogeneous distribution of the ions in the nanoparticle. It would therefore act as core-doped/shell-doped UCNPs and upon excitation at 980 nm, the excited  $\text{Yb}^{3+}$  ions on the shell can effectively transfer energy to  $\text{Er}^{3+}$  ions present on the shell and in the core through excitation energy migration. Further studies (for instance the synthesis of an undoped core /  $\text{Er}^{3+}/\text{Yb}^{3+}$  doped shell / second  $\text{Yb}^{3+}$  doped shell architecture employing the concept of active core-shell systems [107]) would therefore be indispensable to support this claim and to understand the underlying mechanism.

Above described findings are important for FRET based applications as they suggests that the core/shell-doped UCNPs are suitable as FRET-donors since we believe that most of the  $\text{Er}^{3+}$  ions are on the surface of the nanoparticle, thus providing close proximity to an acceptor molecule for efficient energy transfer and long luminescence lifetimes suggest higher QY, which is advantageous for Förster distance.

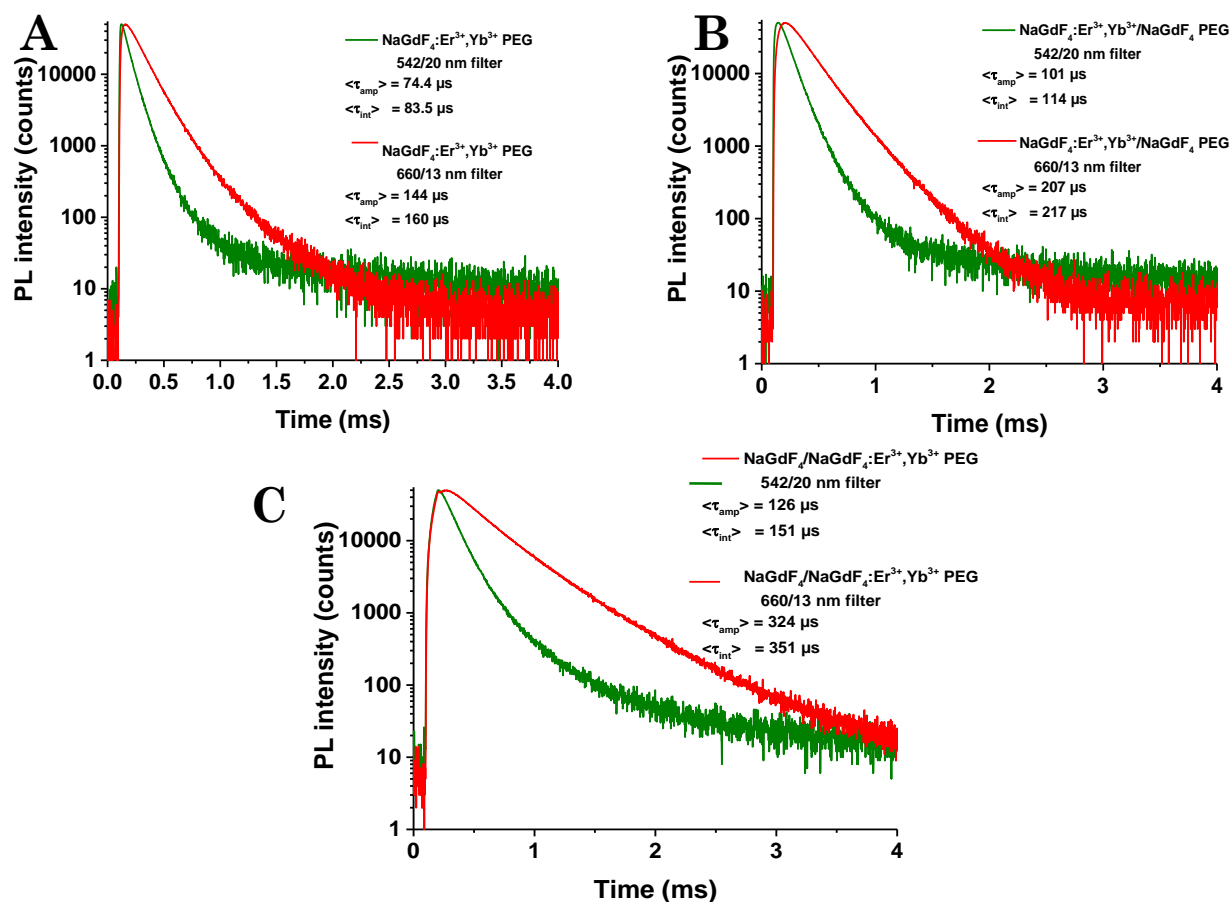


**Figure 6.9.** Upconversion decay lifetimes of (A) core-doped (B) core-doped/shell and (C) core/shell-doped. Green and red curves are the decay curves obtained using bandpass filters at 540/20nm and at 660/13 nm respectively.

**Table 6.3.** Overview of the average amplitude and intensity decay times of core-doped, core-doped/shell and core/shell-doped UCNPs.

PEG-modified UCNPs	< $\tau$ > amplitude		< $\tau$ > intensity	
	@540/20 nm	@660/13 nm	@540/20 nm	@660/13 nm
<b>NaGdF<sub>4</sub>:Er<sup>3+</sup>,Yb<sup>3+</sup></b> <b>(Core-doped)</b>	74.4 $\mu$ s	144 $\mu$ s	83.6 $\mu$ s	180 $\mu$ s
<b>NaGdF<sub>4</sub>:Er<sup>3+</sup>,Yb<sup>3+</sup>/NaGdF<sub>4</sub></b> <b>(Core-doped/shell)</b>	101 $\mu$ s	207 $\mu$ s	144 $\mu$ s	217 $\mu$ s
<b>NaGdF<sub>4</sub>/NaGdF<sub>4</sub>:Er<sup>3+</sup>,Yb<sup>3+</sup></b> <b>(Core/shell-doped)</b>	128 $\mu$ s	324 $\mu$ s	161 $\mu$ s	361 $\mu$ s

### 6.3.3 FRET hybridization assay

Even though we observed low stability of the UCNPs in different aqueous solutions, we tried to establish a proof-of-principal hybridization system between two complementary single stranded DNA based on UCNPs-to-dye FRET assay. As described in the **Materials section 6.2.2.8**, a 23 base pair oligonucleotide was conjugated to the core-doped UCNPs (core/shell-doped UCNPs was not used as donor due to its low brightness and recovery after purification against excess oligos) and used as energy transfer donors to the Cy3.5 organic dye labelled on complementary oligonucleotides. We believe upon hybridization the Cy3.5 on the 3' position will become close to the core-doped UCNPs surface where FRET can take place. Cy3.5 has an emission maximum at around 605 nm and its absorption spectrum overlaps the UCNPs PL in the green between 512 nm and 535 nm and between 535 nm and 570 nm corresponding to the transition states  $^2H_{11/2} \rightarrow ^4I_{15/2}$  and  $^4S_{3/2} \rightarrow ^4I_{15/2}$  respectively. This spectral overlap (**Figure 6.12 left**) shows that upon excitation in the NIR at 980 nm, energy transfer can take place between the UCNPs donor and Cy3.5 acceptor if they are in the Förster distance range assuming they follow the FRET-theory similar to the Tb-to-QD system. The Förster distance ( $R_0$ ) and overlap integral can be calculated by **Equations 2.5 and 2.6** in the overlap range between *ca.* 500 nm to 570 nm.

The fluorescence QY of the UCNPs-donor in the absence of the acceptor for the green emission is not very high. Recently,  $R_0$  was calculated for an UCNP-to-QD FRET system by using an estimated minimum and maximum QY of 0.1 % and 1 % respectively and an overall QY of the UCNPs (because the donor QY should be Er<sup>3+</sup> ions inside the UCNPs) of 5 % [161].  $R_0$  for our UCNP-to-Cy3.5 FRET system was calculated as 2.1 nm for a QY of 0.1 %, 3.1 nm for a QY of 1 % and an even larger Förster distance of 4.1 nm with 5 % QY [161]. Since only a fraction of

the  $\text{Er}^{3+}$  ions near the surface of the UCNPs can participate in energy transfer to a single dye, there will not be a strong difference between the quenched and unquenched PL decay curves UCNPs. However, since excitation in the NIR at 980 nm does not directly excite the Cy3.5 dyes but only the UCNPs-donor and due to the absence of photoluminescence background, FRET-sensitized emission of Cy3.5 dyes can only be caused by energy transfer thus can be sensitively measured. Upon addition of the increasing concentration of the complementary oligo-Cy3.5 to the constant concentration of UCNPs-oligo, no obvious FRET-sensitization of the dye could be observed in the nM range but increasing the Cy3.5 dye concentration to the  $\mu\text{M}$  range yielded obvious sensitized emission due to energy transfer as it can be seen in **Figure 6.10**. Nevertheless, as control measurements using non-complementary oligo-Cy3.5, we also have an observable FRET-sensitized emission of the dye (**Figure 6.11**). One possible explanation could be direct binding of the oligonucleotides on the surface of the UCNPs independent of the sequence in both cases possibly replacing the original ligand. The phosphate groups are able to bind to UCNPs much stronger than carboxylic acids. **Figure 6.12 right** represents the relative PL ratio as a function of the concentration of oligonucleotide labeled with Cy3.5 (complementary and non-complementary) measured in a time-gated window between 100  $\mu\text{s}$  to 300  $\mu\text{s}$  after pulsed-excitation of the acceptor channel from **Figure 6.10 B** and **Figure 6.11 B**.

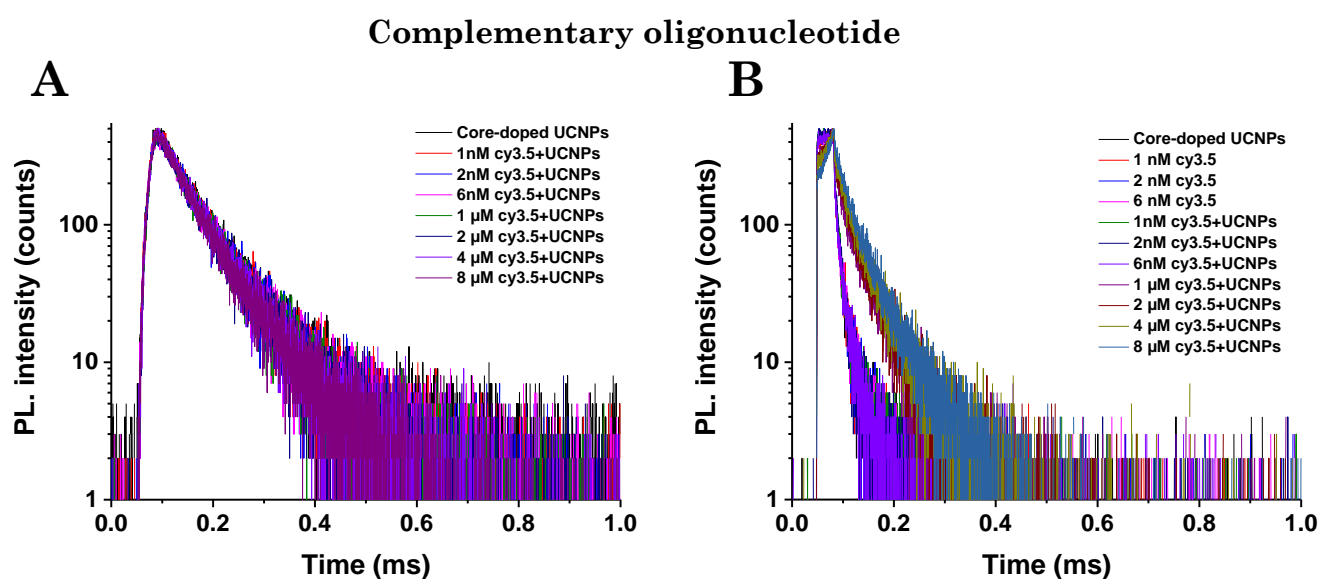


**Figure 6.10.** (A) PL decay curves of core-doped UCNPs and core-doped UCNPs conjugate upon addition of increasing concentration (nM to  $\mu\text{M}$ ) of complementary oligonucleotide labelled with Cy3.5, measured at 542 / 20 nm upon excitation at 980 nm. No quenching of the donor can be observed. (B) Decay curves measured at 607 / 8 nm of the complementary oligonucleotide labelled with Cy3.5 alone and in the presence of the core-doped UCNPs conjugate. At higher micromolar concentration range, visible increase of the PL intensity of the mixture oligos-UCNPs can be observed which can be an indication of energy transfer from the donor to the Cy3.5 dye.

### Non-complementary oligonucleotide

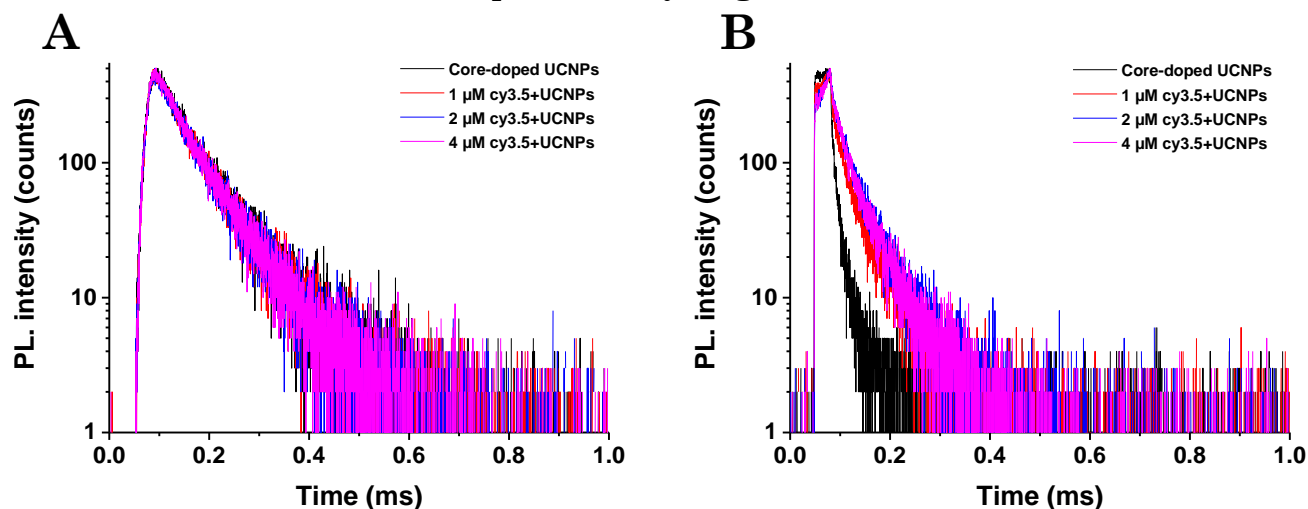


**Figure 6.11.** PL decay curves of core-doped UCNPs and core-doped UCNPs conjugate upon addition of increasing concentration of non-complementary oligonucleotide labelled with Cy3.5 in the  $\mu\text{M}$  range, measured at 542 / 20 nm upon excitation at 980 nm. No quenching of the donor can be observed. (B) Decay curves measured at 607 / 8 nm of the non-complementary oligonucleotide labelled Cy3.5 in the presence of the core-doped UCNPs conjugate. Visible increase of the PL intensity of the mixture oligo-UCNPs can be observed similar to the complementary oligo-UCNPs mixture.

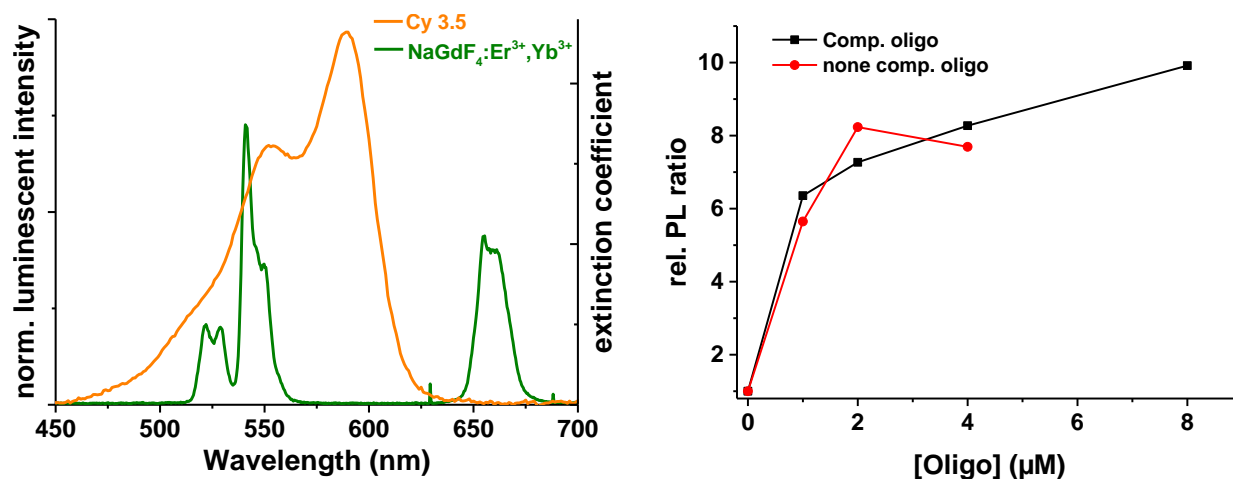


**Figure 6.12.** (Left) Spectral overlap between absorption spectrum of the oligonucleotide labeled with Cy3.5 dye and the normalized area emission of the core-doped UCNPs.  $R_0$  was calculated in the spectral region of 500 – 570 nm which corresponds to the green overlapping region of the UCNPs. (Right) Relative PL ratio of the acceptor channel for the complementary and non-complementary oligonucleotides in presence of the core-doped UCNPs conjugate, measured in a time window between 100 – 300  $\mu\text{s}$ .

## 6.4 Conclusions

Core-doped, core-doped/shell and core/shell-doped UCNPs were synthesized via a thermal decomposition technique from trifluoroacetate precursors in 1-octadecene and oleic acid. Ligand-free UCNPs were obtained by treating the oleic acid coated UCNPs with HCl at pH 4. In acidic pH, the oleate ligands are protonated and are detached from the UCNPs' surface resulting in hydrophilic nanoparticles. Surface functionalization with amino-PEG-COOH was performed through electrostatic interaction in order to generate functional groups on the surface of UCNPs for possible biomolecule attachment. TEM measurements of the UCNPs showed rather spherical particles with mean diameters for core-doped  $17 \pm 2$  nm, core-doped/shell  $24 \pm 3$  nm with a shell thickness of *ca.* 2.5 nm and core/shell-doped  $15 \pm 3$  nm with a shell thickness of *ca.* 2 nm. XRD patterns of the UCNPs showed that they are crystalline and phase-pure with hexagonal  $\beta$ - structure of NaGdF<sub>4</sub> as the only crystalline phase. Further, FTIR spectra confirmed the presence of the amino-PEG-COOH polymer on the surface of the UCNPs. DLS measurements showed that the three types of PEGylated-UCNPs suffered from poor dispersion solubility in the various buffers tested, including physiological buffers, indicating aggregation. Hence, more surface functionalization strategies should be envisaged in order to provide good dispersibility in buffers as conjugation to biomolecules often requires the use of buffers of different pH. Growing a shell around the core of an UCNPs provided protection against surface quenching of the luminescence of Er<sup>3+</sup> ions. Moreover, the core/shell-doped nanoparticles showed unexpected long luminescent lifetimes as compared to the core-doped/shell nanoparticles, favoring them to be potential FRET-donors as the presence of Er<sup>3+</sup> ions on the surface would result in efficient FRET to an acceptor molecule in close distance. The FRET hybridization assays involving the core-doped-oligo and its complementary and a non-complementary oligo labeled with Cy3.5 resulted in both cases to energy transfer possibly due to direct binding of the oligonucleotides on the surface of the core-doped UCNP thereby observing sensitization of the Cy3.5 upon excitation of the FRET systems with 980 nm NIR light.

## 7. Summary and Outlook

### 7.1 Summary

This thesis presents the successful application of FRET as a transduction signal for the sensitive detection of cancer biomarkers using lanthanide complexes (LLC) and QDs as donor and acceptor respectively. All FRET immunoassays for the sensitive detection of the antigens were based on homogeneous time-resolved (TR) measurements, which were possible as a result of the unique photophysical properties of the LLC donor and QD acceptor. The Tb complex we used as donor has an average luminescent decay time of around 2.6 ms, which is several fold longer than the nanosecond lifetimes of the used QDs, which allowed time-resolved measurements for the efficient suppression of transient background from the directly excited QDs and sample autofluorescence (in the nanosecond to microsecond range) especially when excited in the UV. For a nearly background free measurement of our FRET signals, we applied a gating of 800  $\mu$ s with a delay of 100  $\mu$ s after pulsed excitation at 337 nm with a nitrogen laser operating at 20 Hz. In the FRET immunoassays for biomarker (antigen) detection, the donor and acceptor concentrations were kept constant with increasing concentration of the antigens, showing that any new appearance of a short time decay component and quenching/sensitization can only be caused by non-radiative energy transfer from Tb to QD. Ratiometric measurements were involved to build the calibration curves as they help to reduce well-to-well variations by offering an instantaneous suppression of sample and excitation source fluctuations.

Fluorometric sandwich FRET-based immunoassays require two types of antibody bioconjugates which need to be stable, sensitive and specific for the detection of antigens. The marriage of stable and controlled bioconjugation techniques with suitable donor and acceptor probes will give rise to extremely sensitive FRET-based sensing. In a first study, Tb-AB conjugates were obtained by a fully random labeling of Tb-NHS via various amino groups available on the antibody surface. For a less random coupling, using a generic and easily applicable bioconjugation method, we converted three commercially available amino QDs possessing a thick polymer PEG coating (QD605, QD655 & QD705) from Life Technologies to maleimide-activated QDs with sulfo-EMCS, which is a heterobifunctional linker. The maleimide-activated QDs were further conjugated to IgGs and fragmented antibodies F(ab) where the maleimide targets the disulfide bridges at the antibody hinge region. We tested the performance of these bioconjugates in a Tb-to-QD TR-FRET immunoassay for the detection of PSA and only the F(ab)-QD bioconjugates yielded successful calibration curves and sub-nanomolar LOD. As FRET is strongly distance dependent ( $r^{-6}$ ), the large IgG and the bulky polymer PEG coating on

the QDs (IgG conjugated only to QD705) results in negligible FRET. An important finding is that all Tb-QD FRET pairs provide LODs in a concentration range that is clinically relevant and that the 50  $\mu$ L serum samples present clinically relevant solutions. Duplexing capability was demonstrated in PSA assays containing both QD655 and QD705 AB conjugates. The comparison of LODs for the same biomarker is an important tool for a relative comparison of the FRET-pairs in order to adapt the FRET-probes to the required concentration range of different biomarkers (most biomarkers have different cut-off values) in a multiplexed assay and based on these results, QD705 (highest sensitivity) should be used for the biomarker with the lowest cut-off and QD605 for the one with the highest cut-off.

The next step concerned the development of high quantum yield, water soluble and biocompatible compact QDs having a thin coating as compared to the thick PEG coating of the Life Technologies QDs, which limits their use as probes in FRET immunoassays. Three types of QDs were used InPZnS/ZnSe/ZnS (QD530), CdSe/ZnS (QD605), and CdSeTe/ZnS (QD705) core/shell QDs. QD605 and QD705 possess the same core/shell as the Life Technologies QDs and differ mainly in their surface coating. Aqueous phase transfer of the QDs was conducted by surface ligand exchange with penicillamine and post-functionalized with a bifunctional ligand (Mal1) containing a lipoic acid function spaced by three PEG moieties from a maleimide group. The lipoic acid function was anchored on the surface of the QDs and the maleimide group was made available for subsequent bioconjugation to free sulfhydryl groups of antibodies. Both the penicillamine and Mal1 functionalized QDs were colloidally stable for more than two years in aqueous buffer and did not lose their initial quantum efficiency. F(ab) were conjugated via Mal1 to QD530, QD605 and QD705 while IgG, F(ab')<sub>2</sub> and F(ab) were directly attached to the surface of QD705 (highest sensitivity) via metal affinity of thiol to zinc. The successful conjugation of the antibodies were verified in Tb-to-QD FRET immunoassays for the detection of PSA. QD530 bearing a low spectral overlap with Tb donor emission could not be used for LOD quantification and the low concentration recovery of the QD-F(ab')<sub>2</sub> was not enough for statistical evaluation in an immunoassay. The other QD conjugates yielded LODs below the cut-off of PSA with a 25 fold sensitivity improvement using the direct attachment of F(ab) on the surface of the QD (2 ng/mL LOD for QD705 from Life Technologies *vs* 0.08 ng/mL LOD for QD705 having a compact coating).

We also designed a FRET immunoassay for the sensitive and simultaneous detection of three differently sized cancer biomarkers from a single serum sample. NSE, CEA, and TPSA were chosen as biomarkers and monoclonal antibodies against these biomarkers were labelled to Tb and QDs (from eBioscience). Based on the findings of the first study, where QD705 should be

used for the biomarker with the lowest cut-off and QD605 for the one with the highest cut-off, antibodies against TPSA were conjugated to QD705, those against CEA to QD650 and against NSE to QD605. Due to the use of monoclonal antibodies and QDs having narrow and Gaussian emission spectra, no biological crosstalk and negligible optical crosstalk could be observed. All LODs of the biomarkers were below their clinical cut-off levels even though a large background of Tb luminescence was present in the acceptor detector channels (except QD705 channel). A technical “worst case scenario” was constructed, where a combination of high and low concentrations of the biomarkers were present in a single sample, and resulted that CEA, NSE and PSA could be detected with high precision at low nM concentrations with minor deviations from known concentrations.

In an attempt to investigate new nanoparticles for FRET applications, three types of UCNPs, namely NaGdF<sub>4</sub>:Er<sup>3+</sup>,Yb<sup>3+</sup> (core-doped), NaGdF<sub>4</sub>:Er<sup>3+</sup>,Yb<sup>3+</sup>/NaGdF<sub>4</sub> (core-doped/shell) and NaGdF<sub>4</sub>/NaGdF<sub>4</sub>:Er<sup>3+</sup>,Yb<sup>3+</sup> (core/shell-doped) were synthesized via the thermal decomposition technique and rendered water soluble by obtaining ligand-free nanoparticles. These UCNPs were surface functionalized with an amino-PEG-COOH linker through electrostatic interaction in order to generate functional groups on the surface of UCNPs for possible biomolecule attachment. TEM measurements of the UCNPs showed rather spherical particles and XRD patterns of the UCNPs showed that they are highly crystalline and possess a hexagonal  $\beta$ -structure of NaGdF<sub>4</sub>. FTIR spectra confirmed presence of the amino-PEG-COOH polymer on the surface of the UCNPs. DLS measurements showed that the three types of PEGylated-UCNPs were not at all stable in various buffers including physiological buffers where aggregation was observed. Growing a shell around the core of an UCNPs showed protection against surface OH-vibrational quenching of the luminescence of Er<sup>3+</sup> ions. Moreover, the core/shell-doped UCNPs showed unexpected long luminescent lifetimes as compared to the core-doped/shell nanoparticles, favoring them to be suitable FRET-donors as the presence of Er<sup>3+</sup> ions on the surface would result in efficient FRET to an acceptor molecule in close distance FRET assays involving a core-doped-UCNP-DNA and its complementary DNA as well as a non-complementary DNA labeled with cy3.5 resulted in both cases to non-specific interactions, thereby observing sensitization of the cy3.5 upon excitation of the FRET systems at 980 nm. More surface functionalization strategies of the UCNPs should be envisaged in order to produce good dispersibility in buffers as conjugation to biomolecules often requires using buffers of different pH.

## 7.2 Outlook

The use of QDs emitting in the 700 nm region has shown so far to be the most sensitive probes in Tb-to-QD FRET systems due to negligible Tb PL emission beyond 700 nm. QDs emitting in the NIR region would thus be ideal for FRET immunoassays in order to yield sensitive biomarker detection with very low LOD with the adequate NIR-IR PMT. The compact QDs obtained by phase transfer offers the possibility to bind biomolecules that have free sulfhydryl groups on its surface, which decrease the donor-acceptor distance and lead more FRET-efficiency. These compact QDs could be used for multiplexed detection either for micro-RNA or protein biomarkers.

We already started to work on procalcitonin (PCT) and mid regional pro-adrenomedullin (MR-proADM), which are two biomarkers for the diagnosis of bacterial infection. For the moment their antibodies are conjugated to commercially available QD705 from Life Technologies and detected in a Tb-to-QD FRET immunoassay which does not yield the desired sensitive detection. The polyclonal antibodies, as they are known to be unstable, against PCT and MR-proADM should be carefully conjugated to the compact QDs, with optimized and improved purification techniques. A duplex format should then be performed to simultaneously detect these two biomarkers from a single sample as their combination can maximize patient safety by accurately assessing the immediate risk of septic infection. A last, but not least step would be to measure real patients samples (CEA, NSE, TPSA, PCT & MR-proADM) from our calibration curves either by using our already established FRET system involving commercial QDs or by using the compact QDs and also to measure in a multiplexed format on the approved KRYPTOR clinical fluorescence plate reader.

## 8. Appendix

### 8.1 Abbreviations

AB – antibody

AG - antigen

BSA – bovine serum albumin

CEA – carcinoembryonic antigen

ChA – acceptor channel

ChB – donor channel

CTC – circulating tumor cells

Da – Dalton

DHLA – dihydrolipoic acid

D—A – donor to acceptor distance

DLS – dynamic light scattering

DNA – deoxyribonucleic acid

EI – Edinburgh instruments

eQD – eBioscience quantum dot

ESA – excited state absorption

ETU – energy transfer upconversion

FDA – food and drug administration

FRET – Förster resonance energy transfer

FTIR – Fourier transform infrared

FWHM – full width at half maximum

GMBW – guaranteed minimum bandwidth

IgG – immunoglobulin G

iQD – ITK (Life Technologies) quantum dot

IR – infrared

IRF – instrument response function

LED – light emitting diode

LLC – luminescent lanthanide complexes

Ln – lanthanide

LOD – limit of detection

LOQ – limit of quantification

MCS – multi channel scalers

ms- millisecond  
MWCO- molecular weight cut-off  
ns – nanosecond  
NP - nanoparticle  
NSE – neuron-specific enolase  
PA – photon avalanche  
Pen – penicillamine  
PEG – polyethylene glycol  
PL – photoluminescence  
PMT – photomultiplier tube  
QD – quantum dot  
QY – quantum yield  
RNA – ribonucleic acid  
SD – standard deviation  
SDS-PAGE - sodium dodecyl sulfate polyacrylamide gel electrophoresis  
sm-FRET – single molecule-FRET  
ssDNA – single stranded DNA  
Tb – Lumi4-terbium complex  
TCSPC – time correlated single photon counting  
TEM – transmission electron microscopy  
TPSA – total prostate specific antigen  
TR – time resolved  
UCNP – upconversion nanoparticle  
UV – ultraviolet  
Vis – visible  
XRD – X-ray diffraction

## 8.2 Antibody fragmentation SDS-PAGE

### 8.2.1 Fragmentation of CEA antibody G15 to F(ab')<sub>2</sub>

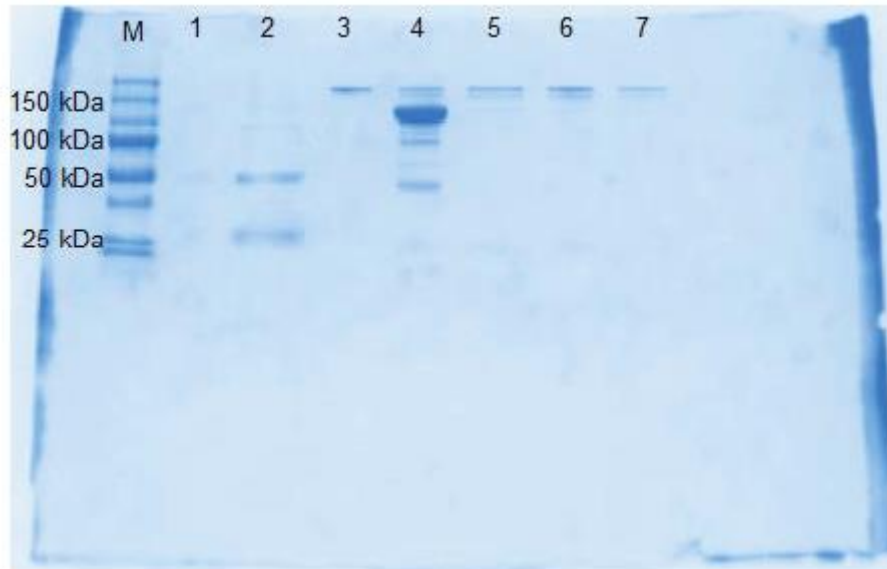


**Figure 8.1.** SDS-PAGE image of CEA F(ab')<sub>2</sub>. M: MW marker, 1: reduced IgG, 2: reduced F(ab')<sub>2</sub>, 3: non-reduced IgG, 4: non-reduced F(ab')<sub>2</sub>, 5: non-reduced protein A column elution 1, 6: non-reduced protein A column elution 2, 7: non-reduced protein A column elution 3.

### 8.2.2 Fragmentation of NSE antibody E20 to F(ab')<sub>2</sub>

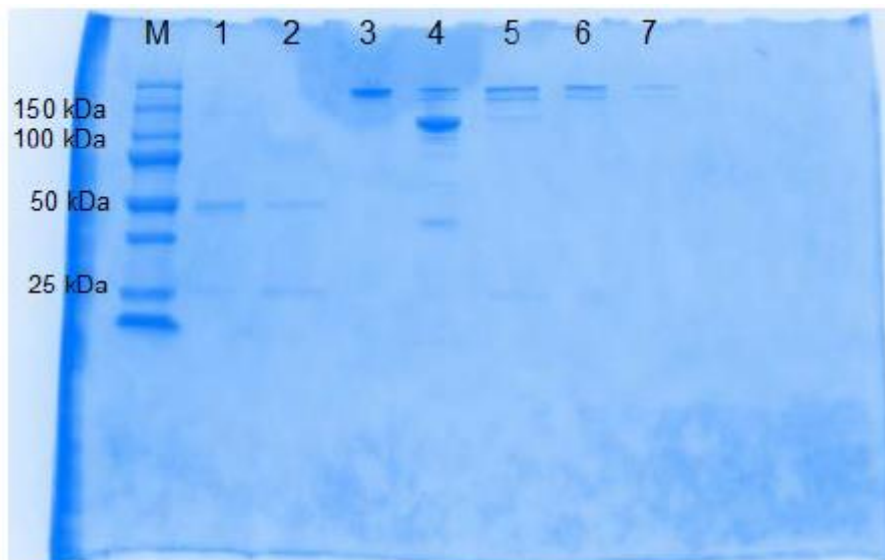


**Figure 8.2.** SDS-PAGE image of NSE F(ab')<sub>2</sub>. M: MW marker, 1: reduced IgG, 2: reduced F(ab')<sub>2</sub>, 3: non-reduced IgG, 4: non-reduced F(ab')<sub>2</sub>, 5: non-reduced protein A column elution 1, 6: non-reduced protein A column elution 2, 7: non-reduced protein A column elution 3.

### 8.2.3 Fragmentation of TPSA antibody PSR222 to F(ab')<sub>2</sub> and F(ab)

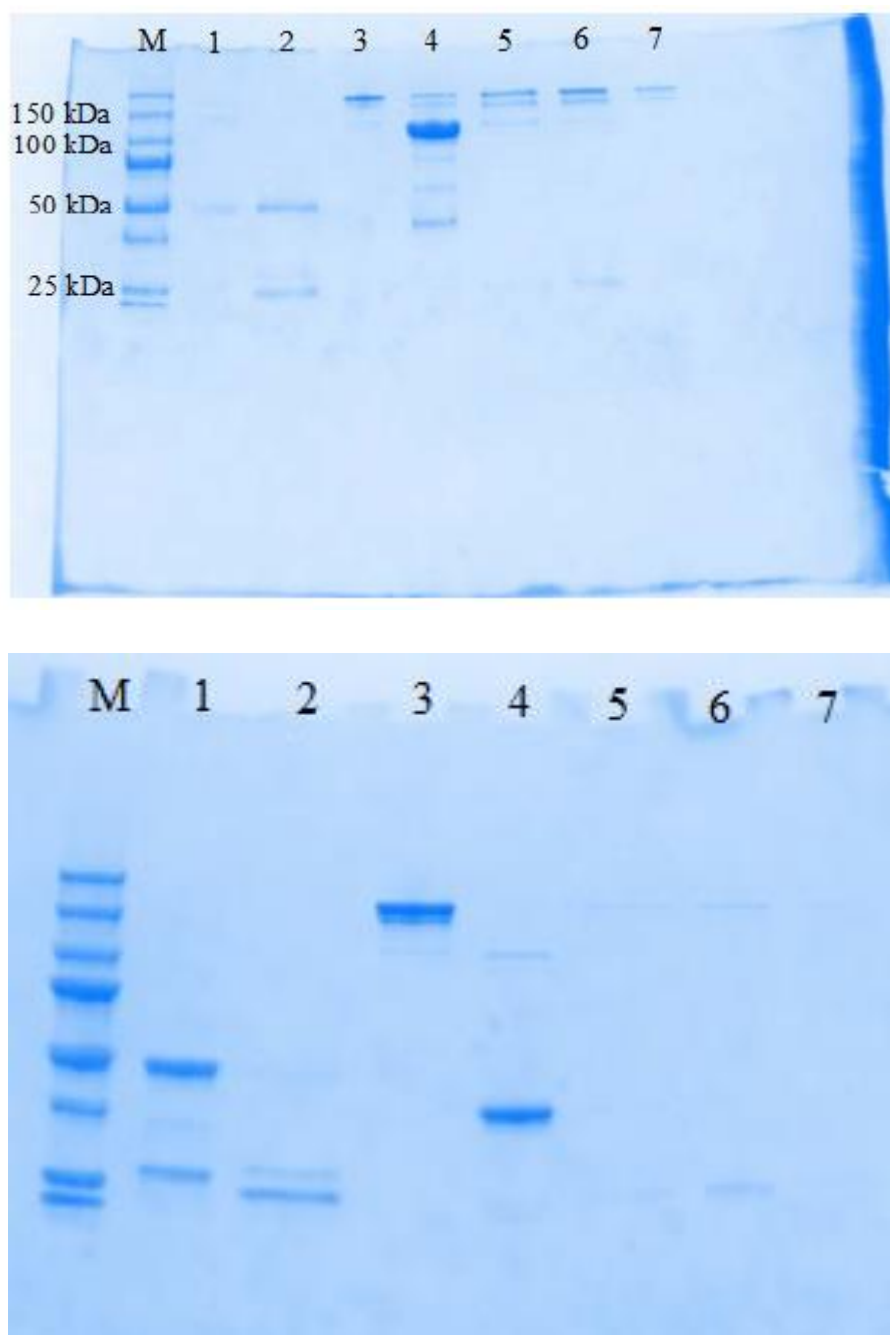


**Figure 8.3.** SDS-PAGE image of TPSA (top) F(ab')<sub>2</sub> and (bottom) F(ab). M: MW marker, 1: reduced IgG, 2: reduced F(ab')<sub>2</sub>, 3: non-reduced IgG, 4: non-reduced F(ab')<sub>2</sub>, 5: non-reduced protein A column elution 1, 6: non-reduced protein A column elution 2, 7: non-reduced protein A column elution 3.

### 8.3 Decay curve fitting

#### 8.3.1 Decay curve fitting of QD705-d-Fab

Fitted from 0.04 to 8 ms (fixed Tb background decay time)

Donor Channel		$R_0 = 11$ nm									
#	QD (nM)	$\tau_1$	$\eta_{\text{FRET1}}$	$A_1$	$\alpha_{\text{DA}^*1}$	$\alpha_{\text{DA1}}$	$\tau_2$	$\eta_{\text{FRET2}}$	$A_2$	$\alpha_{\text{DA}^*2}$	$\alpha_{\text{DA2}}$
0	0.00	<b>D in the absence of A (double-exponential)</b>					790	0.64	1057	0.13	1.00
F3	0.30										
F4	0.60										
F5	1.00										
F6	3.00	180	0.92	778	0.09	0.18	1300	0.41	3556	0.39	0.82
F7	4.00	240	0.89	862	0.10	0.18	1300	0.41	4006	0.45	0.82
F8	6.00	390	0.82	1198	0.13	0.21	1400	0.36	4547	0.51	0.79
F9	9.00	330	0.85	1075	0.12	0.18	1400	0.36	4783	0.54	0.82
F10											
F11											
average 2-9		290	0.87			0.19	1350	0.38			0.81
distance $r$ (nm)		8.0	8.0		fraction: 19%		11.9	11.9		fraction: 81%	

#	QD (nM)	fixed	$\tau_0$	$A_0$	$\alpha_{\text{DA}^*0}$	$\langle \tau \rangle$	$z(D)$	$\langle \tau_{\text{DA}} \rangle$	$\langle \eta_{\text{FRET}} \rangle$
0	0.00		2400	7225	0.87	2190			
F3	0.30								
F4	0.60								
F5	1.00								
F6	3.00		2400	4737	0.52	1780	0.08	1120	0.49
F7	4.00		2400	4051	0.45	1700	0.07	1140	0.48
F8	6.00		2400	3140	0.35	1620	0.05	1210	0.45
F9	9.00		2400	3025	0.34	1610	0.05	1230	0.44
F10									
F11									
average 2-9			2400					1180	0.46



### 8.3.2 Decay curve fitting of QD705-d-IgG

Donor Channel

#	QD (nm)
0	0.00
G3	0.15
G4	0.30
G5	1.50
G6	3.00
G7	4.50
G8	6.00
G9	12.00
G10	18.00
G11	24.00
average 2-9	
distance $r$ (nm)	

$R_0=11$  nm

Fitted from 0.04 to 8 ms (fixed Tb background decay time)

$\tau_1$	$\eta_{\text{FRET1}}$	$A_1$	$\alpha_{\text{DA}^*1}$	$\alpha_{\text{DA}1}$
D in the absence of A (double-exponential)				
20	0.99	7515	0.46	0.90
18	0.99	10206	0.54	0.92
23	0.99	5664	0.40	0.86
25	0.99	4839	0.36	0.85
18	0.99	9708	0.53	0.92
24	0.99	4585	0.35	0.84
20	0.99			0.88
5.0	5.1		fraction:	88%

$\tau_2$	$\eta_{\text{FRET2}}$	$A_2$	$\alpha_{\text{DA}^*2}$	$\alpha_{\text{DA}2}$
370	0.83	945	0.11	1.00
550	0.75	799	0.05	0.10
650	0.70	870	0.05	0.08
730	0.67	916	0.06	0.14
710	0.67	860	0.06	0.15
710	0.67	886	0.05	0.08
710	0.67	882	0.07	0.16
630	0.69			0.12
9.5	9.6		fraction:	12%

#	QD (nm)
0	0.00
G3	0.15
G4	0.30
G5	1.50
G6	3.00
G7	4.50
G8	6.00
G9	12.00
G10	18.00
G11	24.00
average 2-9	
distance $r$ (nm)	

fixed	$\tau_0$	$A_0$	$\alpha_{\text{DA}^*0}$
	2400	7867	0.89
	2400	7991	0.49
	2400	7786	0.41
	2400	7635	0.54
	2400	7726	0.58
	2400	7756	0.42
	2400	7693	0.58
	2400		
	>> $R_0$		

$\langle \tau \rangle$	$z_D$	$\langle \tau_{\text{DA}} \rangle$	$\langle \eta_{\text{FRET}} \rangle$
2180			
1210	0.06	50	0.98
1030	0.05	50	0.98
1350	0.06	100	0.95
1440	0.07	110	0.95
1060	0.05	60	0.97
1460	0.07	120	0.94
		80	0.96
		6.4	6.4

Acceptor Channel  $R_0 = 11 \text{ nm}$

#	QD (nM)	$\tau_1$	$\eta_{\text{FRET1}}$	$A_1$	$\alpha_{\text{AD}^*1}$	$k_{\text{FRET1}}$	$\alpha_{\text{AD1}}$
G2	0						
G3	0.15						
G4	0.30						
G5	1.50						
G6	3.00	36	0.98	4788	0.90	0.0273	0.153
G7	4.50	35	0.98	5028	0.89	0.0281	0.117
G8	6.00	38	0.98	3709	0.86	0.0259	0.076
G9	12.00	37	0.98	4388	0.88	0.0266	0.108
G10	18.00	37	0.98	4597	0.89	0.0266	0.096
G11	24.00	36	0.98	4548	0.88	0.0273	0.114
average 1-9		37	0.98				0.111
distance $r$		5.6	5.6			fraction: 11%	

Fitted from 0.05 to 5 ms (fixed  $T_b$  background decay time)

$\tau_2$	$\eta_{\text{FRET2}}$	$A_2$	$\alpha_{\text{AD}^*2}$	$k_{\text{FRET2}}$	$\alpha_{\text{AD2}}$
250	0.89	399	0.07	0.00355	0.10
260	0.88	412	0.07	0.00339	0.08
290	0.87	396	0.09	0.00299	0.07
280	0.87	400	0.08	0.00312	0.08
310	0.86	374	0.07	0.00277	0.07
280	0.87	395	0.08	0.00312	0.09
278	0.87				0.082
8.0	8.0			fraction: 8%	

$\tau_3$	$\eta_{\text{FRET3}}$	$A_3$	$\alpha_{\text{AD}^*3}$	$k_{\text{FRET3}}$	$\alpha_{\text{AD3}}$
1800	0.18	86	0.02	0.00010	0.75
1800	0.18	124	0.02	0.00010	0.80
1800	0.18	162	0.04	0.00010	0.85
1700	0.23	165	0.03	0.00013	0.81
1800	0.18	151	0.03	0.00010	0.83
1700	0.23	157	0.03	0.00013	0.80
1767	0.20				0.807
13.9	13.9			fraction: 81%	

#	QD (nM)
1	0.06
2	0.10
3	0.15
4	0.20
5	0.25
6	0.30
7	0.40
8	0.50
9	0.60
average 1-9	
distance $r$	

fixed	$\tau_0$	$A_0$	$\alpha_{\text{AD}^*0}$
	2400	57	0.011
	2400	56	0.010
	2400	55	0.013
	2400	55	0.011
	2400	55	0.011
	2400	55	0.011
	2400	55	0.011
average 1-9	2400		
distance $r$	>>R <sub>0</sub>		

$\langle \tau \rangle$	$z(\text{A})$	$\langle \tau_{\text{DA}} \rangle$	$\langle \eta_{\text{FRET}} \rangle$
110	0.0012	1378	0.37
110	0.0011	1473	0.33
160	0.0014	1562	0.29
140	0.0012	1402	0.36
130	0.0012	1521	0.31
130	0.0012	1389	0.37
		1454	0.34
		12.3	12.3

## 8.4 Calibration curves for LOD calculation

### 8.4.1 Linear part of calibration curves from Chapter 4

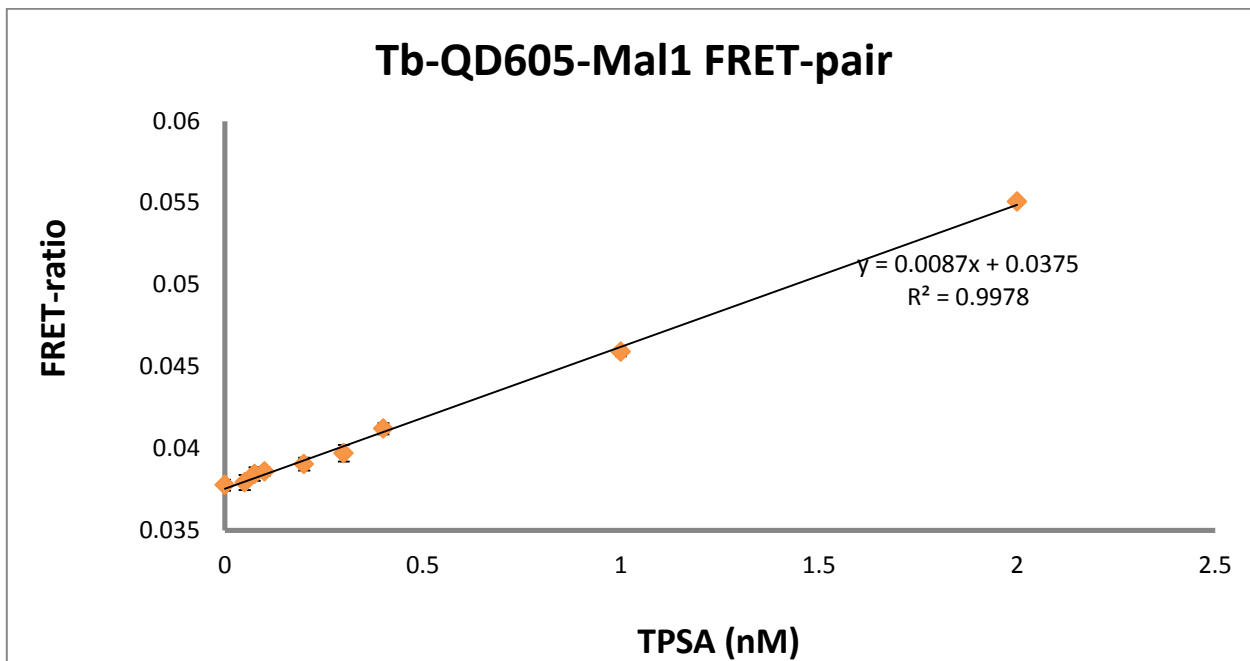


**Figure 8.4.** Linear part of calibration curve from **Figure 4.11 B** corresponding to Tb-QD605-Mal1 FRET-pairs

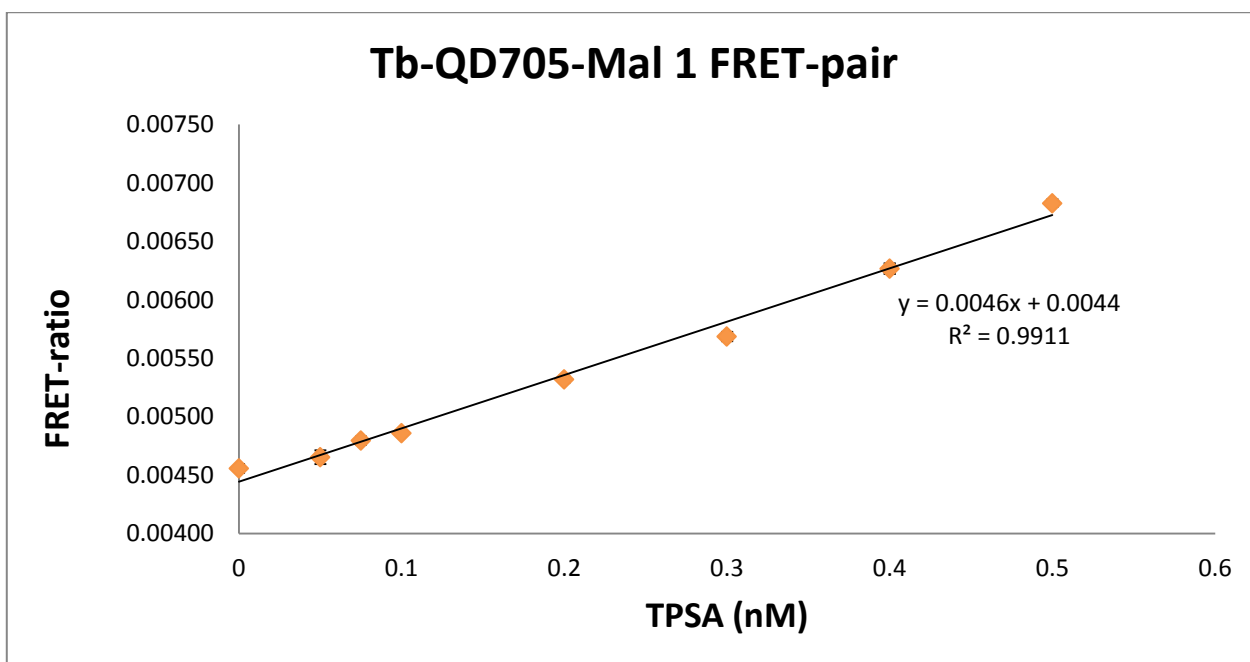


**Figure 8.5.** Linear part of calibration curve from **Figure 4.11 C** corresponding to Tb-QD705-Mal1 FRET-pairs

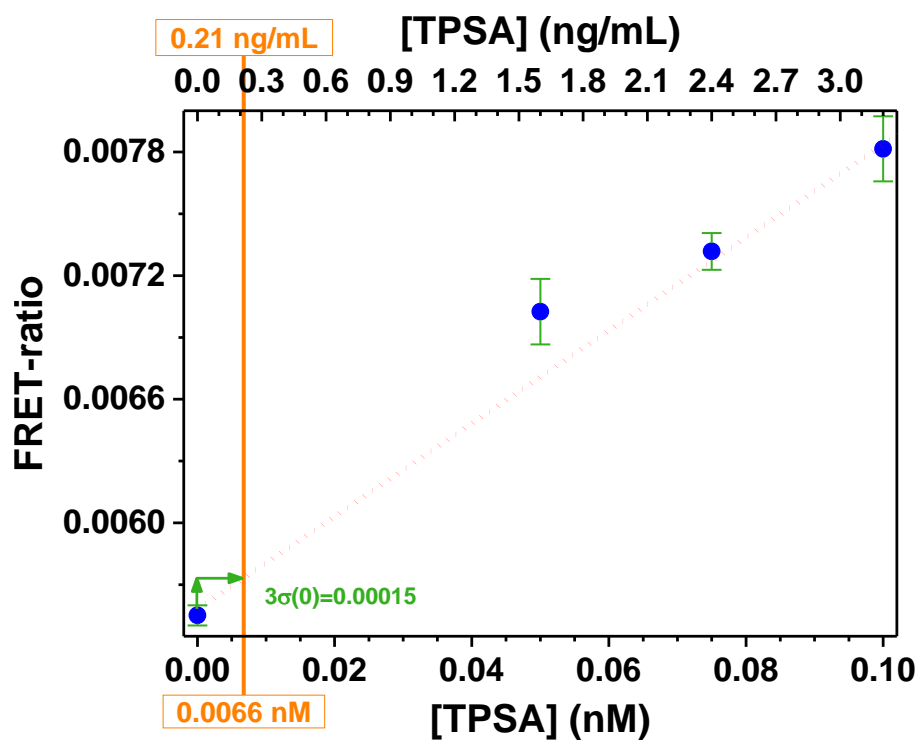


Figure 8.6. Linear part of calibration curve from Figure 4.12 D corresponding to Tb-QD705-d-IgG FRET-pairs

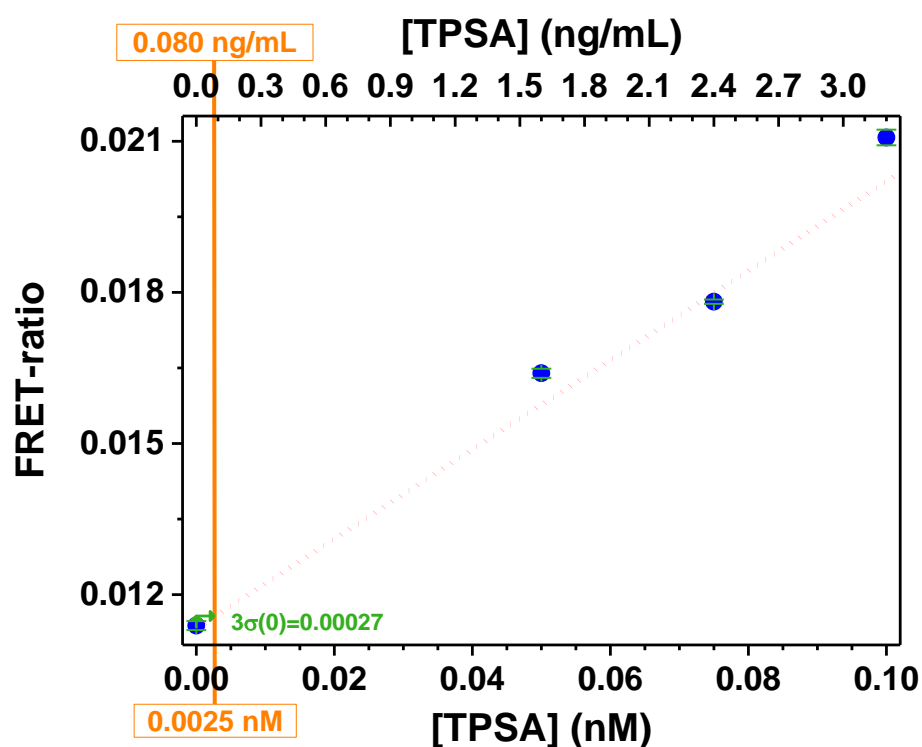
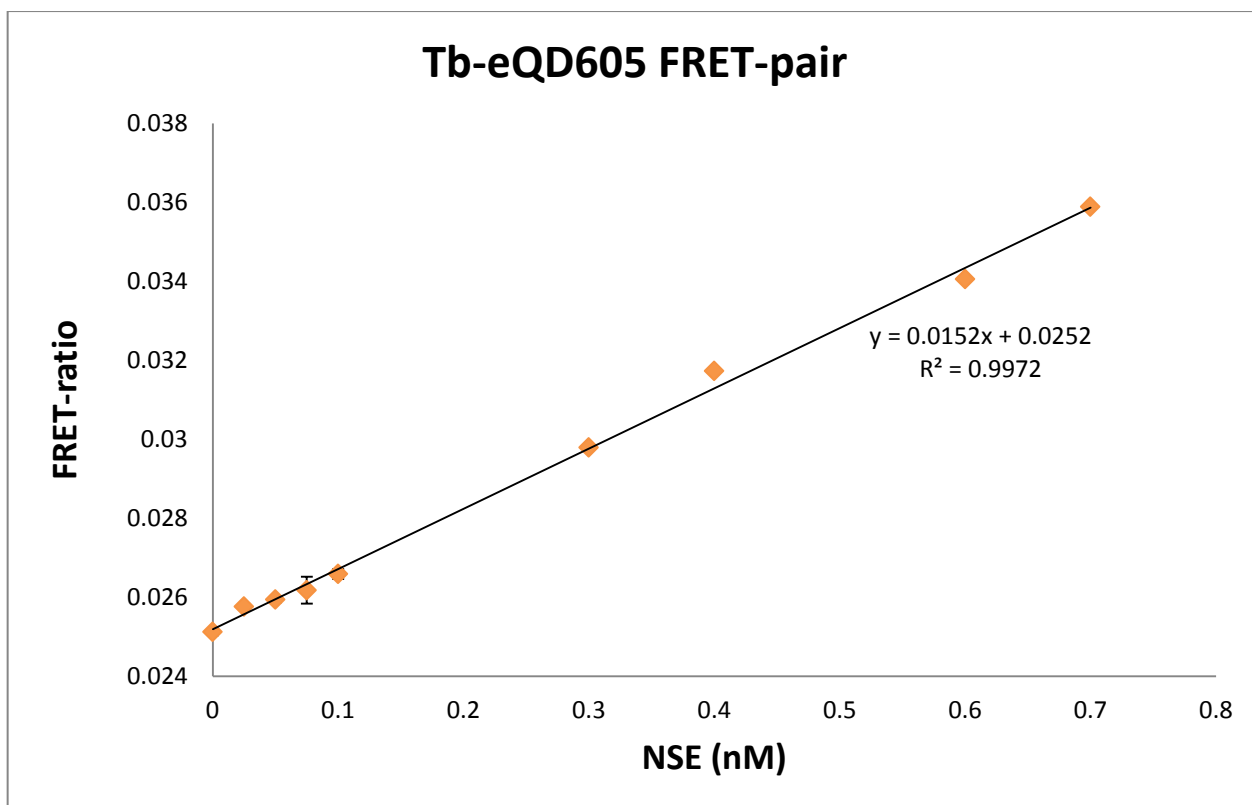
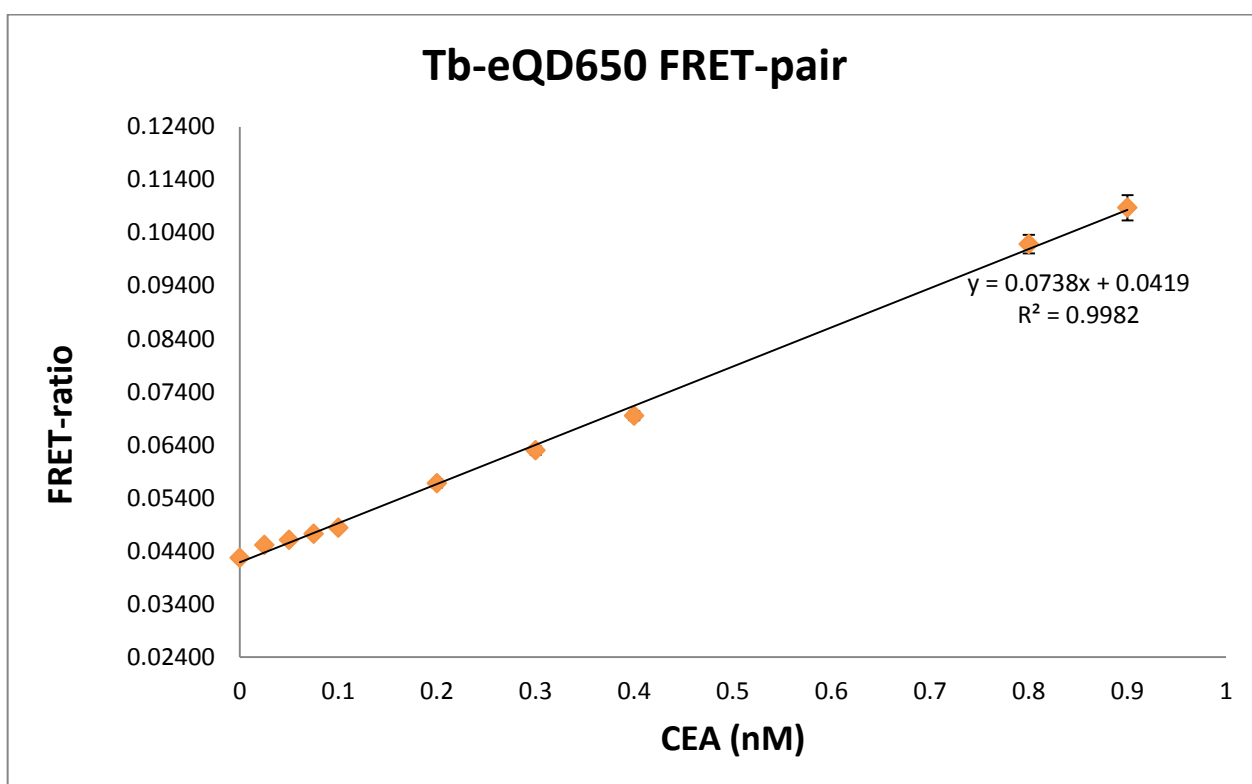


Figure 8.7. Linear part of calibration curve from Figure 4.12 D corresponding to Tb-QD705-d-IgG FRET-pairs



**Figure 8.8.** Linear part of calibration curve from **Figure 4.5 B** corresponding to Tb-eQD605 FRET-pairs



**Figure 8.9.** Linear part of calibration curve from **Figure 4.5 A** corresponding to Tb-eQD650 FRET-pairs

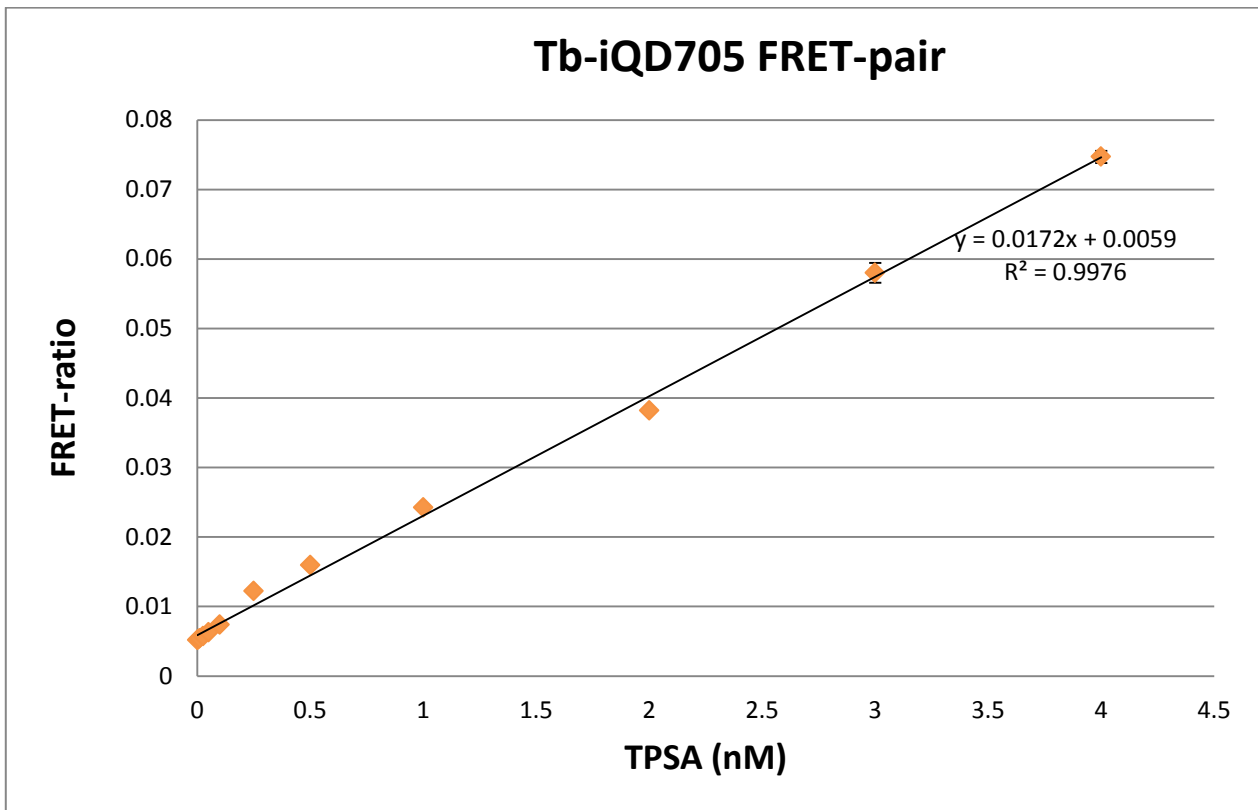


**Figure 8.10.** Linear part of calibration curve from **Figure 4.5 C** corresponding to Tb-eQD650 FRET-pairs

## 9. Bibliography

- [1]. Gerber, C.; Lang, H. P. How the doors to the nanoworld were opened. *Nat. Nanotechnol.* **2006**, *1*, 3–5.
- [2]. Laurent, L., Villain, J., Boisseau, P. & Loubaton, B. Nanoscience and nanotechnologies: hopes and concerns Nanomedicine, nanotechnology in medicine. *Comptes Rendus Phys.* **12**, 620–636 (2011).
3. Liotta, L. A.; Ferrari, M.; Petricoin, E. Clinical proteomics: written in blood. *Nature* **2003**, *425*, 905–905.
4. Simpson, R. J.; Bernhard, O. K.; Greening, D. W.; Moritz, R. L. Proteomics-driven cancer biomarker discovery: looking to the future. *Curr. Opin. Chem. Biol.* **2008**, *12*, 72–77.
5. Kosaka, P. M.; Pini, V.; Ruz, J. J.; Silva, R. A. da; González, M. U.; Ramos, D.; Calleja, M.; Tamayo, J. Detection of cancer biomarkers in serum using a hybrid mechanical and optoplasmonic nanosensor. *Nat. Nanotechnol.* **2014**, *9*, 1047–1053.
6. *Principles of Fluorescence Spectroscopy*; Lakowicz, J. R., Ed.; Springer US: Boston, MA, 2006.
7. Wiley-VCH - Medintz, Igor / Hildebrandt, Niko (eds.) - FRET - Förster Resonance Energy Transfer <http://www.wiley-vch.de/publish/en/books/forthcomingTitles/NT00/3-527-32816-5/?sID=62dtk9j7hdfvqmbulc712jh914> (accessed Nov 24, 2015).
8. Chen, G.; Song, F.; Xiong, X.; Peng, X. Fluorescent Nanosensors Based on Fluorescence Resonance Energy Transfer (FRET). *Ind. Eng. Chem. Res.* **2013**, *52*, 11228–11245.
9. Sapsford, K. E.; Berti, L.; Medintz, I. L. Materials for Fluorescence Resonance Energy Transfer Analysis: Beyond Traditional Donor–Acceptor Combinations. *Angew. Chem. Int. Ed.* **2006**, *45*, 4562–4589.
10. Wild, D. The Immunoassay Handbook, 4th Edition | <http://store.elsevier.com/The-Immunoassay-Handbook/isbn-9780080970387/> (accessed Nov 23, 2015).
11. Geißler, D.; Stufler, S.; Löhmansröben, H.-G.; Hildebrandt, N. Six-Color Time-Resolved Förster Resonance Energy Transfer for Ultrasensitive Multiplexed Biosensing. *J. Am. Chem. Soc.* **2013**, *135*, 1102–1109.
12. Morgner, F.; Stufler, S.; Geißler, D.; Medintz, I. L.; Algar, W. R.; Susumu, K.; Stewart, M. H.; Blanco-Canosa, J. B.; Dawson, P. E.; Hildebrandt, N. Terbium to Quantum Dot FRET Bioconjugates for Clinical Diagnostics: Influence of Human Plasma on Optical and Assembly Properties. *Sensors* **2011**, *11*, 9667–9684.
13. Cardoso Dos Santos, M.; Hildebrandt, N. Recent developments in lanthanide-to-quantum dot FRET using time-gated fluorescence detection and photon upconversion. *TrAC Trends Anal. Chem.*
14. Sy, M.; Nonat, A.; Hildebrandt, N.; Charbonnière, L. J. Lanthanide-based luminescence biolabelling. *Chem. Commun.* **2016**, *52*, 5080–5095.
15. Ruggiero, E.; Castro, S. A.; Habtemariam, A.; Salassa, L. Upconverting nanoparticles for the near infrared photoactivation of transition metal complexes: new opportunities and challenges in medicinal inorganic photochemistry. *Dalton Trans.* **2016**, *45*, 13012–13020.
16. Bednarkiewicz, A.; Nyk, M.; Samoc, M.; Streck, W. Up-conversion FRET from Er<sup>3+</sup>/Yb<sup>3+</sup>:NaYF<sub>4</sub> Nanophosphor to CdSe Quantum Dots. *J. Phys. Chem. C* **2010**, *114*, 17535–17541.
17. Li, Z.; Zhang, Y.; Jiang, S. Multicolor Core/Shell-Structured Upconversion Fluorescent Nanoparticles. *Adv. Mater.* **2008**, *20*, 4765–4769.

18. Nguyen, T.-L.; Spizzirri, P.; Wilson, G.; Mulvaney, P. Tunable light emission using quantum dot-coated upconverters. *Chem. Commun.* **2007**.
19. Yan, C.; Dadvand, A.; Rosei, F.; Perepichka, D. F. Near-IR Photoresponse in New Up-Converting CdSe/NaYF<sub>4</sub>:Yb,Er Nanoheterostructures. *J. Am. Chem. Soc.* **2010**, *132*, 8868–8869.
20. Alivisatos, A. P. Semiconductor Clusters, Nanocrystals, and Quantum Dots. *Science* **1996**, *271*, 933–937.
21. Yin, Y.; Alivisatos, A. P. Colloidal nanocrystal synthesis and the organic–inorganic interface. *Nature* **2005**, *437*, 664–670.
22. Geißler, D.; Hildebrandt, N. Recent developments in Förster resonance energy transfer (FRET) diagnostics using quantum dots. *Anal. Bioanal. Chem.* **2016**, *408*, 4475–4483.
23. Algar, W. R.; Kim, H.; Medintz, I. L.; Hildebrandt, N. Emerging non-traditional Förster resonance energy transfer configurations with semiconductor quantum dots: Investigations and applications. *Coord. Chem. Rev.* **2014**, *263–264*, 65–85.
24. Hildebrandt, N.; Wegner, K. D.; Algar, W. R. Luminescent terbium complexes: Superior Förster resonance energy transfer donors for flexible and sensitive multiplexed biosensing. *Coord. Chem. Rev.* **2014**, *273–274*, 125–138.
25. Wegner, K. D.; Jin, Z.; Lindén, S.; Jennings, T. L.; Hildebrandt, N. Quantum-Dot-Based Förster Resonance Energy Transfer Immunoassay for Sensitive Clinical Diagnostics of Low-Volume Serum Samples. *ACS Nano* **2013**, *7*, 7411–7419.
26. Sulfo-EMCS (N--maleimidocaproyl-oxysulfosuccinimide ester) - Thermo Fisher Scientific <https://www.thermofisher.com/order/catalog/product/22307> (accessed Nov 30, 2015).
27. Wang, M.; Abbineni, G.; Clevenger, A.; Mao, C.; Xu, S. Upconversion nanoparticles: synthesis, surface modification and biological applications. *Nanomedicine Nanotechnol. Biol. Med.* **2011**, *7*, 710–729.
28. Zhou, B.; Shi, B.; Jin, D.; Liu, X. Controlling upconversion nanocrystals for emerging applications. *Nat. Nanotechnol.* **2015**, *10*, 924–936.
29. Strimbu, K.; Tavel, J. A. What are Biomarkers? *Curr. Opin. HIV AIDS* **2010**, *5*, 463–466.
30. Biomarkers Definitions Working Group Biomarkers and surrogate endpoints: Preferred definitions and conceptual framework. *Clin. Pharmacol. Ther.* **2001**, *69*, 89–95.
31. Biomarkers and risk assessment: concepts and principles (EHC 155, 1993) <http://www.inchem.org/documents/ehc/ehc/ehc155.htm> (accessed Sep 12, 2016).
32. Mayeux, R. Biomarkers: Potential Uses and Limitations. *NeuroRx* **2004**, *1*, 182–188.
33. PMC.com : Types of Biomarkers [http://www.personalizedmedicinecoalition.org/Education/Types\\_of\\_Biomarkers](http://www.personalizedmedicinecoalition.org/Education/Types_of_Biomarkers) (accessed Sep 12, 2016).
34. Majewski, I. J.; Bernards, R. Taming the dragon: genomic biomarkers to individualize the treatment of cancer. *Nat. Med.* **2011**, 304.
35. Vasan, R. S. Biomarkers of Cardiovascular Disease. *Circulation* **2006**, *113*, 2335–2362.
36. Tumor Markers for Gastrointestinal Cancers <http://www.cancer.net/research-and-advocacy/asco-care-and-treatment-recommendations-patients/tumor-markers-gastrointestinal-cancers> (accessed Sep 1, 2016).
37. Nimse, S. B.; Sonawane, M. D.; Song, K.-S.; Kim, T. Biomarker detection technologies and future directions. *Analyst* **2016**, *141*, 740–755.
38. Sparano, J. A.; Gray, R. J.; Makower, D. F.; Pritchard, K. I.; Albain, K. S.; Hayes, D. F.; Geyer, C. E.; Dees, E. C.; Perez, E. A.; Olson, J. A.; Zujewski, J.; Lively, T.; Badve, S. S.; Saphner, T. J.; Wagner, L. I.; Whelan, T. J.; Ellis, M. J.; Paik, S.; Wood, W. C.; Ravdin, P.; Keane, M. M.; Gomez Moreno, H. L.; Reddy, P. S.; Goggins, T. F.; Mayer, I. A.; Brufsky, A. M.; Toppmeyer, D. L.; Kaklamani, V. G.; Atkins, J. N.; Berenberg, J. L.; Sledge, G. W.

- Prospective Validation of a 21-Gene Expression Assay in Breast Cancer. *N. Engl. J. Med.* **2015**, 373, 2005–2014.
39. Frantzi, M.; Bhat, A.; Latosinska, A. Clinical proteomic biomarkers: relevant issues on study design & technical considerations in biomarker development. *Clin. Transl. Med.* **2014**, 3, 7.
40. Wu, L.; Qu, X. Cancer biomarker detection: recent achievements and challenges. *Chem. Soc. Rev.* **2015**, 44, 2963–2997.
41. pmhdev Cancer - National Library of Medicine <http://www.ncbi.nlm.nih.gov/pubmedhealth/PMHT0015630/> (accessed Sep 12, 2016).
42. Alberts, B.; Johnson, A.; Lewis, J.; Raff, M.; Roberts, K.; Walter, P. *Molecular Biology of the Cell*; 4th ed.; Garland Science, 2002.
43. Man, Y.; Wang, Q.; Kemmner, W. Currently Used Markers for CTC Isolation - Advantages, Limitations and Impact on Cancer Prognosis. *J. Clin. Exp. Pathol.* **2011**, 1.
44. Karachaliou, N.; Mayo-de-las-Casas, C.; Molina-Vila, M. A.; Rosell, R. Real-time liquid biopsies become a reality in cancer treatment. *Ann. Transl. Med.* **2015**, 3.
45. Millner, L. M.; Linder, M. W.; Valdes, R. Circulating Tumor Cells: A Review of Present Methods and the Need to Identify Heterogeneous Phenotypes. *Ann. Clin. Lab. Sci.* **2013**, 43, 295–304.
46. Wit, S. de; Dalum, G. van; Lenferink, A. T. M.; Tibbe, A. G. J.; Hiltermann, T. J. N.; Groen, H. J. M.; van Rijn, C. J. M.; Terstappen, L. W. M. M. The detection of EpCAM+ and EpCAM– circulating tumor cells. *Sci. Rep.* **2015**, 5, 12270.
47. Coumans, F. A. W.; Dalum, G. van; Beck, M.; Terstappen, L. W. M. M. Filtration Parameters Influencing Circulating Tumor Cell Enrichment from Whole Blood. *PLOS ONE* **2013**, 8, e61774.
48. What is the CELLSEARCH® Circulating Tumor Cell (CTC) Test? | CELLSEARCH® <https://www.cellsearchctc.com/about-cellsearch/what-is-cellsearch-ctc-test> (accessed Sep 13, 2016).
49. Pantel, K.; Speicher, M. R. The biology of circulating tumor cells. *Oncogene* **2016**, 35, 1216–1224.
50. pmhdev How do cancer cells grow and spread? *PubMed Health* **2013**.
51. Patient Guide to Tumor Markers | OncoLink <https://www.oncolink.org/cancer-treatment/procedures-diagnostic-tests/blood-tests-tumor-diagnostic-tests/patient-guide-to-tumor-markers> (accessed Sep 14, 2016).
52. Kulasingam, V.; Diamandis, E. P. Strategies for discovering novel cancer biomarkers through utilization of emerging technologies. *Nat. Clin. Pract. Oncol.* **2008**, 5, 588–599.
53. Lescuyer, P.; Hochstrasser, D.; Rabilloud, T. How Shall We Use the Proteomics Toolbox for Biomarker Discovery? *J. Proteome Res.* **2007**, 6, 3371–3376.
54. Sanz-Pamplona, R.; Berenguer, A.; Sole, X.; Cordero, D.; Crous-Bou, M.; Serra-Musach, J.; Guinó, E.; Pujana, M. Á.; Moreno, V. Tools for protein-protein interaction network analysis in cancer research. *Clin. Transl. Oncol.* **2012**, 14, 3–14.
55. Guest, P. C.; Gottschalk, M. G.; Bahn, S. Proteomics: improving biomarker translation to modern medicine? *Genome Med.* **2013**, 5, 17.
56. Wulfkuhle, J. D.; Liotta, L. A.; Petricoin, E. F. Early detection: Proteomic applications for the early detection of cancer. *Nat. Rev. Cancer* **2003**, 3, 267.
57. Duffy, M. J.; Sturgeon, C. M.; Sölétormos, G.; Barak, V.; Molina, R.; Hayes, D. F.; Diamandis, E. P.; Bossuyt, P. M. M. Validation of New Cancer Biomarkers: A Position Statement from the European Group on Tumor Markers. *Clin. Chem.* **2015**, 61, 809–820.
58. Füzéry, A. K.; Levin, J.; Chan, M. M.; Chan, D. W. Translation of proteomic biomarkers into FDA approved cancer diagnostics: issues and challenges. *Clin. Proteomics* **2013**, 10, 13.

59. Darwish, I. A. Immunoassay Methods and their Applications in Pharmaceutical Analysis: Basic Methodology and Recent Advances. *Int. J. Biomed. Sci. IJBS* **2006**, *2*, 217–235.
60. Charles A Janeway, J.; Travers, P.; Walport, M.; Shlomchik, M. J. The structure of a typical antibody molecule. **2001**.
61. Rajpal, A.; Strop, P.; Yeung, Y. A.; Chaparro-Riggers, J.; Pons, J. Introduction: Antibody Structure and Function. In *Therapeutic Fc-Fusion Proteins*; Chamow, S. M.; Ryll, T.; Lowman, H. B.; Farson, D., Eds.; Wiley-VCH Verlag GmbH & Co. KGaA, 2014; pp. 1–44.
62. Merck Millipore An introduction to Antibodies and their applications. *Drug Target Rev.* 2016.
63. Lundblad, R. L. Considerations for the Use of Blood Plasma and Serum for Proteomic Analysis. *Internet J. Genomics Proteomics* **2003**, *1*.
64. Dean, L. *Blood group antigens are surface markers on the red blood cell membrane*; National Center for Biotechnology Information (US), 2005.
65. Charles A Janeway, J.; Travers, P.; Walport, M.; Shlomchik, M. J. Antigen Recognition by B-cell and T-cell Receptors. **2001**.
66. Reverberi, R.; Reverberi, L. Factors affecting the antigen-antibody reaction. *Blood Transfus.* **2007**, *5*, 227–240.
67. Esteban, J. M.; Paxton, R.; Mehta, P.; Battifora, H.; Shively, J. E. Sensitivity and specificity of Gold types 1 to 5 anti-carcinoembryonic antigen monoclonal antibodies: Immunohistologic characterization in colorectal cancer and normal tissues. *Hum. Pathol.* **1993**, *24*, 322–328.
68. Wu, J. T. *Circulating Tumor Markers of the New Millennium: Target Therapy, Early Detection, and Prognosis*; Amer. Assoc. for Clinical Chemistry, 2002.
69. Esscher, T.; Bergh, J.; Steinholtz, L.; Nöu, E.; Nilsson, K.; Pählman, S. Neuron-specific enolase in small-cell carcinoma of the lung: the value of combined immunocytochemistry and serum determination. *Anticancer Res.* **1989**, *9*, 1717–1720.
70. Odelstad, L.; Phlman, S.; Läckgren, G.; Larsson, E.; Grotte, G.; Nilsson, K. Neuron specific enolase: A marker for differential diagnosis of neuroblastoma and Wilms' tumor. *J. Pediatr. Surg.* **1982**, *17*, 381–385.
71. Barry, M. J. Prostate-Specific–Antigen Testing for Early Diagnosis of Prostate Cancer. *N. Engl. J. Med.* **2001**, *344*, 1373–1377.
72. Végvári, Á.; Rezeli, M.; Sihlbom, C.; Häkkinen, J.; Carlsohn, E.; Malm, J.; Lilja, H.; Laurell, T.; Marko-Varga, G. Molecular Microheterogeneity of Prostate Specific Antigen in Seminal Fluid by Mass Spectrometry. *Clin. Biochem.* **2012**, *45*, 331–338.
73. Boyer, J.-C.; Vetrone, F.; Cuccia, L. A.; Capobianco, J. A. Synthesis of Colloidal Upconverting NaYF<sub>4</sub> Nanocrystals Doped with Er<sup>3+</sup>, Yb<sup>3+</sup> and Tm<sup>3+</sup>, Yb<sup>3+</sup> via Thermal Decomposition of Lanthanide Trifluoroacetate Precursors. *J. Am. Chem. Soc.* **2006**, *128*, 7444–7445.
74. Bünzli, J.-C. G. Review: Lanthanide coordination chemistry: from old concepts to coordination polymers. *J. Coord. Chem.* **2014**, *67*, 3706–3733.
75. Armelao, L.; Quici, S.; Barigelletti, F.; Accorsi, G.; Bottaro, G.; Cavazzini, M.; Tondello, E. Design of luminescent lanthanide complexes: From molecules to highly efficient photo-emitting materials. *Coord. Chem. Rev.* **2010**, *254*, 487–505.
76. Bünzli, J.-C. G.; Piguet, C. Taking advantage of luminescent lanthanide ions. *Chem. Soc. Rev.* **2005**, *34*, 1048–1077.
77. Sorace, L.; Gatteschi, D. Electronic Structure and Magnetic Properties of Lanthanide Molecular Complexes. In *Lanthanides and Actinides in Molecular Magnetism*; Layfield, R. A.; Murugesu, M., Eds.; Wiley-VCH Verlag GmbH & Co. KGaA, 2015; pp. 1–26.

78. Charbonnière, L. J.; Hildebrandt, N. Lanthanide Complexes and Quantum Dots: A Bright Wedding for Resonance Energy Transfer (Eur. J. Inorg. Chem. 21/2008). *Eur. J. Inorg. Chem.* **2008**, *2008*, 3231–3231.
79. Han, S.; Deng, R.; Xie, X.; Liu, X. Enhancing Luminescence in Lanthanide-Doped Upconversion Nanoparticles. *Angew. Chem. Int. Ed.* **2014**, *53*, 11702–11715.
80. Bünzli, J.-C. G. On the design of highly luminescent lanthanide complexes. *Coord. Chem. Rev.* **2015**, *293–294*, 19–47.
81. Eliseeva, S. V.; Bünzli, J.-C. G. Lanthanide luminescence for functional materials and bio-sciences. *Chem. Soc. Rev.* **2009**, *39*, 189–227.
82. Bünzli, J.-C. G.; Eliseeva, S. V. Basics of Lanthanide Photophysics. In *Lanthanide Luminescence*; Hänninen, P.; Härmä, H., Eds.; Springer Series on Fluorescence; Springer Berlin Heidelberg, 2010; pp. 1–45.
83. Moore, E. G.; Samuel, A. P. S.; Raymond, K. N. From Antenna to Assay: Lessons Learned in Lanthanide Luminescence. *Acc. Chem. Res.* **2009**, *42*, 542–552.
84. Weissman, S. I. Intramolecular Energy Transfer The Fluorescence of Complexes of Europium. *J. Chem. Phys.* **1942**, *10*, 214–217.
85. Hyppänen, I.; Lahtinen, S.; Ääritalo, T.; Mäkelä, J.; Kankare, J.; Soukka, T. Photon Upconversion in a Molecular Lanthanide Complex in Anhydrous Solution at Room Temperature. *ACS Photonics* **2014**, *1*, 394–397.
86. Heffern, M. C.; Matosziuk, L. M.; Meade, T. J. Lanthanide Probes for Bioresponsive Imaging. *Chem. Rev.* **2014**, *114*, 4496–4539.
87. Xu, J.; Corneillie, T. M.; Moore, E. G.; Law, G.-L.; Butlin, N. G.; Raymond, K. N. Octadentate Cages of Tb(III) 2-Hydroxyisophthalamides: A New Standard for Luminescent Lanthanide Labels. *J. Am. Chem. Soc.* **2011**, *133*, 19900–19910.
88. Luminescent Lanthanide Labels <http://benthamscience.com/journals/current-inorganic-chemistry/volume/1/issue/1/page/2/> (accessed Sep 26, 2016).
89. Gnach, A.; Bednarkiewicz, A. Lanthanide-doped up-converting nanoparticles: Merits and challenges. *Nano Today* **2012**, *7*, 532–563.
90. Wang, F.; Liu, X. Recent advances in the chemistry of lanthanide-doped upconversion nanocrystals. *Chem. Soc. Rev.* **2009**, *38*, 976–989.
91. Hemmer, E.; Yamano, T.; Kishimoto, H.; Venkatachalam, N.; Hyodo, H.; Soga, K. Cytotoxic aspects of gadolinium oxide nanostructures for up-conversion and NIR bioimaging. *Acta Biomater.* **2013**, *9*, 4734–4743.
92. Haase, M.; Schäfer, H. Upconverting Nanoparticles. *Angew. Chem. Int. Ed.* **2011**, *50*, 5808–5829.
93. Shen, J.; Chen, G.; Vu, A.-M.; Fan, W.; Bilsel, O. S.; Chang, C.-C.; Han, G. Engineering the Upconversion Nanoparticle Excitation Wavelength: Cascade Sensitization of Tri-doped Upconversion Colloidal Nanoparticles at 800 nm. *Adv. Opt. Mater.* **2013**, *1*, 644–650.
94. Jayakumar, M. kumara gnanasammandhan; Idris, N. M.; Huang, K.; Zhang, Y. A paradigm shift in the excitation wavelength of upconversion nanoparticles. *Nanoscale* **2014**, *6*, 8441–8443.
95. Bagheri, A.; Arandiyani, H.; Boyer, C.; Lim, M. Lanthanide-Doped Upconversion Nanoparticles: Emerging Intelligent Light-Activated Drug Delivery Systems. *Adv. Sci.* **2016**, *3*, n/a-n/a.
96. Sedlmeier, A.; Gorris, H. H. Surface modification and characterization of photon-upconverting nanoparticles for bioanalytical applications. *Chem. Soc. Rev.* **2015**, *44*, 1526–1560.
97. Boyer, J.-C.; Cuccia, L. A.; Capobianco, J. A. Synthesis of Colloidal Upconverting NaYF<sub>4</sub>: Er<sup>3+</sup>/Yb<sup>3+</sup> and Tm<sup>3+</sup>/Yb<sup>3+</sup> Monodisperse Nanocrystals. *Nano Lett.* **2007**, *7*, 847–852.

98. Boyer, J.-C.; Manseau, M.-P.; Murray, J. I.; van Veggel, F. C. J. M. Surface Modification of Upconverting NaYF<sub>4</sub> Nanoparticles with PEG–Phosphate Ligands for NIR (800 nm) Biolabeling within the Biological Window. *Langmuir* **2010**, *26*, 1157–1164.
99. Liebherr, R. B.; Soukka, T.; Wolfbeis, O. S.; Gorris, H. H. Maleimide activation of photon upconverting nanoparticles for bioconjugation. *Nanotechnology* **2012**, *23*, 485103.
100. Arppe, R.; Hyppänen, I.; Perälä, N.; Peltomaa, R.; Kaiser, M.; Würth, C.; Christ, S.; Resch-Genger, U.; Schäferling, M.; Soukka, T. Quenching of the upconversion luminescence of NaYF<sub>4</sub>:Yb<sup>3+</sup>,Er<sup>3+</sup> and NaYF<sub>4</sub>:Yb<sup>3+</sup>,Tm<sup>3+</sup> nanophosphors by water: the role of the sensitizer Yb<sup>3+</sup> in non-radiative relaxation. *Nanoscale* **2015**, *7*, 11746–11757.
101. Boyer, J.-C.; Veggel, F. C. J. M. van Absolute quantum yield measurements of colloidal NaYF<sub>4</sub>:Er<sup>3+</sup>,Yb<sup>3+</sup> upconverting nanoparticles. *Nanoscale* **2010**, *2*, 1417–1419.
102. Wang, F.; Wang, J.; Liu, X. Direct Evidence of a Surface Quenching Effect on Size-Dependent Luminescence of Upconversion Nanoparticles. *Angew. Chem. Int. Ed.* **2010**, *49*, 7456–7460.
103. Wu, X.; Zhang, Y.; Takle, K.; Bilsel, O.; Li, Z.; Lee, H.; Zhang, Z.; Li, D.; Fan, W.; Duan, C.; Chan, E. M.; Lois, C.; Xiang, Y.; Han, G. Dye-Sensitized Core/Active Shell Upconversion Nanoparticles for Optogenetics and Bioimaging Applications. *ACS Nano* **2016**, *10*, 1060–1066.
104. Prorok, K.; Pawlyta, M.; Stręk, W.; Bednarkiewicz, A. Energy Migration Up-conversion of Tb<sup>3+</sup> in Yb<sup>3+</sup> and Nd<sup>3+</sup> Codoped Active-Core/Active-Shell Colloidal Nanoparticles. *Chem. Mater.* **2016**, *28*, 2295–2300.
105. Chen, B.; Peng, D.; Chen, X.; Qiao, X.; Fan, X.; Wang, F. Establishing the Structural Integrity of Core–Shell Nanoparticles against Elemental Migration using Luminescent Lanthanide Probes. *Angew. Chem. Int. Ed.* **2015**, *54*, 12788–12790.
106. Prorok, K.; Bednarkiewicz, A.; Cichy, B.; Gnach, A.; Misiak, M.; Sobczyk, M.; Stręk, W. The impact of shell host (NaYF<sub>4</sub>/CaF<sub>2</sub>) and shell deposition methods on the up-conversion enhancement in Tb<sup>3+</sup>, Yb<sup>3+</sup> codoped colloidal α-NaYF<sub>4</sub> core–shell nanoparticles. *Nanoscale* **2014**, *6*, 1855–1864.
107. Vetrone, F.; Naccache, R.; Mahalingam, V.; Morgan, C. G.; Capobianco, J. A. Upconverting Nanoparticles: The Active-Core/Active-Shell Approach: A Strategy to Enhance the Upconversion Luminescence in Lanthanide-Doped Nanoparticles (Adv. Funct. Mater. 18/2009). *Adv. Funct. Mater.* **2009**, *19*, NA-NA.
108. Suffren, Y.; Goleosorkhi, B.; Zare, D.; Guénée, L.; Nozary, H.; Eliseeva, S. V.; Petoud, S.; Hauser, A.; Piguet, C. Taming Lanthanide-Centered Upconversion at the Molecular Level. *Inorg. Chem.* **2016**.
109. Algar, W. R.; Massey, M.; Krull, U. J. Semiconductor Quantum Dots and FRET. In *FRET – Förster Resonance Energy Transfer*; Medintz, I.; Hildebrandt, N., Eds.; Wiley-VCH Verlag GmbH & Co. KGaA, 2013; pp. 475–605.
110. Hemmer, E.; Venkatachalam, N.; Hyodo, H.; Hattori, A.; Ebina, Y.; Kishimoto, H.; Soga, K. Upconverting and NIR emitting rare earth based nanostructures for NIR-bioimaging. *Nanoscale* **2013**, *5*, 11339–11361.
111. Hemmer, E.; Benayas, A.; Légaré, F.; Vetrone, F. Exploiting the biological windows: current perspectives on fluorescent bioprobes emitting above 1000 nm. *Nanoscale Horiz.* **2016**, *1*, 168–184.
112. Bruchez, M.; Moronne, M.; Gin, P.; Weiss, S.; Alivisatos, A. P. *Science*. 1998, p. 2013.
113. Warren C. W. Chan; Nie, S. *Science*. 1998, p. 2016.
114. Medintz, I. I.; Uyeda, H. t.; Goldman, E. r.; Mattoussi, H. Quantum dot bioconjugates for imaging, labelling and sensing. *Nat. Mater.* **2005**, *4*, 435–446.
115. Hildebrandt, N. Biofunctional Quantum Dots: Controlled Conjugation for Multiplexed Biosensors. *ACS Nano* **2011**, *5*, 5286–5290.

116. Li, L.; Reiss, P. One-pot Synthesis of Highly Luminescent InP/ZnS Nanocrystals without Precursor Injection. *J. Am. Chem. Soc.* **2008**, *130*, 11588–11589.
117. Wegner, K. D.; Hildebrandt, N. Quantum dots: bright and versatile in vitro and in vivo fluorescence imaging biosensors. *Chem. Soc. Rev.* **2015**, *44*, 4792–4834.
118. Reiss, P.; Carrière, M.; Lincheneau, C.; Vaure, L.; Tamang, S. Synthesis of Semiconductor Nanocrystals, Focusing on Nontoxic and Earth-Abundant Materials. *Chem. Rev.* **2016**, *116*, 10731–10819.
119. Murphy, C. J.; Coffey, J. L. Quantum Dots: A Primer. *Appl. Spectrosc.* **2002**, *56*, 16A–27A.
120. Algar, W. R.; Susumu, K.; Delehanty, J. B.; Medintz, I. L. Semiconductor Quantum Dots in Bioanalysis: Crossing the Valley of Death. *Anal. Chem.* **2011**, *83*, 8826–8837.
121. Clapp, A. R.; Pons, T.; Medintz, I. L.; Delehanty, J. B.; Melinger, J. S.; Tiefenbrunn, T.; Dawson, P. E.; Fisher, B. R.; O'Rourke, B.; Mattoussi, H. Two-Photon Excitation of Quantum-Dot-Based Fluorescence Resonance Energy Transfer and Its Applications. *Adv. Mater.* **2007**, *19*, 1921–1926.
122. Valizadeh, A.; Mikaeili, H.; Samiei, M.; Farkhani, S.; Zarghami, N.; kouhi, M.; Akbarzadeh, A.; Davaran, S. Quantum dots: synthesis, bioapplications, and toxicity. *Nanoscale Res. Lett.* **2012**, *7*, 480.
123. Sapsford, K. E.; Algar, W. R.; Berti, L.; Gemmill, K. B.; Casey, B. J.; Oh, E.; Stewart, M. H.; Medintz, I. L. Functionalizing Nanoparticles with Biological Molecules: Developing Chemistries that Facilitate Nanotechnology. *Chem. Rev.* **2013**, *113*, 1904–2074.
124. Susumu, K.; Uyeda, H. T.; Medintz, I. L.; Pons, T.; Delehanty, J. B.; Mattoussi, H. Enhancing the Stability and Biological Functionalities of Quantum Dots via Compact Multifunctional Ligands. *J. Am. Chem. Soc.* **2007**, *129*, 13987–13996.
125. Mattera, L.; Bhuckory, S.; Wegner, K. D.; Qiu, X.; Agnese, F.; Lincheneau, C.; Senden, T.; Djurado, D.; Charbonnière, L. J.; Hildebrandt, N.; Reiss, P. Compact quantum dot–antibody conjugates for FRET immunoassays with subnanomolar detection limits. *Nanoscale* **2016**, *8*, 11275–11283.
126. Zrazhevskiy, P.; Sena, M.; Gao, X. Designing multifunctional quantum dots for bioimaging, detection, and drug delivery. *Chem. Soc. Rev.* **2010**, *39*, 4326–4354.
127. Sapsford, K. E.; Wildt, B.; Mariani, A.; Yeatts, A. B.; Medintz, I. Materials for FRET Analysis: Beyond Traditional Dye–Dye Combinations. In *FRET – Förster Resonance Energy Transfer*; Medintz, I.; Hildebrandt, N., Eds.; Wiley-VCH Verlag GmbH & Co. KGaA, 2013; pp. 165–268.
128. Bioconjugate Techniques, 3rd Edition | Greg Hermanson | ISBN 9780123822390 <http://store.elsevier.com/Bioconjugate-Techniques/Greg-Hermanson/isbn-9780123822390/> (accessed Jul 29, 2016).
129. van der Meer, B. W. Förster Theory. In *FRET – Förster Resonance Energy Transfer*; Medintz, I.; Hildebrandt, N., Eds.; Wiley-VCH Verlag GmbH & Co. KGaA, 2013; pp. 23–62.
130. Spindel, S.; Granek, J.; Sapsford, K. E. In Vitro FRET Sensing, Diagnostics, and Personalized Medicine. In *FRET – Förster Resonance Energy Transfer*; Medintz, I.; Hildebrandt, N., Eds.; Wiley-VCH Verlag GmbH & Co. KGaA, 2013; pp. 269–322.
131. Masters, B. R. Paths to Förster's resonance energy transfer (FRET) theory. *Eur. Phys. J. H* **2013**, *39*, 87–139.
132. Wiley: Molecular Fluorescence: Principles and Applications, 2nd Edition - Bernard Valeur, Mário Nuno Berberan-Santos <http://eu.wiley.com/WileyCDA/WileyTitle/productCd-3527328378.html> (accessed Sep 15, 2016).
133. Förster, T. Energiewanderung und Fluoreszenz. *Naturwissenschaften* **33**, 166–175.
134. Förster, T. Zwischenmolekulare Energiewanderung und Fluoreszenz. *Ann. Phys.* **1948**, *437*, 55–75.

135. Hildebrandt, N. How to Apply FRET: From Experimental Design to Data Analysis. In *FRET – Förster Resonance Energy Transfer*; Medintz, I.; Hildebrandt, N., Eds.; Wiley-VCH Verlag GmbH & Co. KGaA, 2013; pp. 105–163.
136. Zadran, S.; Standley, S.; Wong, K.; Otiniano, E.; Amighi, A.; Baudry, M. Fluorescence resonance energy transfer (FRET)-based biosensors: visualizing cellular dynamics and bioenergetics. *Appl. Microbiol. Biotechnol.* **2012**, *96*, 895–902.
137. Kohl, T.; Heinze, K. G.; Kuhlemann, R.; Koltermann, A.; Schwille, P. A protease assay for two-photon crosscorrelation and FRET analysis based solely on fluorescent proteins. *Proc. Natl. Acad. Sci.* **2002**, *99*, 12161–12166.
138. Pons, T. Single-Molecule Applications. In *FRET – Förster Resonance Energy Transfer*; Medintz, I.; Hildebrandt, N., Eds.; Wiley-VCH Verlag GmbH & Co. KGaA, 2013; pp. 323–356.
139. Gubala, V.; Harris, L. F.; Ricco, A. J.; Tan, M. X.; Williams, D. E. Point of Care Diagnostics: Status and Future. *Anal. Chem.* **2012**, *84*, 487–515.
140. Meier, R. J.; Simbürger, J. M. B.; Soukka, T.; Schäferling, M. A FRET based pH probe with a broad working range applicable to referenced ratiometric dual wavelength and luminescence lifetime read out. *Chem. Commun.* **2015**, *51*, 6145–6148.
141. Ullman, E. F.; Schwarzbarg, M.; Rubenstein, K. E. Fluorescent excitation transfer immunoassay. A general method for determination of antigens. *J. Biol. Chem.* **1976**, *251*, 4172–4178.
142. Wei, Q.; Lee, M.; Yu, X.; Lee, E. K.; Seong, G. H.; Choo, J.; Cho, Y. W. Development of an open sandwich fluoroimmunoassay based on fluorescence resonance energy transfer. *Anal. Biochem.* **2006**, *358*, 31–37.
143. Chen, M.-J.; Wu, Y.-S.; Lin, G.-F.; Hou, J.-Y.; Li, M.; Liu, T.-C. Quantum-dot-based homogeneous time-resolved fluoroimmunoassay of alpha-fetoprotein. *Anal. Chim. Acta* **2012**, *741*, 100–105.
144. Qiu, X.; Wegner, K. D.; Wu, Y.-T.; van Bergen en Henegouwen, P. M. P.; Jennings, T. L.; Hildebrandt, N. Nanobodies and Antibodies for Duplexed EGFR/HER2 Immunoassays Using Terbium-to-Quantum Dot FRET. *Chem. Mater.* **2016**.
145. Qiu, X.; Hildebrandt, N. Rapid and Multiplexed MicroRNA Diagnostic Assay Using Quantum Dot-Based Förster Resonance Energy Transfer. *ACS Nano* **2015**, *9*, 8449–8457.
146. Heyduk, E.; Heyduk, T. Fluorescent homogeneous immunosensors for detecting pathogenic bacteria. *Anal. Biochem.* **2010**, *396*, 298–303.
147. Wang, R. E.; Tian, L.; Chang, Y.-H. A homogeneous fluorescent sensor for human serum albumin. *J. Pharm. Biomed. Anal.* **2012**, *63*, 165–169.
148. Mathis, G. Rare earth cryptates and homogeneous fluoroimmunoassays with human sera. *Clin. Chem.* **1993**, *39*, 1953–1959.
149. Geißler, D.; Hildebrandt, N. Lanthanide Complexes in FRET Applications. *Curr. Inorg. Chem.* **2011**, *1*, 17–35.
150. Geißler, D.; Linden, S.; Liermann, K.; Wegner, K. D.; Charbonnière, L. J.; Hildebrandt, N. Lanthanides and Quantum Dots as Förster Resonance Energy Transfer Agents for Diagnostics and Cellular Imaging. *Inorg. Chem.* **2014**, *53*, 1824–1838.
151. Wegner, K. D.; Morgner, F.; Oh, E.; Goswami, R.; Susumu, K.; Stewart, M. H.; Medintz, I. L.; Hildebrandt, N. Three-Dimensional Solution-Phase Förster Resonance Energy Transfer Analysis of Nanomolar Quantum Dot Bioconjugates with Subnanometer Resolution. *Chem. Mater.* **2014**, *26*, 4299–4312.
152. Jin, Z.; Geißler, D.; Qiu, X.; Wegner, K. D.; Hildebrandt, N. A Rapid, Amplification-Free, and Sensitive Diagnostic Assay for Single-Step Multiplexed Fluorescence Detection of MicroRNA. *Angew. Chem. Int. Ed.* **2015**, *54*, 10024–10029.

153. DELFIA Time-resolved Fluorescence Assays | Application Support Knowledgebase | Lab Products & Services <http://www.perkinelmer.com/lab-products-and-services/application-support-knowledgebase/delfia/delfia-trf-assays.html> (accessed Sep 29, 2016).
154. HTRF® Technology | Cisbio Bioassays <http://www.cisbio.com/usa/htrf-technology> (accessed Sep 29, 2016).
155. TRACE technology - B·R·A·H·M·S-INSTRUMENTS <http://www.brahms-instruments.com/b%C2%B7r%C2%B7a%C2%B7h%C2%B7m%C2%B7s-kryptor-intro/trace-technology.html> (accessed Sep 29, 2016).
156. LANCE TR-FRET <http://www.perkinelmer.com/category/lance-tr-fret> (accessed Sep 29, 2016).
157. LanthaScreen™ Technology Overview <https://www.thermofisher.com/fr/fr/home/industrial/pharma-biopharma/drug-discovery-development/target-and-lead-identification-and-validation/kinasebiology/kinase-activity-assays/lanthascreen-tr-fret-toolbox/lanthascreen-tr-fret-technology-overview.html#> (accessed Sep 29, 2016).
158. Zhang, P.; Rogelj, S.; Nguyen, K.; Wheeler, D. Design of a Highly Sensitive and Specific Nucleotide Sensor Based on Photon Upconverting Particles. *J. Am. Chem. Soc.* **2006**, *128*, 12410–12411.
159. Zhu, H.; Ding, Y.; Wang, A.; Sun, X.; Wu, X.-C.; Zhu, J.-J. A simple strategy based on upconversion nanoparticles for a fluorescent resonant energy transfer biosensor. *J. Mater. Chem. B* **2014**, *3*, 458–464.
160. Doughan, S.; Uddayasankar, U.; Krull, U. J. A paper-based resonance energy transfer nucleic acid hybridization assay using upconversion nanoparticles as donors and quantum dots as acceptors. *Anal. Chim. Acta* **2015**, *878*, 1–8.
161. Mattsson, L.; Wegner, K. D.; Hildebrandt, N.; Soukka, T. Upconverting nanoparticle to quantum dot FRET for homogeneous double-nano biosensors. *RSC Adv.* **2015**, *5*, 13270–13277.
162. Lahtinen, S.; Wang, Q.; Soukka, T. Long-Lifetime Luminescent Europium(III) Complex as an Acceptor in an Upconversion Resonance Energy Transfer Based Homogeneous Assay. *Anal. Chem.* **2016**, *88*, 653–658.
163. Schäferling, M. Nanoparticle-based luminescent probes for intracellular sensing and imaging of pH. *Wiley Interdiscip. Rev. Nanomed. Nanobiotechnol.* **2016**, *8*, 378–413.
164. Meier, R. J.; Simbürger, J. M. B.; Soukka, T.; Schäferling, M. Background-Free Referenced Luminescence Sensing and Imaging of pH Using Upconverting Phosphors and Color Camera Read-out. *Anal. Chem.* **2014**, *86*, 5535–5540.
165. Arppe, R.; Näreoja, T.; Nylund, S.; Mattsson, L.; Koho, S.; Rosenholm, J. M.; Soukka, T.; Schäferling, M. Photon upconversion sensitized nanoprobes for sensing and imaging of pH. *Nanoscale* **2014**, *6*, 6837–6843.
166. O'Connor, D. V.; Ware, W. R.; Andre, J. C. Deconvolution of fluorescence decay curves. A critical comparison of techniques. *J. Phys. Chem.* **1979**, *83*, 1333–1343.
167. Overview of Photon Counting Techniques. In *Advanced Time-Correlated Single Photon Counting Techniques*; Jr, P. A. W. C.; Toennies, P. J. P.; Zinth, P. W., Eds.; Springer Series in Chemical Physics; Springer Berlin Heidelberg, 2005; pp. 11–25.
168. Becker, W. *The bh TCSPC Handbook*; Becker & Hickl, 2006.
169. Techniques and Methods | PicoQuant [https://www.picoquant.com/scientific/technical-and-application-notes/category/technical\\_notes\\_techniques\\_and\\_methods](https://www.picoquant.com/scientific/technical-and-application-notes/category/technical_notes_techniques_and_methods) (accessed Sep 22, 2016).
170. Degorce, F.; Card, A.; Soh, S.; Trinquet, E.; Knapik, G. P.; Xie, B. HTRF: A Technology Tailored for Drug Discovery –A Review of Theoretical Aspects and Recent Applications. *Curr. Chem. Genomics* **2009**, *3*, 22–32.

171. Chen, Z.-H.; Wu, Y.-S.; Chen, M.-J.; Hou, J.-Y.; Ren, Z.-Q.; Sun, D.; Liu, T.-C. A Novel Homogeneous Time-Resolved Fluoroimmunoassay for Carcinoembryonic Antigen Based on Water-Soluble Quantum Dots. *J. Fluoresc.* **2013**, *23*, 649–657.
172. Wegner, K. D.; Lindén, S.; Jin, Z.; Jennings, T. L.; Khoulati, R. el; van Bergen en Henegouwen, P. M. P.; Hildebrandt, N. Nanobodies and Nanocrystals: Highly Sensitive Quantum Dot-Based Homogeneous FRET Immunoassay for Serum-Based EGFR Detection. *Small* **2014**, *10*, 734–740.
173. Adhyam, M.; Gupta, A. K. A Review on the Clinical Utility of PSA in Cancer Prostate. *Indian J. Surg. Oncol.* **2012**, *3*, 120–129.
174. Bazin, H.; Préaudat, M.; Trinquet, E.; Mathis, G. Homogeneous time resolved fluorescence resonance energy transfer using rare earth cryptates as a tool for probing molecular interactions in biology. *Spectrochim. Acta. A. Mol. Biomol. Spectrosc.* **2001**, *57*, 2197–2211.
175. Bhuckory, S.; Lefebvre, O.; Qiu, X.; Wegner, K. D.; Hildebrandt, N. Evaluating Quantum Dot Performance in Homogeneous FRET Immunoassays for Prostate Specific Antigen. *Sensors* **2016**, *16*, 197.
176. The Molecular Probes Handbook | Thermo Fisher Scientific <https://www.thermofisher.com/fr/fr/home/references/molecular-probes-the-handbook.html> (accessed Jul 28, 2016).
177. Lim, J.; Bae, W. K.; Lee, D.; Nam, M. K.; Jung, J.; Lee, C.; Char, K.; Lee, S. InP@ZnSeS, Core@Composition Gradient Shell Quantum Dots with Enhanced Stability. *Chem. Mater.* **2011**, *23*, 4459–4463.
178. Sjöback, R.; Nygren, J.; Kubista, M. Absorption and fluorescence properties of fluorescein. *Spectrochim. Acta. A. Mol. Biomol. Spectrosc.* **1995**, *51*, L7–L21.
179. Handbook of Optical Materials <https://www.crcpress.com/Handbook-of-Optical-Materials/Weber/p/book/9780849335129> (accessed Jul 27, 2016).
180. Tamang, S.; Beaune, G.; Texier, I.; Reiss, P. Aqueous Phase Transfer of InP/ZnS Nanocrystals Conserving Fluorescence and High Colloidal Stability. *ACS Nano* **2011**, *5*, 9392–9402.
181. Marrian, D. H. 322. The reactions of substituted maleimides with thiols. *J. Chem. Soc. Resumed* **1949**, 1515–1516.
182. Thuy, U. T. D.; Liem, N. Q.; Thanh, D. X.; Protière, M.; Reiss, P. Optical transitions in polarized CdSe, CdSe/ZnSe, and CdSe/CdS/ZnS quantum dots dispersed in various polar solvents. *Appl. Phys. Lett.* **2007**, *91*, 241908.
183. nanoComposix Technical Note - Zeta/pH curves and isoelectric point data for standard nanoComposix silver citrate and PVP nanoparticle dispersions.
184. Greene, K. L.; Albertsen, P. C.; Babaian, R. J.; Carter, H. B.; Gann, P. H.; Han, M.; Kuban, D. A.; Sartor, A. O.; Stanford, J. L.; Zietman, A.; Carroll, P. Prostate Specific Antigen Best Practice Statement: 2009 Update. *J. Urol.* **2013**, *189*, S2–S11.
185. Global Cancer Facts & Figures | American Cancer Society <http://www.cancer.org/research/cancerfactsstatistics/global> (accessed Sep 1, 2016).
186. Ferlay, J.; Soerjomataram, I.; Dikshit, R.; Eser, S.; Mathers, C.; Rebelo, M.; Parkin, D. M.; Forman, D.; Bray, F. Cancer incidence and mortality worldwide: Sources, methods and major patterns in GLOBOCAN 2012. *Int. J. Cancer* **2015**, *136*, E359–E386.
187. Molina, R.; Filella, X.; Augé, J. M.; Fuentes, R.; Bover, I.; Rifa, J.; Moreno, V.; Canals, E.; Viñolas, N.; Marquez, A.; Barreiro, E.; Borrás, J.; Viladiu, P. Tumor markers (CEA, CA 125, CYFRA 21-1, SCC and NSE) in patients with non-small cell lung cancer as an aid in histological diagnosis and prognosis. Comparison with the main clinical and pathological prognostic factors. *Tumour Biol. J. Int. Soc. Oncodevelopmental Biol. Med.* **2003**, *24*, 209–218.

188. Molina, R.; Auge, J. M.; Escudero, J. M.; Marrades, R.; Viñolas, N.; Carcereny, E.; Ramirez, J.; Filella, X. Mucins CA 125, CA 19.9, CA 15.3 and TAG-72.3 as tumor markers in patients with lung cancer: comparison with CYFRA 21-1, CEA, SCC and NSE. *Tumour Biol. J. Int. Soc. Oncodevelopmental Biol. Med.* **2008**, *29*, 371–380.
189. Pfister, C.; Basuyau, J.-P. Current usefulness of free/total PSA ratio in the diagnosis of prostate cancer at an early stage. *World J. Urol.* **2005**, *23*, 236–242.
190. Sturgeon, C. M.; Duffy, M. J.; Stenman, U.-H.; Lilja, H.; Brünner, N.; Chan, D. W.; Babaian, R.; Bast, R. C.; Dowell, B.; Esteva, F. J.; Haglund, C.; Harbeck, N.; Hayes, D. F.; Holten-Andersen, M.; Klee, G. G.; Lamerz, R.; Looijenga, L. H.; Molina, R.; Nielsen, H. J.; Rittenhouse, H.; Semjonow, A.; Shih, I.-M.; Sibley, P.; Sölétormos, G.; Stephan, C.; Sokoll, L.; Hoffman, B. R.; Diamandis, E. P. National Academy of Clinical Biochemistry Laboratory Medicine Practice Guidelines for Use of Tumor Markers in Testicular, Prostate, Colorectal, Breast, and Ovarian Cancers. *Clin. Chem.* **2008**, *54*, e11–e79.
191. Cooper, E. H.; Splinter, T. A. W. Neuron-specific enolase (NSE): A useful marker in small cell lung cancer. *Lung Cancer* **1987**, *3*, 61–66.
192. Ferrigno, D.; Buccheri, G.; Giordano, C. Neuron-specific enolase is an effective tumour marker in non-small cell lung cancer (NSCLC). *Lung Cancer* **2003**, *41*, 311–320.
193. Jennings, T. L.; Becker-Catania, S. G.; Triulzi, R. C.; Tao, G.; Scott, B.; Sapsford, K. E.; Spindel, S.; Oh, E.; Jain, V.; Delehanty, J. B.; Prasuhn, D. E.; Boeneman, K.; Algar, W. R.; Medintz, I. L. Reactive Semiconductor Nanocrystals for Chemoselective Biolabeling and Multiplexed Analysis. *ACS Nano* **2011**, *5*, 5579–5593.
194. HTRF® ratio and data reduction | Cisbio Bioassays <http://www.cisbio.com/drug-discovery/htrf-ratio-and-data-reduction> (accessed Aug 30, 2016).
195. Hilderbrand, S. A.; Shao, F.; Salthouse, C.; Mahmood, U.; Weissleder, R. Upconverting luminescent nanomaterials: application to in vivo bioimaging. *Chem. Commun.* **2009**, 4188–4190.
196. Bogdan, N.; Vetrone, F.; Ozin, G. A.; Capobianco, J. A. Synthesis of Ligand-Free Colloidally Stable Water Dispersible Brightly Luminescent Lanthanide-Doped Upconverting Nanoparticles. *Nano Lett.* **2011**, *11*, 835–840.
197. Yoshimura, Y.; Ohara, K. Thermochemical studies on the lanthanoid complexes of trifluoroacetic acid. *J. Alloys Compd.* **2006**, *408–412*, 573–576.
198. van der Kolk, E.; Dorenbos, P.; Krämer, K.; Biner, D.; Güdel, H. U. High-resolution luminescence spectroscopy study of down-conversion routes in NaGdF<sub>4</sub>:Nd<sup>3+</sup> and NaGdF<sub>4</sub>:Tm<sup>3+</sup> using synchrotron radiation. *Phys. Rev. B* **2008**, *77*, 125110.
199. Aebischer, A.; Heer, S.; Biner, D.; Krämer, K.; Haase, M.; Güdel, H. U. Visible light emission upon near-infrared excitation in a transparent solution of nanocrystalline β-NaGdF<sub>4</sub>:Yb<sup>3+</sup>, Er<sup>3+</sup>. *Chem. Phys. Lett.* **2005**, *407*, 124–128.
200. Liu, C.; Gao, Z.; Zeng, J.; Hou, Y.; Fang, F.; Li, Y.; Qiao, R.; Shen, L.; Lei, H.; Yang, W.; Gao, M. Magnetic/Upconversion Fluorescent NaGdF<sub>4</sub>:Yb,Er Nanoparticle-Based Dual-Modal Molecular Probes for Imaging Tiny Tumors in Vivo. *ACS Nano* **2013**, *7*, 7227–7240.
201. Krämer, K. W.; Biner, D.; Frei, G.; Güdel, H. U.; Hehlen, M. P.; Lüthi, S. R. Hexagonal Sodium Yttrium Fluoride Based Green and Blue Emitting Upconversion Phosphors. *Chem. Mater.* **2004**, *16*, 1244–1251.
202. Zhu, W.; Wu, Q.; Zhao, S.; Liang, Z.; Yang, Y.; Zhang, J.; Xu, Z. Enhanced upconversion fluorescence and altered particle size of β-NaGdF<sub>4</sub>:Yb<sup>3+</sup>/Er<sup>3+</sup> nanocrystals by codoping with Mo<sup>3+</sup> ions. *Opt. Mater. Express* **2016**, *6*, 3001.

NNT : 2016SACLS447

THESE DE DOCTORAT  
DE  
L'UNIVERSITE PARIS-SACLAY  
PREPAREE A  
UNIVERSITE PARIS-SUD

ECOLE DOCTORALE N° 575

Physique et ingénierie : électrons, photons, sciences du vivant  
(Electrical, optical, bio-physics and engineering)

Spécialité de doctorat : Physique

**M. Shashi BHUCKORY**

Boîtes quantiques et nanoparticules à conversion ascendante: Bioconjugaison et spectroscopie multiplexé de FRET résolue en temps pour le diagnostic du cancer

*(SYNTHESE EN FRANÇAIS DU MANUSCRIT DE THESE)*

**Thèse présentée et soutenue à Orsay, le 13.12.2016 :**

**Directeur de thèse :**

**Civilité, Nom, prénom**  
M. Hildebrandt, Niko

**Fonction et établissement d'exercice**  
Professeur, Université Paris-Sud

**Laboratoire**  
NanoBioPhotonique,  
I2BC

**Titre :** Boîtes quantiques et nanoparticules à conversion ascendante: Bioconjugaison et spectroscopie multiplexé de FRET résolue en temps pour le diagnostic du cancer

**Mots clés :** Boîtes quantiques, complexe de lanthanides, FRET, bioconjugaison, nanoparticules à conversion ascendante, spectroscopie résolue en temps

**Résumé :** La haute sensibilité et l'analyse simultanée de plusieurs biomarqueurs (multiplexage) sont des enjeux essentiels pour permettre des avancées significatives pour le diagnostic médical. De telles avancées permettraient d'augmenter la précocité des diagnostics pour de nombreuses maladies comme le cancer ou des maladies cardiaques. Les immunodosages de FRET (transfer d'énergie par resonance de type Förster) sont basées sur la reconnaissance de biomarqueurs par des anticorps marqués avec des fluorophores et le FRET qui résulte du processus de reconnaissance immunologique. Aujourd'hui des telles immunodosages sont établis en utilisant des lanthanides comme donneurs de FRET et des fluorophores organiques comme accepteurs de FRET.

Néanmoins, ils ne permettent pas de réaliser un multiplexage efficace car l'utilisation de plusieurs différents fluorophores organiques résulte dans un recouvrement spectral. Ce projet a pour but de mettre en application les propriétés optiques exceptionnelles des complexes de terbium (Tb) et des boîtes quantiques (QDs) pour parvenir à des analyses biologiques de FRET multiplexées et ultrasensibles. Nous avons également étudié les propriétés optiques et morphologiques de nouvelles nanoparticules à conversion ascendante de type coeur et coeur/coquille dopées à l'ytterbium (Yb) et des ions d'erbium (Er) comme donneurs de FRET.

## 10. Synthèse en français

Le but de cette thèse est d'utiliser les propriétés photophysiques exceptionnelles des complexes de terbium (Tb) et des boîtes quantiques (QDs) pour la détection des marqueurs cancéreux protéiniques par des immunodosages multiplexés ultrasensibles de transfert d'énergie par résonance de type Förster résolue en temps (TR-FRET), ainsi que l'étude des propriétés optiques et morphologiques de nouvelles nanoparticules à conversion ascendante de type cœur et cœur/coquille dopées à l'ytterbium (Yb) et des ions d'erbium (Er) comme donneurs de FRET potentiel pour des biocapteurs. Le FRET est un transfert d'énergie non radiatif entre deux molécules et est fortement dépendant de la distance. Le transfert d'énergie non radiatif se produit à partir d'une molécule excitée (donneur de FRET) vers une molécule acceptrice (accepteur de FRET) dans son état fondamental par des interactions dipôle-dipôle à longue portée. Le donneur de FRET doit être un fluorophore et l'accepteur de FRET doit être capable d'absorber la lumière à la (les) longueur (s) d'émission du donneur mais n'a pas nécessairement besoin de réémettre des photons. Pour que le FRET se produise, le spectre d'émission du donneur doit se recouvrir avec le spectre d'absorption de l'accepteur, il faut donc prendre grand soin en choisissant les paires de FRET appropriées pour les expériences planifiées. Ce recouvrement spectral peut être décrit en termes de distance de Förster ( $R_0$ ), qui définit la distance entre le donneur et l'accepteur pour lequel l'efficacité de FRET est de 50%. Il existe une multitude de paires de FRET pour la bioanalyse, parmi lesquelles on peut trouver des colorants organiques, des protéines fluorescentes, des chélates métalliques (par exemple des complexes de lanthanides) et des nanocristaux semi-conducteurs (boîtes quantiques). Le  $R_0$  typique entre les colorants et/ou les protéines fluorescentes est généralement compris entre 2 et 5 nm et peut s'étendre jusqu'à 11 nm en utilisant des lanthanides et des boîtes quantiques. La forte dépendance en distance de  $r^{-6}$ , où  $r$  correspond à la distance entre les paires de FRET, permet d'obtenir des informations sur des petits changements structuraux dans les processus biologiques, des données cinétiques de réactions et des interactions de liaison biologiques entre autres. Le FRET se déroule généralement à une distance *c.a* 1-10 nm qui est comparable aux dimensions de la plupart des interactions biologiques. Dans le cas d'une reconnaissance anticorps-antigène, lorsqu'une paire de FRET marquée sur des anticorps spécifiques pour une reconnaissance spécifique de la cible (antigène) est rapprochée, des changements dans les propriétés photophysiques des paires de FRET apparaissent du fait du transfert d'énergie, qui dépend de la distance entre les paires de FRET [6-9]. Pour les immunodosages de TR-FRET, des anticorps monoclonaux (ABs) contre des marqueurs biologiques (antigènes) de différente masse moléculaire – antigène carcinoembryonnaire (CEA), émolase spécifique des neurones

(NSE) et antigène prostatique spécifique (TPSA) – ont été marqués aux Tb (donneur de FRET) et aux QDs (accepteurs de FRET) émettant à différentes longueurs d'ondes. En présence des antigènes, l'immunodosage provoque la formation de [AB-donneur]-antigène-[AB-accepteur] qui résulte en un rapprochement de Tb et QD suivi de FRET. Il convient de noter que dans notre immunodosage de FRET, l'efficacité de FRET pour plusieurs Tb-donneur par QD-accepteur ne change pas par rapport à un système donneur / accepteur unique. Cependant, il y a une probabilité accrue de QDs qui soient sensibilisés par le FRET avec un nombre croissant de Tb-donneurs en raison de la longue durée de vie lumineuse du Tb [18, 19]. L'utilisation de QDs avec des revêtements épais et de grandes biomolécules telles que les IgG et des antigènes relativement grands, dans un format [AB-donneur]-antigène-[AB-accepteur], pourrait affecter l'efficacité du FRET, par conséquent la sensibilité de détection due à la forte dépendance de distance entre les paires de FRET [7].

La première étude (**Chapitre 3**) démontre la possibilité de surmonter les grandes distances dans des immunodosages de FRET homogènes et de fournir simultanément une grande sensibilité et capacité de multiplexage dans l'utilisation de complexes de terbium luminescents en tant que donneurs de FRET pour des QD revêtus d'un polymère poly(éthylène)glycol (PEG) épais comme accepteurs. Les conjugués Tb-AB ont été obtenus par un marquage entièrement aléatoire de Tb-NHS via divers groupes amino disponibles sur les anticorps. Dans un couplage moins aléatoire, trois QDs disponibles dans le commerce avec des longueurs d'ondes maxima d'émission à 605, 655 et 705 nm (dénommés respectivement QD605, QD655 et QD705) de Life Technologies possédant un revêtement épais de polymère PEG fonctionnalisé par des amines (QD-amino) ont été conjugués à des anticorps fragmentés (F(ab)) par la chimie sulfhydryle [20]. Ces QD-amino ont été convertis en QD-maléimide en utilisant le réticulant hétérobifonctionnel sulfo-EMCS possédant les groupes NHS ester et maléimide [21]. Les QDs activés par la maléimide ont été conjugués au F(ab), par l'intermédiaire de groupes sulfhydryle libres, qui se révèlent avantageux pour les immunodosages de FRET en raison de leur plus petite taille et de la plus grande quantité d'ABs par QD [20]. La performance de nos immunodosages a été évaluée avec les QD605, QD655 et QD705 comme accepteurs avec Tb comme donneurs de FRET car les variations de formes, de tailles, de chevauchement spectral et de leur photoluminescence conduisent à des différences en efficacité de FRET et de détection. Les propriétés photophysiques (stationnaire et résolue en temps) des conjugués Tb-AB et QD-AB, et leurs performances dans les immunodosages de FRET pour la détection de PSA dans de faibles volumes de sérum ont été réalisées. Une telle caractérisation et évaluation dans des immunodosages comparables pour le même antigène sont indispensables pour concevoir et optimiser de tels immunodosages de FRET homogènes, en particulier pour la détection

multiplexée. Le calcul des intégrales de recouvrement a abouti à un  $R_0$  important pour tous les systèmes Tb-QD et a permis une sensibilisation mesurable du QD par FRET dans le système [Tb-AB]-PSA-[QD-AB], même avec un revêtement épais des QDs. Les trois systèmes de FRET, Tb-à-QD, montraient des signaux de FRET à sélection temporelle croissants avec des concentrations de PSA croissantes. Les courbes d'étalonnage correspondant aux trois immunodosage de FRET ont pu être tracées avec succès et les limites de détection (LOD) calculées à l'aide de ces courbes d'étalonnage ont montré la sensibilité la plus élevée (faible LOD) pour le système Tb-QD705 suivi des systèmes Tb-QD655 et Tb-QD605. Nous montrons également que des facteurs comme les rapports de marquage,  $R_0$  et le bruit de fond de la photoluminescence du terbium influent sur la sensibilité de détection. On a aussi démontré la capacité de multiplexer en utilisant différentes paires de FRET de Tb-QD en préparant un immunodosage duplexé contre la PSA qui contenait deux conjugués de QDs (QD655 et QD705) avec les LOD les plus faibles. Leurs courbes d'étalonnage suivaient une tendance similaire qu'avec les paires de FRET dans un immunodosage simple. Les LOD pour la PSA dans 50  $\mu$ L d'échantillons de sérum mesurés sur un lecteur de plaques de fluorescence clinique disponible dans le commerce se situaient dans la gamme de concentration sub-nanomolaire et inférieure à la valeur de seuil clinique de 4 ng/mL pour les paires de FRET basées sur QD655 et QD705. Comme la plupart des biomarqueurs ont des valeurs de seuil clinique différentes, nous avons également conclu que QD705 devrait être utilisé pour le biomarqueur avec la plus faible coupure et QD605 pour celui avec le plus haut seuil. La capacité de duplexage a été démontrée dans des dosages de PSA contenant à la fois des conjugués QD655-AB et QD705-AB. Nos résultats fournissent des informations importantes concernant le développement d'immunodosages de FRET basés sur les QDs pour le diagnostic clinique multiplexé parce que la méthode de conjugaison avec les anticorps que nous avons développée est applicable à tous les QDs fonctionnalisés à l'amine disponible dans le commerce, qui existe dans beaucoup d'autres couleurs que les trois utilisés dans cette étude.

La deuxième étude se porte sur une nouvelle approche de fonctionnalisation et bioconjugaison de QD, qui a abouti à des QDs compactes et stables, et des conjugués QD-AB hautement luminescents afin d'améliorer l'immunodosage de TR-FRET Tb-QD contre le PSA. Ces QDs ont été synthétisés par le laboratoire INAC-SyMMES, du CEA Grenoble. Sur la base des résultats de la première étude mettant en jeu des QD avec un revêtement polymère épais qui montrent la possibilité de détecter la PSA dans une gamme de concentration sub-nanomolaire, la conception de QD compacts permettrait de surmonter les limitations majeures pour le développement d'immunodosages de FRET basés sur des QDs avec des LOD concurrentielles à des kits commerciaux qui sont: (i) une stabilité colloïdale insuffisante des QD

compacts dans les milieux biologiques, (ii) des revêtements de surface QD épais (par exemple PEG, polymères ou des revêtements lipidiques qui protègent la QD inorganique de l'environnement biologique et les rendent hydrosolubles) (iii) les stratégies limitées de conjugaison avec des anticorps pour les QDs avec des couches organiques plus minces. Pour cela, le transfert de phase aqueuse des QDs InPZnS/ZnSe/ZnS émettant à 530 nm (QD530) et des QDs commerciales CdSe/ZnS hydrophobes (Life Technologies) émettant à 605 et 705 nm (QD605 et QD705 respectivement) a été effectué par échange de ligands avec la pénicillamine zwitterionique (Pen). La post-fonctionnalisation a été réalisée pour produire des QDs activés par maléimide en utilisant un ligand bifonctionnel Mal1 contenant une fonction d'ancrage d'acide lipoïque, espacé par trois fragments PEG avec un groupe fonctionnel maléimide pour la conjugaison avec les thiols des F(ab). Nous montrons également pour la première fois une autre stratégie de post-fonctionnalisation qui impliquait le couplage direct d'anticorps (IgGs, F(ab')<sub>2</sub> et F(ab)) à la surface du QD705 compacte (sensibilité la plus élevée) sans aucun agent de réticulation, qui a pour objectif de réduire d'avantage la distance de transfert d'énergie entre Tb-donneur et QD-accepteur. L'analyse par TEM a été réalisée sur les QDs pour confirmer leur taille et leur dispersibilité tandis que les spectres infrarouges à transformée de Fourier (FTIR) et gel-agarose ont prouvé la fonctionnalisation et la conjugaison réussies avec Mal1 et F(ab) respectivement. Pour ces couples Tb-QD FRET, on a calculé des R<sub>0</sub> élevés révélant un R<sub>0</sub> le plus grand pour QD705 et de petites variations des propriétés photophysiques des QD à différents stades de transfert de phase, post-fonctionnalisation avec Mal1 et lors de la conjugaison avec F(ab) ont été observé. Dans cette étude, seule une caractérisation photophysique complète de la conjugaison directe des IgG à QD705 a été réalisée en raison des faibles concentrations collectées après purification provenant de la conjugaison directe avec F(ab')<sub>2</sub> et de F(ab). Les immunodosages de FRET contre la PSA dans des échantillons à base de sérum, en utilisant des QD conjugués à F(ab) via Mal1, correspondant aux systèmes Tb-QD605/705, ont permis la quantification de la LOD, alors que l'essai Tb-QD530 a donné un signal de FRET très faible probablement liée au R<sub>0</sub> petit (6,1 nm), qui n'a pas pu être utilisé pour calculer un LOD. Les dosages de FRET de Tb-QD705 en utilisant la conjugaison directe des anticorps à la surface du QD a fourni des sensibilités encore meilleures comparés aux Mal1. LODs des deux immunoessais Tb-QD FRET (utilisant des QDs émettant à 605 nm et 705 nm) sont non seulement bien en deçà de la valeur seuil clinique du PSA (4 ng/mL), mais l'utilisation des conjugués QD-AB compacts ont également fourni une amélioration de la sensibilité de 6,2 et 25 fois par rapport aux mêmes QD disponibles dans le commerce avec un revêtement à base de PEG/polymère standard comme utilisé dans la première étude. Ces immunodosages Tb-à-QD FRET hautement sensibles et homogènes conviennent à tout autre biomarqueur contre lequel

deux anticorps spécifiques existent. Nos résultats montrent que les conjugués QD-AB compacts ont un grand potentiel pour améliorer les applications diagnostiques et compte tenu de la capacité de multiplexage de Tb-QD FRET, nous sommes convaincus que ces nano-sondes fluorescentes deviendront des acteurs importants du diagnostic clinique *in vitro*.

Dans la troisième étude, nous tentons de détecter les antigènes CEA, NSE et TPSA se trouvant dans un seul échantillon à base de sérum. L'importance de détecter plusieurs biomarqueurs réside dans le fait qu'un seul biomarqueur ne contient pas suffisamment d'informations pour établir un diagnostic clair sur une maladie et que la combinaison de différents biomarqueurs augmente le contenu des informations sur l'état ou le type de cancer. Le CEA et le NSE sont parmi les marqueurs tumoraux où leurs niveaux sont surveillés en combinaison avec d'autres marqueurs tumoraux pour obtenir un diagnostic clair de cancer du poumon à petites cellules (SCLC) et / ou de cancer du poumon non à petites cellules (NSCLC) et TPSA (somme du PSA libre et du PSA lié à des protéines) qui est un marqueur tumoral pour le cancer de la prostate. Comme le FRET est très dépendant de la distance, le choix de la conjugaison avec F(ab')<sub>2</sub> aux QDs donnerait une distance de séparation plus courte entre les QD et Tb dans les immunodosages de FRET « en sandwich », donc des efficacités et des sensibilités de FRET plus élevées que lors de l'utilisation des IgG. En outre, la petite taille des F(ab')<sub>2</sub> simultanément avec ses 2 sites antigéniques pour une plus grande probabilité de liaisons avec les antigènes, serait bénéfique pour les tailles de biomarqueurs croissantes (32 kDa à 180 kDa) dans les immunodosages de FRET. On a réalisé des caractérisations photophysiques des paires de FRET (Tb-donneur et QD-accepteur) et les rapports de marquage de Tb/AB et QD/AB ont été estimés par spectroscopie d'absorption UV/Vis. Comme la première étude a suggéré que pour différentes valeurs de seuil clinique QD705 devrait être utilisé pour le biomarqueur avec la plus faible coupure et QD605 pour celui avec la plus haute coupure, les anticorps contre CEA, NSE et TPSA ont été conjugués aux QDs provenant de eBioscience : eQD650, eQD605 ; et Life Technologies QDs iQD705 respectivement. Notre immunodosage de Tb-QD FRET multiplexé a été capable de détecter simultanément 3 marqueurs tumoraux de taille différente à partir d'un seul échantillon de sérum de CEA (180 kDa), NSE (95 kDa) et PSA (32 kDa) en utilisant des sondes Tb et QD conjuguées à leur anticorps monoclonaux respectifs ne conférant aucune interférence biologique. En utilisant les spectres d'émission étroits et Gaussiens des QD et les bandes d'émission de Tb bien séparées avec des filtres passe-bande appropriés, a permis une interférence optique négligeable. Par conséquent, aucune correction matricielle n'a été nécessaire pour déterminer la concentration des marqueurs tumoraux. Les LODs calculées dans des échantillons à base de sérum de volume 50 µL étaient toutes en dessous des limites de seuil clinique des marqueurs tumoraux, où des LOD plus élevées ont été observées pour le

format triplexé par rapport au format simple sauf pour TPSA. La contamination des canaux de détection eQD605/650 avec un signal de Tb 3 fois plus élevé (pour le format triplexé) a entraîné une augmentation de LOD alors que pratiquement aucune émission de Tb ne peut être détectée dans le canal de détection de l'iQD705. Un «scénario le plus défavorable» a été effectué lorsque nous avons testé notre dosage immunologique de FRET avec une combinaison de concentrations cibles élevées et faibles. Dans l'ensemble, le CEA et la TPSA pouvaient être détectés avec une grande précision, avec des écarts mineurs par rapport aux concentrations connues, à l'exception de la NSE qui présentait une sous-estimation dans ses concentrations dans une gamme de concentration spécifique avec une combinaison de concentrations élevées et faibles de CEA et de faibles concentrations de TPSA. Les limites de détection des marqueurs tumoraux dans la gamme sub-nanomolaire (quelques ng/mL) dans un environnement complexe comme dans le sérum et contenant 9 biomolécules différentes prouvent l'applicabilité immédiate aux applications de diagnostic pour des mesures multiplexées sensibles.

La quatrième étude a consisté à étudier des fluorophores de nouvelle génération, connus sous le nom de nanoparticules à conversion ascendante (UCNP). La conversion ascendante est un processus où la lumière à basse énergie (proche infrarouge (NIR) ou infrarouge (IR)) est convertie en énergie plus élevée (ultraviolette ou visible) au moyen d'absorptions multiples de photons ou de transferts d'énergie, dans un processus non linéaire [22,23]. Cette propriété (entre autres) leur permet de posséder un grand potentiel dans l'imagerie et la biodétection dans des applications *in vitro* et *in vivo* [22]. Similaires aux complexes de lanthanides, les UCNP dopés par les lanthanides possèdent des bandes d'émission très étroites dans le visible, ce qui leur permet de fonctionner comme donneurs d'énergie avec un assortiment d'accepteurs dans la biodétection à base de FRET. Trois types d'UCNPs ont été analysés dans cette thèse afin de choisir le meilleur candidat en tant que donneur de FRET. Nos collaborateurs de l'Institut National de la Recherche Scientifique (INRS) du Québec Canada, ont synthétisé des UCNP de type cœur et cœur/coquille -  $\text{NaGdF}_4:\text{Er}^{3+}, \text{Yb}^{3+}$  (cœur-dopé),  $\text{NaGdF}_4:\text{Er}^{3+}, \text{Yb}^{3+} / \text{NaGdF}_4$  (cœur-dopé/coquille) et  $\text{NaGdF}_4/\text{NaGdF}_4:\text{Er}^{3+}, \text{Yb}^{3+}$  (cœur/coquille-dopé). Ces UCNP ont été rendues « ligand-free » et la fonctionnalisation de surface avec l'amino-PEG-COOH a été réalisée par interaction électrostatique afin de générer des groupes fonctionnels à la surface des UCNP pour une éventuelle conjugaison avec des biomolécules. Les mesures TEM des UCNP ont montré des particules plutôt sphériques et les graphes XRD ont montré qu'ils sont cristallins et la comparaison avec le modèle de référence a révélé une structure hexagonale  $\beta$ -de  $\text{NaGdF}_4$ . Les spectres FTIR ont confirmé la présence du polymère amino-PEG-COOH à la surface des UCNP. Les mesures DLS ont montré que les trois types de PEGylated-UCNP

n'étaient pas du tout stable dans divers tampons, y compris les tampons physiologiques où des agrégats ont été observés. Par conséquent, des stratégies optimisées de fonctionnalisation de surface doivent être envisagées afin de produire une bonne dispersibilité dans des tampons car la conjugaison avec des biomolécules nécessite souvent l'utilisation de tampons de pH différent. On a observé une émission de conversion ascendante dans le visible du spectre électromagnétique pour les trois UCNPs après excitation à 980 nm. Les émissions dans le vert se sont produites aux états de transition suivants: ( $^2H_{11/2}$ ,  $^4S_{3/2}$ )  $\rightarrow$   $^4I_{15/2}$  et l'émission dans le rouge :  $^4F_{9/2} \rightarrow ^4I_{15/2}$ . En comparaison avec les UCNPs cœur/coquille, le temps de vie des nanoparticules cœur-dopé est plus petite et peut être attribuée à l'effet d'atténuation des ions  $Er^{3+}$  à la surface du cœur par des modes d'énergie vibrationnelle élevés des groupes OH correspondant au solvant environnant. L'enrobage du cœur-dopé par une coquille supprime grandement les effets d'atténuation de surface et apporte une meilleure protection entre le cœur et le solvant environnant. Les nanoparticules cœur/coquille-dopé ont montré des temps de vie luminescente longue et inattendue par rapport aux nanoparticules cœur-dopé/coquille, ce qui les favorise pour être des donneurs de FRET adéquats, car la présence d'ions  $Er^{3+}$  à la surface donnerait un FRET efficace avec une molécule accepteur proche de cette surface.

**Titre :** Boîtes quantiques et nanoparticules à conversion ascendante: Bioconjugaison et spectroscopie multiplexé de FRET résolue en temps pour le diagnostic du cancer

**Mots clés :** Boîtes quantiques, complexe de lanthanides, FRET, bioconjugaison, nanoparticules à conversion ascendante, spectroscopie résolue en temps

**Résumé :** La haute sensibilité et l'analyse simultanée de plusieurs biomarqueurs (multiplexage) sont des enjeux essentiels pour permettre des avancées significatives pour le diagnostic médical. De telles avancées permettraient d'augmenter la précocité des diagnostics pour de nombreuses maladies comme le cancer ou des maladies cardiaques. Les immunodosages de FRET (transfert d'énergie par résonance de type Förster) sont basées sur la reconnaissance de biomarqueurs par des anticorps marqués avec des fluorophores et le FRET qui résulte du processus de reconnaissance immunologique. Aujourd'hui des telles immunodosages sont établis en utilisant des lanthanides comme donneurs de FRET et des fluorophores organiques comme accepteurs de FRET.

Néanmoins, ils ne permettent pas de réaliser un multiplexage efficace car l'utilisation de plusieurs différents fluorophores organiques résulte dans un recouvrement spectral. Ce projet a pour but de mettre en application les propriétés optiques exceptionnelles des complexes de terbium (Tb) et des boîtes quantiques (QDs) pour parvenir à des analyses biologiques de FRET multiplexées et ultrasensibles. Nous avons également étudié les propriétés optiques et morphologiques de nouvelles nanoparticules à conversion ascendante de type coeur et coeur/coquille dopées à l'ytterbium (Yb) et des ions d'erbium (Er) comme donneurs de FRET.

**Title :** Quantum dots and upconverting nanoparticles: Bioconjugation and time-resolved multiplexed FRET spectroscopy for cancer diagnostics

**Keywords :** Quantum dots, lanthanide complex, FRET, bioconjugation, upconverting nanoparticles, time-resolved spectroscopy

**Abstract :** Combining high sensitivity with simultaneous analysis of numerous biomarkers (multiplexing) is an essential requirement for significantly improving the field of biomedical diagnostics. Such progresses would allow earlier diagnosis, which is required for numerous diseases such as cancer or cardiac diseases. FRET-immunoassays are based on biomolecular recognition events that occur between biomarkers and two specific antibodies conjugated with different fluorophores. The spatial proximity of the two fluorophores can lead to Förster resonance energy transfer (FRET), which can be detected for biomarker quantification. To date, such assays are established using lanthanide complexes as FRET donors and fluorescence dyes as FRET acceptors.

However, these assays do not provide sufficient multiplexing capability due to spectral overlap, when several acceptor dyes are used. This project aims at exploiting the exceptional photophysical properties of terbium complexes (Tb) and semiconductor quantum dots (QDs) to provide ultrasensitive multiplexed FRET-immunoassays. We also studied the optical and morphological properties of novel core and core/shell upconverting nanoparticles doped with ytterbium (Yb) and erbium (Er) ions as possible FRET-donors for biosensing.

